INVESTIGATING THE TOPOGRAPHIC UNDULATIONS ALONG LAVA CHANNELS ON VENUS

by

SYDNEY BRIGGS

(Under the Direction of Christian Klimczak)

ABSTRACT

Around 80% of the Venusian surface is covered by volcanic plains containing prominent, sinuous, and canali-like lava channels called valles that are hundreds to thousands of kilometers long and maintain constant widths of several kilometers. Along these channels, the topography has changed, which has previously only been reported along Baltis Vallis caused by long-wavelength and short-wavelength topographic undulations from regional uplift, subsidence, or local structures (faults, volcanoes, craters). I conducted a global survey of the channels and mapped 33 using a systematic mapping approach to extract geologic observations, topography, and dynamic topography to document the commonality and nature of these topographic undulations. Many observations are explained by dynamic topography, and it is one of the youngest phenomena to affect the surface. These findings imply that mantle convection is responsible for many topographic changes and that it plays an important role in heat transfer and internal processes on Venus.

INDEX WORDS: Venus, Lava Channels, Surface Deformation, Mantle Convection

INVESTIGATING THE TOPOGRAPHIC UNDULATIONS ALONG LAVA CHANNELS ON VENUS

by

SYDNEY BRIGGS

BS, University of Alabama, 2021

A Thesis Submitted to the Graduate Faculty of The University of Georgia in Partial Fulfillment of the Requirements for the Degree

MASTER OF SCIENCE

ATHENS, GEORGIA

2023

INVESTIGATING THE TOPOGRAPHIC UNDULATIONS ALONG LAVA CHANNELS ON VENUS

by

SYDNEY BRIGGS

Major Professor:	Christian Klimczak
Committee:	Peter James
	Rob Hawman

Electronic Version Approved:

Ron Walcott
Vice Provost for Graduate Education and Dean of the Graduate School
The University of Georgia
May 2023

DEDICATION

To Porthos.

ACKNOWLEDGEMENTS

I want to express my gratitude to my advisor, Christian Klimczak. His insight, instruction, and enduring patience with me have made me push harder than I thought possible. I did not enter graduate school as a researcher, but there is hope for me now, and it's due to Christian. He has made me excited to be curious.

Thank you so much to my committee members, Dr. Peter James at Baylor University and Dr. Rob Hawman, for their contributions to my work. Dr. Peter James was invaluable in this research and instructed me continuously.

The Department of Geology at the University of Georgia has been an amazing support system. The generous grants they awarded allowed me to conduct this research and present it to my peers at the Lunar and Planetary Science Conference. The friendship through fellow graduate students, both commiserating and celebratory, kept me grounded during difficult weeks. Long live the grad lounge!

My labmates, you crazy fools. Stevie, Jupiter, and Aliyu have made me laugh, answered all my 1.36 million questions, been worthy board game adversaries, and truly supported me through this time in my life. I pray that I have been as good of a labmate and friend to each of you.

Thank you to my family. Your love is the only reason I'm able to be here.

Drew, this is for you and the life we're building together.

TABLE OF CONTENTS

Page

LIST OF TABLES

Page

LIST OF FIGURES

Page

CHAPTER 1

INTRODUCTION

Venus and Earth are close in size and mass, and thus they are similar in mean density. These characteristics, as well as their neighboring positions in the solar system, suggest that they are twin planets and formed of the same material, following the same evolutionary path. However, the surface conditions on Venus are far more extreme than those of Earth, with an average temperature of 867 degrees Fahrenheit and a surface pressure 91 times higher than Earth (Walker, 1975). The planet is shrouded in thick sulfuric acid clouds that obscure view of the surface, preventing visible—thermal wavelengths that have been used to image the Moon, Mars, and Mercury (Gilmore et al., 2017). Research on Venus requires close range equipment such as landers, which survive only a brief time before pressure crushes them, and orbiters, which use non-visible light equipment, such as radar. We have successfully visited Venus with 10 landers and 9 orbiters from the Soviet Union, the United States, Europe, and Japan (Williams, 2022). One of these orbiters, NASA's Magellan mission, used synthetic aperture radar (SAR) in the late 1980s and mapped over 98% of the surface, creating the most complete datasets to date (Ford et al., 1993; Saunders et al., 1992).

Other than the Moon, Venus is the next closest planetary body to Earth and yet we know comparatively little about the surface processes, the interior dynamics, or geologic history. Deepening our understanding of our closest planetary neighbor can reveal more about our solar system and its formation as well as improve our understanding of

habitability of exoplanets in other solar systems that lie within the Venus range (Kane et al., 2019). Looking toward the future, NASA and ESA have announced the new orbiter or lander missions, namely Venus Emissivity, Radio science, InSAR, Topography, And Spectroscopy (VERITAS), Deep Atmosphere Venus Investigation of Noble gases, Chemistry, and Imaging (DAVINCI+), and EnVision, that will be launching for Venus within the upcoming decade to try and answer some of these questions (Williams, 2022).

1.1 Volcanism on Venus

On Earth, convergent and divergent plate boundaries endlessly recycle the lithosphere, and volcanism is the result of subduction zones, mid-ocean ridges, or other settings (Airey et al., 2017). The surface dynamics of Venus differ from Earth because volcanism is worldwide, with over 80% of the surface covered in volcanic plains (Basilevsky & Head, 2003; Ford et al., 1993). Due to this, the volcanic activity and features have been greatly studied. Initial surveys of the preliminary data found over 1660 volcanic features, which include both extrusive and intrusive centers of volcanism as well as flow features (Head et al., 1992). The crust is mostly basaltic and similar in composition to Earth, and it likely formed mostly due to effusive volcanism (Head et al., 1992; Kargel et al., 1993; Nimmo & McKenzie, 1998). However, some studies have found variation in the mineralogy between different volcanoes, lava flows, and even different locations within the same flow (Bromiley & Law, 2020; Brossier et al., 2020; Brossier et al., 2021). This crust is much younger than Venus itself, a result of an either gradual or rapid lithospheric overturn by an unknown process that obscured or erased the oldest parts of the geologic history (Smrekar et al., 2010; Strom et al., 1994; Turcotte, 1993).

Despite the lack of new missions and data from Venus, scientists are trying to answer if Venus currently has active volcanism. Current volcanic activity could mean that Venus is still resurfacing (Smrekar et al., 2010) and would further our understanding of the current tectonic regime and the past life of Venus (Rolf et al., 2022). Studies have looked at changes in the SO_2 composition pointing to episodic volcanism (Esposito et al., 1988), surface emissivity to discuss lava flow compositional variation (Smrekar et al., 2010), olivine weathering rates and the lack thereof observed (Filiberto et al., 2020), and local surface temperature anomalies that are interpreted as eruptions (Shalygin et al., 2015) as well as other characteristics to discuss the volcanic activity. These studies all conclude that Venus must currently be volcanically active.

While most of the volcanism on Venus is primarily plains-forming (Basilevsky & Head, 2003), other volcanic features are global and abundant. Colles (sing. collis) are defined as small hills or knobs by the International Astronomical Union (IAU), and they are mapped as shield plains; however, most shield plains have not been labeled as colles (Tanaka et al., 1997). Coronae (sing. corona) are described as ovoid-shaped features, defined by concentric fractures, and they are associated with both volcanism and tectonism (Stofan et al., 1997). They are classified as intrusive volcanism caused by magma movement in the mantle and often interpreted as mantle upwelling locations (Crumpler et al., 1997; Ford et al., 1993). Farra (sing. farrum) and tholi (sing. tholus) are IAU descriptor terms for intermediate-size volcanoes (~20-100 km diameter), with farra describing a pancake-like structure and tholi describing domical shapes (Head et al., 1992; Russell & Johnson, 2021; Tanaka et al., 1997). Fluctūs (sing. fluctus) are flow terrains, or lava flows, and are most often radar bright (Ford et al., 1993).

Another example of global features present on Venus are valles (sing. vallis), the IAU descriptor term for a valley. Valles are long, sinuous, canali-like structures that maintain constant width along the length, which can vary from hundreds to thousands of kilometers (Baker et al., 1997; Baker et al., 1992; Komatsu et al., 1993; Komatsu et al., 1992). The descriptor term vallis does not effectively describe the structure of these channels, so I refer to them as channels from this point forth. The channels of Venus show a variety of structures, including simple and complex channels. The simple channels (e.g., Bennu Vallis) can have small subsidiaries, while the complex channels branch and can form anastomosing and braided structures (e.g., Kallistos Vallis). The channels are mostly located in the lowland volcanic plains, and their walls can be either radar dark or bright; contrastingly, the channel floor is typically the same brightness as the surroundings (Ford et al., 1993).

The formation mechanism of these channels has been heavily debated between either constructional or erosional origins, namely thermal or mechanical erosion (Bussey et al., 1995; Oshigami & Namiki, 2007; Williams-Jones et al., 1998). Constructional mechanisms involve the typical terrestrial and volcanological processes that describe flow in either channel or tube form, creating levees along the flow path. However, the presence of characteristics similar to terrestrial rivers (e.g., cut-off meanders, deltas) leads to the conclusion that a primarily erosional process created the channels (Bussey et al., 1995). Thermal erosion is the result of a turbulent fluid melting the surface beneath its flow path, carrying the material downstream to become levees or causing a braided flow. It was argued that the channels could not have been formed by thermal erosion because the lavas known to us cool too quickly to form channels thousands of kilometers long,

meaning the lava does not remain hot enough to melt the surface along the entire length (Williams-Jones et al., 1998). Alternatively, mechanical erosion is the process that a terrestrial river uses, in which a low-viscosity, turbulent fluid incises the surface it flows over. Since the surface temperature of Venus is too high for liquid water to exist, the turbulent fluid must be lava (Williams-Jones et al., 1998). This formation method aligns most with the characteristics of the channels; thus, studies have ruled out construction and thermal erosion and consider the channels to be formed by primarily mechanical erosion with low-viscosity lava (Bray et al., 2007; Komatsu et al., 1992; Oshigami & Namiki, 2007; Williams-Jones et al., 1998).

Despite the global distribution of the channels, there has not been much research into the topic of tectonic deformation of the channels, with most of the existing work only focusing on Baltis Vallis. Following the early studies focused on broad comparisons between valleys and characteristics of channels (Baker et al., 1997; Baker et al., 1992; Komatsu et al., 1993; Komatsu et al., 1992), research focused on the potential formation processes and necessary fluid composition of extrusive and effusive lavas that would result in the channels (Bray et al., 2007; Bussey et al., 1995; Gregg & Greeley, 1993; Kargel et al., 1994; Williams-Jones et al., 1998). Baltis Vallis then became the focus of this research, which will be discussed later within this work, because of its unmatched length of ~6800 km, making it the longest channel of any type in our solar system (Baker et al., 1992; Oshigami & Namiki, 2007).

Compared with channels on Earth, the channels resemble rivers, with the flow features present as mentioned above, including point bars, cut-off meanders, delta-like structures, and channel braiding (Baker et al., 1992; Williams-Jones et al., 1998).

Terrestrial lava tubes and channels are not fully comparable to the Venusian channels because of this reason. However, two historical basaltic lava flows in Hawai'i were found to propagate much more quickly than the average terrestrial flow, and their dynamics were scaled to compare with planetary volcanism (Baloga et al., 1995). On average, terrestrial flows are less than 100 km in length because of the lack of volume needed to advance farther (Keszthelyi & Self, 1998). On Mars, some channels have the same canali-like structure as seen on Venus; Hrad Vallis, as an example, has an approximate length of 1400 km and has been proposed to be of volcanic origin as well (Hopper & Leverington, 2014). Outflow channels on Mars previously considered to be fluvial have been reevaluated as volcanic in origin through thermal inertia values (Jaeger et al., 2007). Lunar sinuous rilles are another example of this type of structure, formed by low-viscosity lava flowing longer distances than on Earth and also compared to terrestrial rivers (Hurwitz et al., 2013; Hurwitz et al., 2012; Williams et al., 2000). Sinuous rilles are most often found in basaltic plains, called mare, with lengths varying from tens to hundreds of kilometers long (Williams et al., 2000). Their formation mechanism is also debated; there is evidence of a multi-stage formation using thermal erosion and constructional methods in tandem with mechanical erosion (Roberts & Gregg, 2019; Williams et al., 2000). Mercury also has lava flows called valles that are interpreted to have been formed by a low-viscosity, high-temperature lava, and several show topographic undulations along their length (Byrne et al., 2013).

1.2 Tectonics on Venus

Major structures on Venus are linked with tectonics, including ridge belts, tesserae, mountain belts, and coronae. Dorsa (sing. dorsum) is the IAU descriptor term

for ridges and ridge belts, which vary in length from less than 100 km to over 2000 km (Hansen et al., 1997). The ridge belts are considered to form from horizontal shortening and may represent anticlinal folds, overlie thrust faults, or orogenic belts (Banerdt et al., 1997; Byrne et al., 2021; Klimczak et al., 2019). Tesserae (sing. tessera) are deformed terrains with high relief and a high surface roughness, making them appear radar bright in the SAR mosaics; they are interpreted to contain a variety of different fault types and folds (Hansen et al., 1997; Klimczak et al., 2019). Although some studies consider all of the tesserae to be the same age and formed by the same event (Ivanov & Head, 2011), this interpretation is found to be problematic given the variation in tesserae structures and lack of absolute dating techniques (Hansen et al., 1997; Phillips & Hansen, 1994). Montes (sing. mons) are mountains, mountain ranges, and some large volcanoes. Fossae (sing. fossa) and lineae (sing. linea) describe fractures, fracture belts, and graben and differ from ridge belts with their larger widths (Tanaka et al., 1997). These fracture belts are the extensional counterpart to the dorsa and are comprised of normal faults; they have also been called "groove belts" (Byrne et al., 2021; Ivanov & Head, 2011; Klimczak et al., 2019).

Planitiae (sing. Planitia) are the lowland plains that cover ~80% of the surface of Venus (Basilevsky & Head, 2003; Ford et al., 1993; Hansen et al., 1997). The plains are typically radar dark and smooth compared to the other terrain types; however, the plains host faults or fractures throughout their expanse (Hansen et al., 1997; Tanaka et al., 1997). The two most prominent features are wrinkle ridges and small fracture sets. Wrinkle ridges are narrow (although wider than the fracture sets), sinuous features that often form parallel sets with an average spacing of 20 km; because of these

characteristics, they are considered to be thrust faults (Banerdt et al., 1997; Klimczak et al., 2019). The smaller, parallel fracture sets are thin, straight, and have an average spacing of 1-2.5 km, which led to their interpretation of tension fractures (Banerdt et al., 1997). The presence of wrinkle ridges and fracture sets uniformly across the planitiae indicates large-scale deformation that happened early in the lifespan of the plains (Banerdt et al., 1997; Hansen et al., 1997).

Lying within the lowland plains, the long canali-like structure of the Venusian "valles" has been used to infer about local tectonics (Komatsu & Baker, 1994; Oshigami & Namiki, 2007). Along the channels, the topography has changed after they formed, which has been seen along Baltis Vallis caused by both large-scale (long-wavelength) and small-scale (short-wavelength) topographic undulations; these topographic changes have been discussed as surface deformation along Baltis Vallis since its discovery when it was first incorrectly labeled as Hildr Fossa (Baker et al., 1992; Komatsu & Baker, 1994; Parker et al., 1992; Stewart & Head III, 2000; Stewart & Head, 1999). The long-wavelength undulations are caused by regional uplift or subsidence, while the short-wavelength are created by local structures, such as ridge belts or other fault-related terrains. This deformation has been quantified along Baltis Vallis with Fourier Transform analysis, and the longest wavelength topographic changes are proposed to correspond to the dynamic uplift of the crust by mantle plumes (Conrad et al., 2021). Recently, the channels have been surveyed, and the results indicate that ~80% of the channels have been deformed (Lang & Thomson, 2022); however, the primary focus of this survey was not on topographic changes that can be observed along the channels. This is well-known but has not been quantified globally involving other major channels, and therefore a

systematic study of the topography along such channels has exciting potential for the tectonic evolution of Venus.

1.3 Significance

Currently, it is thought that Venus does not have plate tectonics (James et al., 2013; Solomon et al., 1992). Plate tectonics is the process that accounts for a major portion of heat loss on Earth. Without plate tectonics, Venus must have a different process that allows heat to escape the interior, including volcanism or thermal convection (James et al., 2013). Volcanic activity is found to interact with and change the surrounding lithosphere through a variety of processes and can cause noticeable structural expressions on the surface, as has been discussed (Airey et al., 2017; Borrelli et al., 2021; McGovern et al., 2013; Nimmo & McKenzie, 1998). However, the surface has been evaluated and may be comprised of crustal blocks that have undergone lateral motion (Byrne et al., 2021). The upper crust likely fractured from the stresses of mantle convection and split into blocks that continued moving due to the underlying convective cells (Byrne et al., 2021). With volcanism and mantle convection affecting the surface to allow heat loss, the topography may have been changed as a result of these motions in the mantle (Bindschadler et al., 1992; Knicely & Herrick, 2021; McKenzie, 1994; Phillips, 1990; Stofan et al., 1995; Zampa et al., 2018). The global extent and length of the channels have the potential to offer a glimpse of the subsurface and add to the discussion of heat transfer and lithospheric overturn. The laws of physics dictate that lava flows downhill when formed. When the topographic profiles reveal an apparent uphill along the path, then this must be the result of tectonics, either short- or long-wavelength in origin. Mapping the channels systematically and looking at topographic data along the length

could show a relationship between the topographic changes and short/long-wavelength sources, which will give a global view of long-wavelength changes and a better understanding of potential mantle upwellings/downwellings. For this study, a global survey of the channels is carried out that involves documentation of cross-cutting relationships with the surrounding tectonic and volcanic structures and extraction of data derived from topographic and gravity measurements. Such a survey and comparison to geophysical parameters will provide insight into the type, abundance, dimensions, and relative timing of topographic changes that occurred on Venus, which will have important implications for the tectonic and geophysical evolution of the second planet.

CHAPTER 2

METHODS

The most comprehensive data sets for the surface of Venus come from NASA's Magellan mission, which was active from 1989 to 1994 and collected surface and gravity data in five cycles. Magellan studied the surface of Venus with a synthetic aperture radar (SAR) (Saunders et al., 1992). The Magellan SAR mosaic is a combination of Cycle 1 left-look (eastward) and Cycle 2 right-look (westward) rotations. Cycle 1 collected the most data, while Cycle 2 filled in some of the gaps missed in the first cycle. The SAR mosaics have a 75 m pixel resolution and were combined into a global mosaic of several different look angles (Figure 1a). From these SAR mosaics, a topography dataset was derived from altimeter echoes subtracted from the orbiter's radial coordinates to return values of the planetary radius. The topographic data set is in a datum based on subtracting the average radius of 6051 km, and it has a pixel resolution of 4.6 km (Figure 1b) (Ford et al., 1993). Gravity data on Venus was collected by measuring the irregularities in its orbit through Doppler signatures and provided many other data sets (Saunders et al., 1992). The goals of the mission were to map at least 70% of the surface at a resolution better than 300 m with a topographic map at 50 km resolution spatially and 10 km vertically; the goals were exceeded, resulting in over 99% of Venus' surface mapped at a resolution ten times better than all previous data (Ford et al., 1993).

The challenge with radar mosaic interpretation requires knowledge of how natural surfaces affect radar waves. Near-range points of topographic expressions are

compressed compared to the far-range points, somewhat distorting the returned radar mosaic. Small look angles and steep slopes make distortions worse; however, this distortion can be accounted for and corrected during image processing by comparing images of different look-angles. Another characteristic of radar mosaics is brightness. A rough surface causes the radar energy to scatter much more than compared to a smooth surface. Because of this, a rougher terrain will be lighter (radar bright) than smooth surfaces that reflect little to no energy back toward the antenna and thus appears black (radar dark) (Ford et al., 1993).

Additionally, crustal thickness and dynamic topography data sets calculated by Peter James are included in this study (Figures 1c and d). The crustal thickness is derived from the Magellan gravity data set by performing a two-layered inversion with additional calculations to solve for missing variables due to the lack of internal information about Venus (Figure 1c) (James et al., 2013). The crustal thickness was subtracted from the topography along each channel to result in a profile that represents the bottom of the crust in terms of radius, or the crust-mantle boundary, also known as the MOHO. These profiles are called depth to the mantle or MOHO within this study. In creating this profile, I am able to observe the behavior of the crustal thickness along the length and discuss crustal thinning/thickening. The dynamic topography data was inferred from the gravity anomalies from the Magellan gravity data and is a calculated measure of mantle convection (Figure 1d). The total mass anomaly in the mantle is also published by James et al. (2013). Positive values represent where a hot plume has induced upward flow within the mantle, causing the surface to be topographically elevated, while negative values are where the mantle is downwelling and the surface dips (personal

communication with Peter James). The dynamic topography dataset has a resolution of spherical harmonic degree 40, which equals a spatial block size of ~477 km. This resolution limits interpretation to channels longer than ~500 km.

Geological interpretations are taken from Ivanov and Head (2011). Within their paper, they discuss the stratigraphic age of each unit, which is not used for this study. Each unit is for identification purposes only. The geological units are tessera (t), densely lineated plains (pdl), ridged plains (pr), mountain belts (mb), groove belts (gb), shield plains (psh), regional plains (rp1, rp2), shield clusters (sc), smooth plains (ps), lobate plains (lb), and rift zones (rz). Densely lineated plains (pdl) are regions of dense, narrow lineaments. Ridged plains (pr) are lava plains that have been deformed by long, broad ridges. Shield plains (psh) host many small volcanic edifices interpreted as shield volcanoes. The regional plains (rp1, rp2) are lava flows that are smooth, homogeneous, and can be either radar dark or radar bright. Shield clusters (sc) are similar to the shield plains but are undeformed and have small lava flows surrounding the volcanoes. Smooth plains (ps) are undeformed and featureless surfaces. Lobate plains (pl) typically are smooth regionals that are deformed by several extensional features; they have a pattern of radar dark and bright features and are interpreted as massive volcanic eruptions. Rift zones (rz) are similar to groove belts but broader and longer. Tesserae (t), mountain belts (mb), and groove belts (gb) have been discussed previously. When these units are used in the descriptions, I include the correct identifying abbreviation.

A Geographic Information System (GIS) was created in ESRI's ArcGIS software, and all datasets were loaded into it. Before the mapping of the channels could commence, several challenges pertaining to the data collection had to be considered. Frequent

reprojecting along each channel is necessary due to their extensive lengths to ensure consistent data sampling. Without consistent reprojection, the map would be distorted away from the center of projection, which would affect subsequent sampling of geophysical data. Mapping the channels on Venus poses a unique problem with reprojection because of their sinuous nature and their length. I chose to create geographic bins that defined projection areas independent of the channel's structures. To define these bins, I created a ten-by-ten decimal degree (DD) grid from across the globe and added a centroid point grid in the Equirectangular Venus projection with the Venus 2000 datum coordinate system. I reproject to the centroid of each bin that hosted a portion of a channel. The reprojection method ensures that every point of each channel is no more than $5\sqrt{2}$ DD from the center of the projection.

To locate all channels, I loaded into our GIS the IAU nomenclature shapefile available in the Gazetteer of Planetary Nomenclature that identifies all the named features on the surface of Venus. Within our GIS, I located the channels by their descriptor term "vallis" and traced each channel while reprojecting along their length. For the tracing, I created polylines, using a streaming tolerance of 1 point per 1000 map units, which equates to equally spaced vertices placed at every 1 km along the channels, and I consistently mapped on a 1:100,000 map scale. When both channel walls were visible, I mapped in the center of the channel floor; otherwise, I followed the wall that was visible. I created a different shape file for every geographic bin that a channel was in, but overlapping the endpoints of each polyline to ensure that seamless merging would be possible. After mapping, I merged all the shapefiles for that channel into a single map trace for analysis (Figure 1e).

Streaming is the best method to consistently map along linear structures of a global scale; however, streaming may result in some replicated points or skipped vertices due to human error. To prevent errors in data extraction and analysis, data management was required; thus, I checked each vertex for accidental duplication, deleting the anomalous points. I report this data cleanup with each channel. I converted the vertices of the polyline into an ordered point file which facilitated the subsequent extraction of geophysical measurements.

Using the vertices point file from each channel, I extracted topography, crustal thickness, and dynamic topography information at each point. I converted the attribute tables into excel spread sheets, then saved them as comma-delimited files to be compatible with RStudio. From this data, I created topography, crustal thickness, and dynamic topography profiles along the length of each channel, with the topography and crustal thickness in terms of the planetary radius. Subtracting the crustal thickness from the elevation resulted in a profile illustrating the depth to the mantle, which shows the MOHO and is a visual of the bottom of the crust. Along the channels, I have also collected geological phenomena, such as coronae, faults, wrinkle ridges, and craters, with which the channels interact to infer the relative timing of the formation of landforms using the general geologic map from Ivanov & Head (2011). I further described the wavelengths and amplitudes as well as causes of topographic changes, where possible, and discussed the general orientation of each channel.

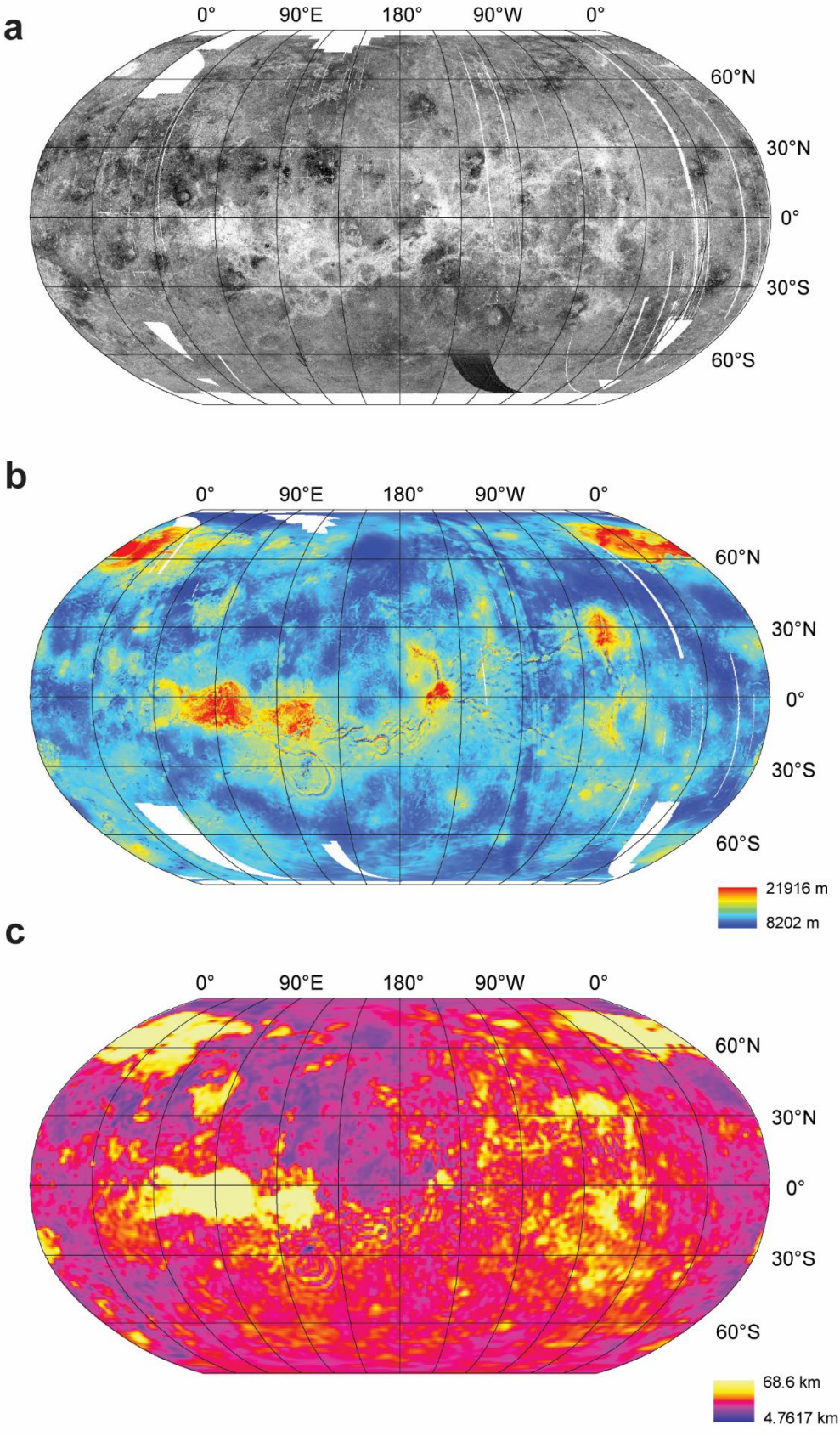
a
0°
90°E
180°
90°W
0°
60°N
30°N
0°
30°S
60°S
b
0°
90°E
180°
90°W
0°
60°N
30°N
0°
30°S
60°S
21916 m
8202 m
c
0°
90°E
180°
90°W
0°
60°N
30°N
0°
30°S
60°S
68.6 km
4.7617 km

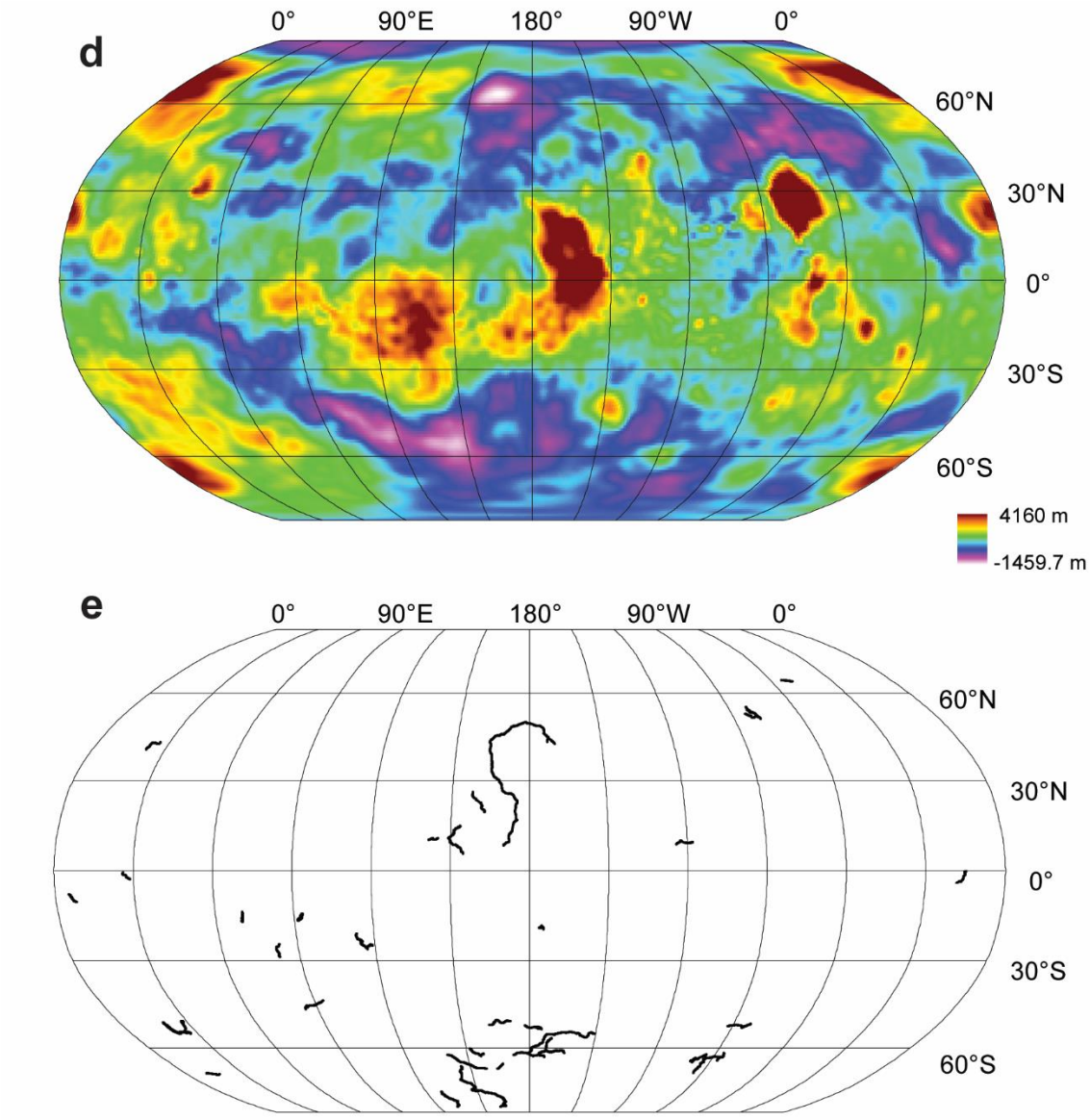

Figure 1: The data sets used for this study: (a) Magellan SAR left-look and SAR right-look mosaics, (b) Magellan global topography derived from the SAR mosaics, (c) crustal thickness, (d) dynamic topography, and (e) the resulting global map of channels. All datasets are projected to be centered on 180°, 0° in a Robinson projection.

CHAPTER 3

FINDINGS

3.1 Overview of Observations

I surveyed 33 lava channels (Figure 1e) of the 72 listed valles from the IAU Nomenclature for Venus. Channels were picked based on length (>200 km), clarity of data, and global distribution. The longest channel is Baltis Vallis, which I identified at a length of at least 7430 km, while the shortest channel I considered was Lunang Vallis at 230 km. The average geodesic length of the mapped channels is 1011 km. I find that 28 of the 33 channels showed noticeable topographic changes, with 22 of them displaying more than one pronounced topographic undulation. The observed wavelengths of the topographic undulations range from 26 km to 2216 km with an average of 317 km. The observed amplitudes range from 87 m to 2780 m with an average of 405 m. With most channels, a source or flow direction are not determinable due to the current data quality, so I discuss the trend of each channel instead. Globally, there is no preferred primary orientation. I find that ten channels show N/S orientations, 11 are oriented E/W, seven are oriented NE/SW, and six follow a NW/SE orientation. In the following, each mapped channel and its topographic, crustal thickness, and dynamic profiles are presented, and their structural and geological are described.

3.2 Description of Channels

3.2.1 Baltis Vallis

Baltis Vallis (BV) is the longest channel on the surface of Venus. Because of its incredible length and structure, BV has been the center of most research focused on the channels, and the surrounding geology and structures have been looked at extensively. BV lies near wrinkle ridged plains, tesserae, ridged plains, ridge belts, lobate plains, coronae, and craters (Basilevsky & Head, 1995; Basilevsky & Head, 1996; Oshigami & Namiki, 2007; Stewart & Head III, 2000). Additionally, geologic maps of the Venus quadrangles containing BV are available through USGS. Studies have analyzed the topographic undulations along BV and found that a long-wavelength deformation that corresponds with mantle plumes was underlying the small-wavelength features such as wrinkle ridges and ridged plains (Conrad & Nimmo, 2022; Conrad et al., 2021; Stewart & Head, 1999).

I mapped BV following the left-look Magellan SAR mosaic through eleven of our 10x10 DD bins. After mapping, I removed 23 anomalous points, leaving a total of 6520 vertices. I calculated the geodesic length to be 6749.59 km of visible channel. There are 15 sections where the channel is not visible, and these sections add 681.85 km, resulting in a minimum length total of 7431.44 km. The straight-line distance is 4,059.12 km, resulting in a channel sinuosity of 1.83.

Figures 2 and 3 are maps showing the flow extent of BV with a color-coded line depicting the elevation. Figure 4 illustrates the topography, depth to the mantle, and dynamic topography along the length. The elevation shows that BV has many topographic undulations on both long and short wavelengths. From the depth to the

mantle graph (red line), BV has a nearly constant crustal thickness, although the crust is thicker until 1400 km along the channel length, where it thins until 2300 km, remains constant until 2700 km with slight thickening onward. Then the crustal thickness remains constant until the northwestern terminus, where it thickens. The dynamic topography (green line) follows the surface elevation closely, meaning that dynamic topography is preserved at the surface and affects the surface after the formation of BV. If BV formed after this deformation, then the topographic profile would not reflect the same trend as dynamic topography. This relationship reveals that dynamic topography is one of the youngest tectonic phenomena in this region. Since dynamic topography is a calculated measure of mantle convection, this illustrates that mantle convection recently affected the surface and may be active. The long-wavelength undulation has a value of ~2216 km and an amplitude of ~1177 m, corresponding to the regional mantle convection resulting from the Fourier transform found in Conrad et al. (2021); the small wavelength changes have values around 200 – 400km, corresponding to ridges and local uplifts/depressions (Conrad et al., 2021; McKenzie, 1994).

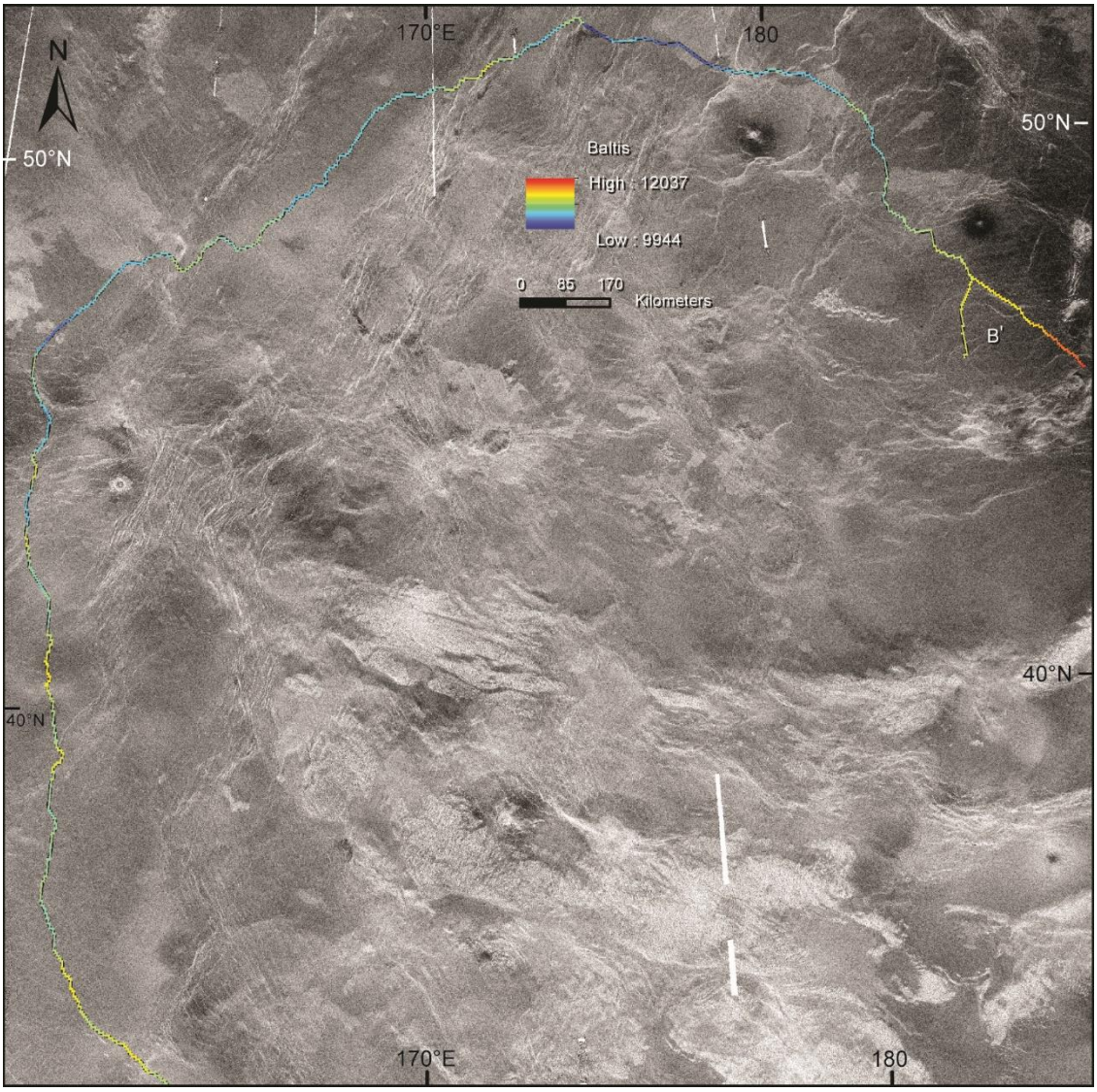

Figure 2: Magellan left-look SAR mosaic projected to be centered on 170° E, 32° N in an orthographic projection, showing the northern portion of Baltis Vallis. The channel is shown by a color-coded line indicating elevation with higher topography shown in red with a maximum of 12037 m and lower topography shown in dark blue with a minimum elevation of 9944 m. The white rectangles are gaps (gores) in the SAR data.

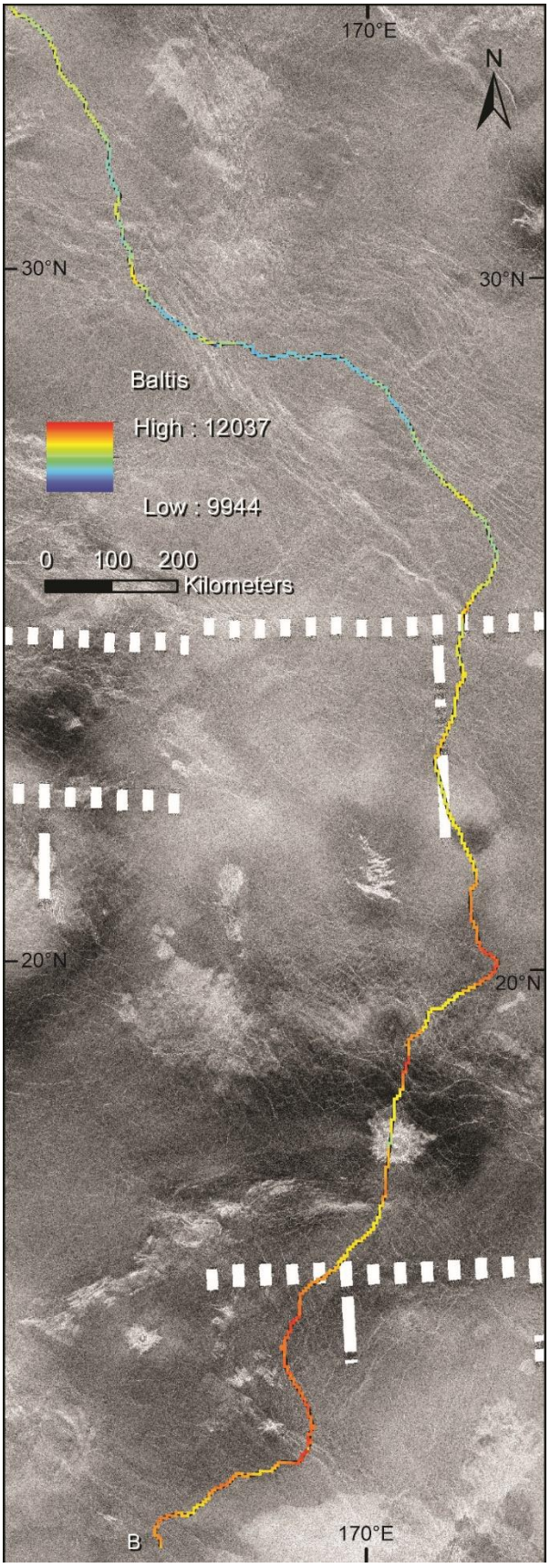

Figure 3: Magellan SAR left-look mosaic centered to 170° E, 32° N in an orthographic projection showing the southern portion of Baltis Vallis. Same color-coding as in Figure 2. The white rectangles are gaps (gores) in the SAR data.

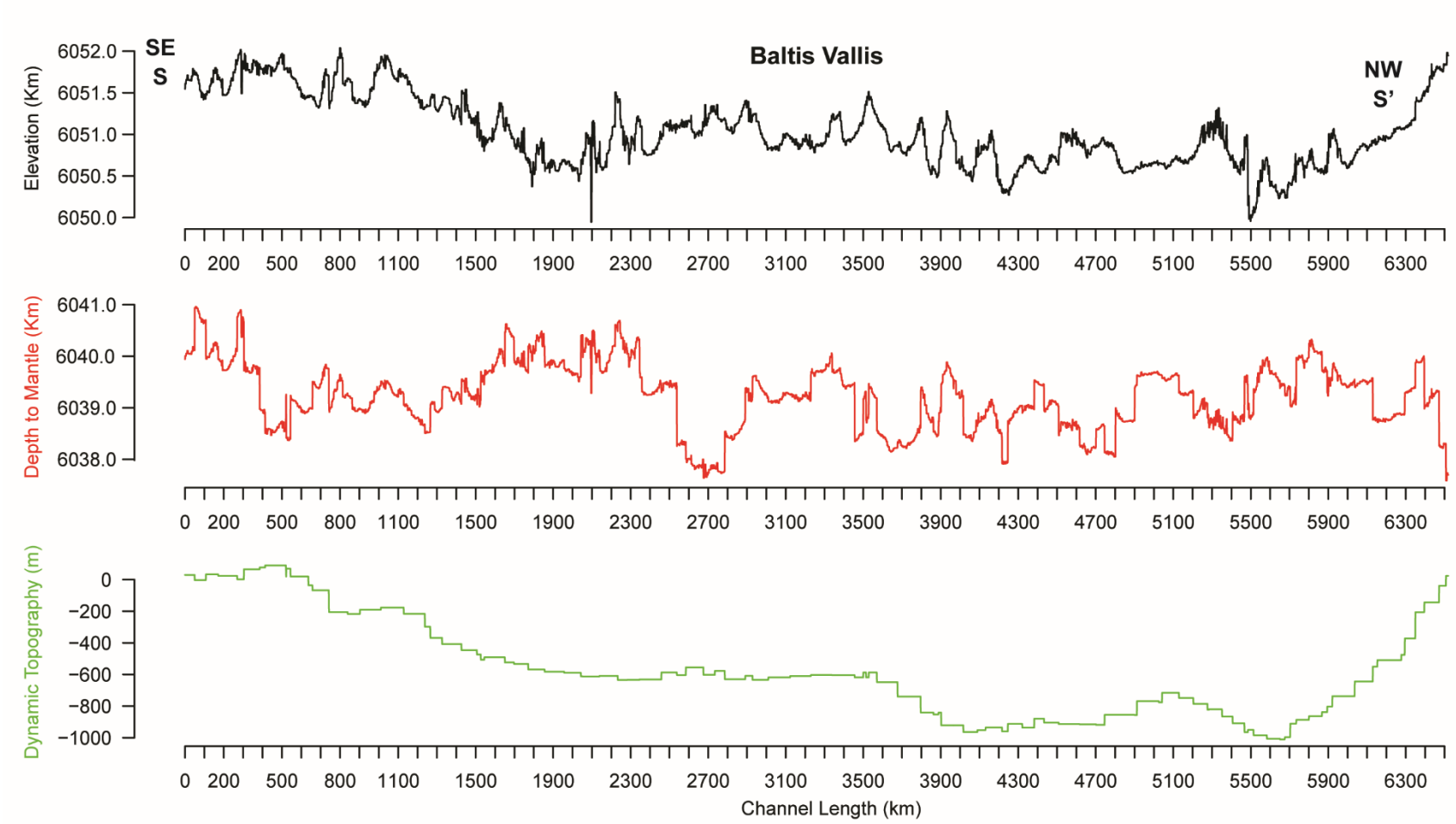

Figure 4: Profile view of topography in terms of radius (black line), depth to the mantle (red line), and dynamic topography (green line) along the flow path of Baltis Vallis.

3.2.2 Citlalpul Vallis

Citlalpul Vallis (C-C') lies within a channel system with Vesper Vallis (V-V'), Xulab Vallis (X-X'), and Dilbat Vallis (D-D') (Figure 5). I mapped Citlalpul Vallis (CV) on the left-look Magellan SAR mosaic, excluding between 162° W and 154° W, where the right-look has clearer visibility through five bins from our 10x10 DD grid. After mapping, I removed nine anomalous points, leaving a total of 2989 vertices. The visible length of CV is 3027 km, but considering the data gaps and coverage, the total minimum length is 3177 km. Dividing by the straight-line distance between the endpoints, which is 2331 km, results in an overall channel sinuosity of 1.36.

Describing the behavior seen in Figure 5, the southwestern-most terminus of CV is ~250 km from Fotla Corona (not on map), which is a candidate site of the origin of the channel; however, a groove belt (gb) obscures any possible relationship (Ivanov & Head, 2011). Besides Fotla Corona, Utset Corona (not on map) is northwest by ~400 km, and Tonatzin Corona (not on map) is further northwest by 700 km. CV continues out of a shield plain (psh) into a regional plain (rp1) with NE/SW oriented wrinkle ridges and into a depression before curving north, meaning the depression formed after channel formation. The entirety of the rest of CV lies within this regional plain. The channel runs parallel to surrounding volcanic features but does not cross or interact with a different unit. At this turning point, CV and Vesper Vallis interact, as seen in Figure 7a. Because of their similar structure and interaction at this location, I believe they are the same channel with the same source. CV then is topographically elevated but curves around the current highest point elevation. This relationship shows that a topographic high was already present when CV first formed and that topographic changes have continued after

the emplacement of the channel. There is no obvious landform associated with the topographic high visible in the SAR mosaic. The surrounding surface is radar homogonous and contains no features besides small-scale wrinkle ridges, which crosscut the channel floor. CV continues northward and shows another topographic undulation with no landforms associated with the topographic high until it turns sharply east right at Ulla crater (Figure 5). This topographic high thus formed after the channel was emplaced. CV continues east through another undefined topographically elevated region and into a depression. The depression still has wrinkle ridges present, but they are less radar-bright than in previous instances. CV passes Barrymore crater to the south and Migazesh Colles (a shield plain) to the north (not on map), which could explain the irregular topography along CV in this region. The channel turns to a southeasterly orientation, where the wrinkle ridges are closely spaced and obscure parts of the channel. CV turns northeast when it encounters Vaiva Dorsum to avoid the topographic high; however, CV still is topographically elevated, as seen in Figure 7b. This relationship shows that Vaiva Dorsum formed during the active flow stage of the channel. The channel is no longer traceable in a highly fractured region. In at least two locations, CV revealed that deformation was extended and continued past the formation of CV.

As seen in the elevation profile in Figure 6, the topographic undulations are harmonic, with wavelengths of ~330 km and amplitude of ~370 m. The depth to the mantle (red line) shows deeper roots under the higher topography, meaning crustal thickening and thinning. The areas of crustal thinning are at 500 km and 1900 km, while crustal thickening is at 100 km, 700 to 1700 km, and 2900 km. The dynamic topography (green line) follows the general topography expression, with a slight increase at 500 km,

decreasing until 1500 km, then increasing until the northeast terminus. The small-wavelength features showed a variety of relative ages compared to CV, but most affected the channel after emplacement, with some deforming actively as the channel formed. The relationship seen between the dynamic topography and the elevation shows that dynamic topography is preserved at the surface but obscured slightly by the small-wavelength structures. This suggests that dynamic topography is one of the more recent tectonic phenomena within this region but not the youngest. Since dynamic topography is a calculated measure of mantle convection, I infer that mantle convection deformed the surface after the emplacement of CV and before the small-wavelength undulations. From Figure 6, the experienced deformation from dynamic topography is in the form of downwelling. The small-wavelength undulations that had no corresponding structure or apparent cause are undetermined and require improved data to discuss their origin.

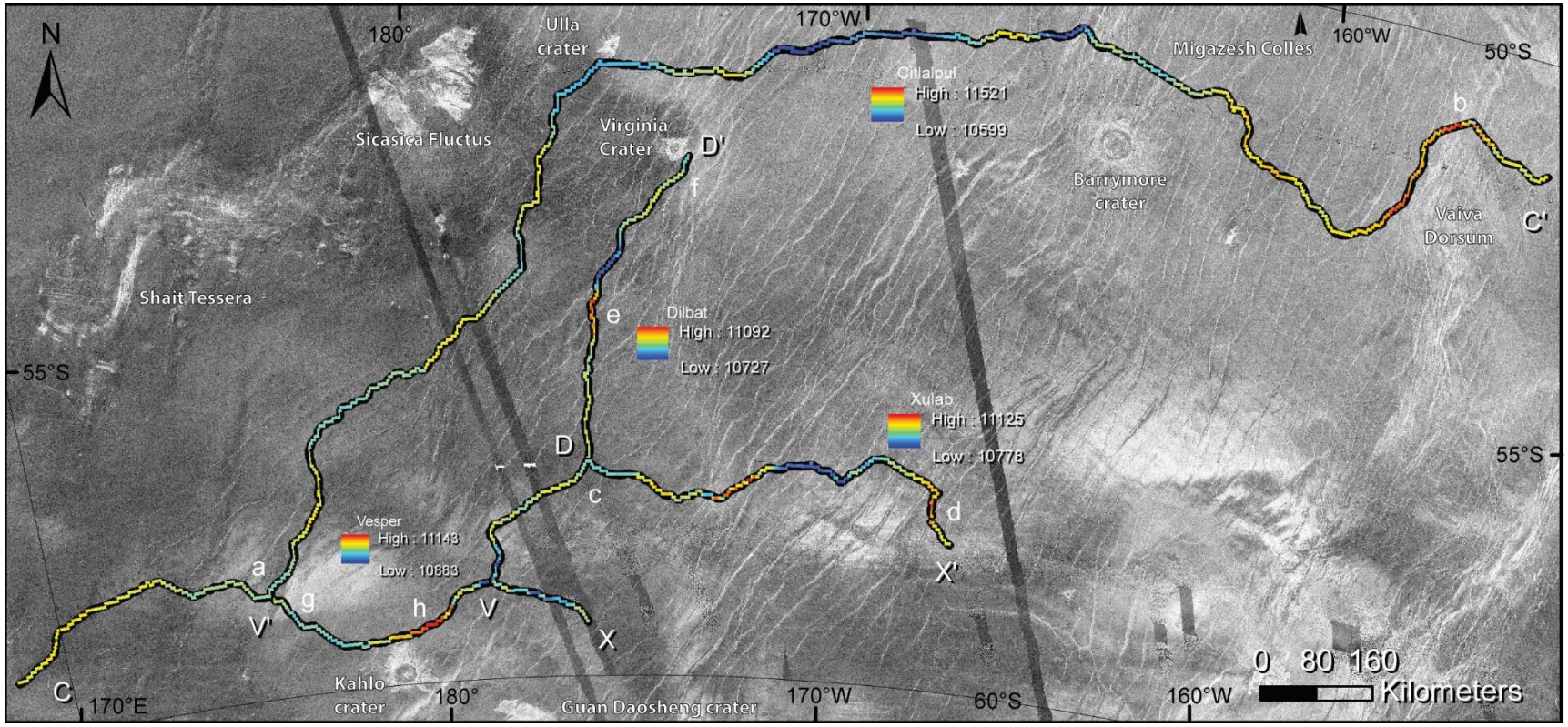

Figure 5: Magellan left-look SAR mosaic is projected to be centered on the center 175° W, 55° S in an orthographic projection showing Citlalpul Vallis (C-C'), Vesper Vallis (V-V'), Xulab Vallis (X-X'), and Dilbat Vallis (D-D') in a complex. Each channel is shown by a color-coded line indicating elevation, with higher elevation shown in red and lower topography shown in dark blue. The dark rectangles are gores in the left-look SAR mosaics. Close-up views of a, b, c, d, e, f, and g are in Figures 6 and 7.

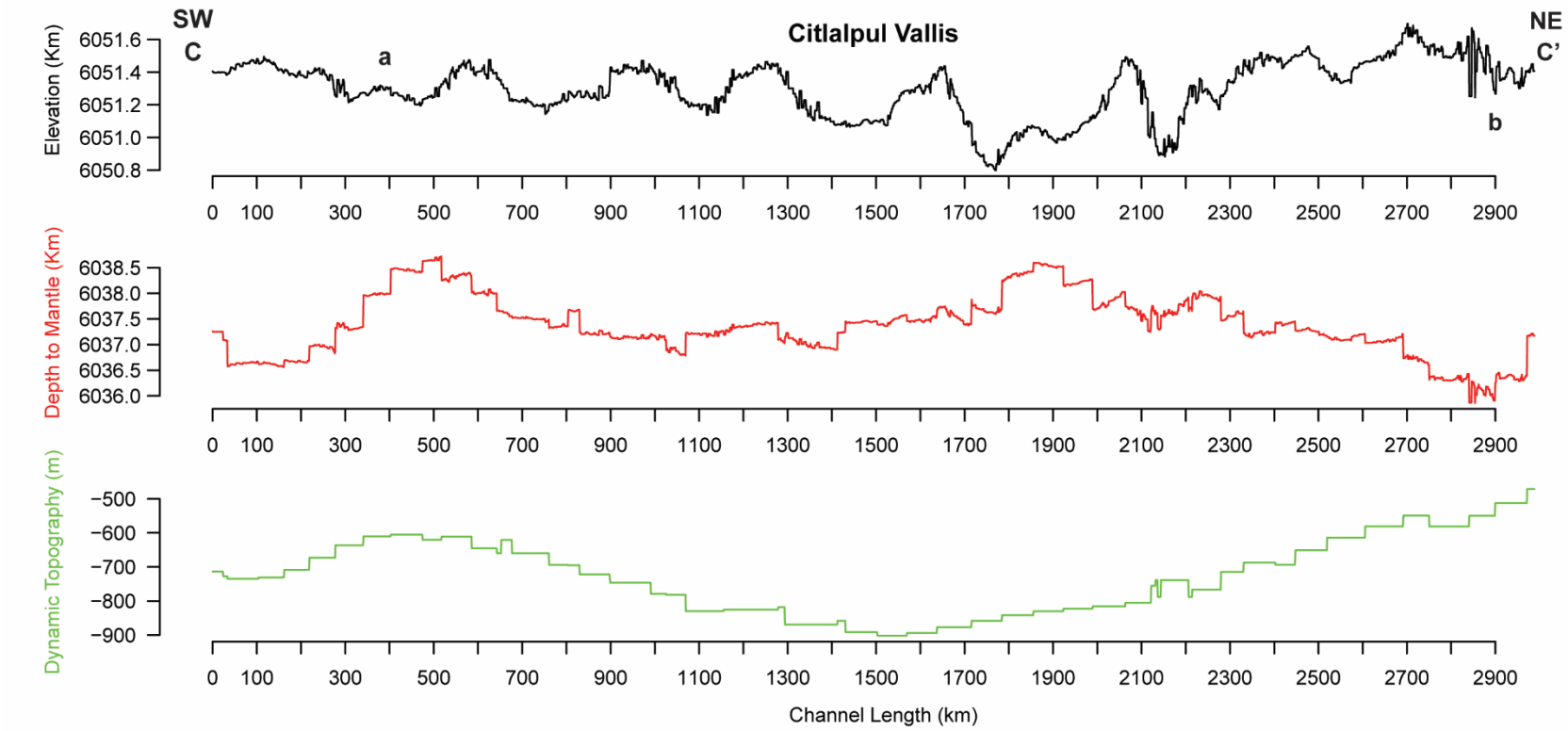

Figure 6: Profile view of topography in terms of radius (black line), depth to the mantle (red line), and dynamic topography (green line) along the flow path of Citlalpul Vallis.

3.2.3 Xulab Vallis

I mapped Xulab Vallis (XV) following mostly the left-look Magellan SAR mosaic through two bins of our 10x10 DD grid. In this region, the left-look SAR mosaics are not complete, and the right-look was used in these areas. After mapping, four points were removed, leaving a total of 1067 vertices. The geodesic length is 1079 km, and the straight-line distance is 526 km, resulting in an overall channel sinuosity of 2.05.

Describing from X to X' in Figure 5, the channel is faint at the southern terminus and lies entirely within a regional plain with no interactions with other units (rp1) (Ivanov & Head, 2011). The channel might continue further south than I have mapped, but the imprint is too faded to map with confidence. As shown in Figure 5, XV continues perpendicular to the wrinkle ridges, which have a primary NE/SW orientation with a small perpendicular set. These ridges are the only feature in the immediate vicinity. XV curves northwest around a large topographic increase that lies between Kahlo crater and Guan Daosheng crater, meaning the topographically elevated region was present before XV's emplacement. Then XV encounters Vesper Vallis, where it turns immediately north and crosses a small topographically elevated region. This topographic undulation has no landform or structure associated and is relatively younger than XV. These short-wavelength topographic undulations have a wavelength of ~94 km and an amplitude of ~202 m. After crossing this topographic increase, XV turns northeast, staying just south of a topographically elevated region, which clearly was present at the formation of XV. XV enters a wrinkle ridge for a short distance, as seen in Figure 7c, relatively dating the wrinkle ridge as older than the channel. At this point, the southern terminus of Dilbat Vallis is present and potentially connected to XV. XV cuts sharply to the east and avoids

a topographic depression, instead passing over a topographically elevated region, meaning the surface deformed after the emplacement of XV. The radar mosaics are not as clear in this area, and these topographic changes have no landform or structure associated. XV is heavily affected by the wrinkle ridges, in some areas completely obscured. This interaction shows that XV flowed when some wrinkle ridges were already in place and either deformed further or new ones propagated after the flow stopped. Continuing east, XV continues through undulating terrain, a topographically elevated region, a depression, and another hill. This movement can be seen in the profile (Figure 9) between 500 and 1000 km. The topographic increase has a wavelength of ~375 km and an amplitude of ~347 m. All of the topographic changes do not have apparent structures or landforms causing them, and they are all younger than XV and affect its original elevation. The depression has a wavelength of ~341 km and an amplitude of ~347 m. XV turns south towards a long topographically elevated region and interacts with a fault, either crosscutting it or being crosscut. The data is not clear enough to choose either option, shown in Figure 7d. The channel is no longer visible where the radar data is heavily pixilated. The overview of XV in Figure 5 (X-X') makes it appear as if XV flowed to avoid two topographic lows and stays at an intermediate elevation, which is not expected for a downward flow of lava channels. This relationship means that the surface along and around XV was heavily deformed after emplacement.

The depth to the mantle (red line) follows along with the topography until 500 km, where it shows crustal thickening all the way to the northeastern terminus (Figure 8). The dynamic topography also follows the underlying pattern of the elevation, although the topographic rise between 500-700 km is not explained by the dynamic topography or

associated with a landform or structure, lending mystery to the complete structural history of this channel. The dynamic topography increases to 200 km, then decreases to 700 km, and increases until the northeast terminus. The small-wavelength undulations slightly obscure the relationship between the topography and dynamic topography, so I infer that the dynamic topography affected the surface first after channel emplacement, followed by the small-wavelength deformations. Since the dynamic topography represents mantle convection, mantle convection is one of the youngest processes in this region, with only small-wavelength undulations younger. The deformation along XV is downwelling from the values in Figure 8.

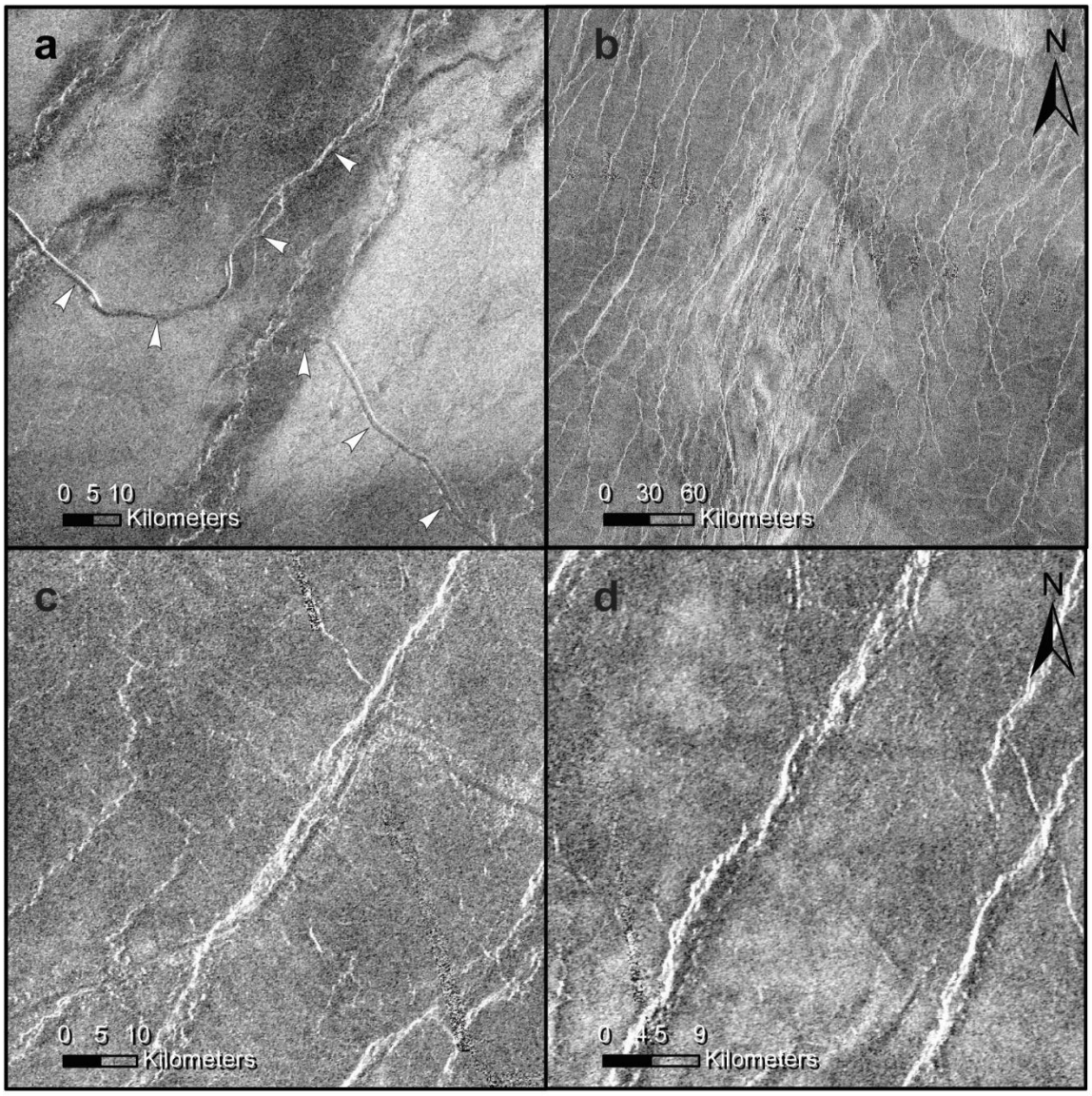

Figure 7: Magellan SAR left-look mosaic is projected to be centered on 175° W, 55° S in an orthographic projection showing details from Citlalpul Vallis (a, b) and Xulab Vallis (c, d). White arrows point out the channel. (a) Citlalpul Vallis and Vesper Vallis intersection. (b) CV curves north to flow around the topographic high of Vaiva Dorsum. (c) Xulab Vallis uses a fault to propagate, and the southern terminus of Dilbat Vallis is seen coming from this fault. (d) Xulab Vallis interacts with a fault (wrinkle ridge) and either crosscuts or is crosscut by the feature.

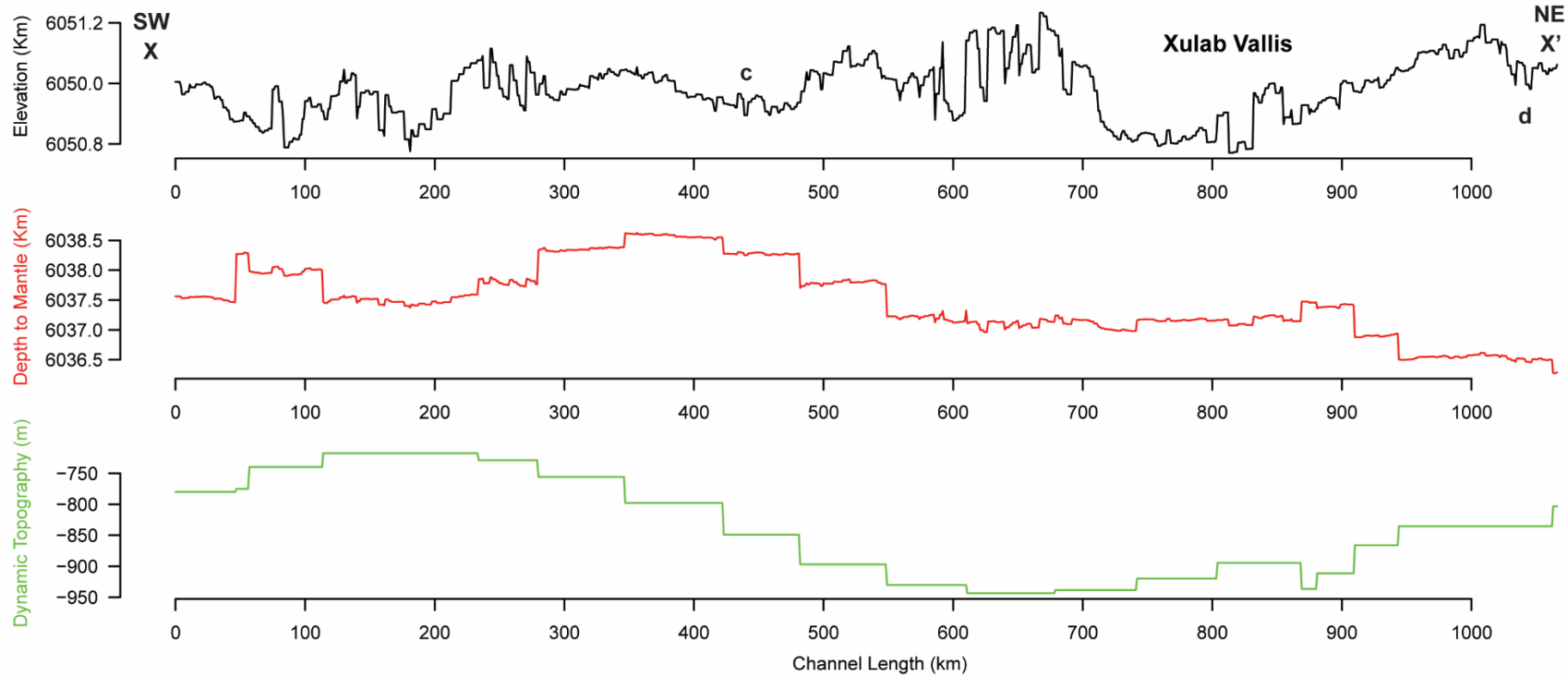

Figure 8: Profile view of topography in terms of radius (black line), depth to the mantle (red line), and dynamic topography (green line) along the flow path of Xulab Vallis.

3.2.4 Dilbat Vallis

I mapped Dilbat Vallis (DV) following both the right-look and left-look Magellan SAR mosaic through one bin from our 10x10 DD grid. I followed the left look for the longest section and the right look for the northernmost section past the straight line for visibility. After mapping, I removed three anomalous points, leaving a total of 476 vertices. The geodesic length is 482 km; however, a small section is not visible. The straight line that connects over this blind spot adds another 29 km for a total minimum length of 511 km. The straight-line distance is 459 km, and the overall sinuosity is 1.11.

Describing from D to D', the southern terminus of DV interacts with the middle of Xulab Vallis, as seen in Figure 5. DV is potentially a secondary channel for XV, but the current available data does not show this relationship clearly, so I describe it as its own channel. DV lies entirely within the regional plain with no interactions with other units (rp1) (Ivanov & Head, 2011). In the surrounding region, consistently spaced wrinkle ridges have a NE/SW orientation. The wrinkle ridges do interfere with the channel, and their deformation is present in the channel floor, meaning they are younger than the channel. DV continues north alongside a topographically elevated region to the west and a local depression to the east. The channel must be older than the topographic depression; otherwise, the lava would have chosen that direction. DV crosses this topographically elevated region, which is shown in Figure 10e. The channel is, therefore, older than the topographic change. There is no apparent reason for this topographic change in the current data. The calculated wavelength is ~157 km, and the amplitude is ~365 m. After crossing the topographically elevated region, DV turns to match the NE/SW orientation of the wrinkle ridges and crosses a smaller topographically elevated region, meaning the

topographic increase is younger than the channel (wavelength ~142 km, amplitude ~232 m). The northern terminus is in a topographic low by Virginia crater, as seen in Figure 10f. It is possible that the channel continues past the crater, but the ejecta obscures the path.

The depth to the mantle profile (red line) in Figure 9 illustrates that DV has varied states of crustal thickness: the thickness is constant until ~115 km, where it thickens until 300 km. After the small section of crustal thinning, then the crust thickens to the northern terminus. The dynamic topography (green line) decreases from D to D', which does not follow the topographic profile closely. However, the length of Dilbat Vallis is too short to interpret the dynamic topography, which has a spatial block size of ~477 km.

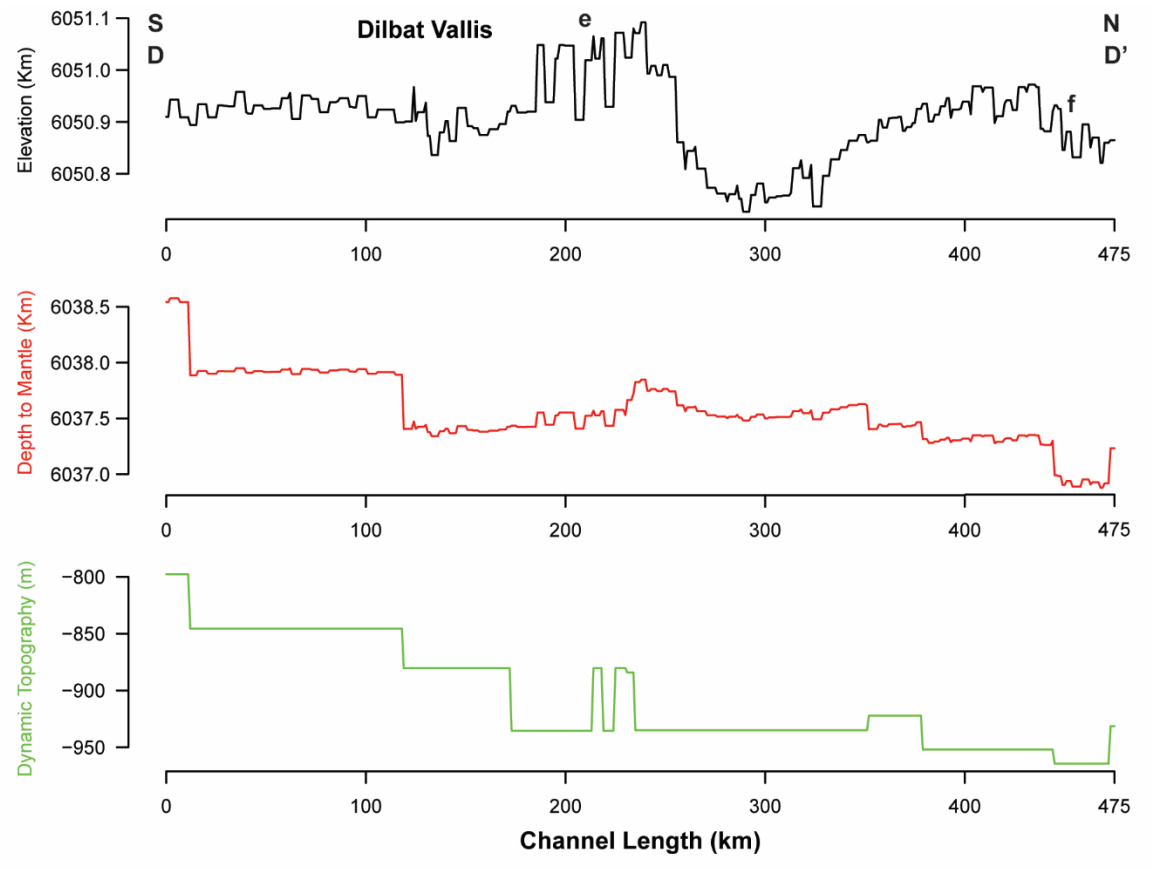

Figure 9: Profile view of topography in terms of radius (black line), depth to the mantle (red line), and dynamic topography (green line) along the flow path of Dilbat Vallis.

3.2.5 Vesper Vallis

I mapped Vesper Vallis (VV) following the left-look Magellan SAR mosaic through two bins from our 10x10 DD grid. After mapping, I removed five anomalous points, leaving a total of 374 vertices. The geodesic length is calculated to be 377 km, and the straight-line distance between endpoints as 313 km, resulting in an overall channel sinuosity of 1.21.

Describing from V to V', VV interacts with the southern part of Xulab Vallis and could potentially be the same channel; however, the current data does not show this relationship clearly. VV lies entirely within the regional plain with no interactions with other units (rp1). The eastern terminus of VV lies in a topographic depression and continues west, quickly increasing in elevation as it passes through a topographically elevated region. This elevation increase relatively dates VV as older than the topographic deformation. There is no visually determinable reason for this topographic change, which has a wavelength of ~252 km and an amplitude of ~184 m. The wrinkle ridges have a NE/SW orientation and can be seen within the channel floor, meaning they are younger than VV. VV continues to the southwest, passing Kahlo crater, which lies further south, as seen in Figure 10g. After passing the crater, VV lowers in elevation consistently and turns northwest. The western terminus lies near the southwestern part of Citlalpul Vallis and shows some angular directional changes, which are not typical behavior for channels (Figure 10h). These “kinks” could be the result of interacting with faults or interacting fracture sets, but any such structures are not visible in the radar mosaics with the current resolution.

The depth to the mantle (red line) shows crustal thinning towards the west (Figure 11). The dynamic topography illustrates opposite behavior as the elevation: increases toward the west. However, the spatial block size of ~477 km prevents interpretation due to the length of VV being too short.

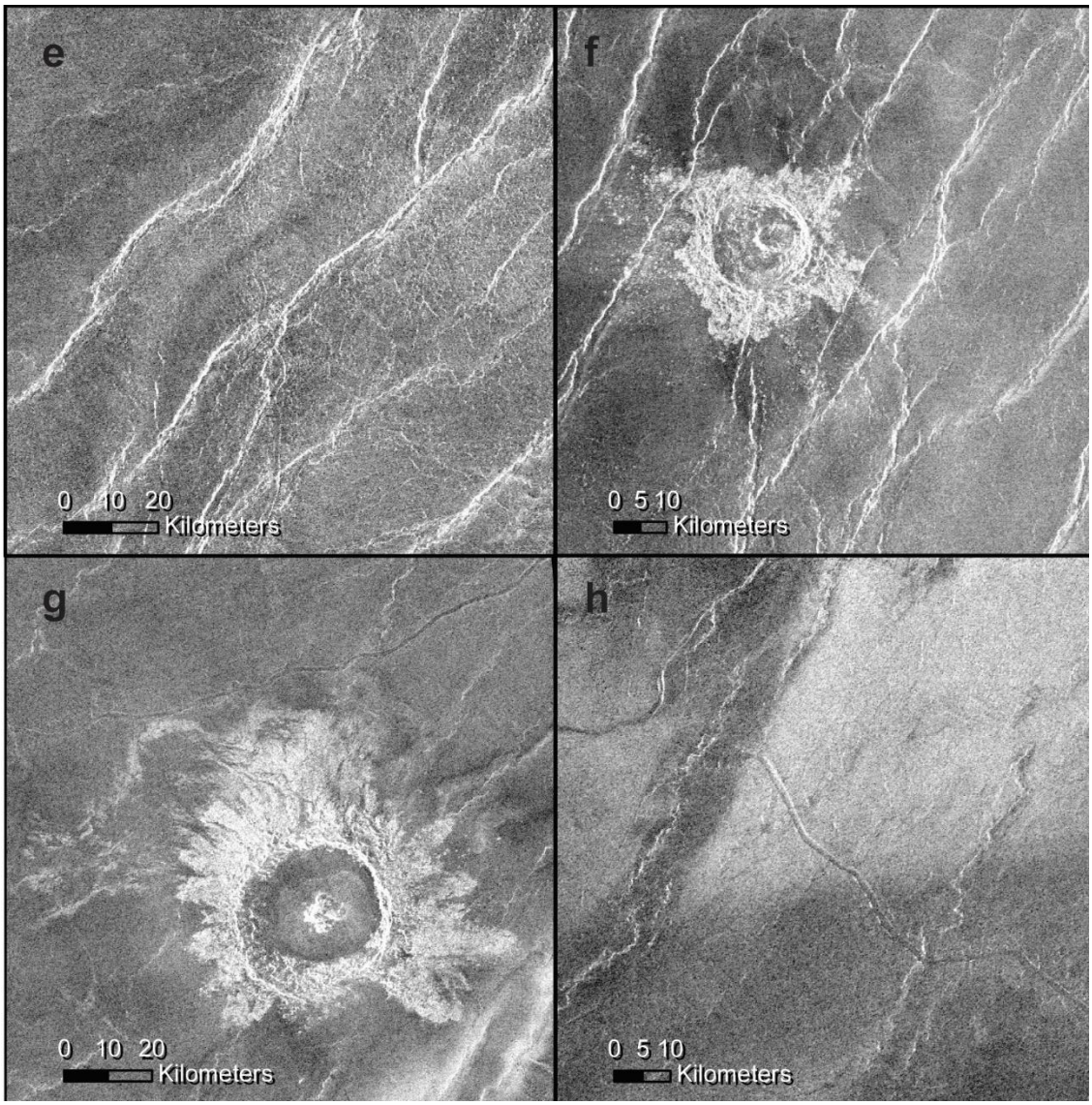

Figure 10: Magellan SAR left-look mosaic is projected to be centered on 175° W, 55° S in an orthographic projection showing details from Dilbat Vallis (e, f) and Vesper Vallis (g, h). (e) Dilbat Vallis crosses over a topographically elevated region that is not visible within the radar. (f) The northern terminus of Dilbat Vallis is seen next to Virginia crater. (g) Vesper Vallis flows north of and avoids Kahlo crater. (h) Vesper Vallis curves with sharp angles, but the underlying structures causing these dramatic changes are not visible within the radar.

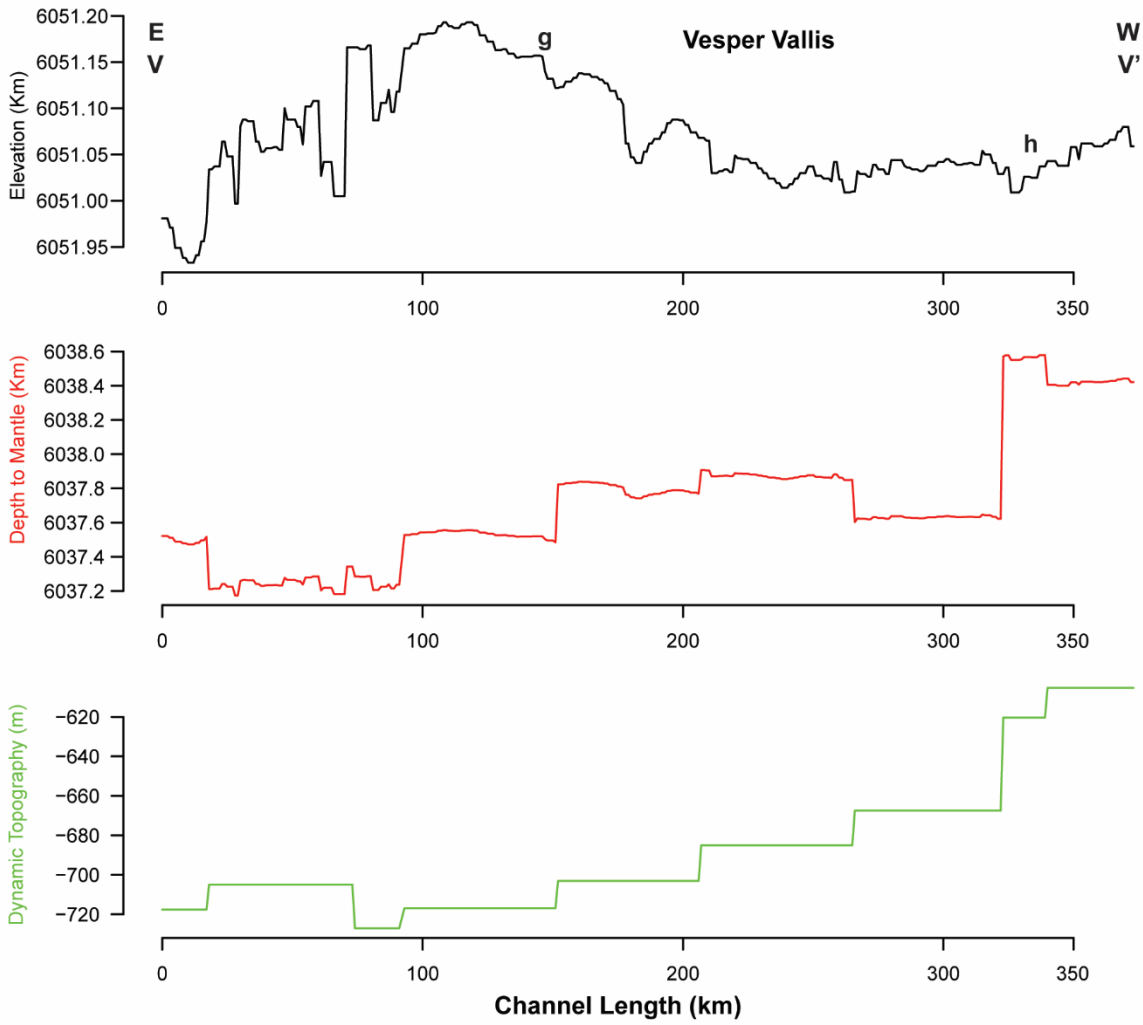

Figure 11: Profile view of topography in terms of radius (black line), depth to the mantle (red line), and dynamic topography (green line) along the flow path of Vesper Vallis.

3.2.6 Laidamlulum Vallis

I mapped Laidamlulum Vallis (LV) following the right-look Magellan SAR mosaic through five quadrants from the 10x10 DD grid. After mapping, 11 anomalous points were removed, leaving a total of 2211 vertices. The left-look SAR mosaic is not present in this location, and LV also continues off the map at 80° S since the south pole does not have any radar coverage in this data set. This lack of data means the length recorded is the minimum length possible. I measured a length of 2250 km, but there are gaps equaling 253 km where the channel is not visible. Including this distance results in a total minimum length is 2503 km. The distance between endpoints is 1825 km which makes the overall sinuosity equal 1.37 when calculated with the added length.

The southern terminus of LV is not covered by the Magellan SAR dataset, so I begin describing where it becomes visible at L (Figure 12). The channel appears in a radar homogonous zone mapped as a regional plain (rp1) and increases in elevation (Ivanov & Head, 2011). This plain seems to be named Yagami Fluctus, but the point is not within the SAR boundary and thus cannot be verified. Whatitiri Corona (not on map) is also named near Yagami Fluctus, south of the SAR boundary. Yagami Fluctus (not on map potentially), and Whatitiri Corona, by extension, are the candidates for the origin of LV. LV continues north through many small topographic fluctuations not associated with features while decreasing in overall elevation. The channel passes Shelikhova Patera, small irregular craters that are hypothesized to be volcanic in origin and mapped as a shield plain (psh). The increase in elevation followed by this gradual decrease (0 to 600 km in Figure 13, black line) has a wavelength of ~622 km and an amplitude of ~577 m. The channel then continues through a topographically elevated region that is part of the

volcanic field (Figure 12a), and the surrounding region contains faint wrinkle ridges oriented NW/SE. This topographically elevated region is younger than the channel and deformed its path, with a wavelength of ~268 km and an amplitude of ~393 m. Further north, LV curves around Odzerchen Dorsa and is not covered by the topography dataset. This relationship reveals LV to be younger than Odzerchen Dorsa. LV continues past the dorsa and Giliani crater (Figure 12b) and passes through a topographically elevated region upon reentering the bounds of the dataset. The topographic change corresponds with an extension of Odzerchen Dorsa, showing that the dorsa continued deforming the surface after channel emplacement. Within Figure 12b, LV has several sharp turns, which are not typical behavior of the channels, but there is no structure or landform in the radar to explain these turns. LV turns north into a radar homogonous zone and through another topographically elevated region mapped as a groove belt (gb), relatively dating the groove belt as younger than the channel. After this undulation, LV continues northwest and out of the topography dataset bounds again. Faint wrinkle ridges with an N/S orientation are visible, and LV curves north. The wrinkle ridges change orientation to E/W, and LV is highly sinuous for a small section before reaching the northern terminus near Melanie crater.

From the depth to the mantle profile (red line) in Figure 13, LV has mostly a constant crustal thickness with small variations. Between 200 and 500 km, the crust is thicker, also seen between 1000 and 1900 km. Crustal thinning is seen at 600 km and beneath the northern terminus. The dynamic topography (green line) has the same general trend as the elevation: decreasing to the north. This means that the dynamic topography is preserved at the surface and has affected the surface recently. The topographic increase

between the data gores is not reflected in the dynamic topography because it is the result of Odzerchen Dorsa, which was found to be older/concurrent with LV. The relative age between the topographic increase at 700 km due to the volcanic plain and the dynamic topography cannot be determined because both are younger than LV. Because of this relationship, dynamic topography (a measure of mantle convection) is the youngest observed large-scale phenomenon in this region, and I infer that mantle convection is the most recent process that affected the surface and is potentially still active. The deformation along LV is subsidence caused by downwelling.

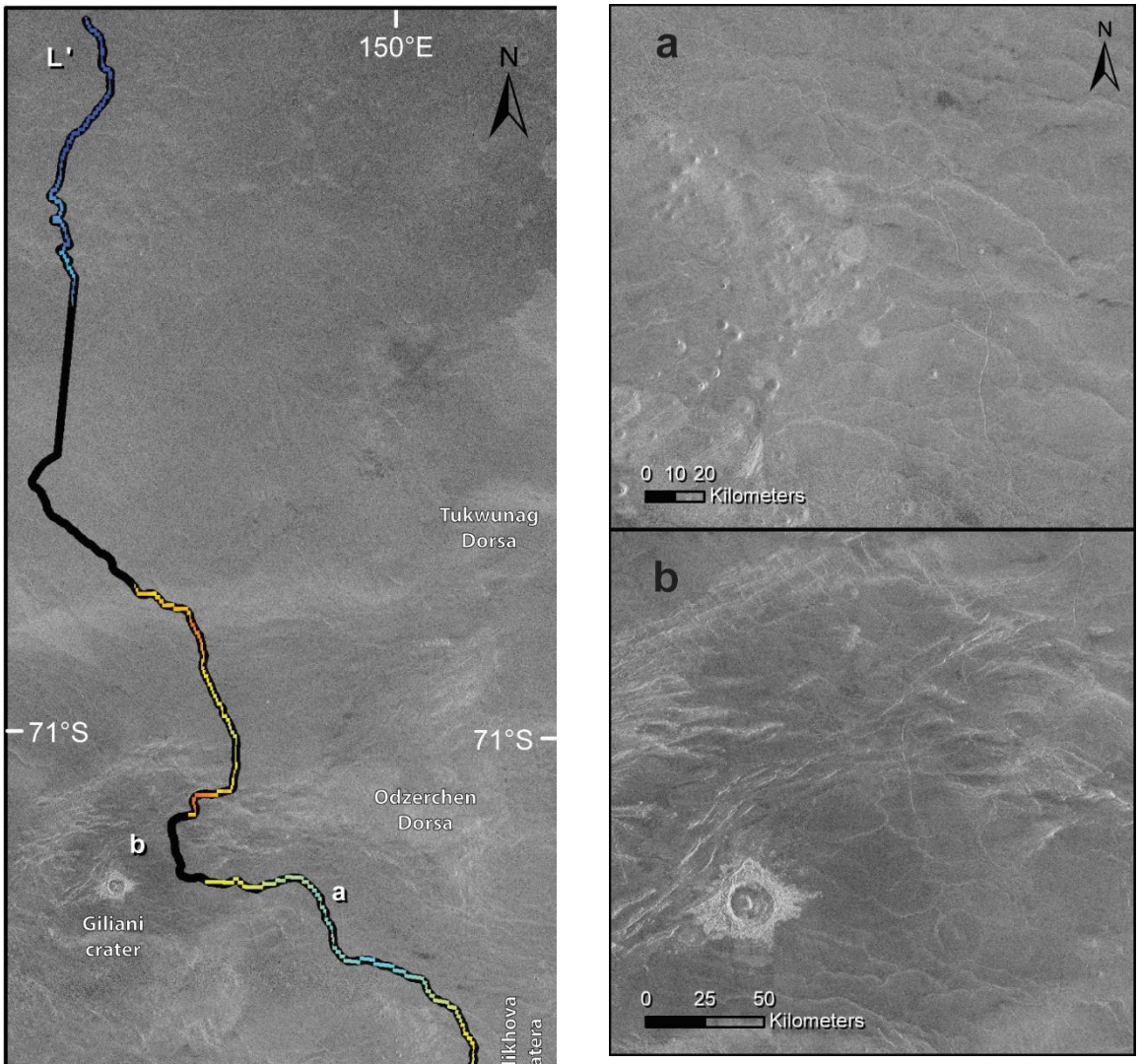

Figure 12: Magellan right-look SAR mosaic is projected to be centered on 145° E, 70° S in an orthographic projection showing Laidamlulum Vallis. The length is illustrated by a color-coded line indicating elevation, with higher elevation shown in red and lower topography shown in dark blue. The dark sections of the line are gores in the DEM. (a) shows a topographically elevated volcanic field. (b) shows LV in close proximity to Giliani crater.

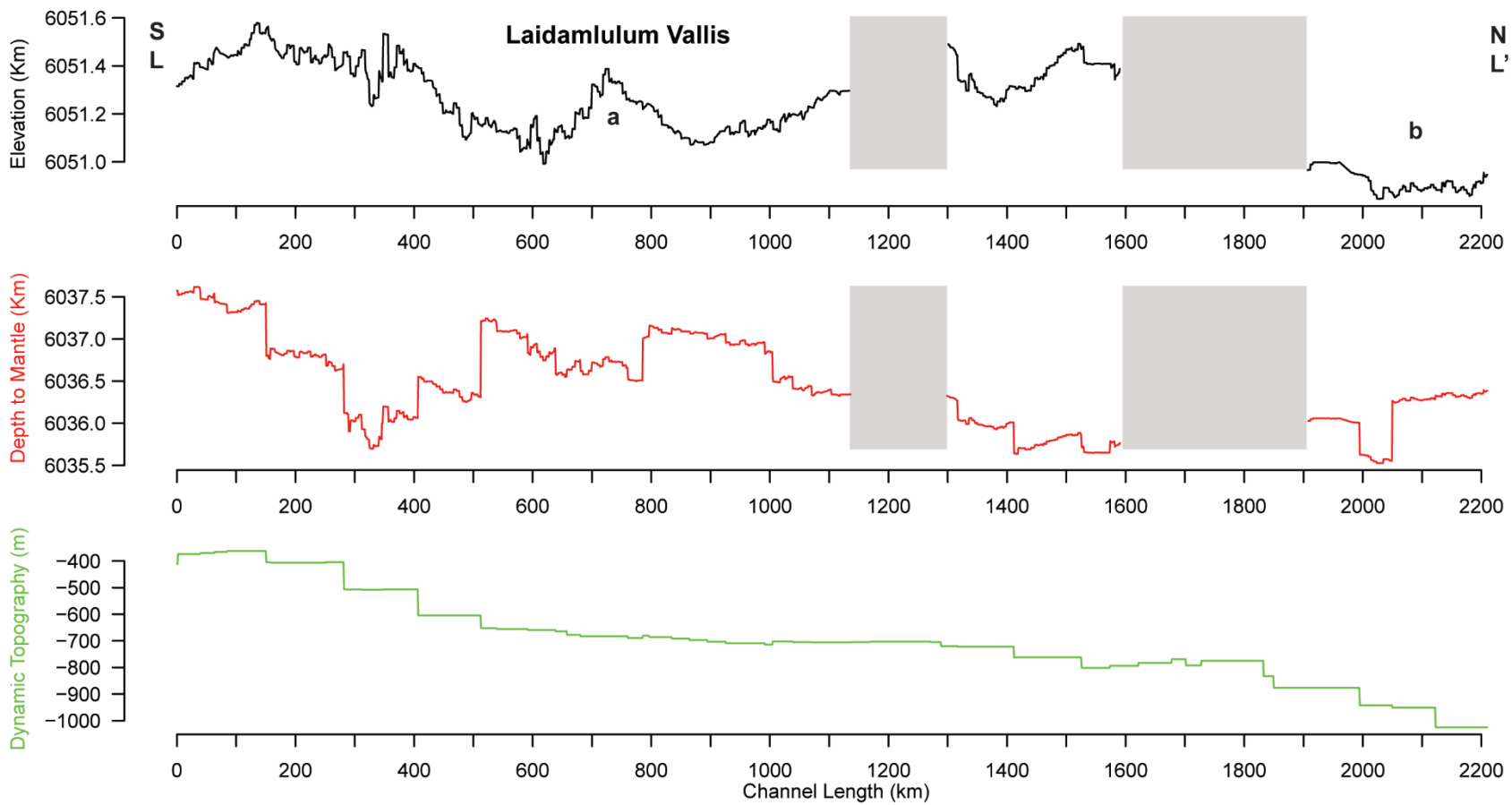

Figure 13: Profile view of topography in terms of radius (black line), depth to the mantle (red line), and dynamic topography (green line) along the flow path of Laidamlulum Vallis.

3.2.7 Ikhwezi Vallis

Ikhwezi Vallis (IV) is most visible following the left-look Magellan SAR mosaic, which was done through four bins from our 10x10 DD grid. After mapping, nine anomalous points were removed, leaving a total of 1809 vertices. The visible parts of the channel in the SAR mosaic have a length of 1836 km, shown in Figure 14. There are three sections that are not covered by the radar data set and one section that is not visible, and these add a length of 83 km (straight-line distance) for a total minimum length of 1919 km. From I to I', the straight-line distance is 1005 km, thus making the overall sinuosity 1.91 with the additional length from the lack of data.

Describing from I to I' in Figure 14, the southern terminus of IV is near lava flows in a highly fractured region. Continuing north, IV has a cross-cutting relationship with a fracture without any indication of relative age for either, and then IV crosses featureless plains where the SAR mosaic is homogeneous in color and has no notable features. IV curves around a topographically elevated region called Urutanga Colles, which is mapped as a shield plain (psh), staying within the regional plain (rp1). Urutanga Colles was present with IV formed. IV then crosses a topographically elevated region that is not associated with a structure or landform and increases in sinuosity. This topographic change is, therefore, younger than the channel. A small ridged plain (pr) to the southwest contains Olena crater and is topographically elevated. IV curves around the ridged plain yet still passes through the topographically elevated region that extends beyond the ridge plain (Figure 15a). This relationship reveals that the topographically elevated region was present during the channel emplacement and continued to deform after formation. The surrounding regional plains show wrinkles with a NE/SW orientation. Then IV curves

around a topographically elevated region mapped as a groove belt (gb) called Barbale Dorsa, which has an NW/SE orientation, which dates Barbale Dorsa relatively as older than IV. IV changes directions from a primary NW/SE orientation to NE/SW, notably perpendicular to the dorsa. IV continues through an elongated topographic elevated region until encountering more groove belts, which the channel weaves between (Figure 15b), then continues over wrinkle ridge plains. Thus, IV is younger than the groove belts, and this area was topographically changed following both of their formations, as seen by the topographic high at point "b" on the topographic profile in Figure 16 (black line). The northern terminus of IV lies in a radar bright section mapped as regional plains (rp2) near the Escoda crater. Where IV meets with the radar bright area, the channel floor has the same radar bright quality, as seen in Figure 15c. IV is not visible beyond the lava flow, and the relationship with the lava flow is unclear. Either the lava flow covered the continuation of IV, was the source of IV, or was supplied by IV.

The elevation profile in Figure 16 (black line) reveals one large-wavelength topographic change that has a wavelength of ~1691 km and an amplitude of ~1127 m. The depth to the mantle (red line) shows crustal thickening at both ends, with crustal thinning at the center. The dynamic topography (green line) shows a strong relationship with the elevation, mimicking the structure nearly perfectly by decreasing to 1000 km, remaining constant until 1500 km, then increasing toward the northern terminus. This reveals that the dynamic topography and, by extension, mantle convection is the youngest phenomenon to alter the surface in the form of downwelling.

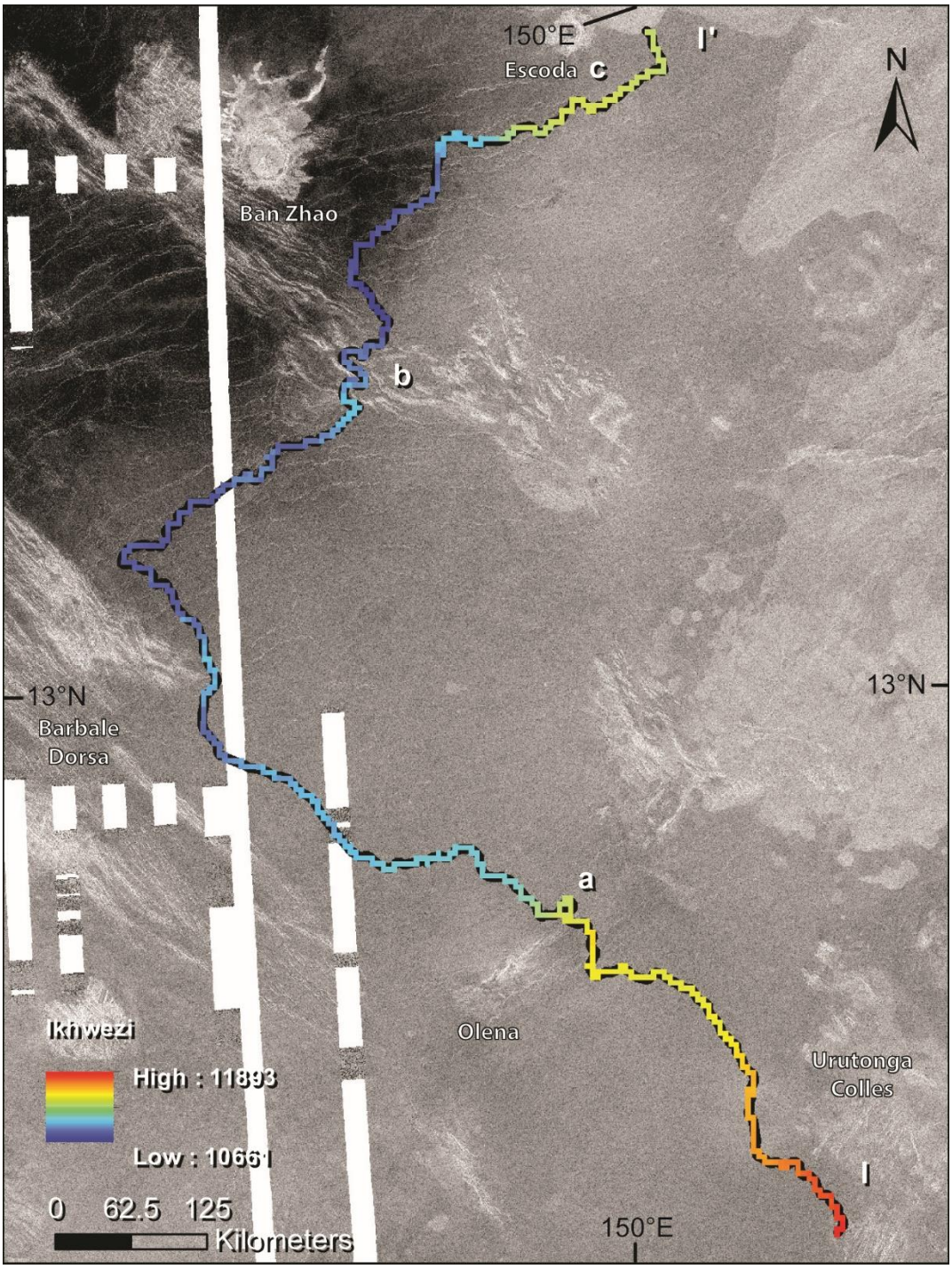

Figure 14: Magellan SAR left-look mosaic is projected to be centered on 150° E, 14° N in an orthographic projection showing Ikhwezi Vallis. The length is illustrated by a color-coded line indicating elevation, with higher elevation shown in red and lower topography shown in dark blue.

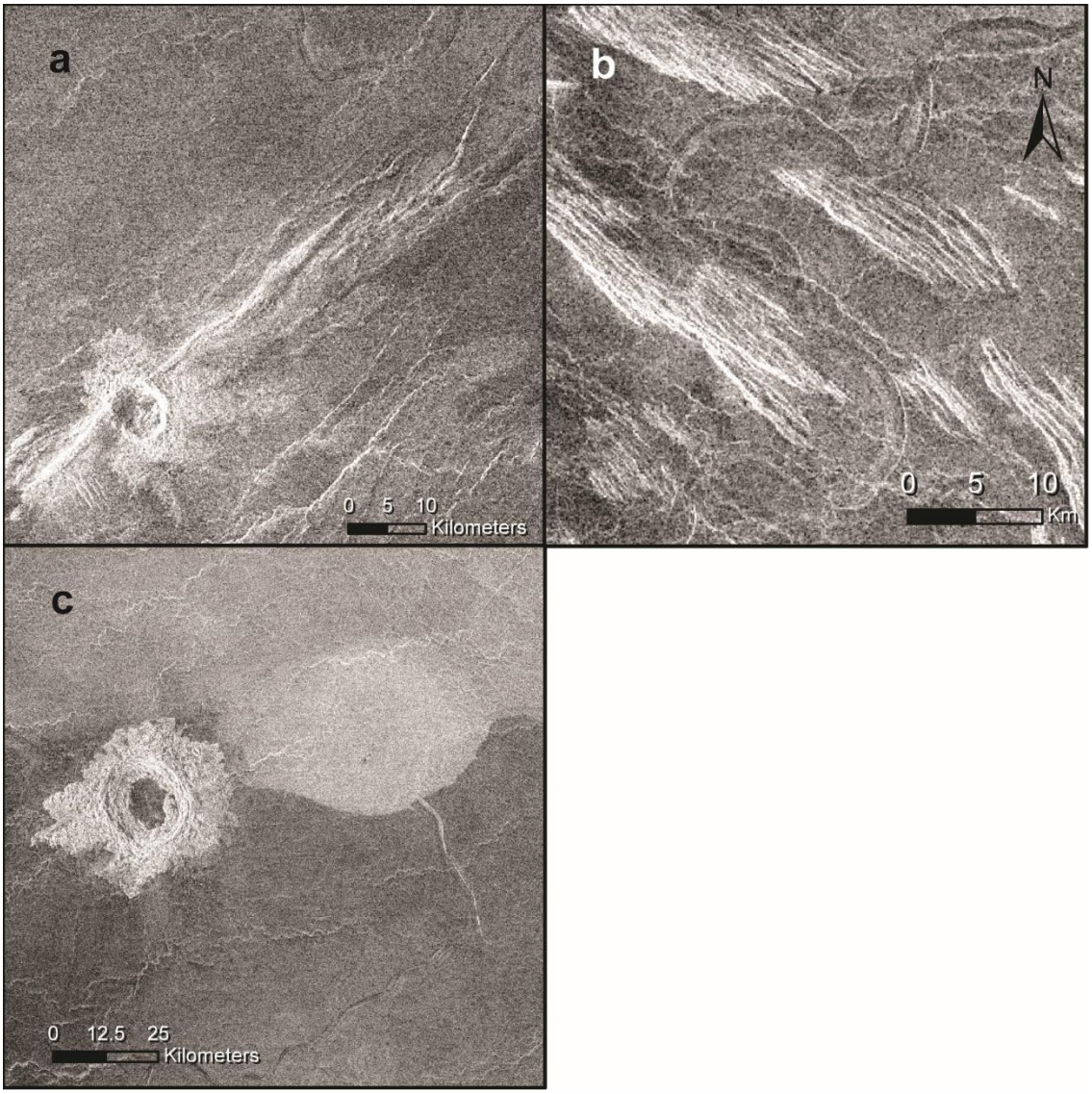

Figure 15: Magellan SAR left-look mosaics are projected to be centered on 150° E, 14° N in an orthographic projection showing close up sections of Ikhwezi Vallis. (a) shows IV flowing over a topographically elevated region near Olena crater. (b) shows IV weaving through a groove belt. (c) shows the northern terminus of Ikhwezi near Escoda crater, with a radar bright inclusion in the channel floor.

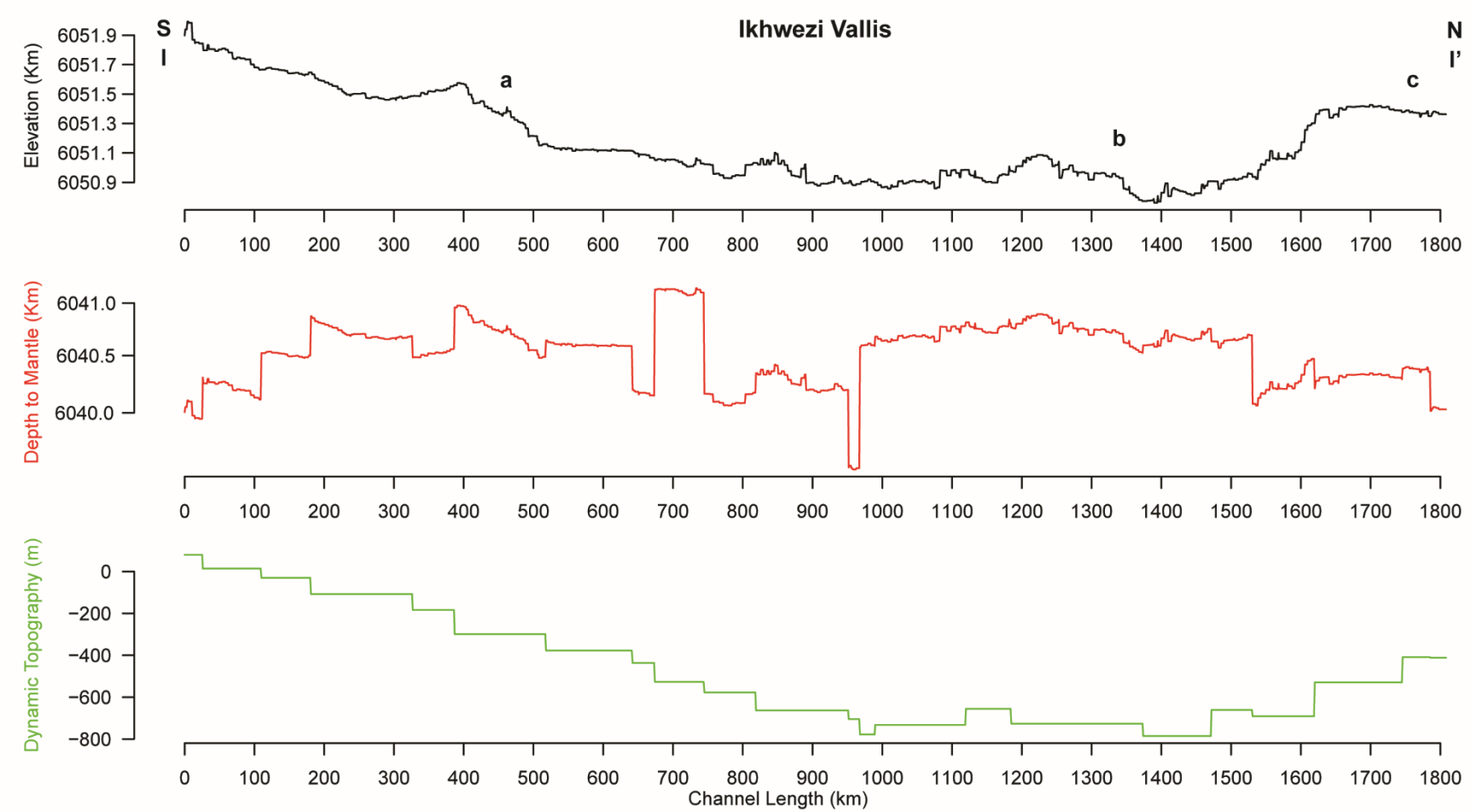

Figure 16: Profile view of topography in terms of radius (black line), depth to the mantle (red line), and dynamic topography (green line) along the flow path of Ikhwezi Vallis.

3.2.8 Gendenwitha Vallis

I mapped Gendenwitha Vallis (GV) following the left-look Magellan SAR mosaic through three bins from the 10x10 DD grid. After mapping, I removed five anomalous points, leaving a total of 1262 vertices. The radar data for this channel is worse, requiring an aspect ratio of 1:300,000 in some areas to map. The length of GV is broken by a fault; no line is added for missing length. The geodesic length is 1286 km without the two small offshoots. The straight-line distance from G to G' is 885 km, and dividing channel length by this value returns an overall channel sinuosity of 1.45.

GV is almost entirely found in a regional plain (rp1), as seen in Figure 17 (Ivanov & Head, 2011). The northeastern terminus of the channel crosses into/ borders a shield plain (psh). From G to G', the southern terminus is in a heavily fractured region near the Mamajan crater. Continuing north, the channel crosses wrinkle ridges that are NW/SE in orientation. At this point, GV splits with a smaller broken channel that I will call an offshoot. The offshoot continues south and terminates after ~15 km. The elevation increases from a densely lineated plain (pdl) to the east (the radar bright spot in the center of Figure 17), and GV is topographically elevated but curves around the most elevated part, which is radar bright and shows no ridge deformation on the top. This relationship means that the densely lineated plain was present before GV but continued to deform after the channel's emplacement. GV continues and crosses Sui-ur Linea; the linea curve around the topographically elevated region, as seen in Figure 18a. GV then turns and changes direction to NE/ SW, while the wrinkle ridge deformation is still primarily NW/SE. GV curves around a topographically elevated region (that is not associated with a landform or structure) mostly but still shows an elevation increase, indicating that the

surface continued to deform after the lava channel formed. The channel continues east to avoid a heavily deformed region in the north and decreases in elevation drastically. From the southern terminus to this point, GV has passed through a large topographic change, shown in Figure 19, from 0 to 840 km. This topographic change has a wavelength of ~840 km and an amplitude of ~802 m. GV splits again (Figure 18b), and the offshoot continues south while the main channel continues east and increases in elevation before continuing into a local depression. GV then turns north and passes over a small, topographically elevated region. From the split to this elevation decrease, the wavelength is ~274 km, and the amplitude is ~242 m. The main channel weaves between two circular features that are mapped as shield volcanoes (Figure 18c), and GV increases in elevation, meaning the shield volcanoes are older than GV and continued to deform after channel formation. Further north, a fracture separates the channel, relatively dating the fracture as younger than GV. GV decreases in elevation quickly and terminates in a small, radar bright lava flow. This topographic change around the fault has a wavelength of ~118 km and an amplitude of ~400 m.

The depth to the mantle profile (red line) in Figure 19 shows a constant crustal thickness under GV with a small exception under the southern terminus, where the crust is thinned. The dynamic topography is generally opposite of the elevation: generally increasing to the northeast while the elevation generally decreases. Since the topography and dynamic topography do not correlate, the topographic change must be caused by another phenomenon and cannot be explained by dynamic topography.

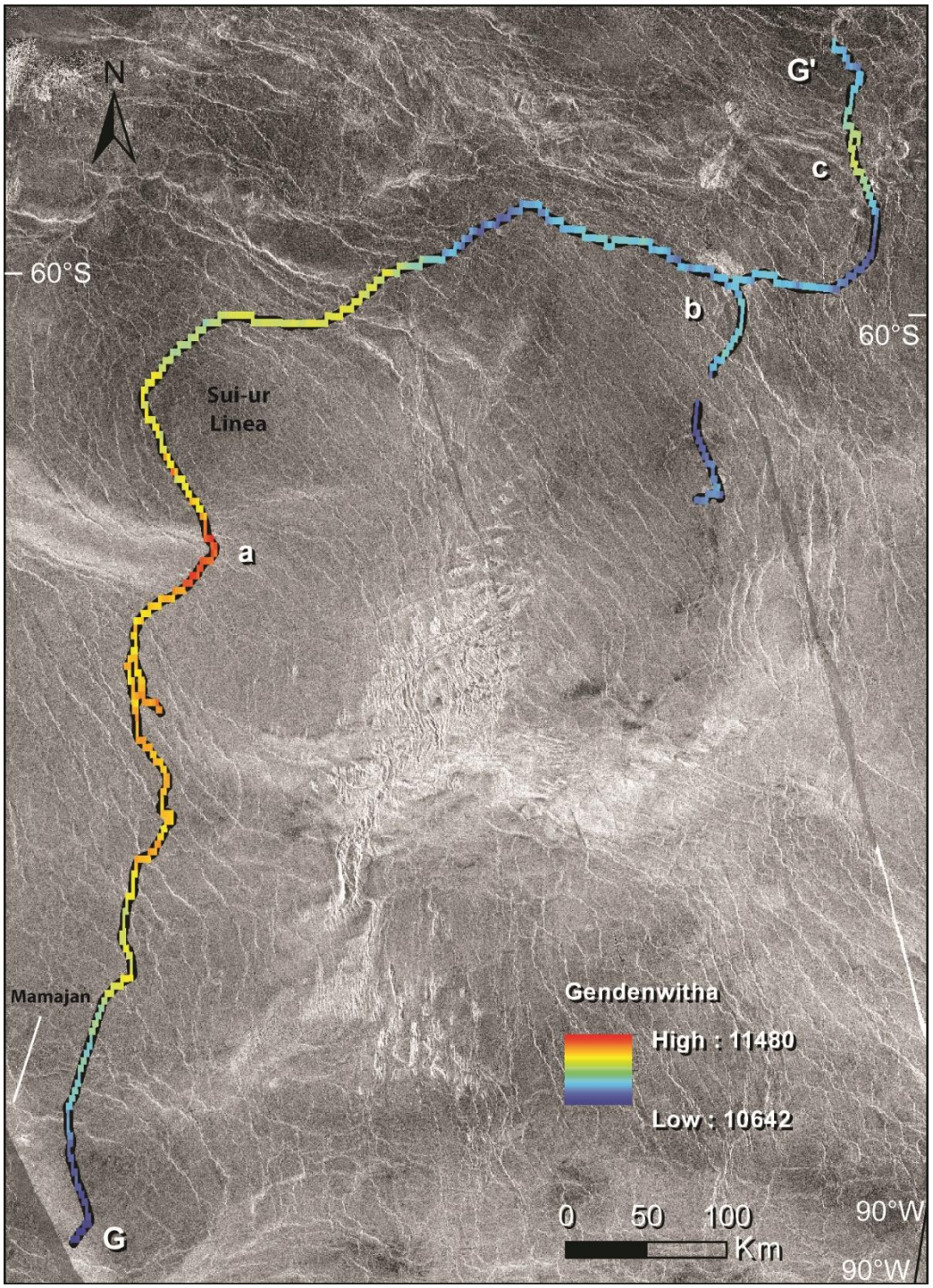

Figure 17: Magellan SAR left-look mosaic is projected to be centered at 100° W, 60° S in an orthographic projection showing Gendenwitha Vallis. The length is illustrated by a color-coded line indicating elevation, with higher elevation shown in red and lower topography shown in dark blue.

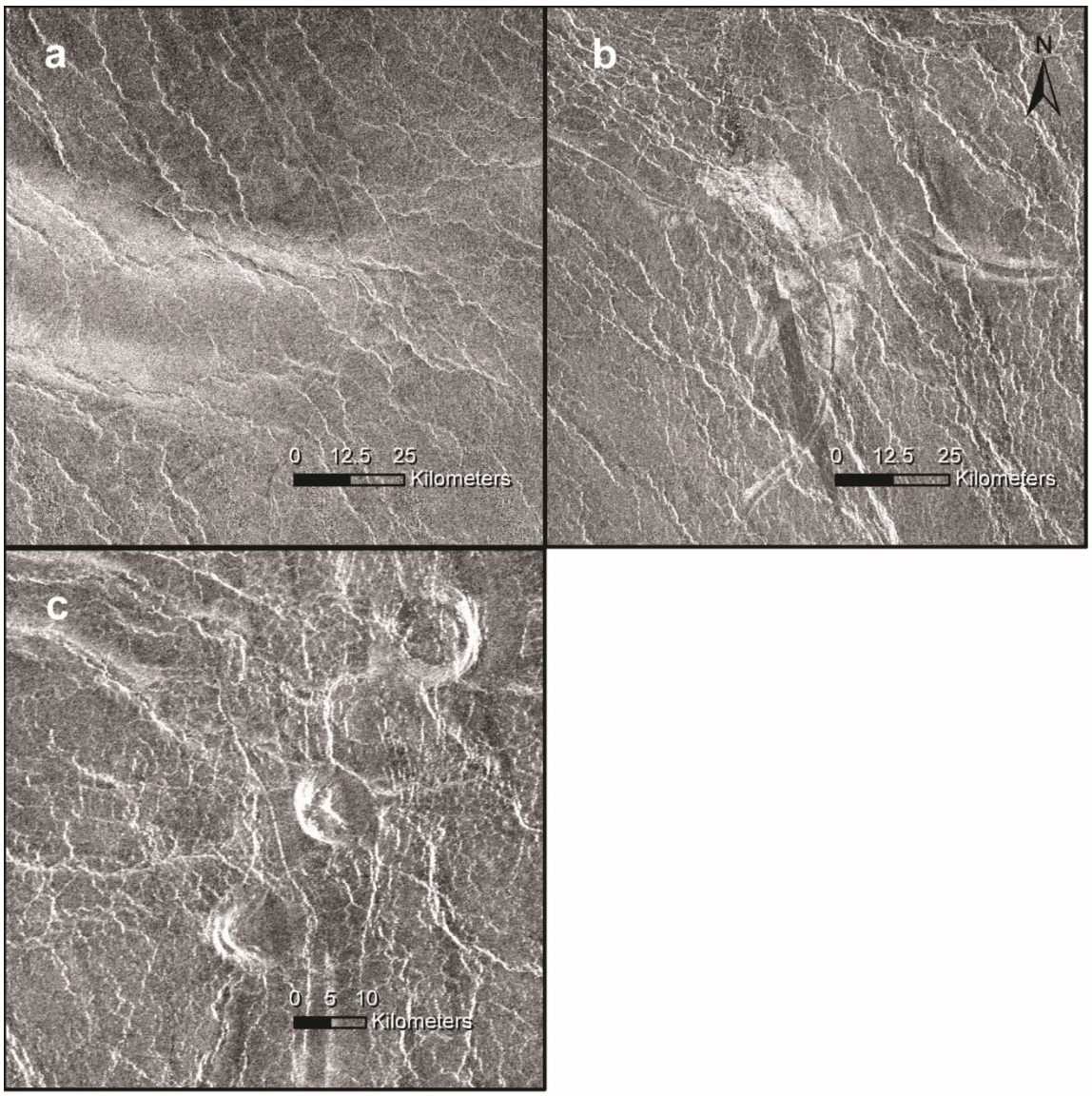

Figure 18: Magellan SAR left-look mosaics are projected to be centered on 100° W, 60° S in an orthographic projection showing close up sections of Gendenwitha Vallis. (a). GV curves over Sui-ur Linea, while the linea curves around the topographically elevated region. (b) GV splits into two channels, with the offshoot continuing south. (c) GV weaves between shield volcanoes by its northern terminus.

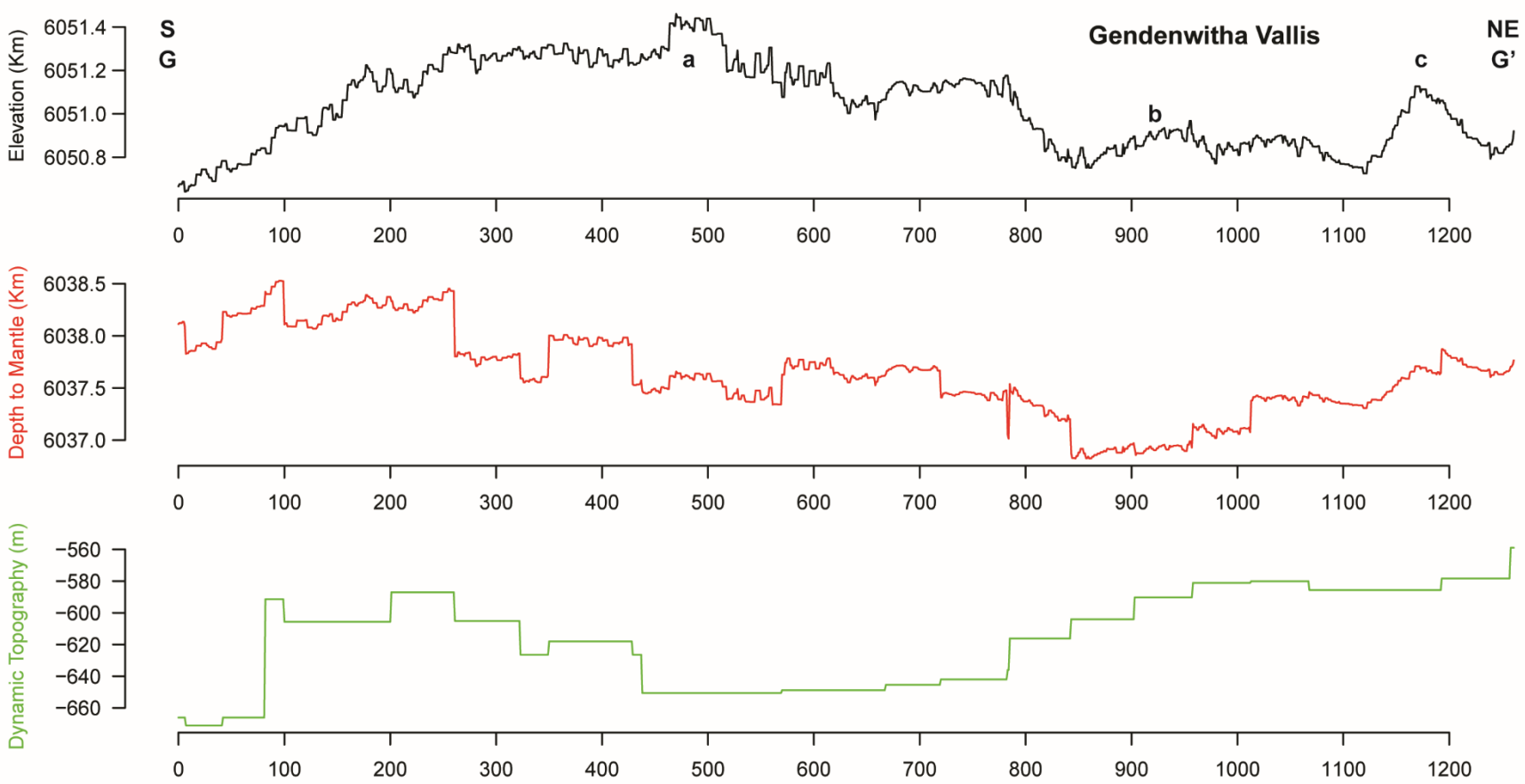

Figure 19: Profile view of topography in terms of radius (black line), depth to the mantle (red line), and dynamic topography (green line) along the flow path of Gendenwitha Vallis.

3.2.9 Kallistos Vallis

I mapped Kallistos Vallis (KV) following the left-look Magellan SAR mosaic through four quadrants from our 10x10 DD grid. After mapping, two anomalous points were removed, leaving a total of 1233 vertices. This channel is more complicated than I mapped, but I show some of the anastomosing nature of the channel while using the longest continuous line for my analysis. The length of this line is 1254 km. The straight-line distance connecting the endpoints is 653 km, which results in an overall channel sinuosity of 1.92.

The northwestern terminus of KV is a collection of pools that lie ~92 km from Derceto Corona (not on map) to the northeast (Figure 20). However, there is no clear relationship to determine the source of KV. Most of the channel is mapped in the lobate plains (pl), and any further mentions of geology will be where KV interacts with other units (Ivanov & Head, 2011). From K to K', KV moves south through a radar homogonous area before bordering a groove belt (gb) and continuing south (Figure 20). On the west side of the groove belt is a steep depression called Hanghepiwi Chasma. KV splits into several anastomosing channels and curves east, staying in lower elevations with the groove belt guiding it (Figure 21a). The multiple channels come back together at the southern-most part, but KV splits again as it weaves through the groove belt (Figure 21b). The topography has remained constant until this point. KV continues east while increasing in elevation, passing through a radar bright lava flow. The main channel splits into three, two of them continuing to the east while the third turns north. All three interact with a ridged plain (pr), with the southern two disappearing within the deformation. The northern channel continues to gain elevation, following along the west side of the ridged

plain. This ridged plain is an extension of Vaidilute Rupes, a series of scarps with a length of ~1900 km. This parallel path along the rupes indicates that Vaidilute Rupes was present during the formation of KV, and the topographic increase that KV undergoes reveals that the rupes continued to deform the surface after emplacement. On the graph of topography along the channel, KV shows a rapid drop in elevation at 1000 km which is not associated with a landform or structure (Figure 21c). KV passes through Ubastet Fluctus, a radar bright lava flow that covers this region around the ridged plain. KV undulates over the northern part of the ridged plain and decreases in elevation until it disappears within the lava flow to the east and south, potentially a source of the flow (Figure 21d).

As seen in Figure 22, the topographic rise from 550 km to 1250 km is substantial. The wavelength is ~660 km, and the amplitude is ~439 m. The depth to the mantle (red line) reveals that KV has a constant crustal thickness, except at ~1000 km, where the topographic drop is present and results in a thinner crust. However, the resolution of both datasets is not fine enough to know if this is a real result or an artifact. The dynamic topography (green line) increases to the east, similar to the topographic expression from 250 km to 950 km, meaning that the dynamic topography is preserved at the surface here. Since dynamic topography is a calculated measure of mantle convection, I infer that mantle convection is one of the most recent phenomena to affect the surface. Considering the positive values for dynamic topography, this region has undergone mantle uplift, which corresponds with the location of Vaidilute Rupes. Since scarps are contractional features and not created through uplift, this points to Vaidilute Rupes forming first, which is corroborated by its relationship with KV. As described, the surface along the rupes

continued to deform after the emplacement of KV, and I interpret this topographic change to be caused by the mantle uplift. In regards to the sections of elevation that do not follow the same trend as the dynamic topography, I still claim that the mantle uplift is the youngest surface-altering event. With the flow direction being defined as K to K', the west side of the channel would originally be the highest topographically along the channel with constantly decreasing elevation to the east. Then the mantle uplift topographically elevated the west side of the channel where it now lies even with the hypothesized source. The small decrease in elevation from 1000 km to 1250 km is too short of a length to be considered in the dynamic topography. Therefore, mantle uplift has affected this region and is the youngest phenomenon to do so.

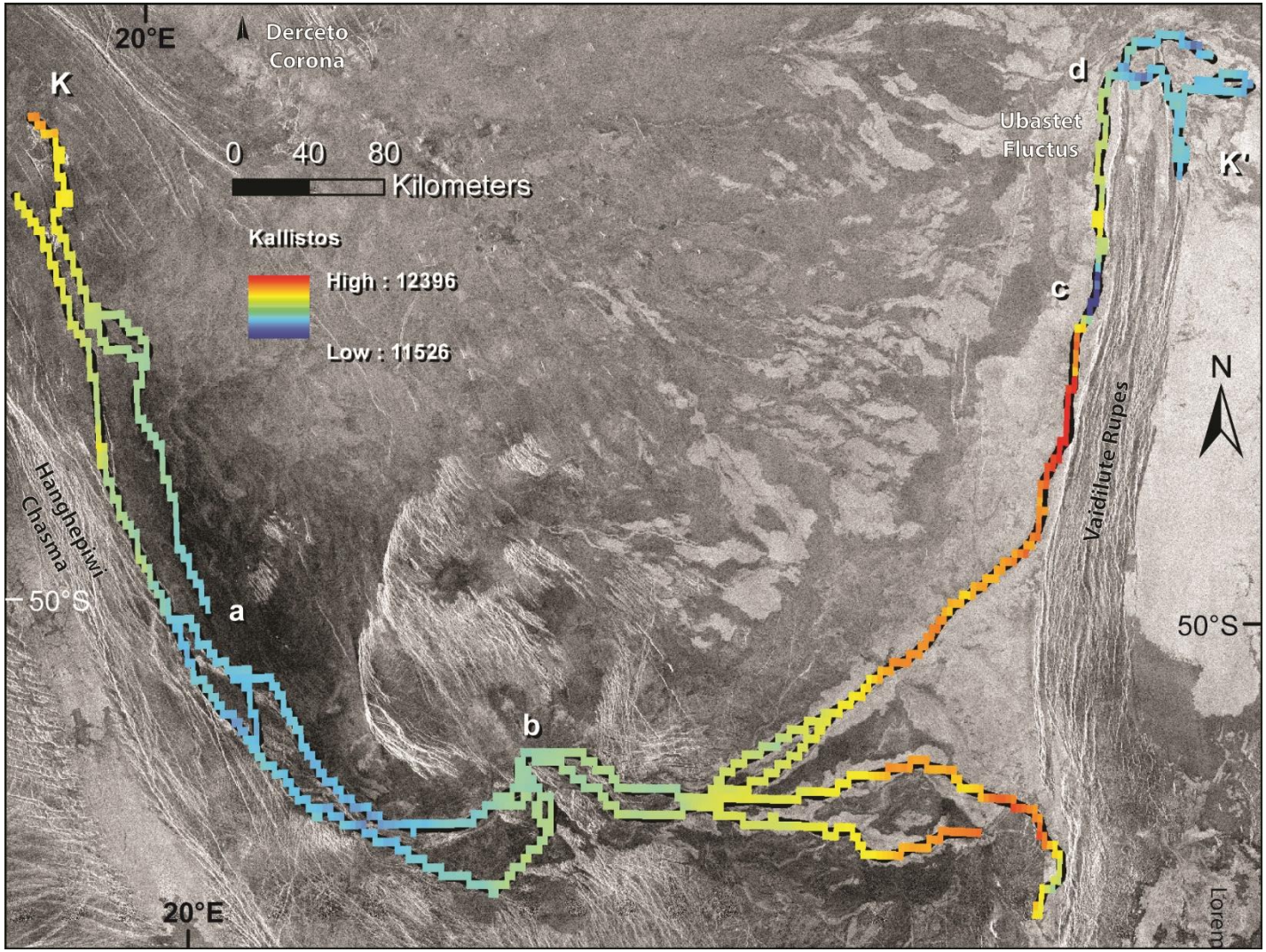

Figure 20: Magellan SAR left-look mosaic is projected to be centered on 23° E, 50° S in an orthographic projection showing Kallistos Vallis. The length is illustrated by a color-coded line indicating elevation, with higher elevation shown in red at 12396 m, and lower topography shown in dark blue equaling 11526 m.

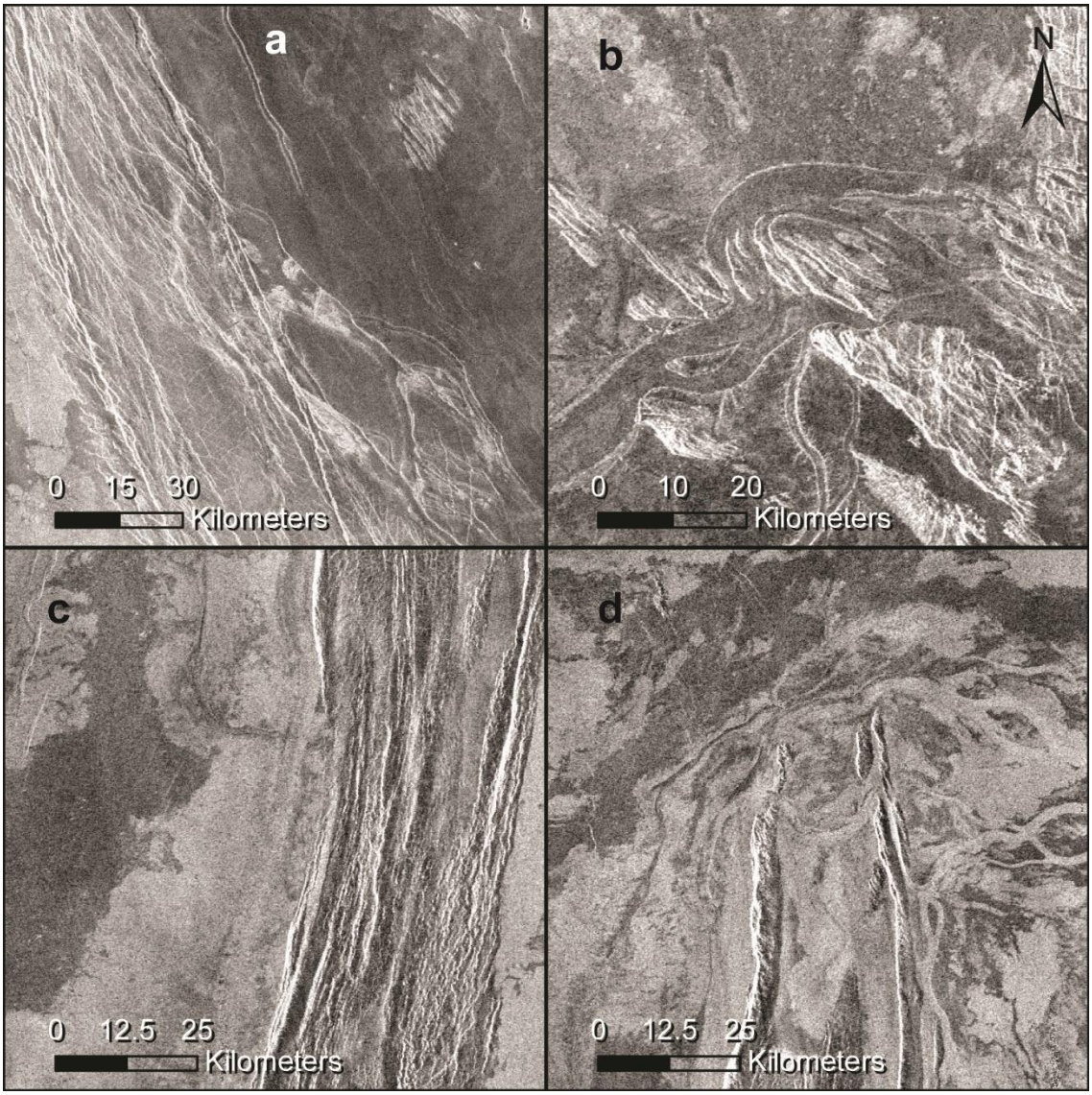

Figure 21: Magellan SAR left-look mosaics are projected to be centered on 23° E, 50° S in an orthographic projection showing close up sections of Kallistos Vallis. (a). KV splits into braiding channels. (b) The main channel splits into several channels as KV passes over a groove belt. (c) the location of the topographic drop at ~1000 km in Figure 22, in which nothing is visible. (d) KV crosses the rupes and disappears within the surrounding lava flow.

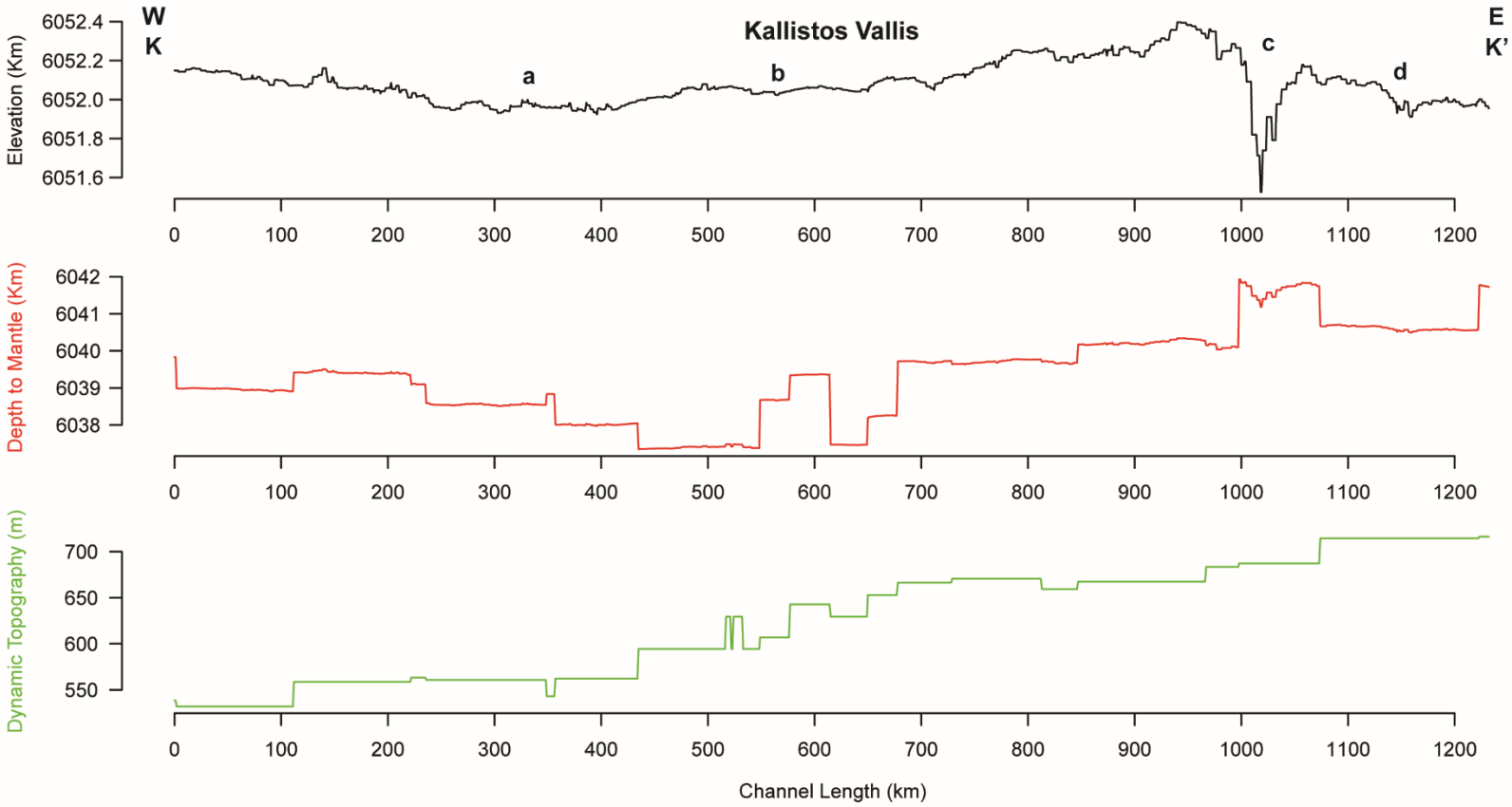

Figure 22: Profile view of topography in terms of radius (black line), depth to the mantle (red line), and dynamic topography (green line) along the flow path of Kallistos Vallis.

3.2.10 Sholpan Vallis

Sholpan Vallis (SV) had to be mapped following both left-look and right-look Magellan SAR mosaics through four bins from the 10x10 DD grid. Five anomalous points were removed, leaving a total of 1049 vertices. Most of SV is not covered by the SAR left-look mosaic, so the right-look was followed east of 143° E, 61° S. SV has a geodesic length of 1080 km, but there are two sections where the channel is not visible. The straight-line length for these sections adds a minimum of 33 km for a total minimum length of 1113 km. The distance between endpoints is 1019 km, and the overall sinuosity is 1.09.

A potential source, or ending point, for SV is a radar brighter lava flow called Rafara Fluctus that might come from Fotla Corona (not on map). On the east side of Rafara Fluctus, Merak Vallis (page 67) is present and also interacts with the lava flow. Sholpan and Merak Valles have the same structure and orientation, making it likely that they are the same channel, bisected by the lava flow. For the purposes of this study, I consider them separately. Another channel, Laidamlulum Vallis (page 41), is just to the south of SV, but their respective flows are in different orientations, so it is unlikely these are the same channel.

From S to S' in Figure 23, the southeastern terminus of SV is found in the regional plain (rp2) and continues through a shield plain (psh) and into another regional plain (rp1) (Ivanov & Head, 2011). From the southeastern terminus, SV continues northwest into a radar homogonous region called Imapinua Planitia with small wrinkle ridges that start with an N/S orientation but transition to an E/W orientation as SV continues northeast. SV passes Melanie crater and Laidamlulum Vallis to the west, and at

this point, the left-look SAR mosaic is present (Figure 23). There is an unclassified feature just north of SV and south of Blixen crater. After the left-look SAR boundary, the channel continues in its northwest direction. The left-look SAR mosaic reveals that the wrinkle ridges are larger than visible in the right-look, and they also affect the channel, meaning they are younger than SV. At point "a" in Figure 24, there is a topographic high on the topographic profile, but there is no landform or structure visible to explain this change (Figure 23a). Since the channel is unaffected by the topographic change and does not curve to avoid it, the topographic elevation is younger than the channel. The wavelength is ~239 km, and the amplitude is ~189 m. From the southeastern terminus, SV decreases in elevation in Imapinua Planitia until interacting with and bordering a radar bright terrain mapped as a regional plain (rp2), where it drastically increases in elevation to the northwestern terminus (Figure 23b). This topographic decrease and increase have a wavelength of ~293 km and an amplitude of ~241 m. SV becomes difficult to see and disappears within the lava flow called Nambubi Fluctus, which appears to have come from Latmikaik Corona (not on map) to the southwest.

In either flow direction, there was a topographic change resulting in the middle being the lowest elevation. SV could have originated from either Nambubi Fluctus or Rafara Fluctus. Within both lava flows, SV is seen over top of the flow. This overprinting favors a separate source, either Egle Mons (not on map), which is ~200 km west of the NW point of the mapped channel, or Xcacati Corona (not on map), which is further northwest and created the large Arubani Fluctus (not on map).

The depth to the mantle profile (red line) shows that the crust under SV is thickened under the termini based on the deeper roots underneath the higher elevations

seen in Figure 24. The center shows crustal thinning where the topographic low is present. The dynamic topography (green line) decreases until 700 km when it begins to increase toward the northwestern terminus. This trend is the same as the elevation behavior, revealing that the dynamic topography is preserved at the surface, meaning it is a relatively young process. Mantle convection is represented by dynamic topography and thus is the driving force behind the surface expression of topography. Specifically, SV has undergone subsidence by mantle downwelling. The short-wavelength between 600 and 800 km did not have a visible cause but was too short of a length to be seen within the dynamic topography.

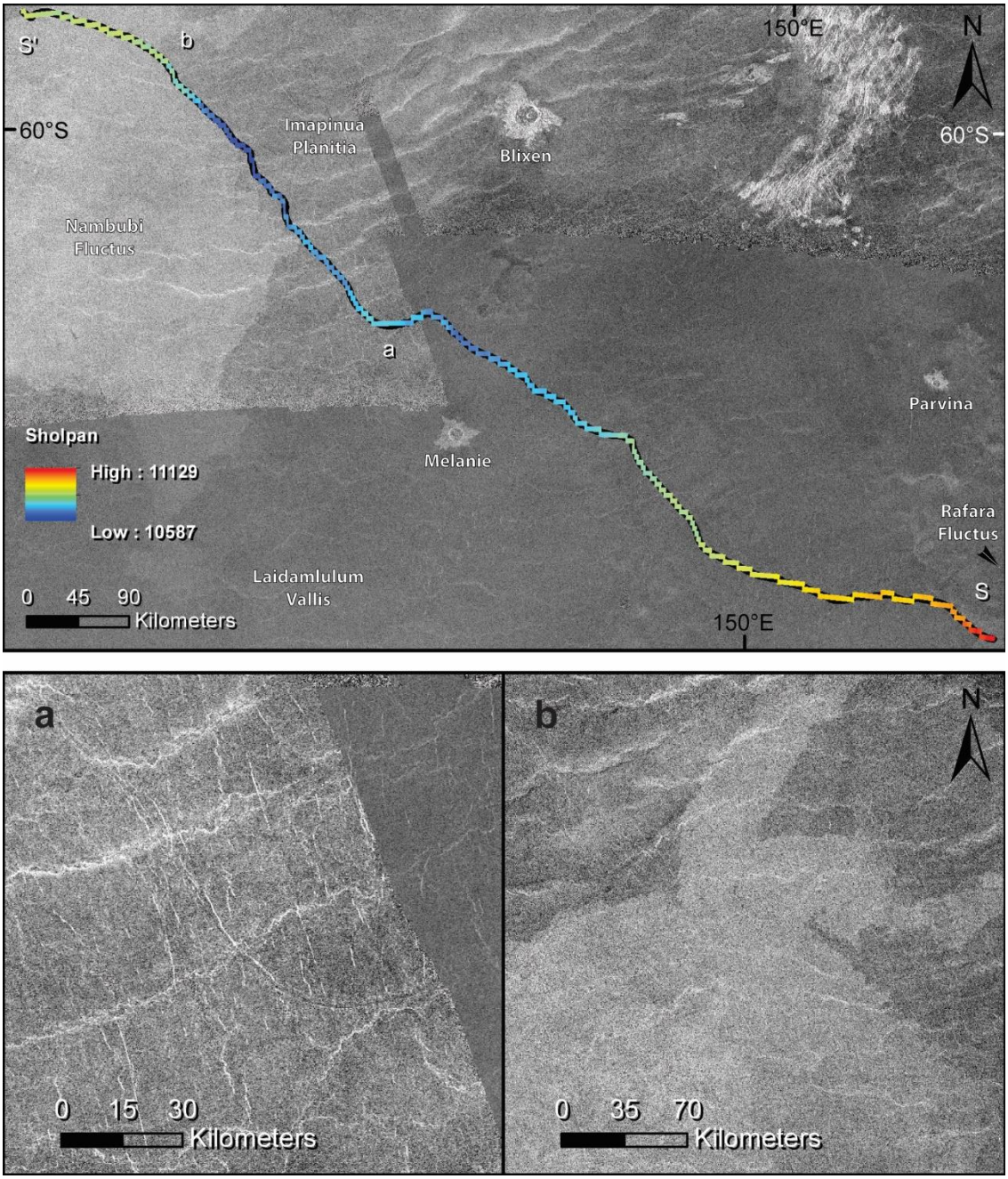

Figure 23: Magellan right-look and SAR left-look mosaics are projected to be centered on 145° E, 60° S in an orthographic projection showing Sholpan Vallis. The length is illustrated by a color-coded line indicating elevation, with higher elevation shown in red and lower topography shown in dark blue. (a) and (b) are close views. (a) Sholpan Vallis crosses into the SAR left-look mosaic and crosses a topographically elevated region. (b) SV enters the radar bright lava flow and increases in elevation.

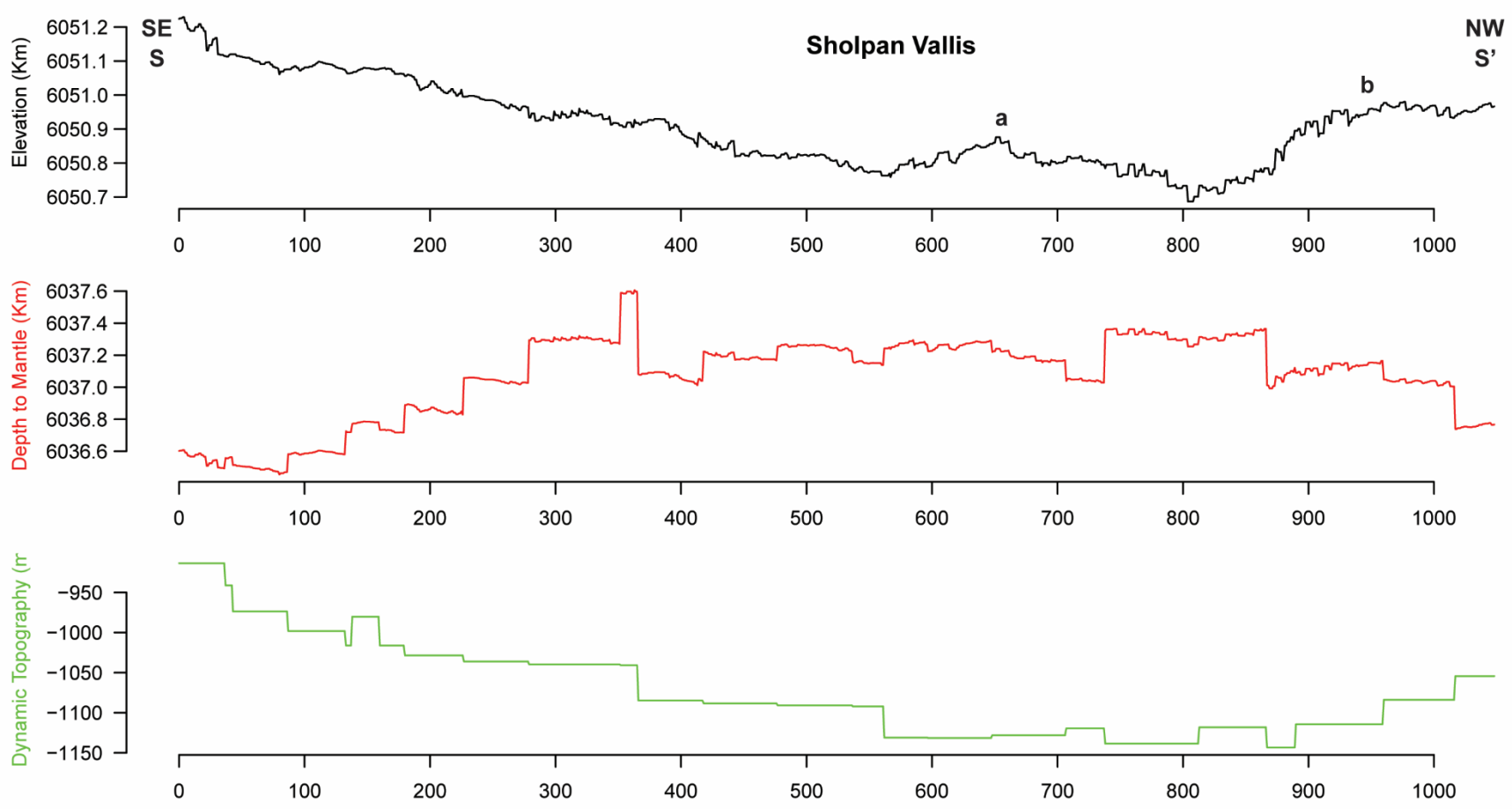

Figure 24: Profile view of topography in terms of radius (black line), depth to the mantle (red line), and dynamic topography (green line) along the flow path of Sholpan Vallis.

3.2.11 Merak Vallis

Merak Vallis (MV) is more visible in the right-look Magellan SAR and moves through two bins from the 10x10 DD grid. One anomalous point needed to be removed, leaving a total of 266 vertices. The geodesic length is 269 km, and from M to M', the straight-line distance is 254 km, resulting in an overall channel sinuosity of 1.06.

Fotla Corona (not on map) lies 400 km north of MV, the only corona nearby. Other potential sources are Salofa Colles (not on map) which lies east of MV by ~200 km, and Rafara Fluctus, which lies just west. As discussed, Merak and Sholpan Valles are likely the same channels due to their identical characteristics and orientation, which favors Fotla Corona as the source. The entirety of MV lies within a regional plain (rp1), although the southwestern terminus is near Rafara Fluctus, which is mapped as an rp2 regional plain (Ivanov & Head, 2011). The overall behavior of MV flows between this rp2 regional plain to the west and a shield plain (Salofa Colles) to the east. Describing from M to M', the southwestern terminus is ~25 km east of the fluctus and is found in the radar dark featureless regional plain (Figure 25). The channel is straight until the elevation begins to increase, and then the channel becomes sinuous. MV passes through a topographically elevated region that is not associated with a landform or structure, shown in Figure 25a. Although, in the overview picture, the topographic change is radar brighter than the surroundings. This change has a wavelength of ~149 km and an amplitude of ~144 m. The channel does not change its orientation, continuing NE/SW unperturbed by the topographically elevated region, meaning that the deformation happened after channel emplacement. Continuing northeast, MV appears to undulate with the topography; however, these drastic changes appear to be an artifact of the topography raster because

they are sharp lines and not true information, so I disregard it for the purpose of this study. The channel continues from the topographic elevation and returns to a lower sinuosity, then fades into the northeastern terminus less than 20 km from the fluctus to the west.

The depth to the mantle (red line) shows crustal thinning beneath the southwestern terminus, then crustal thickening until ~100 km, where the thickness becomes constant towards the northeastern terminus (Figure 26). The dynamic topography (green line) increases towards the northeast; however, the length of the channel is shorter than the spatial block size of ~477 km, making interpretation impossible.

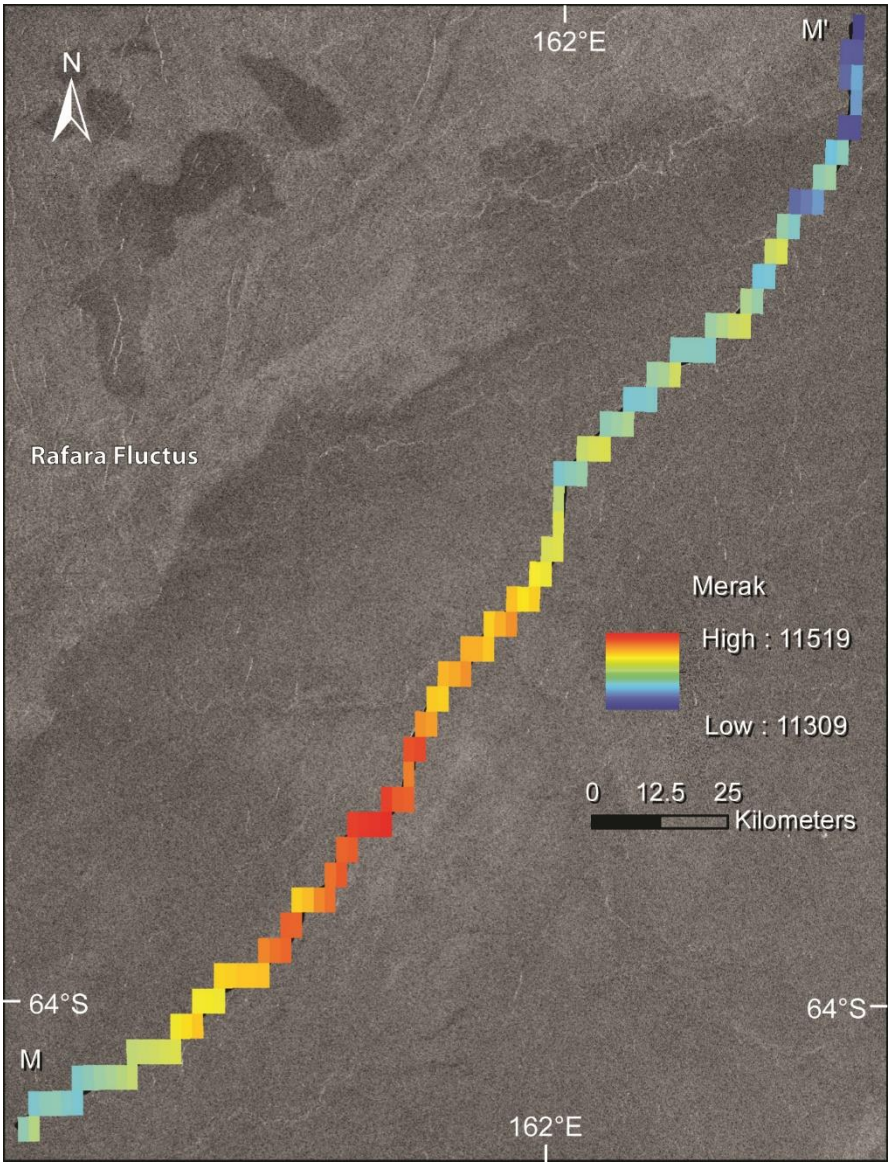

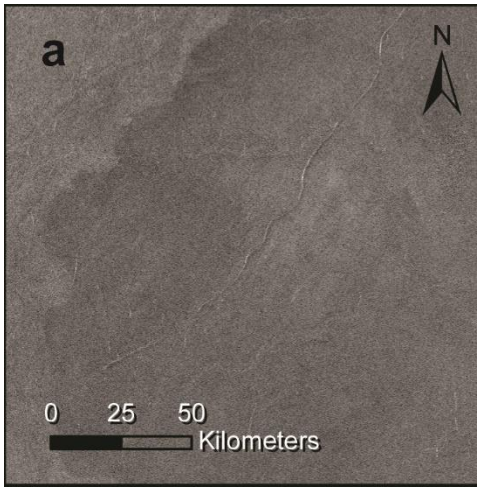

Figure 25: Magellan SAR right-look mosaic is projected to be centered on 161° E, 63° S in an orthographic projection showing Merak Vallis. The length is illustrated by a color-coded line indicating elevation, with higher elevation shown in red and lower topography shown in dark blue. (a) MV passes over a topographically elevated region indistinguishable from the surrounding radar.

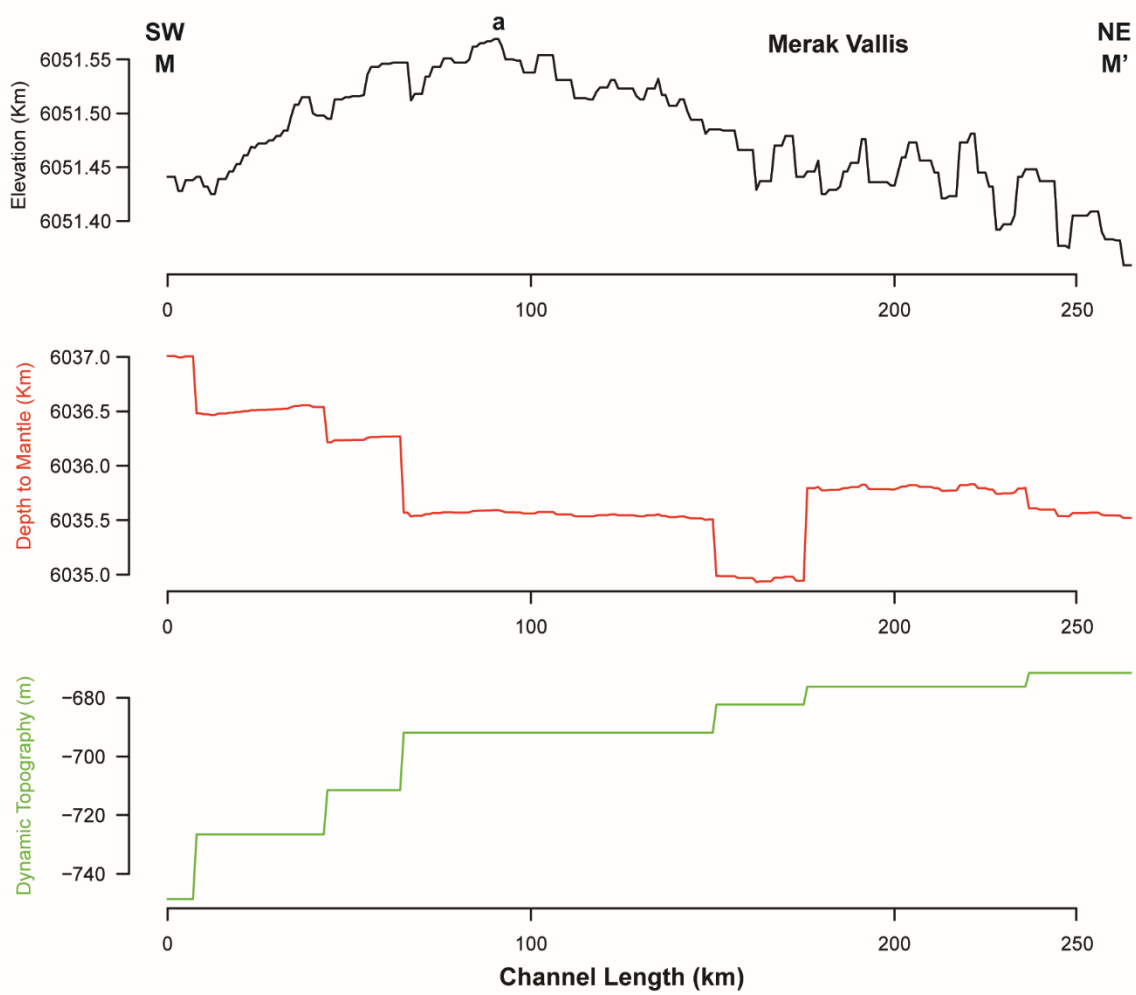

Figure 26: Profile view of topography in terms of radius (black line), depth to the mantle (red line), and dynamic topography (green line) along the flow path of Merak Vallis.

3.2.12 Jutrzenka Vallis

I mapped Jutrzenka Vallis (JV) following the left-look Magellan SAR mosaic through one bin from the 10x10 DD grid. After mapping, three anomalous points were removed, leaving a total of 877 vertices. While the length of the visible channel is 864 km, there are two small sections not covered by data and one section where a lava flow covers the channel, nearly bisecting it. These three combined add a minimum length of 168 km for a total minimum length of 1033 km. The straight-line distance between the endpoints is 839 km. From these calculations with the added length, the overall sinuosity is 1.23. The additional 168 km is the shortest path connecting each endpoint of missing data, and the channel likely did not flow in a straight line. Therefore, 1033 km is the minimum length for JV.

From J to J', the southeastern terminus of JV is found in tesserae (Figure 27). JV might continue further southeast, but the characteristics are vastly different and thus are not considered. Southwest of this terminus is two potential sources not on the map: ~630 km away is Ituana Corona, and ~670 km away is Zaltu Mons. JV sharply turns to the northwest, 90 degrees from the original flow direction, and passes through a topographically elevated region called Oya Dorsa that is mapped as a ridged plain (pr) (Ivanov & Head, 2011). JV curves with the dorsa indicating post-formation deformation (Figure 28a). This topographic undulation has a wavelength of ~184 km and an amplitude of ~811 m. It is worth noting that JV flows around the higher topography, which shows that a feature was present when JV formed and continued deformation, which topographically elevated the channel. JV continues west and begins to gradient into radar bright just before bordering a lava flow, mapped as a regional plain (rp2) (Figure 28b).

This regional plain is relatively lower topographically than the surrounding areas. JV continues north and increases in elevation while bordering a ridged plain (pr) that is topographically elevated (Figure 28c), relatively dating the topographic increase as younger than the channel. The topographic change seen here has a wavelength of ~222 km and an amplitude of ~566 m. This ridged plain is a continuation of Oya Dorsa. The channel then becomes less distinct, turning northwest, and is overprinted by small wrinkle ridges. JV then mostly disappears in a radar bright lava flow (regional plain, rp2). Despite the lava flow, a faint trail of the channel remains visible in the radar mosaics (Figure 28d), and the channel reappears at the west side ~80 km away. JV retains the radar bright quality for ~ 80 km before reverting to the radar dark floors and radar bright walls, as seen earlier in the structure. This lava flow could have formed before, during, or after the lava channel. However, formation before or during JV seems more likely because of the faint print of the flow path. The radar bright material found in the channel leading out of the regional plain could be a small amount from the lava flow that utilized the path. Within the lava flow, JV curves around a topographically elevated region; however, the faint path through the lava flow is not considered for this study; instead, a straight line is used to connect the two sides. JV continues northwest indiscriminate of the topography, ignoring a topographic low and passing through a topographically elevated region, which indicates that JV is older than both deformations and neither is associated with a structure or landform. JV enters a radar homogonous region (regional plain, rp1) with wrinkle ridges that have a NE/SW orientation. The wrinkle ridges continue over the channel, in some cases obscuring it, which dates them as younger than the channel. JV turns north right when the wrinkle ridges change orientation to E/W. The

channel runs parallel to a long topographically elevated region but does not enter the topographic low to the east, staying at moderate elevation, which points to post-formation deformation; otherwise, the channel would have continued downslope. JV passes through a topographically elevated region that extends from a ridge plain (pr) from the east and gets lost in a heavily deformed region that is lower topographically than the surrounding terrain.

The last three topographic undulations are harmonic and change 228 m over 91 km. In Figure 29, the depth to the mantle (red line) shows a nearly constant crustal thickness with small artifacts creating jumps in the data. The dynamic topography (green line) increases slightly to 200 km, then decreases toward the northwest terminus. The trend does not follow the elevation well, meaning that the topographic undulations are caused by a different process. Both substantial topographic changes are caused by Oya Dorsa.

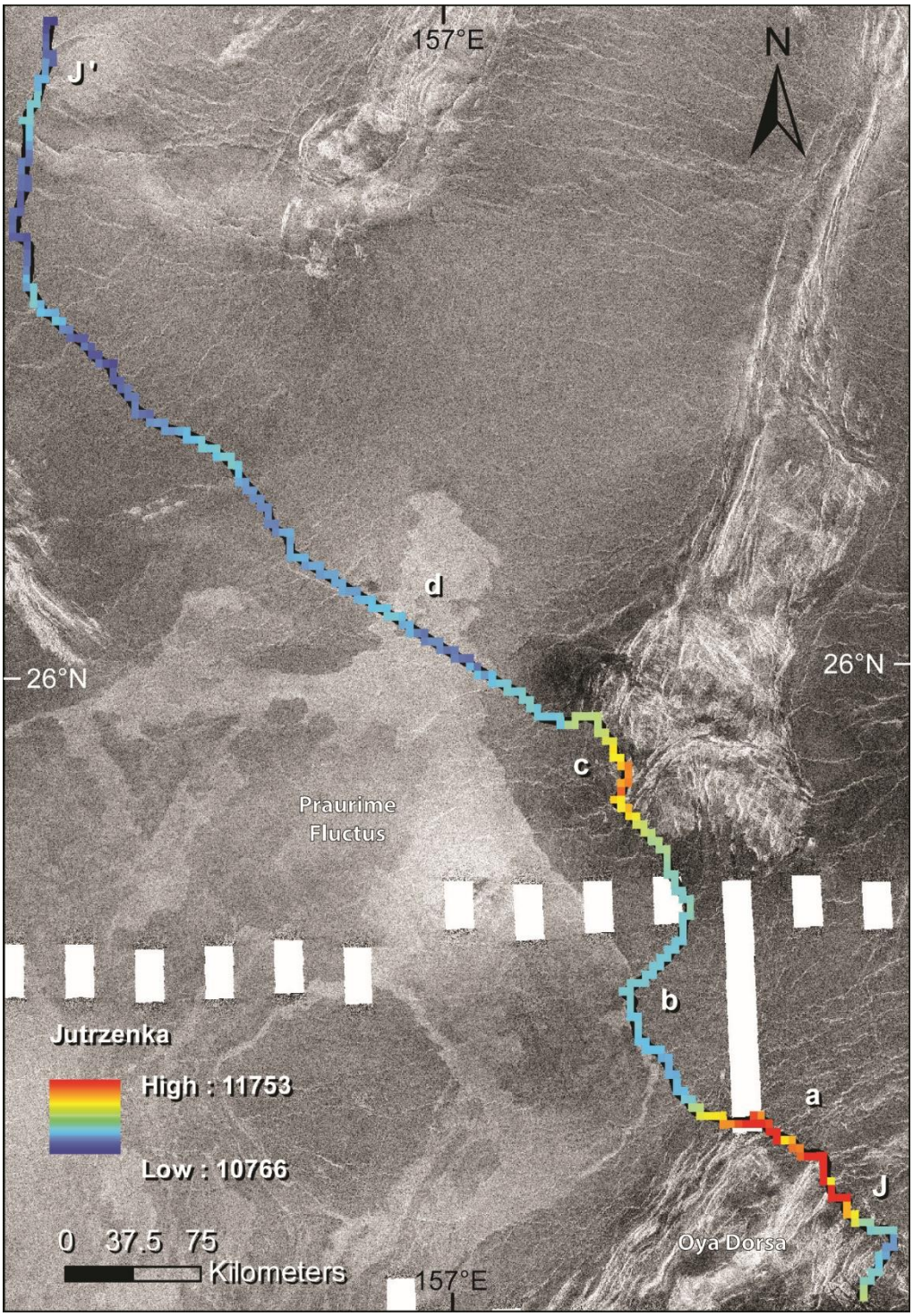

Figure 27: Magellan SAR left-look mosaic is projected to be centered on 157° E, 25° N in an orthographic projection showing Jutrzenka Vallis. The length is illustrated by a color-coded line indicating elevation, with higher elevation shown in red and lower topography shown in dark blue.

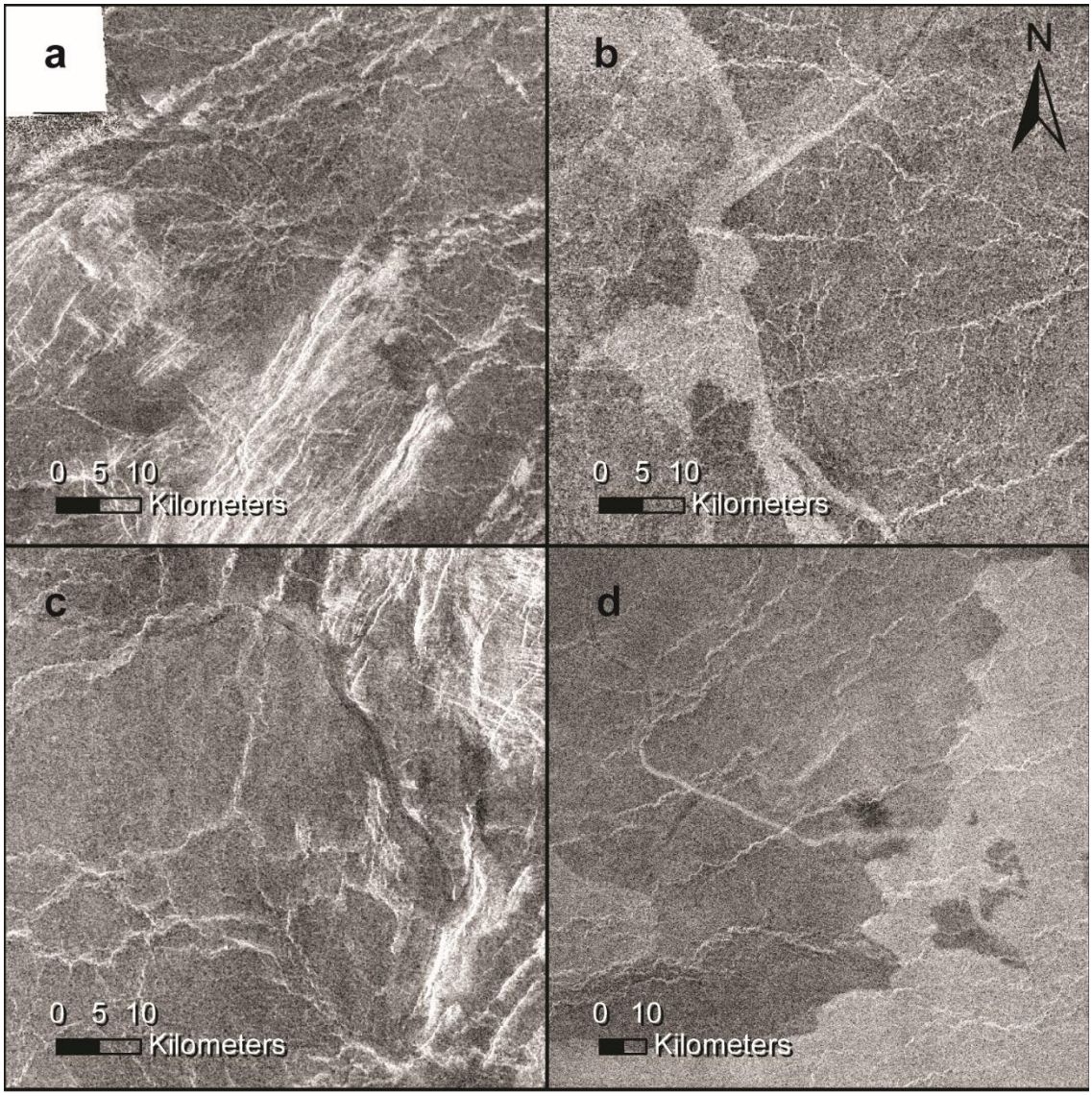

Figure 28: Magellan SAR left-look mosaics are projected to be centered on 157° E, 25° N in an orthographic projection showing close up sections of Jutrzenka Vallis. (a). JV curves with the section of Oya Dorsa. (b) The channel floor of JV transitions to radar bright as it enters a lava flow. (c) JV flows over a topographically elevated ridge plain. (d) JV is seen on the western side of the lava flow. Note the faint channel floor within the flow itself.

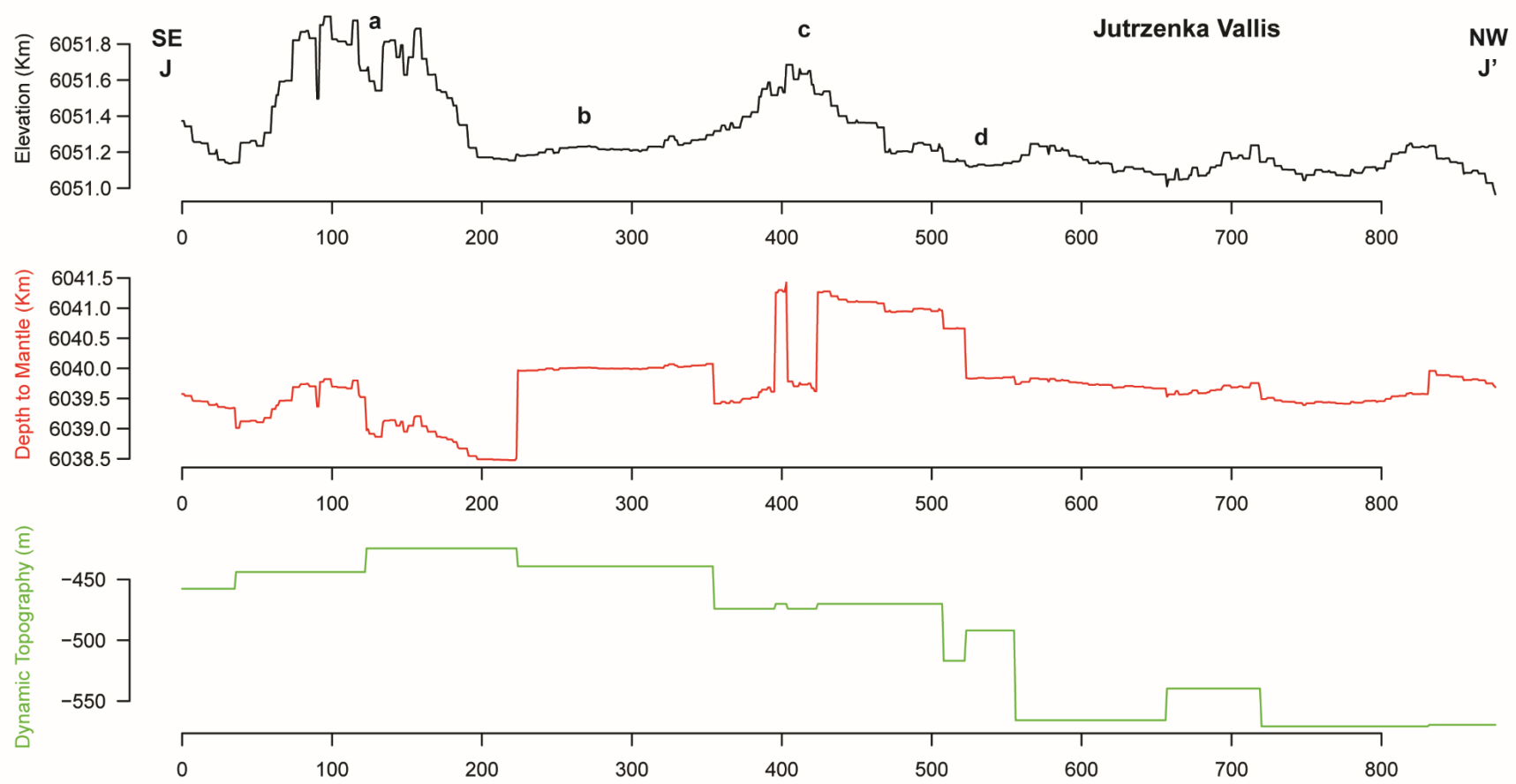

Figure 29: Profile view of topography in terms of radius (black line), depth to the mantle (red line), and dynamic topography (green line) along the flow path of Jutrzenka Vallis.

3.2.13 Lusaber Vallis

I mapped Lusaber Vallis (LV) following the left-look Magellan SAR mosaic through two bins from our 10x10 DD grid (Figure 30). Two points were removed after mapping, leaving a total of 897 vertices. The measured geodesic length is 907 km, and the straight-line distance is 669 km. Dividing the former by the latter results in an overall channel sinuosity of 1.36.

LV lies in a regional plain and stays entirely within this unit (rp1) (Ivanov & Head, 2011). To the south, Nortia Tesserae (~65 km, not on map) and Mena Colles (~450 km, not on map) (psh) are present around Tonatzin Corona (not on map), which is ~550 km farther south. To the west, by ~1700 km, lies the large and complex structure of Artemis Corona (not on map). The source for LV is not clear due to the large distance from each of these coronae. Describing from L to L', the western terminus of LV borders the tesserae to the south in a radar dark spot that is homogonous. LV sharply turns north, sinuously, and continues through a local depression but does not pass through the topographic low and turns southeast to increase in elevation (Figure 30a). This relationship reveals that the topographic depression was not present during the channel formation and was created after emplacement. LV then enters a radar brighter area with wrinkle ridges oriented NE/SW that are present in the channel floor, relatively dating the wrinkle ridges as younger. From this point, topography increases gradually until L'. Within this wrinkle ridged area, LV is much straighter and does not have small sinuous changes. LV curves around a topographically elevated region to the north that is radar darker, meaning the topographic elevation was present when the lava flowed, then the channel enters a higher topographic region that does not have wrinkle ridges, is radar

darker, and is homogonous. Upon entering this region, the small sinuous fluctuations reappear until the eastern terminus, as seen in Figure 30b.

The entire channel is affected by a topographic change as it forms a bowl with a wavelength of ~792 km with an amplitude of ~362 m (Figure 31). Within the topographic profile (black line), there is also a small undulation between 400 – 500 km. This change has a wavelength of ~112 km and an amplitude of ~146 m. The depth to the mantle (red line) shows that the crust underneath LV is thickened under both topographically elevated ends, and the center is thinner under the topographic low. The dynamic topography (green line) remains constant until 400 km, then increases to the eastern terminus. The relationship of topography to dynamic topography is more complicated, with the last 500 km mimicking the elevation. From 500 km, the dynamic topography is the result of the topographic expression, meaning that mantle convection has affected the surface recently since dynamic topography is a calculated measure of mantle convection. Specifically, LV underwent subsidence caused by mantle downwelling. The first 400 km do not show this relationship. This means that the western half of the channel either represents the undeformed downward flow or there is another unspecified tectonic cause.

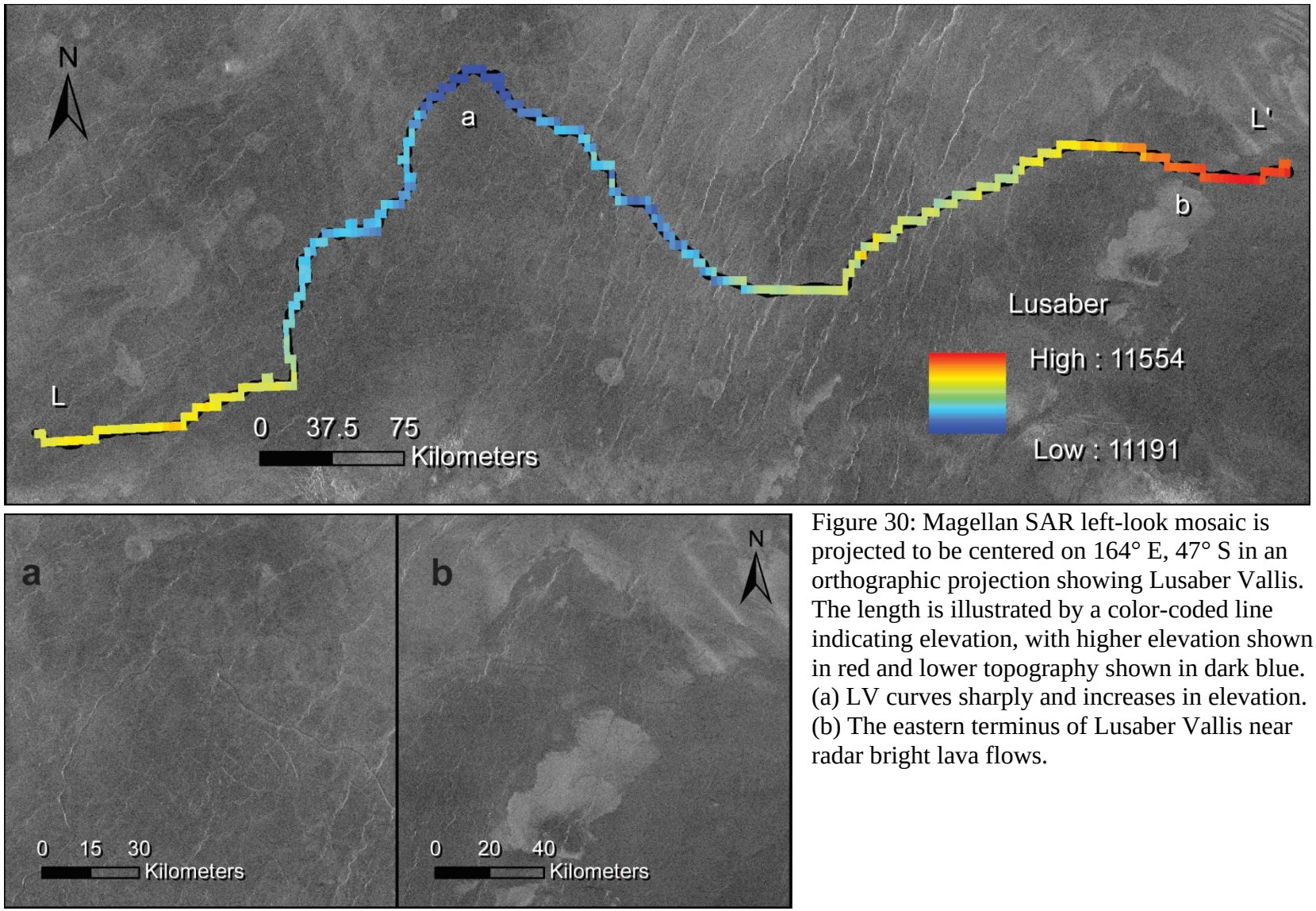

Figure 30: Magellan SAR left-look mosaic is projected to be centered on 164° E, 47° S in an orthographic projection showing Lusaber Vallis. The length is illustrated by a color-coded line indicating elevation, with higher elevation shown in red and lower topography shown in dark blue. (a) LV curves sharply and increases in elevation. (b) The eastern terminus of Lusaber Vallis near radar bright lava flows.

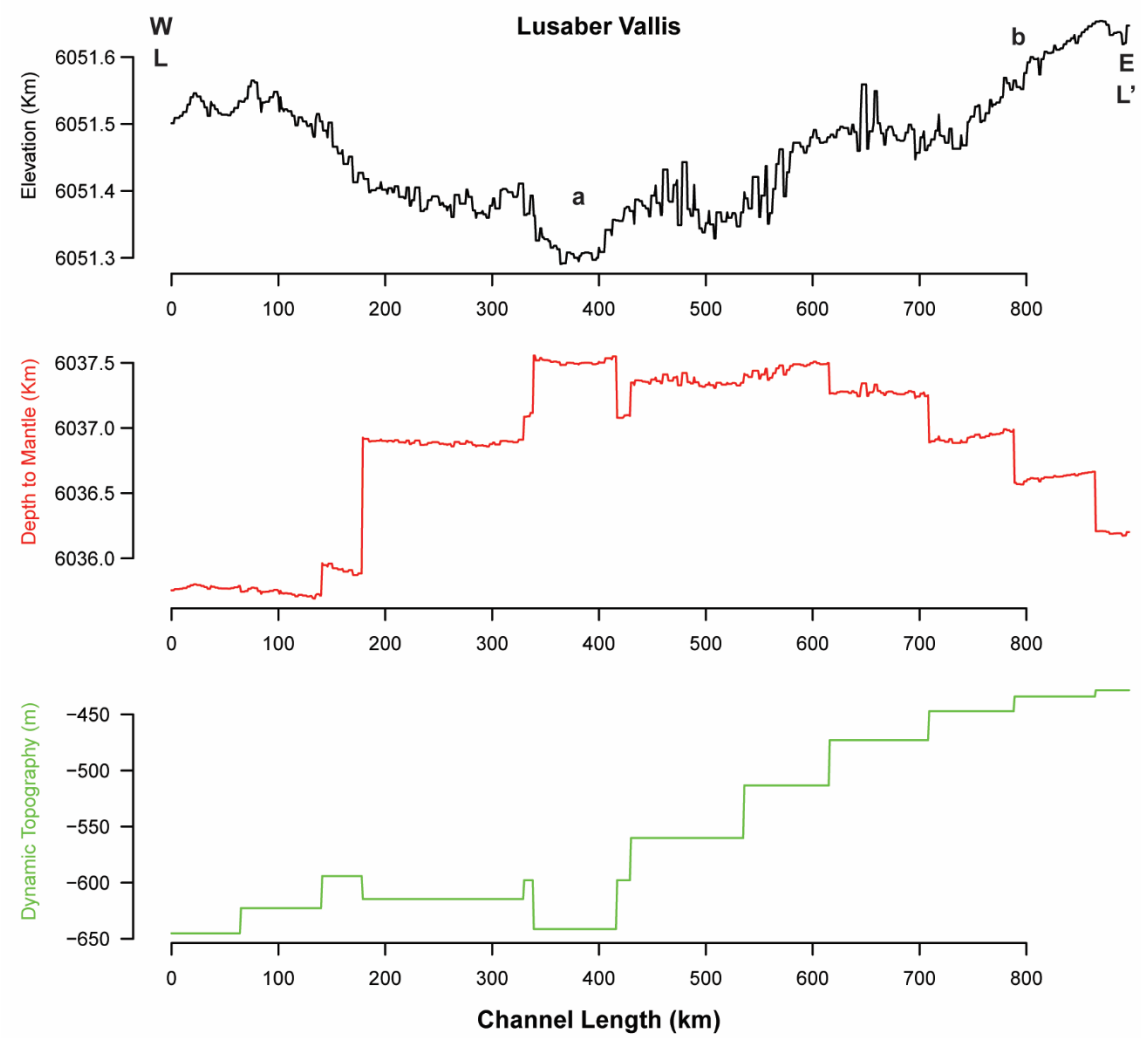

Figure 31: Profile view of topography (black line), depth to the mantle (red line), and dynamic topography (green line) along the flow path of Lusaber Vallis.

3.2.14 Sinann Vallis

I mapped Sinann Vallis (SV) following the left-look Magellan SAR mosaic through two bins from the 10x10 DD grid (Figure 32). After mapping, I did not have to remove any points from the 846 vertices. I measured the geodesic length as 856 km and the distance between endpoints as 668 km. This results in an overall channel sinuosity of 1.28.

The potential sources around SV are Enekeler Corona (not on map) to the north by ~250 km, Tangba Corona (not on map) ~330 km northwest, and Ama Corona (not on map) by ~470 km to the east. Another feature is Norna Tesserae, just south of the channel. SV is mapped in a regional plain, with small interactions with other units described below (rp1) (Ivanov & Head, 2011). There are shield plains north and south of the channel, but SV does not cross into either unit (psh). Describing from S to S', the western terminus is found in a radar homogonous plain and continues east into N/S oriented wrinkle ridges, some of which the channel crosscuts and others crosscut the channel, indicating ongoing fault forming processes. SV then curves around a densely lineated plain that lies around Enekeler Corona and passes through a small cut-through, weaving between the lineations and increasing in elevation (pdl). SV crosses this topographically elevated region, as seen in Figure 32a and Figure 33 (black line), meaning the surface deformed after channel emplacement. The topographic change seen in the profile is harmonic and has a wavelength of ~262 km and an amplitude of ~230 m. After decreasing in elevation, SV continues through a valley that shows N/S-oriented wrinkle ridges, experiencing small sinuous curves. SV continues through another small topographically elevated region that is not associated with a landform or structure and is

younger than the channel. The wrinkle ridges are denser, and radar brighter here. SV then turns southeast and curves around another topographically elevated region partially. This reveals that a topographic elevation was present during formation, but the surface continued to deform after emplacement. SV curves sharply and continues east, where the radar is no longer as bright. SV curves north of a radar bright spot and through small circular features, shown in Figure 32b. The channel then increases in elevation as it continues through a topographically elevated region, and its eastern terminus lies near a heavily deformed region. This topographic increase is also radar bright, and fractures follow along and emphasis a peanut shape. The channel is older than this topographic change and has been deformed. 100 km south of the eastern terminus is a small channel, ~115 km long. This small channel could be part of SV, but since there is no conclusive relationship, it is not considered.

The depth to the mantle (red line) follows the same trend as the topography (black line), meaning a constant crustal thickness (Figure 33). The dynamic topography (green line) also follows the trend, increasing to the east. Point "a" is caused by the uplift from the densely lineated plain and would not be within the dynamic topography data. Since dynamic topography is a calculated measure of mantle convection, the deformation caused by mantle convection is preserved at the surface, meaning it is one of the youngest processes to deform the surface. The relative ages between the densely lineated plain and the dynamic topography cannot be determined because they are both younger than the channel. The deformation that SV underwent is subsidence due to mantle downwelling.

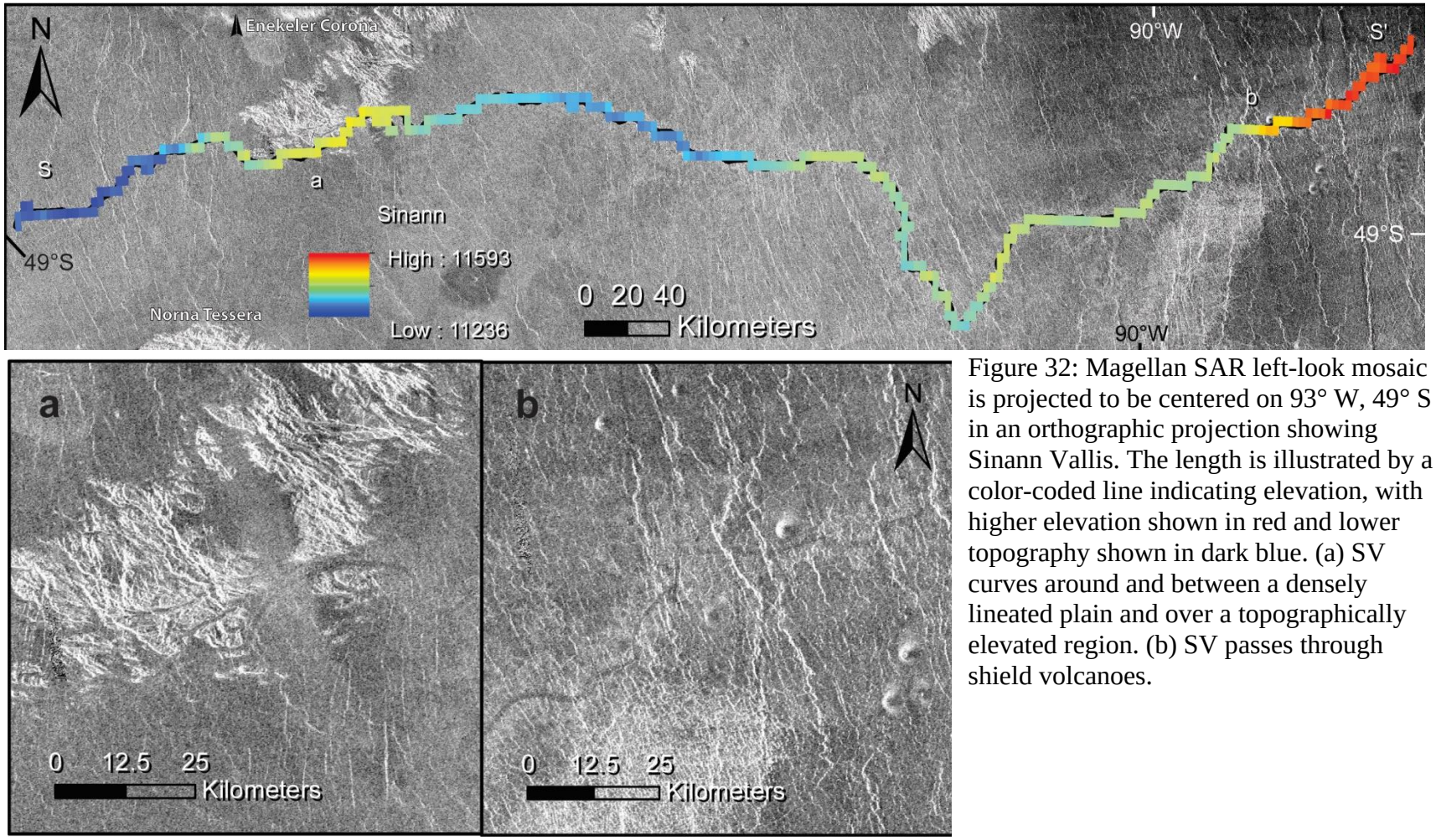

Figure 32: Magellan SAR left-look mosaic is projected to be centered on 93° W, 49° S in an orthographic projection showing Sinann Vallis. The length is illustrated by a color-coded line indicating elevation, with higher elevation shown in red and lower topography shown in dark blue. (a) SV curves around and between a densely lineated plain and over a topographically elevated region. (b) SV passes through shield volcanoes.

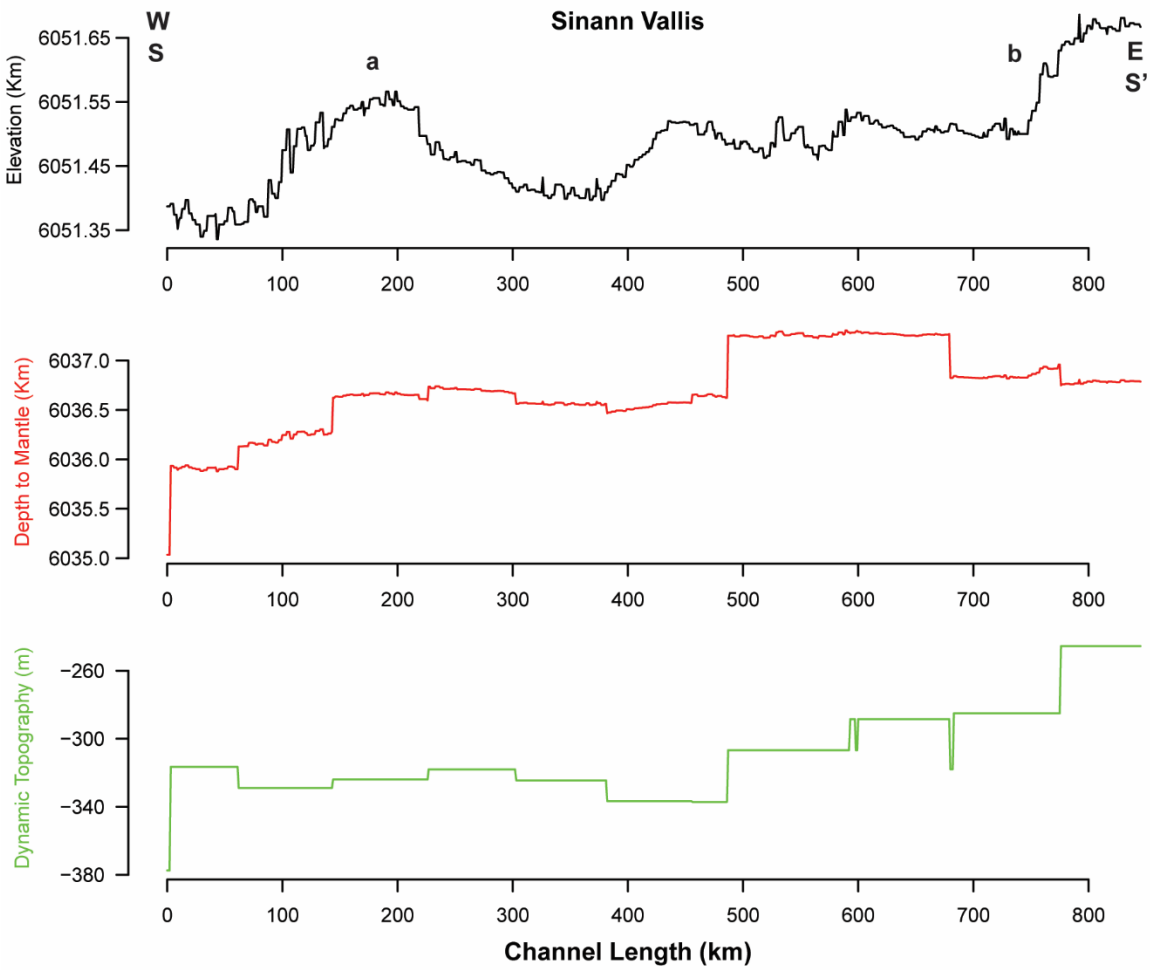

Figure 33: Profile view of topography (black line), depth to the mantle (red line), and dynamic topography (green line) along the flow path of Sinann Vallis.

3.2.15 Morongo Vallis

I mapped Morongo Vallis following the right-look and left-look Magellan SAR mosaics through two bins from the 10x10 DD grid (Figure 34). There is also a smaller perpendicular channel that is discussed separately from the main channel. After mapping, I removed six anomalous points from the long channel, leaving a total of 797 vertices. I removed one point for the short channel, leaving 300 vertices. I followed the right-look for this channel mostly because the left look is striped through and inconsistent, but the left-look was used where available in bin 1. The geodesic length is 811 km for the long channel. The perpendicular, short channel has a length of 305 km. Both channels have offshoots. The main channel has a small section that is not visible due to data resolution, and this adds a length of 15 km for a total minimum length of 826 km. The straight-line distance for the longer one is 652 km. The shorter channel straight line distance is 251 km. The overall sinuosity for the longer channel is 1.27 with the added length. The shorter channel's sinuosity is 1.21.

Morongo Vallis lies within Viriplaca Planum, and the closest corona is Inari Corona to the northeast by ~530 km. Starting with the main channel of Morongo Vallis (MV), I describe from northwest to southeast (M to M'). The northwestern terminus of MV is visible near a rift zone (rz) (Ivanov & Head, 2011). Continuing south, MV crosses into a lobate plain (pl) that is radar dark initially. Small fractures interrupt the imprint of the channel, meaning they are younger. The lobate plain becomes radar bright and homogonous further south, and MV shows increased sinuosity through this transition. The channel splits and forms a small offshoot, which continues through a topographically elevated region. This relationship shows that the topographic change is younger than the

channel. The main channel continues southeast, decreasing in elevation and bordering a regional plain (rp1) and a shield plain (psh), staying just east of the formations. MV passes through an unidentifiable radar dark spot (Figure 35a), then begins increasing in elevation and continuing through a topographically elevated region that is not associated with a landform or structure. This relatively dates the channel as older than the topographic change. The channel continues southeast and interacts with the secondary, shorter channel of MV, which is described below (Figure 35b). The southeastern terminus lies at a fissure. MV either flows into or out of this fissure with obvious pits along it (Figure 35c).

The shorter channel (MoV) is described from southeast to northwest (Mo to Mo'). Most of the channel stays within the lobate plain (pl), with the exceptions listed below. MoV interacts with the large channel through several branches flowing perpendicular from MV, as shown in Figure 35b. MoV curves around a topographic high but still increases in elevation, revealing that the surface has continued to deform after emplacement. This topographic change has a wavelength of ~80 km and an amplitude of ~87 m. Right at this topographically elevated region is a fracture NW/SE in orientation that does not disrupt the channel. The relationship and relative aging are unclear between the channel and the fracture. MoV continues northeast, splitting several times into small southwest-oriented offshoots. The channel curves around a regional plain (rp1), avoiding entering the plain but turning east to follow the border, as seen in Figure 35d. MoV gradually increases in elevation and fades. Further east is a heavily deformed rift zone (rz). Because of the proximity to Inari Corona, this is possibly the source of the smaller

channel for MoV, meaning that the flow direction would be opposite of how I have described it here.

The entire channel (MV) is the topographic undulation, illustrated by the elevation profile (black line) in Figure 36. This deformation change is 390 m over 744 km. Both the depth to the mantle (red line) and dynamic topography (green line) datasets have odd unexplained jumps that render interpretation difficult. The depth to the mantle shows crustal thickening underneath both topographically elevated termini with crustal thinning in the center at 480 km. The dynamic topography generally decreases until ~480 km, then increases toward the southeastern terminus. This trend is similar to the topographic behavior, meaning that the dynamic topography is preserved at the surface. Dynamic topography is a calculated measure of mantle convection, meaning that mantle convection is the process that deformed the topography and is the youngest process to do so. From the graph, the mantle was upwelled, and the surface was uplifted. For MoV in Figure 37, the depth to the mantle shows a constant crustal thickness until the northeastern terminus, where it is thickened. The dynamic topography increases toward the northeast, showing the same behavior as the topography. However, the length of MoV is too short to interpret from the dynamic topography due to the limited resolution.

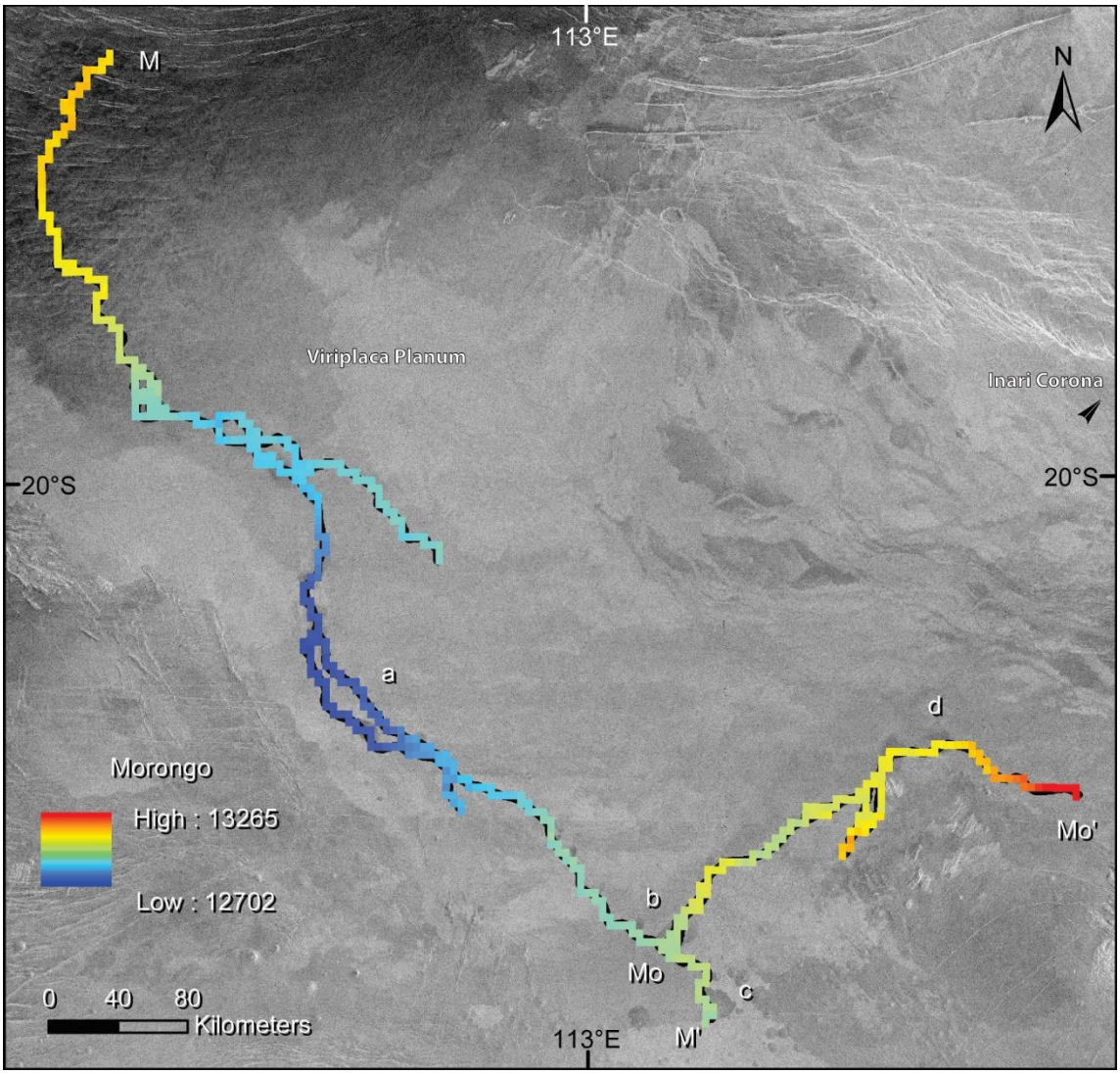

Figure 34: Magellan SAR left-look mosaic is projected to be centered on 112° E, 21° S in an orthographic projection showing Morongo Vallis. The length is illustrated by a color-coded line indicating elevation, with higher elevation shown in red and lower topography shown in dark blue.

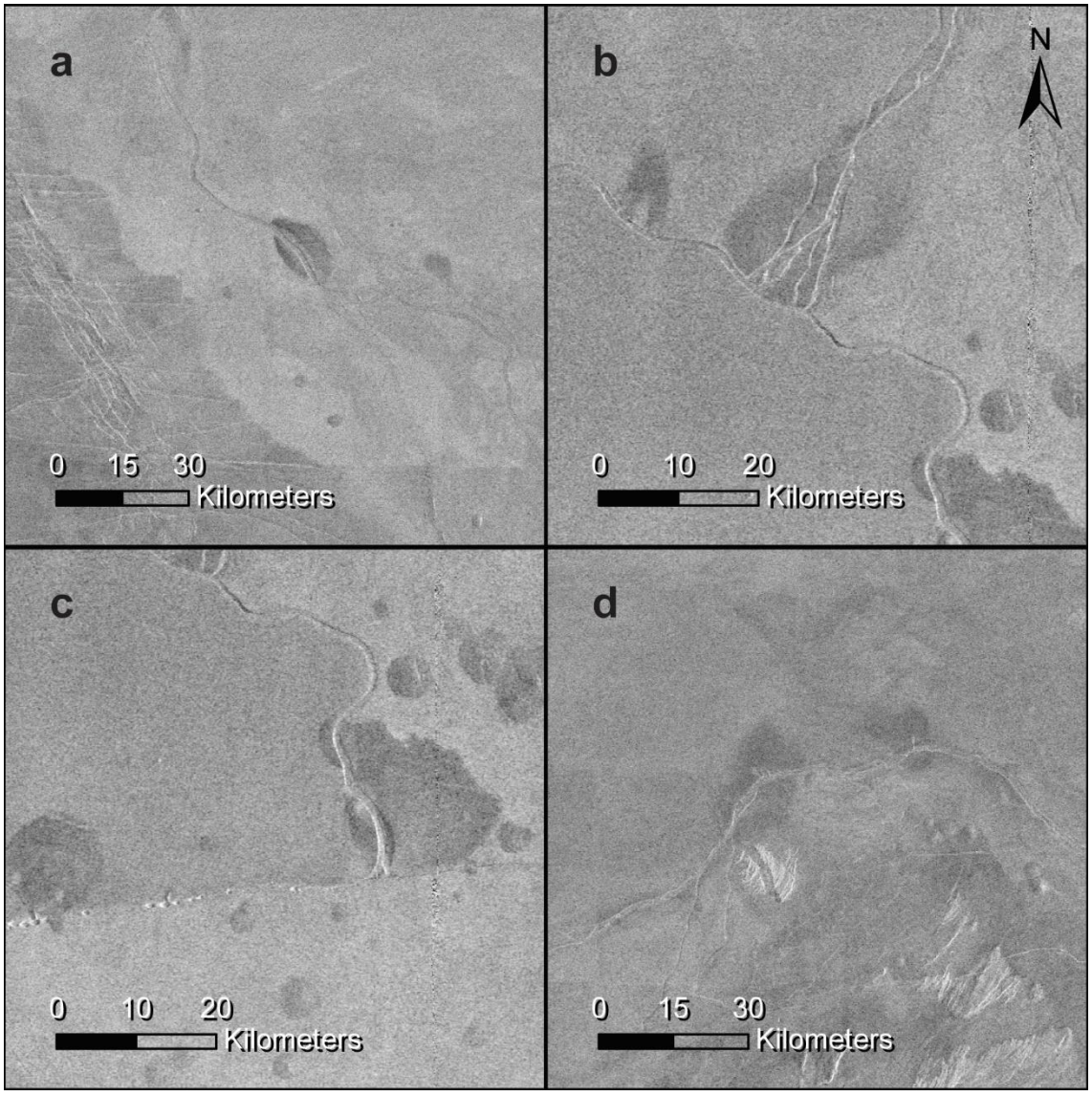

Figure 35: Magellan SAR left-look mosaics are projected to be centered on 112° E, 21° S in an orthographic projection showing close up sections of Morongo Vallis. (a). MV passes through a radar dark spot. (b) The intersection of MV and MoV. (c) The southeastern terminus of MV interacts with the fissure. (d) MoV continues over the topographically elevated region.

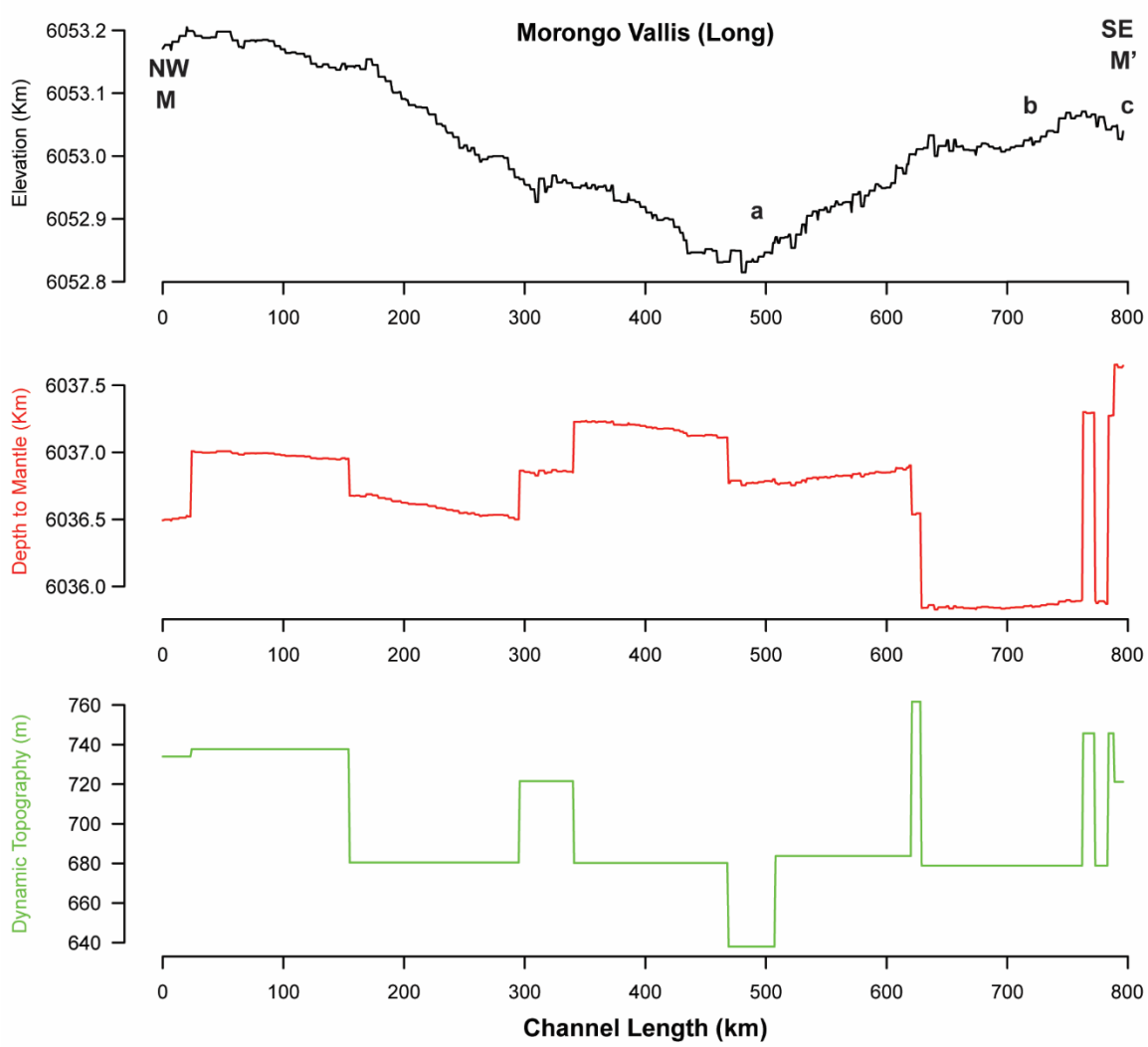

Figure 36: Profile view of topography (black line), depth to the mantle (red line), and dynamic topography (green line) along the flow path of Morongo Vallis.

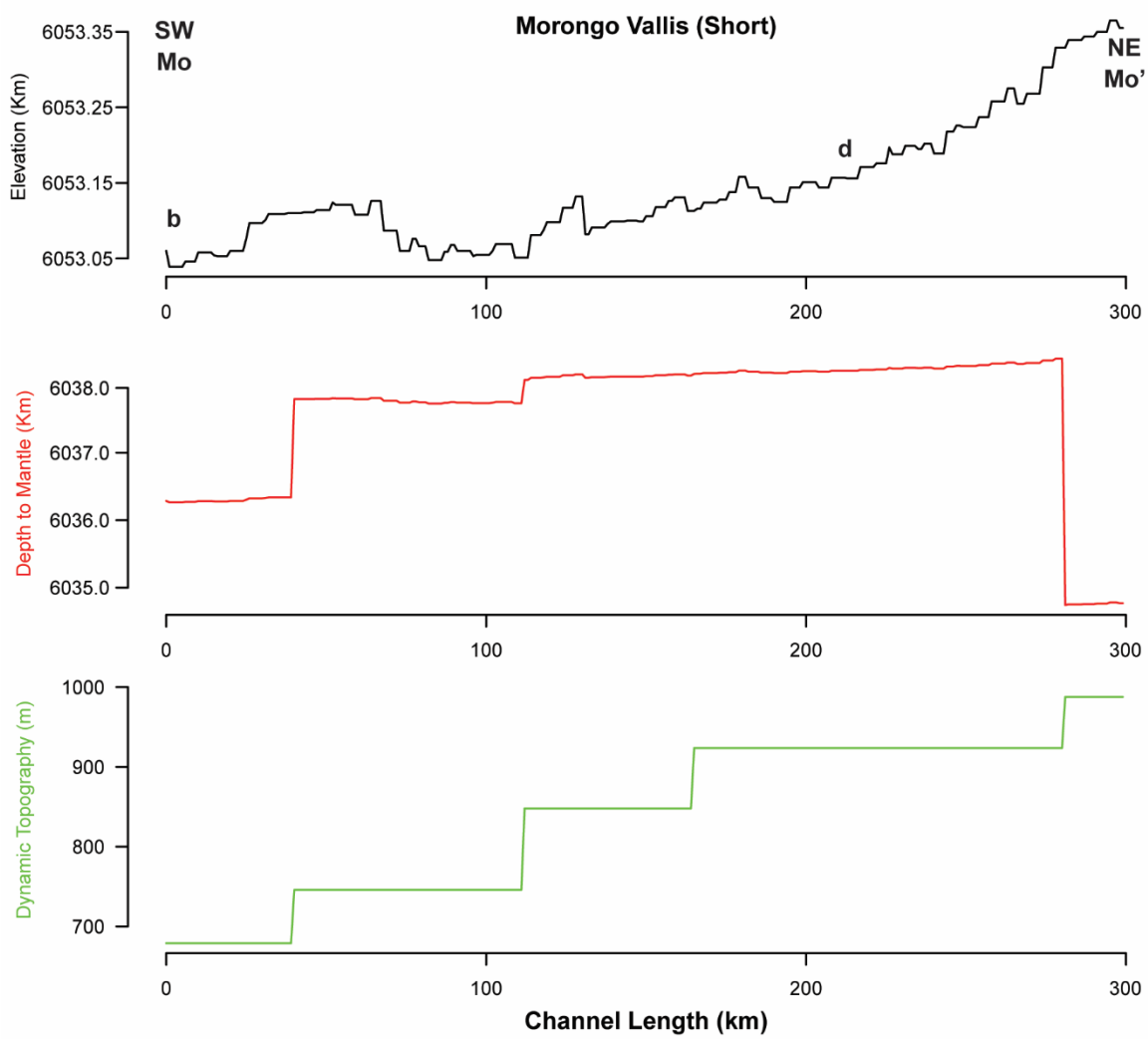

Figure 37: Profile view of topography (black line), depth to the mantle (red line), and dynamic topography (green line) along the flow path of Morongo Vallis (short).

3.2.16 Koidutäht Vallis

Koidutäht Vallis (KV) was mapped following the right-look Magellan SAR mosaic through two bins from the 10x10 DD grid (Figure 38). One point was removed after mapping, leaving a total of 801 vertices. The southern terminus is cut off by the lack of information at the south pole, visible at 131° E, 80° S, so these length measurements are the minimum length measured. I calculated the geodesic length as 811 km and the straight-line distance as 728 km. Dividing geodesic length by the straight-line distance results in an overall channel sinuosity of 1.11.

Naunet Fluctus (~130 km southeast, not on map) and Whatitiri Corona (~340 km south, not on map) are located south of where the SAR mosaic cuts out, but they could be the origin of the channel. The channel floor of KV is radar dark and highly visible in the radar homogonous terrain, which is mapped as a regional plain (rp1) (Ivanov & Head, 2011). KV lies exclusively within the regional plain except for the interaction mentioned below. Describing from K to K', KV becomes visible in the SAR mosaic and continues north over a topographically elevated region with a wavelength of ~271 km and an amplitude of ~277 m. The topographic change has no associated landform or structure and is younger than the channel, thus deforming its elevation profile from 0 to 280 km (Figure 39). The inconsistent SAR left-look mosaic shows wrinkle ridges with varied orientations. KV continues over them as it passes into a local depression, then changes direction to NW/SE. The channel continues around a topographically elevated region that is slightly radar brighter, has more wrinkle ridges, and has small volcanic features. Since KV curves around the region, the topographic elevation must have been present at the time of channel formation. In Figure 38a, KV continues parallel with a shield plain (psh)

and increases in elevation (wavelength ~246 km, amplitude ~307 m), relatively dating the topographic change as younger than the channel. KV continues through a radar darker spot and enters a shield plain (psh), increasing in sinuosity as it passes Simbya crater to the east and Angrboda Tholus to the west. KV continues north through a small depression and starts to climb in elevation before reaching the northern terminus.

From Figure 39, the depth to the mantle (red line) shows three sections of crustal thickening: 0 to 280 km, 280 to 540 km, then 540 km to the northern terminus. Thus, the crust is thinned at 280 km and 540 km. The dynamic topography (green line) acts opposite of the elevation, meaning that the topographic changes cannot be explained by mantle processes and are currently undetermined tectonic processes.

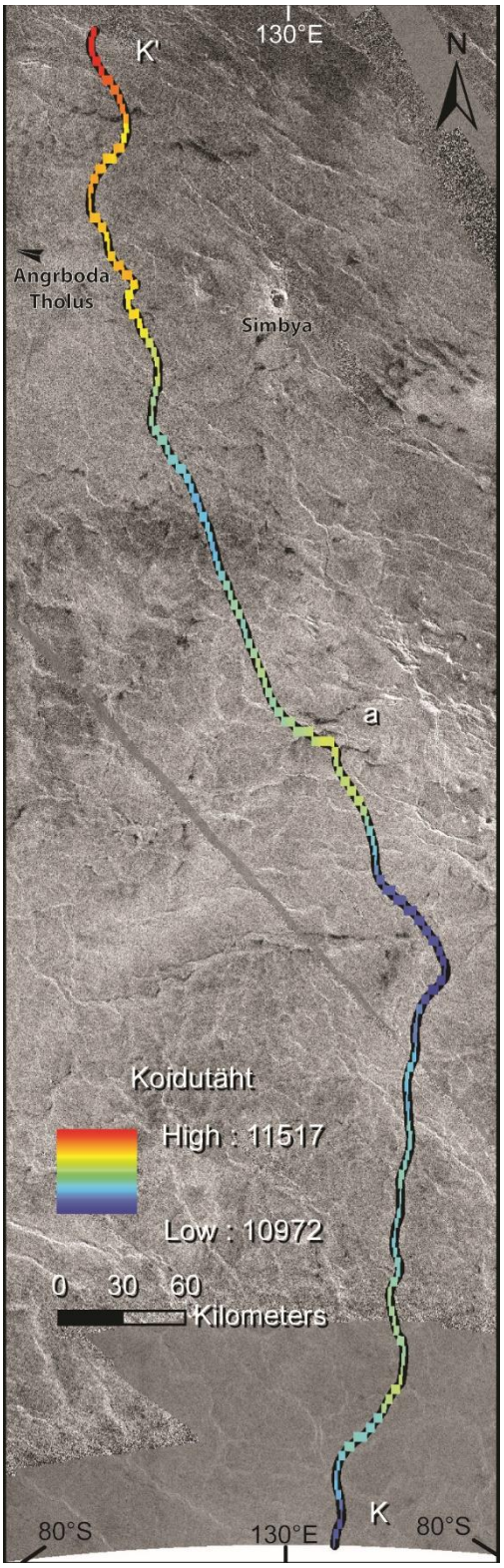

Figure 38: Magellan SAR right-look mosaic is projected to be centered on 130° E, 76° S in an orthographic projection showing Koidutäht Vallis. The length is illustrated by a color-coded line indicating elevation, with higher elevation shown in red and lower topography shown in dark blue. (a) KV increases in elevation while flowing alongside a shield plain.

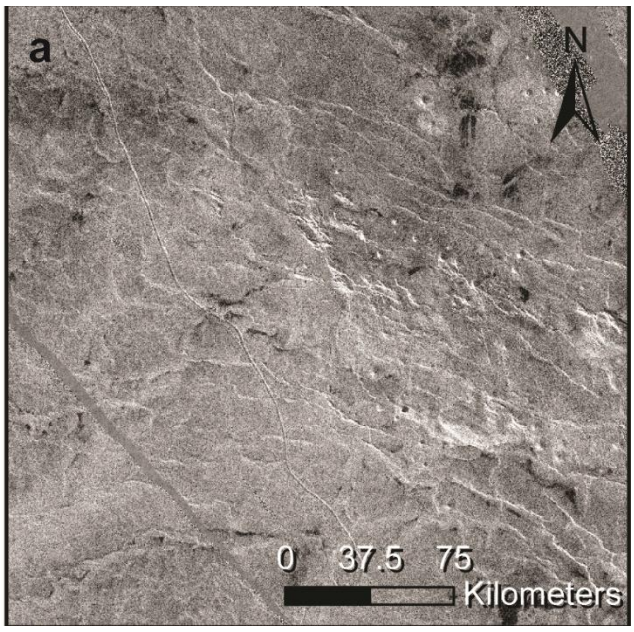

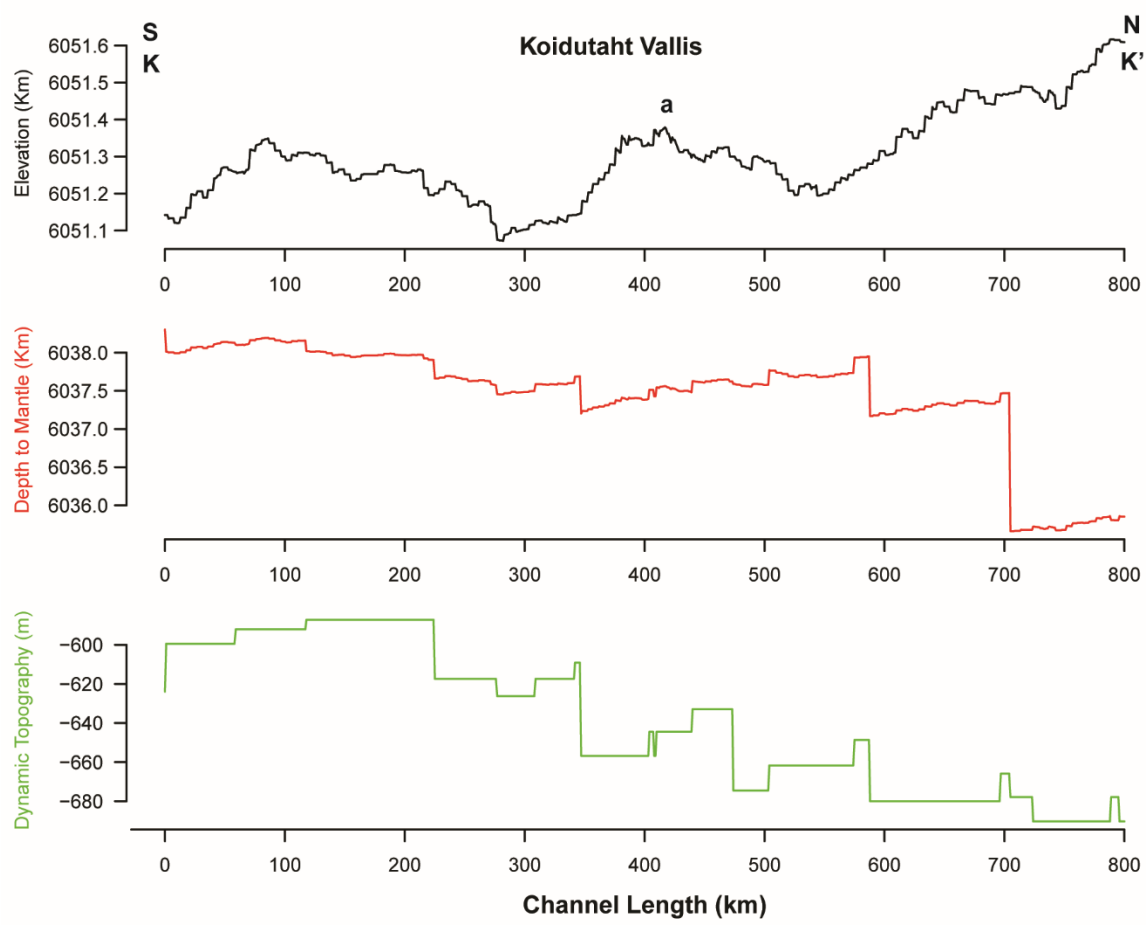

Figure 39: Profile view of topography (black line), depth to the mantle (red line), and dynamic topography (green line) along the flow path of Koidutäht Vallis.

3.2.17 Uottakh-sulus Vallis

I mapped Uottakh-sulus Vallis (UV) following the left-look Magellan SAR mosaic through one bin from the 10x10 DD grid. After mapping, I removed five anomalous points, leaving a total of 611 vertices. The geodesic length is 620 km; however, adding a straight-line measurement for each section that has no data (146 km) increases the minimum length to 766 km. The straight-line distance is 664 km. The channel's overall sinuosity is 1.15, with the added length from the sections with no coverage.

This channel is not completely covered in radar data, so there are large gaps in our knowledge of UV (Figure 40). The entire channel, with one exception, lies within the lobate plains (pl) (Ivanov & Head, 2011). UV also declines in elevation steadily from U to U', with a small exception mentioned below (Figure 42). To the west of the channel, Perchta Corona lies ~400 km north of UV, Gashan Ki Corona lies ~400 km east, and Ixtab Mons lies ~400 km northeast (none on map). Any of these could potentially be the source of UV. Describing from U to U', the western terminus of the channel is a radar dark channel floor surrounded by a radar bright lava flow. UV most likely continues further west; however, the information is lost with a lack of coverage. The channel has a NE/SW orientation to avoid several mapped units, including a rift zone (rz), shield plain (psh), and a smooth plain (ps). The NE/SW orientation also avoids a topographically elevated region to the south, meaning this topographic change was present at the time of formation. The channel continues sinuously northeast, and the channel floor becomes radar bright, with the radar bright lava flow feathering around the channel floor, shown in Figure 41a. UV encounters the smooth plain and curves around the unit, following the

path of the lowest elevation, shown in Figure 41b. This relationship reveals that the smooth plain was in place before channel emplacement. At this point, the radar mosaic has several gaps, and UV is difficult to distinguish; however, the channel curves and orients SE/NW. This change in orientation also mirrors and avoids a heavily deformed area to the north mapped as a rift zone (rz), meaning the rift zone is older than the channel. The faults are oriented NW/SE. Within this area with poor coverage, UV crosses the radar dark smooth plain and reenters the radar bright lobate plains for the remainder of its length. UV continues east, staying between the groove belt (gb) in the south, the rift zone in the north, and the eastern terminus of the channel is lost in the groove belt. Within the lobate plains, UV has small braiding offshoots, shown in Figure 41c. The drastic topographic decrease seen in the profile (black line) is not associated with a landform or structure; therefore, it is likely faulty calculations or is a feature not visible with the available data and is not considered for this study.

Except for the anomalous dip at 590 km, UV does not appear to have undergone topographic changes (Figure 42, black line). The depth to the mantle (red line) shows a constant crustal thickness, except for the data jump at 220 km. This could be an artifact of the data set and is not considered. The dynamic topography (green line) increases until 230 km, then decreases towards the eastern terminus. This behavior does not follow the topographic trend because it decreases more quickly than the topographic profile in the eastern half. Since it is undetermined if UV has undergone any deformation, there is no relationship to discuss.

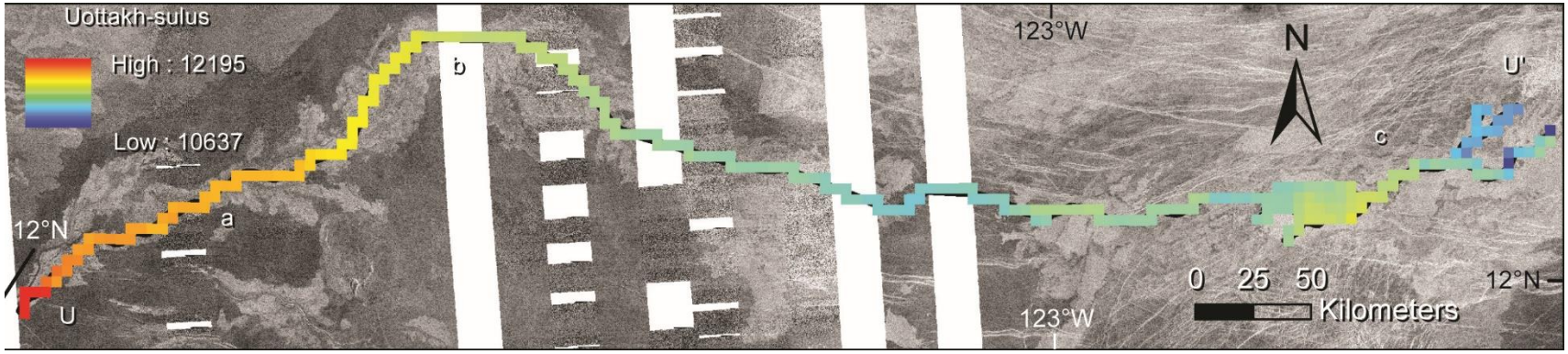

Figure 40: Magellan SAR left-look mosaic is projected to be centered on 124° W, 12° N in an orthographic projection showing Sinann Vallis. The length is illustrated by a color-coded line indicating elevation, with higher elevation shown in red and lower topography shown in dark blue. The white polygons are data gores.

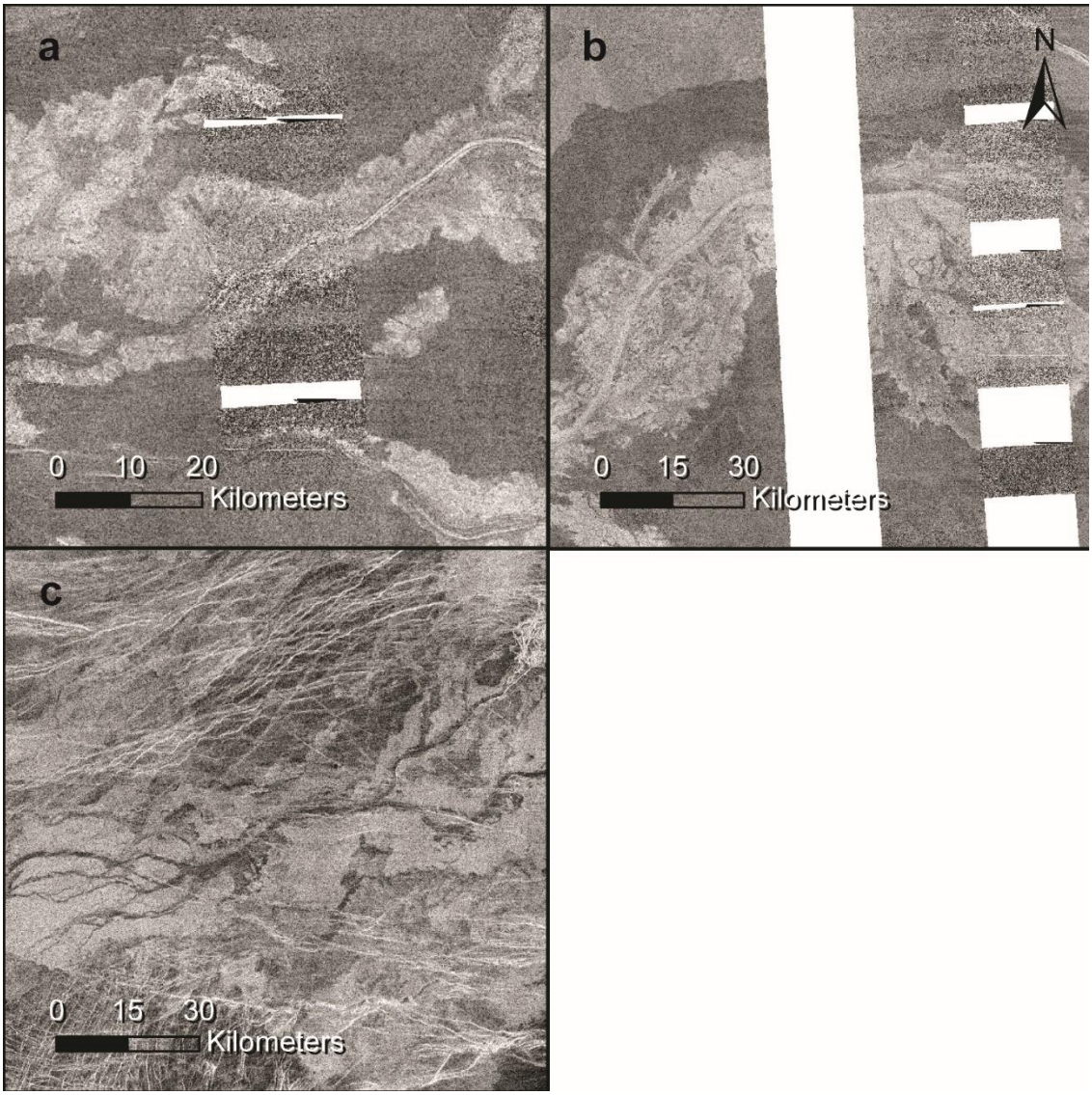

Figure 41: Magellan SAR left-look mosaics are projected to be centered on 124° W, 12° N in an orthographic projection showing close up sections of Uottakh-sulus Vallis. The white polygons are data gores. (a) A radar bright lava flow feathers around UV. (b) UV curves around a smooth plain. (c) Small, braided offshoots within the lava flow.

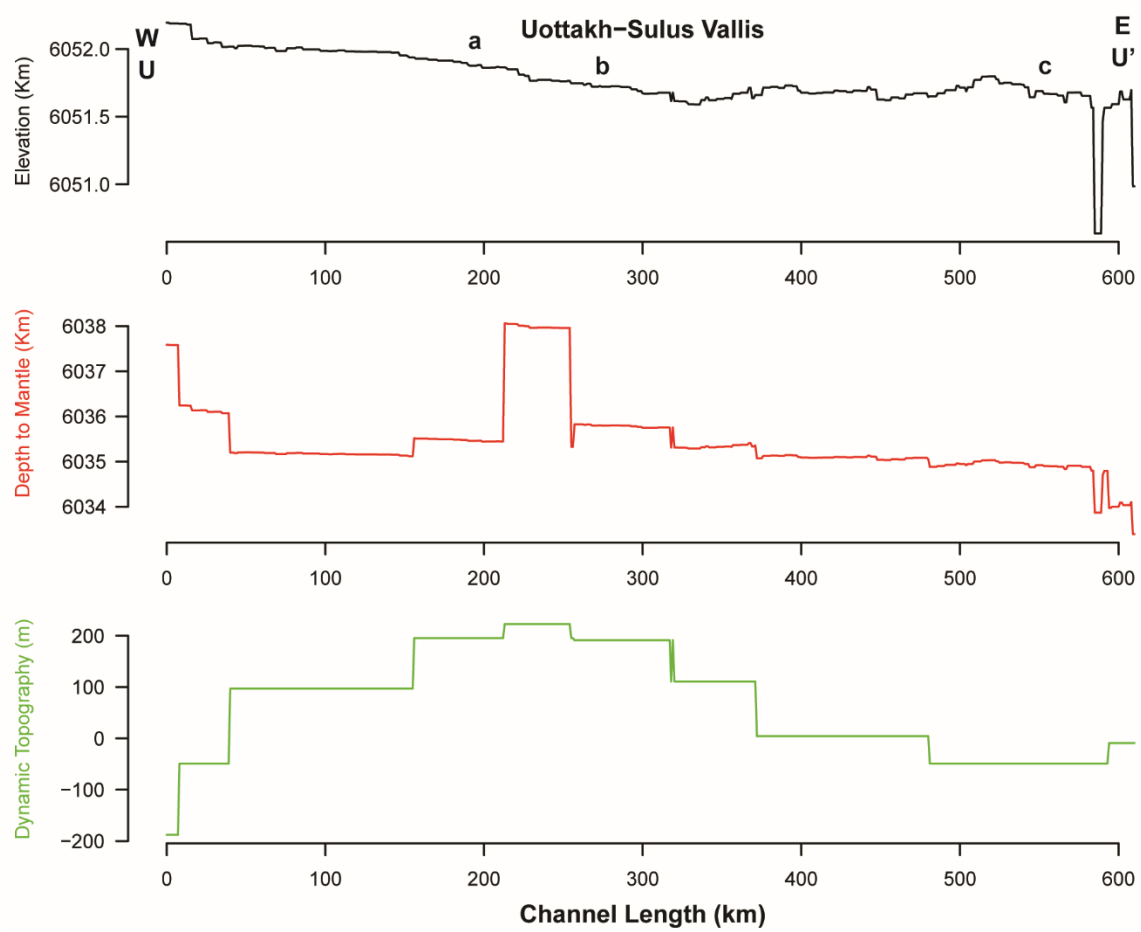

Figure 42: Profile view of topography (black line), depth to the mantle (red line), and dynamic topography (green line) along the flow path of Uottakh-sulus Vallis.

3.2.18 Tan-yondozo Vallis

Tan-yondozo Vallis (TV) is visible within the left-look Magellan SAR mosaic through two of our 10x10 DD bins. After mapping, I removed 24 anomalous points, leaving a total of 840 vertices. The geodesic length is 848 km of the main channel, with a significant offshoot with a length of 189 km. The main channel straight-line distance is 760 km which results in an overall channel sinuosity of 1.12.

TV has at least nine coronae in the immediate vicinity, from ~500 to ~1000 km away. Because of this, there is no clear sign which could be the source of TV. North of TV lies Nommo Valles. Describing from T to T', most of the channel length is mapped within a regional plain (rp2) with small exceptions listed below (Ivanov & Head, 2011). The southwestern terminus of TV is located within Ilaheva Fluctus, which is radar bright. The channel could have continued further southwest, but the region is obscured by faults. The wrinkle ridges surrounding TV are oriented NW/SE and crosscut the channel floor, meaning they are younger than the channel. TV curves east and through a depression and increases in elevation. The topographic increase must have formed after the channel. This first depression has a wavelength of ~60 km and an amplitude of ~105 m. At this point, TV has split in two for ~200 km, shown in Figure 44a. The offshoots meet northeast from the end, and the shape of both suggests that they curved around the regional plain (rp1) and shield plain (psh) to the south, meaning both units were present during the formation of the channel. The channel curves east after the meeting point of the offshoots and through a homogonous region with only faint wrinkle ridges present. TV steadily decreases in elevation before continuing through another local depression, in which the channel curves southeast and then sharply northeast, shown in Figure 44b. This

depression has a wavelength and amplitude of ~151 km and ~91 m, respectively. Both depressions are not associated with landforms or structures and formed after the channel; otherwise, TV would not continue straight through and increase in elevation again. Beyond the depression, TV curves northeast, perpendicular to the wrinkle ridges, and passes through a radar dark spot, shown in Figure 44c. The channel continues northeast with small eyelets, then curves further north upon crossing into a different regional plain (rp1), which is radar darker. TV crosses this regional plain and reenters the rp2 regional plain, which is a local depression that is radar bright and has a wavelength of ~129 km and amplitude of ~171 m. The channel disappears after regaining elevation and reentering the rp1 regional plain that is radar dark.

The depth to the mantle profile (red line) within Figure 45 shows various states of crustal thickness. The crust is constant thickness until 115 km, then is thickened until 390 km. The thickness remains constant from 390 to 820 km, with a small exception from 550 km to 650 km, where it is thickened. The dynamic topography (green line) follows the surface trend and decreases toward the northeast. This reveals that dynamic topography is preserved at the surface still and relatively young. Since mantle convection is the cause of dynamic topography, I infer that mantle convection is relatively young and deformed the channel. In this case, the mantle is downwelling and causes subsidence at the surface. The relative age between the dynamic topography and the local depressions cannot be determined since both processes are relatively younger than the channel.

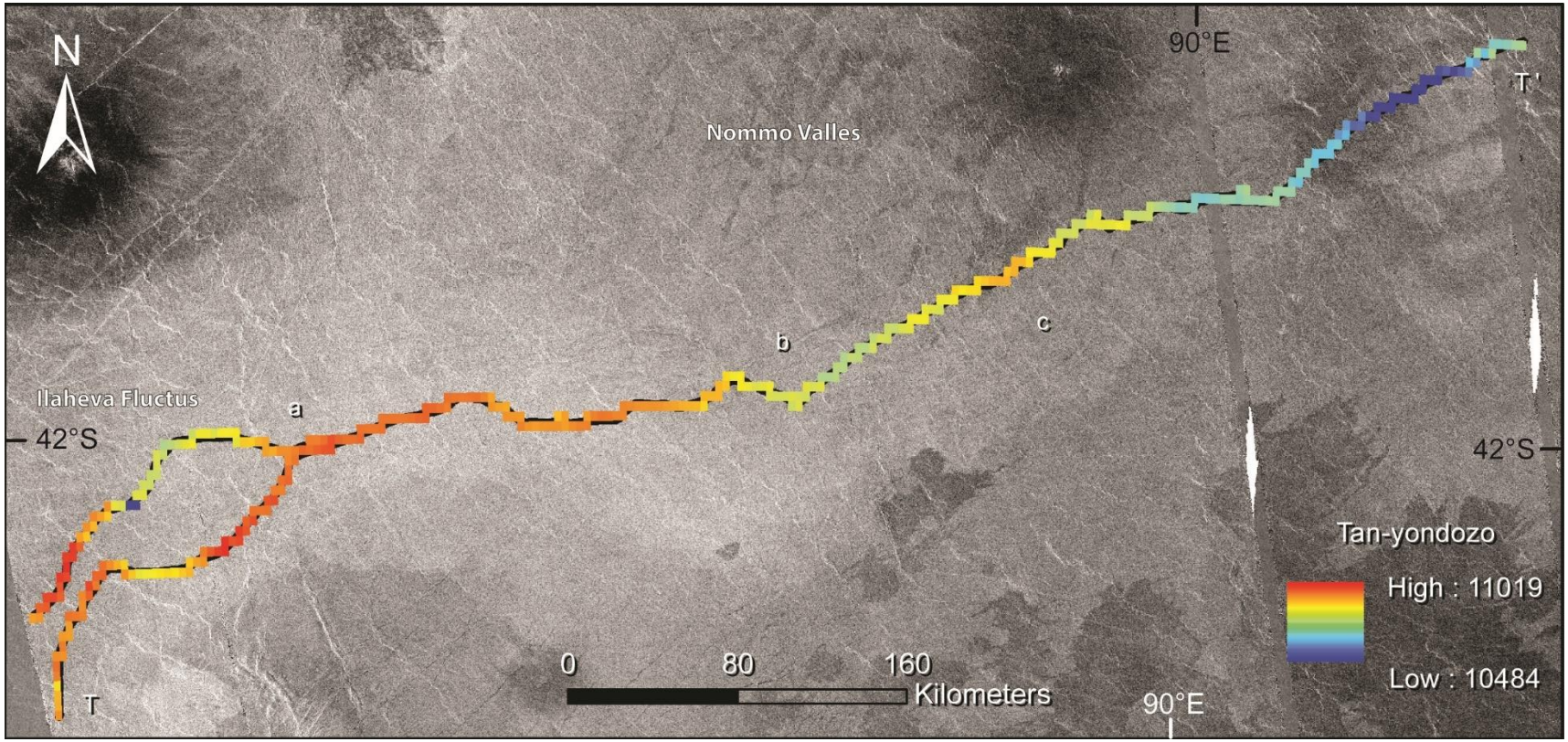

Figure 43: Magellan SAR left-look mosaic is projected to be centered on 87° E, 42° S in an orthographic projection showing Tan-yondozo Vallis. The length is illustrated by a color-coded line indicating elevation, with higher elevation shown in red and lower topography shown in dark blue. The white polygons are data gores.

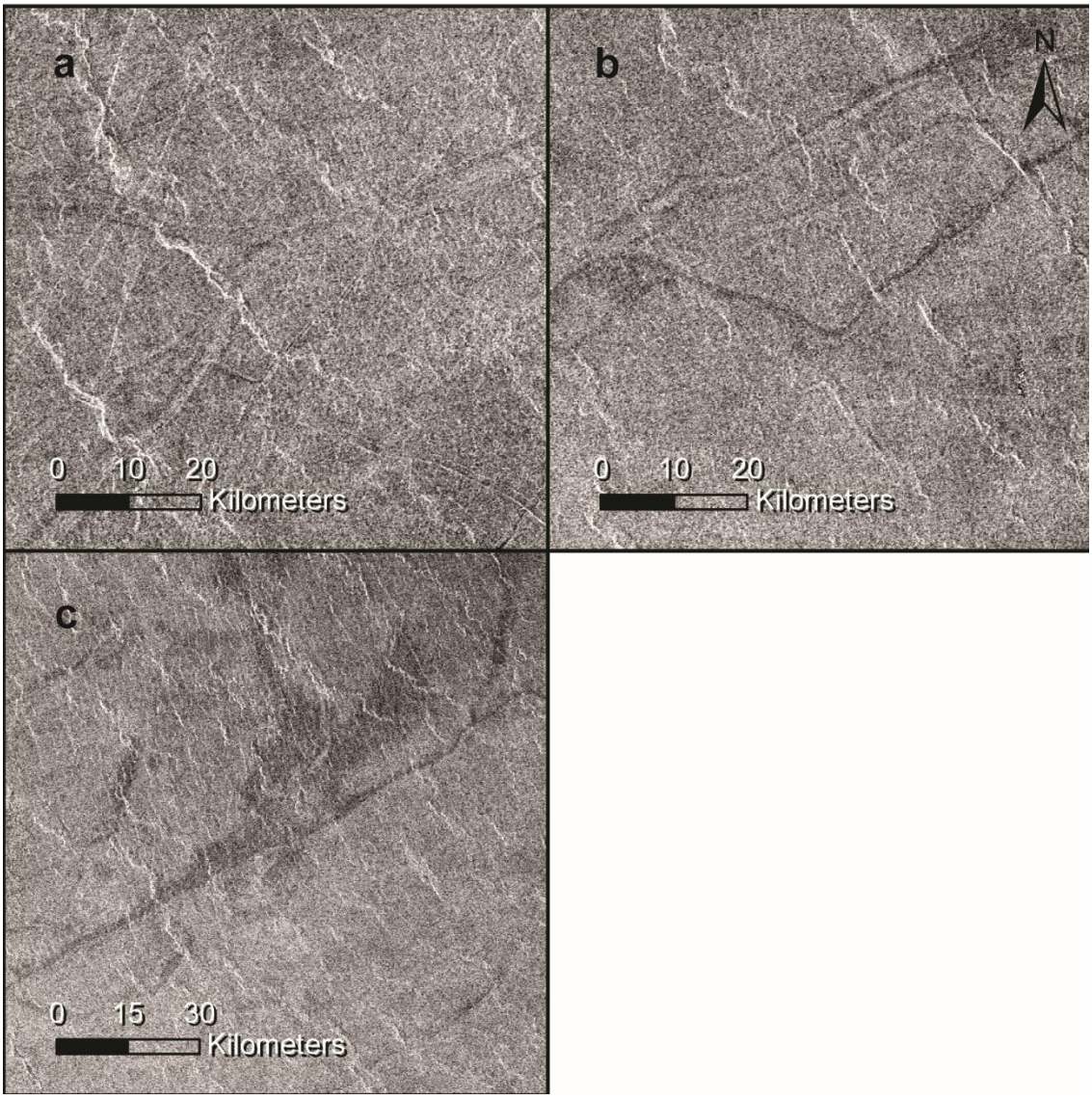

Figure 44: Magellan SAR left-look mosaics are projected to be centered on 87° E, 42° S in an orthographic projection showing close up sections of Tan-yondozo Vallis. (a) TV splits into two channels. (b) TV curves through a topographic depression. (c) TV passes through a radar dark spot.

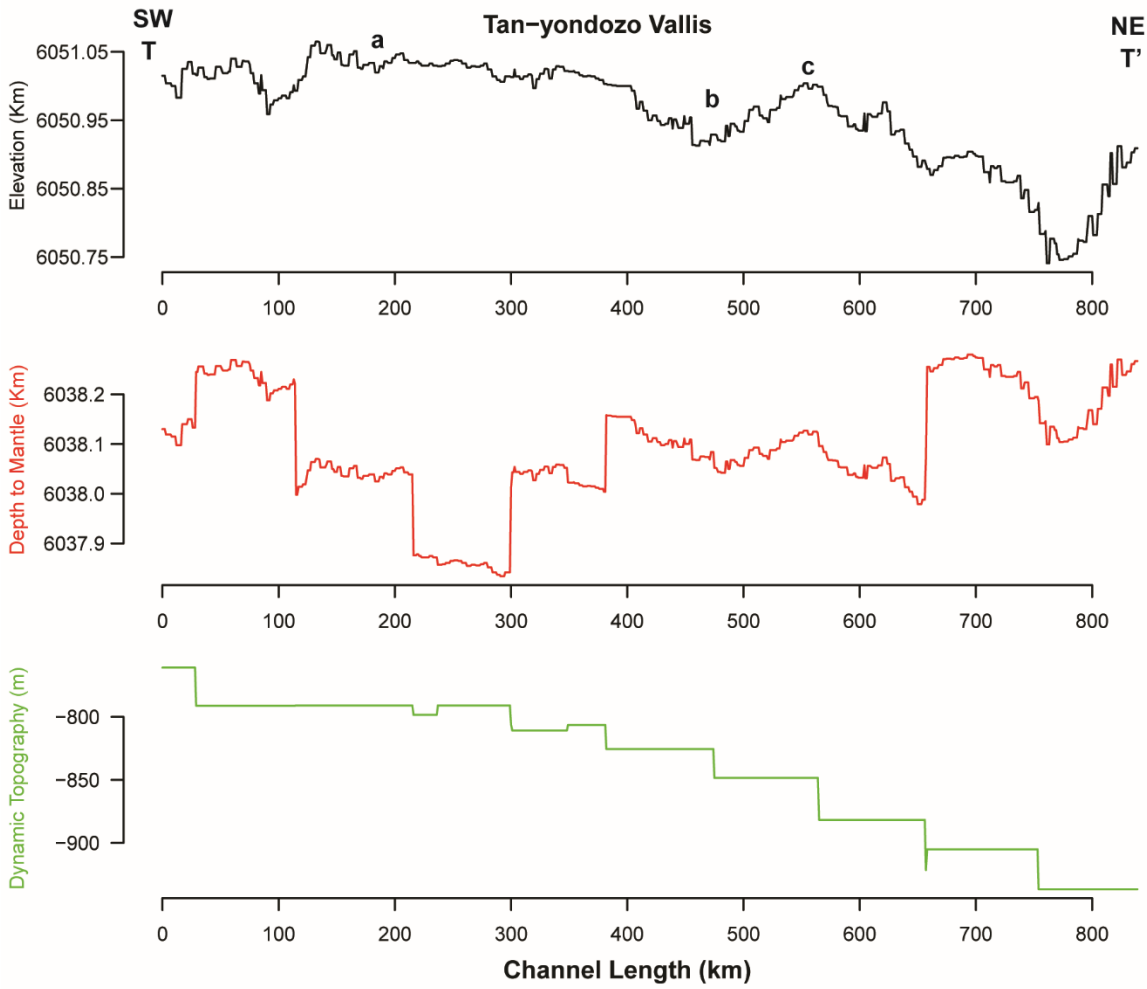

Figure 45: Profile view of topography (black line), depth to the mantle (red line), and dynamic topography (green line) along the flow path of Tan-yondozo Vallis.

3.2.19 Bennu Vallis

I mapped Bennu Vallis (BV) following the left-look Magellan SAR mosaic through three bins from our 10x10 DD grid. After mapping, 24 anomalous points were removed for a total of 741 vertices. The geodesic length is 753 km with a straight-line distance of 612 km, resulting in an overall channel sinuosity of 1.23.

The entirety of BV lies within a regional plain (rp1), with its southwestern side ending at the border of another regional plain (rp2) (Ivanov & Head, 2011). The largescale behavior of BV seems to curve around the rp2 regional plain to the west, as seen in Figure 46. The surrounding features include Yanbike Corona (not on map) ~1000 km west, and Eingana Corona (not on map) ~800 km east. Heng-o Corona (not on map) is also ~800 km east and significantly larger than the other two coronae with a diameter ~800 km wide. Considering the distance from these coronae, I cannot name a potential source for BV. Other features are Mortim-Ekva Fluctus west of BV and radar bright, Kodu crater west by ~250 km and Comnena crater east by ~250 km.

Describing from B to B', the southwestern terminus becomes visible out of a radar bright area, the rp2 regional plain that is likely part of Mortim-Ekva Fluctus. The channel curves northeast into the rp1 regional plain that has wrinkle ridges with NW/SE and NE/SW orientations. The wrinkle ridges crosscut BV, and the deformation is visible in the channel floor, meaning they are younger than the channel. BV increases in elevation and curves around a small portion but still continues through the topographically elevated region. This relationship reveals that a topographic high was already present when BV was emplaced, as shown by BV curving to avoid the feature. The surface continued to deform after emplacement, such that the channel shows the

observed topographic undulation. The topographically elevated region is radar bright compared to the surroundings but is unclassified within the radar mosaic and geology, shown in Figure 46a. After the topographic increase, BV curves NE and reduces in elevation while continuing sinuously. The channel curves north briefly, and the radar is darker. Then BV curves NE again while increasing in elevation. BV curves north to avoid an elevation increase to the east of an area that is more heavily deformed around Comnena crater. This shows that the topographic increase was present during the active flow stage of the channel. BV curves east and increases in elevation but is lost in the surrounding radar dark area. The overall behavior of BV curves around the denser deformation to the east but still has small areas where the surface was deformed.

The depth to the mantle (red line) shows that the crust underlying BV is thickened underneath the topographic change until 300 km, at which point it is thinned (Figure 47). The thickness remains constant until the northeastern terminus, where it is thickened. The dynamic topography (green line) follows an opposite trend when compared to the topography, decreasing until 600 km, then increasing sharply underneath the northeastern terminus. The data has significant jumps, so an improvement in resolution could reveal a better relationship. Since the topographic change at point "a" is caused by a local feature, this channel is considered to be unaffected by the deformation measured by dynamic topography.

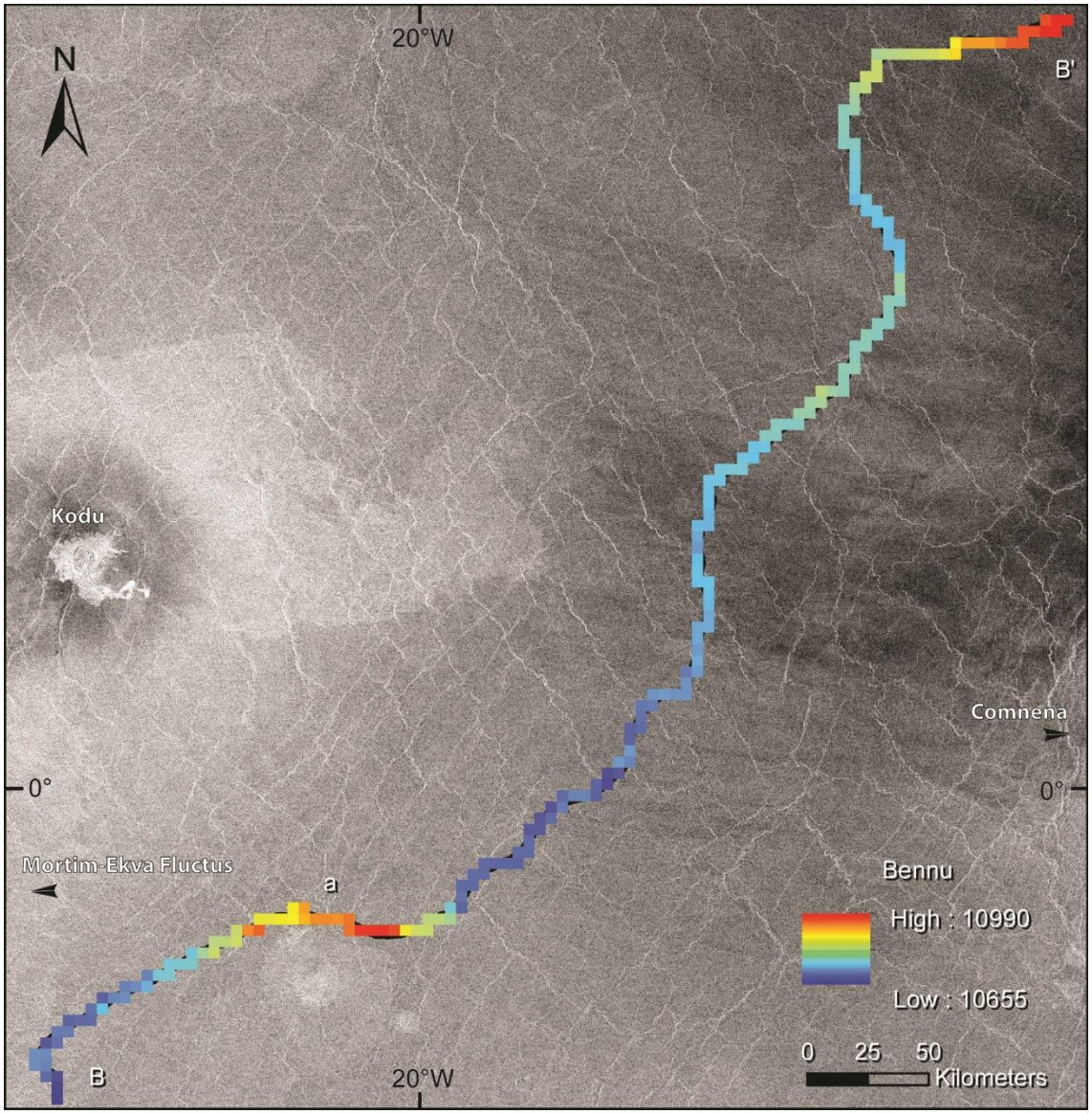

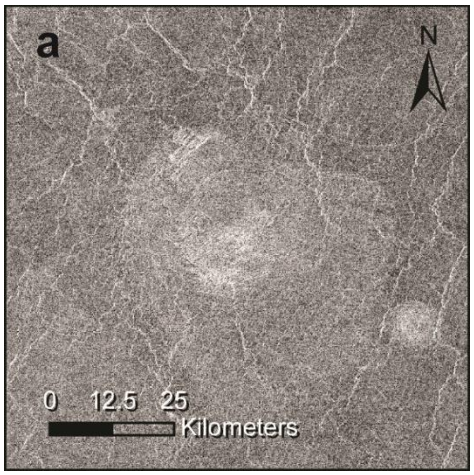

Figure 46: Magellan SAR left-look mosaic is projected to be centered at 19° W, 0° in an orthographic projection showing Bennu Vallis. The length is illustrated by a color-coded line indicating elevation, with higher elevation shown in red and lower topography shown in dark blue. (a) radar bright spot that causes a topographically elevated region.

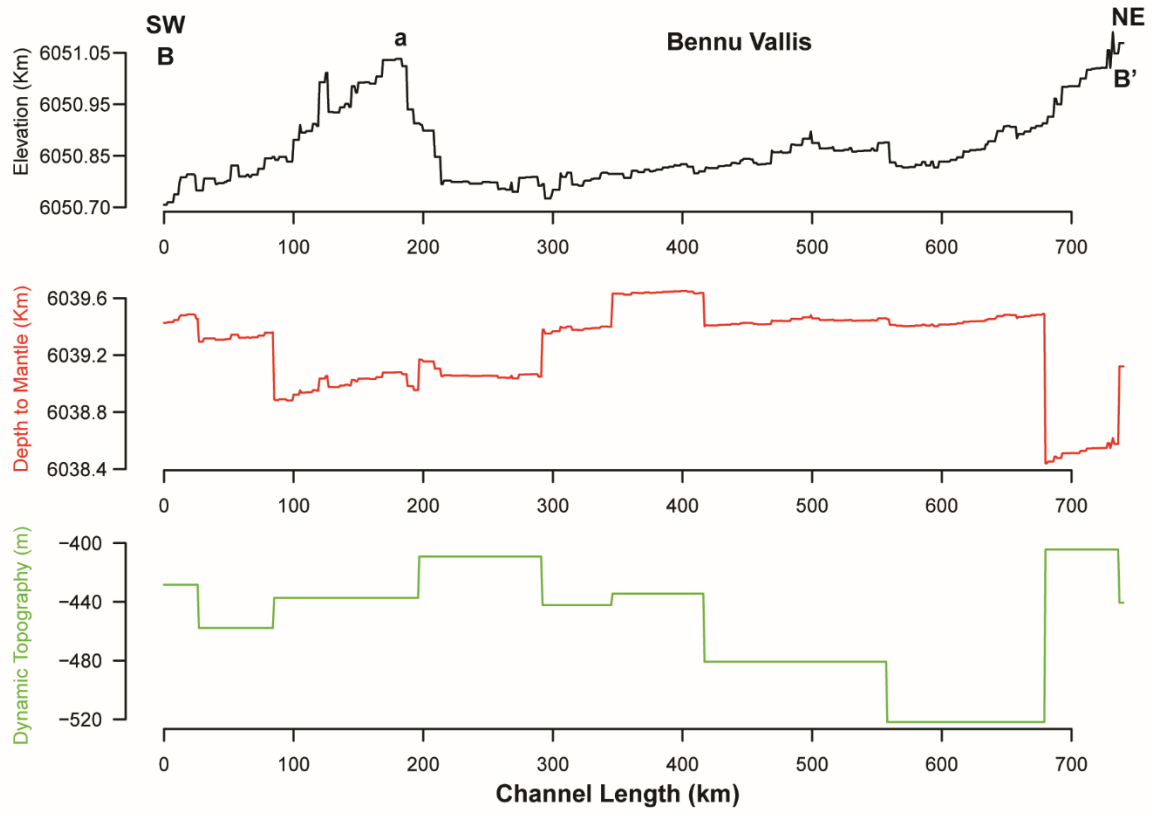

Figure 47: Profile view of topography (black line), depth to the mantle (red line), and dynamic topography (green line) along the flow path of Bennu Vallis.

3.2.20 Ahsabkab Vallis

Ahsabkab Vallis (AV) is visible following the right-look Magellan SAR mosaic through two of the 10x10 DD bins (Figure 48). After mapping, four points were removed, leaving a total of 663 vertices. I calculated the geodesic length to be 671 km, with a straight-line distance of 459 km. These values result in an overall channel sinuosity of 1.46.

The southern terminus of the AV is found right on the boundary of Aramaiti Corona, shown in Figure 49a. This end of the channel is obscured by Narina Tholi (Figure 48), but it is reasonable to state that AV flowed from Aramaiti Corona, and I will describe it as such from A to A'. The channel becomes visible in a topographic low that is radar dark and mapped as a regional plain (rp1) (Ivanov & Head, 2011). The overall behavior of AV stays within the regional plain, curving west to avoid the rp1 regional plain named Tahmina Planitia, and the northern terminus lies near a small shield plain (psh). From A, the channel continues north and crosses into a different regional plain (rp2), where the radar transitions to be brighter. The radar dark areas surrounding the channel have wrinkle ridges that are not visible in the radar bright area. AV then interacts with several faults or fractures, utilizing them for the flow path (Figure 49b). This relationship means that the faults were there before the channel. From the corona to the faults, the channel increases steadily in elevation. There is no structure or landform associated with this topographic increase, and it must be younger than the channel. The channel continues north, and wrinkle ridges become visible in the radar bright regional plain, oriented NW/SE. The channel passes through a topographically elevated region, relatively dating the increase as younger than AV, and it is not explained by a landform

or structure. AV continues north sinuously. From this point, the channel steadily decreases in topography until the northern terminus. AV turns northeast, where Oilule Fluctus is named and uses a wrinkle ridge, shown in Figure 49c. The channel uses the wrinkle ridge for ~80 km, then continues north and fades into the radar bright surroundings.

As seen in the profiles in Figure 50, the topography (black line) shows the entire channel with a wavelength of ~650 km and an amplitude of ~242 m. The depth to the mantle (red line) shows a mostly constant crustal thickness, although it thins slightly towards the north. The dynamic topography (green line) increases until 300 km and then remains constant until 500 km, after which it begins to generally decrease toward the northern terminus. This trend is similar to the topography, which also increases until ~250 km and then decreases toward the north. Because the topography shows the same trend as the dynamic topography, the dynamic topography is preserved at the surface and is geologically young. Otherwise, this relationship would have been obscured through other deformation-causing processes. Dynamic topography is a measure of mantle convection, thus meaning that the attributes of relative age also apply to mantle convection, revealing that mantle convection is the cause of the deformation along this channel. Specifically, the channel endured subsidence caused by mantle downwelling.

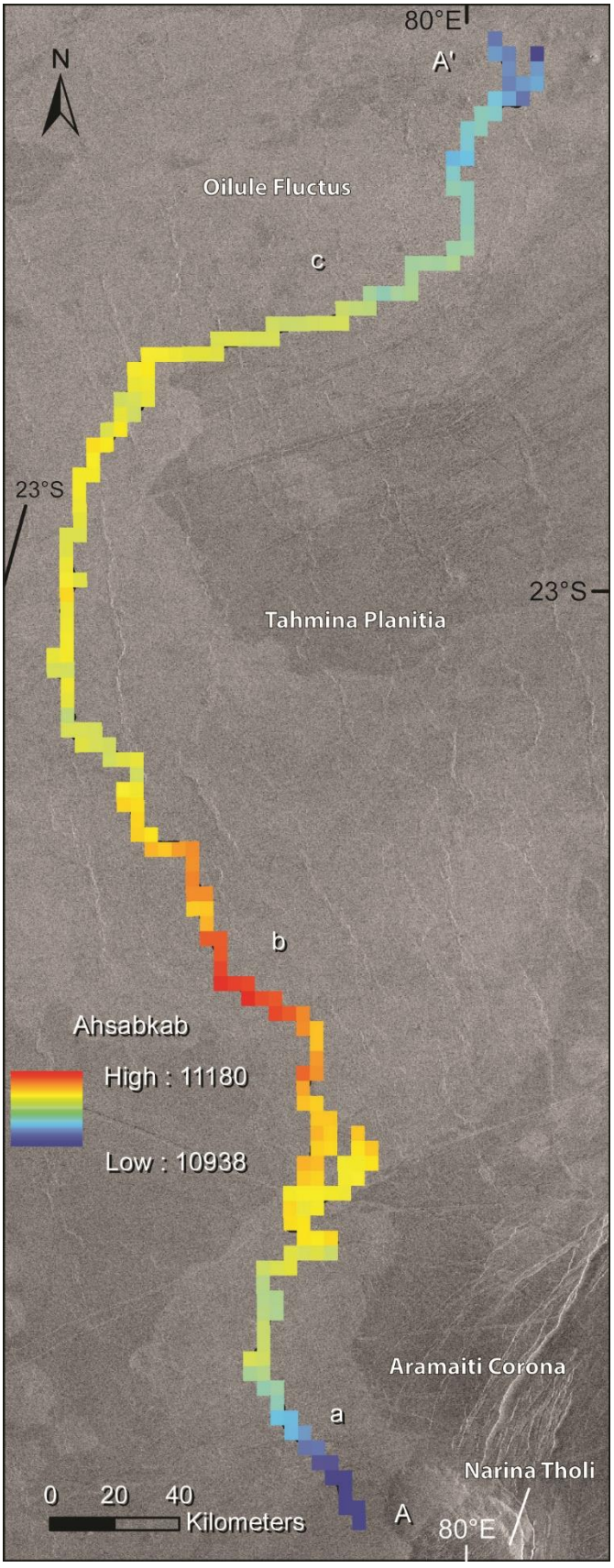

Figure 48: Magellan SAR right-look mosaic is projected to be centered on 80° E, 23° S in an orthographic projection showing Ahsabkab Vallis. The length is illustrated by a color-coded line indicating elevation, with higher elevation shown in red and lower topography shown in dark blue.

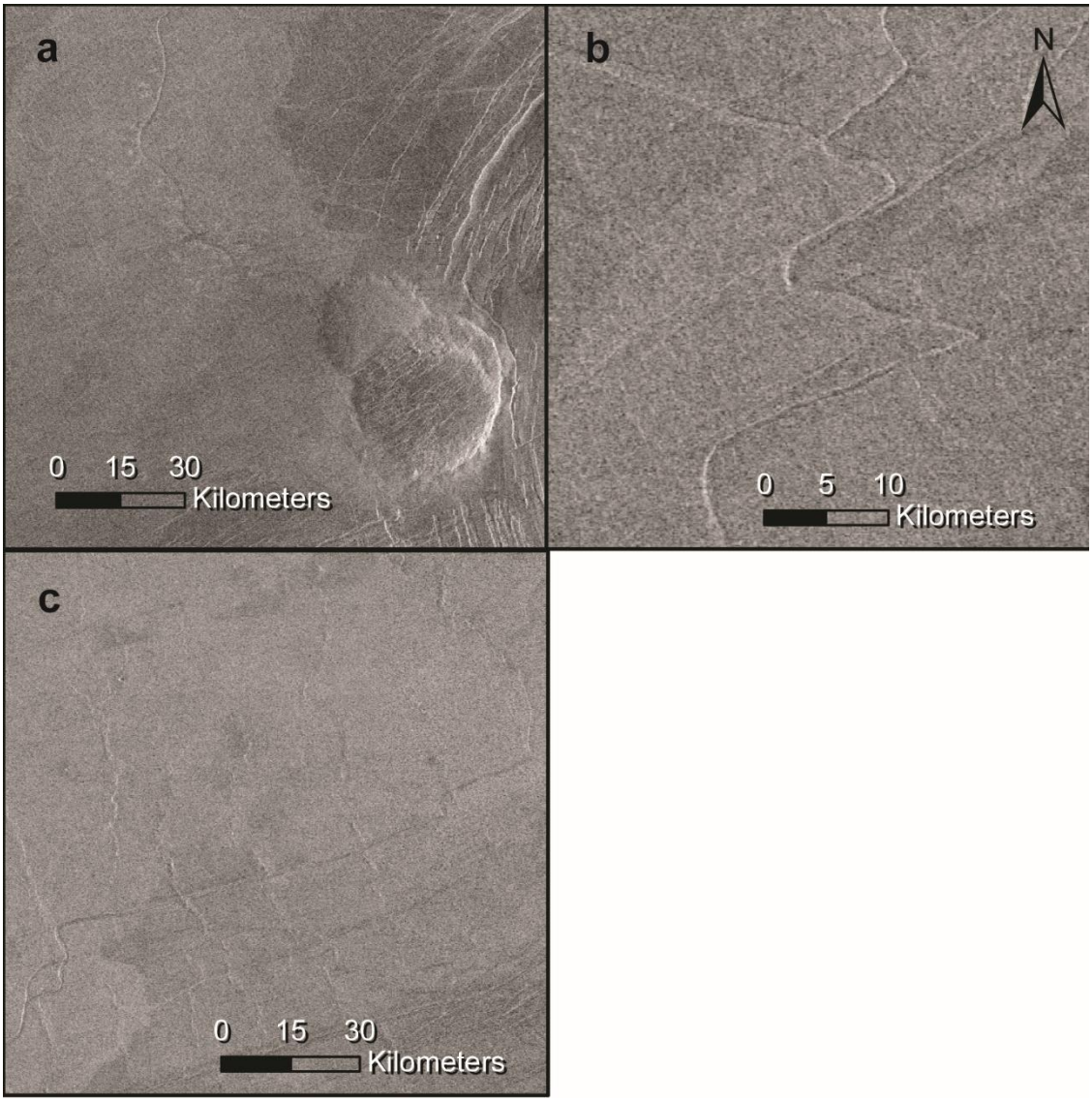

Figure 49: Magellan SAR right-look mosaics are projected to be centered on 80° E, 23° S in an orthographic projection showing close up sections of Ahsabkab Vallis. (a) The southern terminus of AV by Narina Tholi and Aramaiti Corona. (b) AV uses faults to propagate. (c) AV uses a wrinkle ridge to continue.

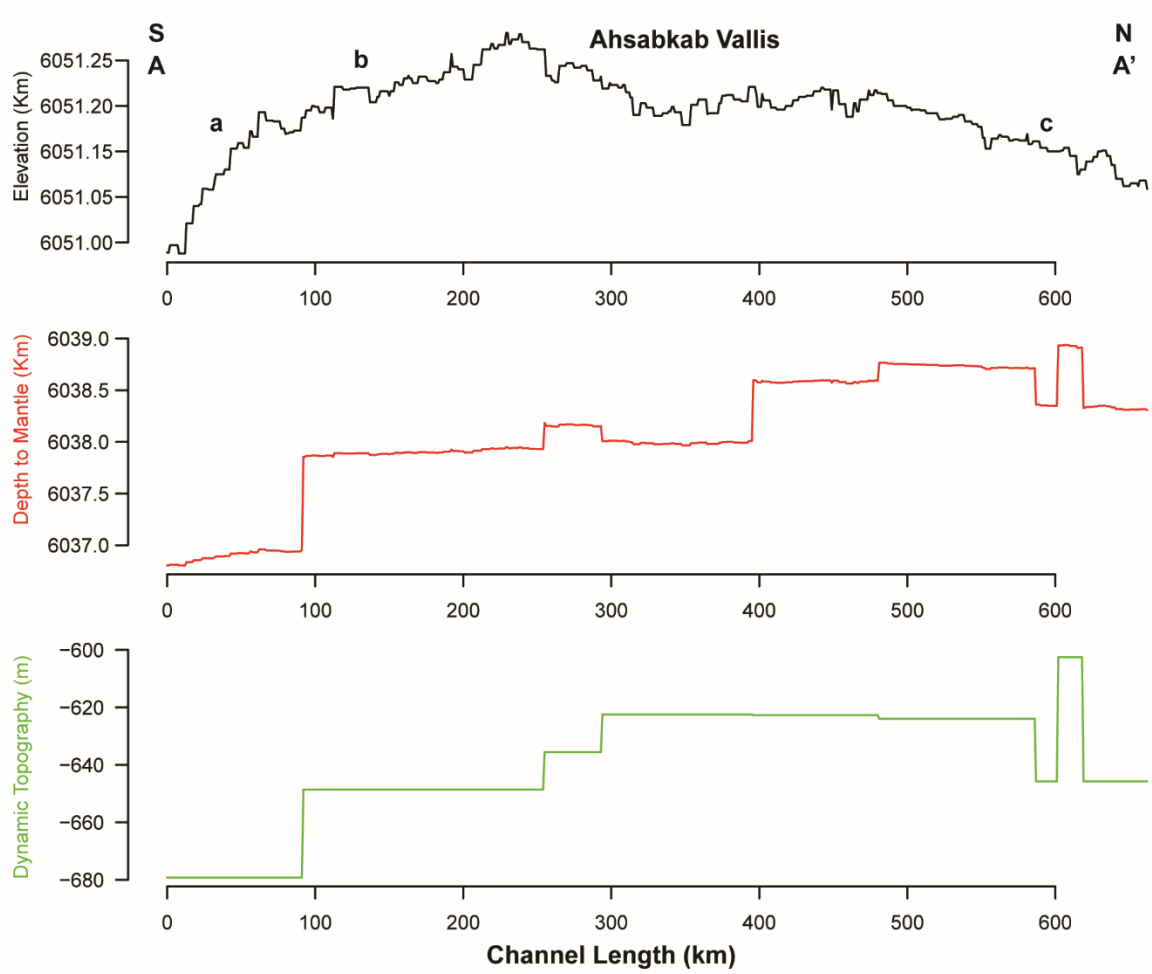

Figure 50: Profile view of topography (black line), depth to the mantle (red line), and dynamic topography (green line) along the flow path of Ahsabkab Vallis.

3.2.21 Austrina Vallis

I mapped Austrina Vallis (AV) following the left-look Magellan SAR mosaic through two of the 10x10 bins (Figure 51). After mapping, I removed four anomalous points, leaving a total of 580 vertices. I mapped using left-look for the majority of the channel except for the longer offshoot that lies more to the north, which was more visible in the SAR right-look mosaic. The calculated geodesic length of the longest piece is 590 km, with an offshoot that is 162 km long. The straight-line distance is 513 km, resulting in an overall channel sinuosity of 1.15.

AV is located NW of the Citlalpul complex (not on map) by ~250 km and east of Lusaber Vallis (not on map) and Khalanasy Vallis (not on map) by ~450 km. Because their ends fade into the background rather than clearly ending, it is possible that Citlalpul (page 24), Lusaber (page 77), and Austrina Valles are the same channel being obscured. The potential sources for AV are the surrounding coronae previously mentioned for Citlalpul Vallis and Lusaber Vallis: Utset Corona (not on map) and Tonatzin Corona (not on map) are the closest. Another potential source nearby is Sicasica Fluctus (not on map), south by ~150 km. The entirety of AV lies within a regional plain (rp1), as seen in Figure 51 (Ivanov & Head, 2011). The channel does gently curve to the south, which follows the shape of the shield plain to the north. Describing from A to A', the western terminus is visible among wrinkle ridges oriented NE/SW that overwrite the channel floor and are thus younger. The channel floor of AV is the same radar dark as the surroundings, but the channel walls are radar bright and feather out. AV curves southeast and reduces in elevation. The channel passes through a local radar bright depression with no wrinkle ridges present. This topographic depression is younger than the channel, revealed by the

fact that AV continues through and increases in elevation further east. There is a small strip that is not covered by the left-look mosaic, so the right-look is followed briefly. AV passes over a small ridge, past which the radar darkens and has wrinkle ridges, shown in Figure 49a. Even though AV continues through this topographically elevated region caused by the ridge, the channel stays between two sections of higher elevation, suggesting that these topographic highs were present at channel formation, but the surface continued to deform and elevate AV. This topographic change has a wavelength of ~138 km and an amplitude of ~321 m. Just after the topographically elevated region, AV splits into two channels, and both steadily decrease in elevation. The extracted data for the profiles is from the longer northern channel. The northern channel is cut by the wrinkle ridges, meaning they are younger, and radar bright lava feathers around the channel as it continues eastward. The southern channel does not change in characteristics from the main channel. Both eastern termini are no longer visible within the radar abruptly, and the channel walls radar brighter than the rest of the channel.

Within Figure 52, the depth to the mantle (red line) illustrates the thickness of the crust, which varies along the length of AV. Underneath both termini, the crust is thickened, with crustal thinning in the center. The dynamic topography (green line) has the same trend as the elevation and decreases steadily to the east. This means that the dynamic topography is preserved at the surface and is one of the most recent processes to alter the surface. This allows the inference that mantle convection is a young process since it is represented by dynamic topography. Because mantle convection is young, it may be active today. The deformation along the length of AV caused by mantle processes is subsidence from mantle downwelling.

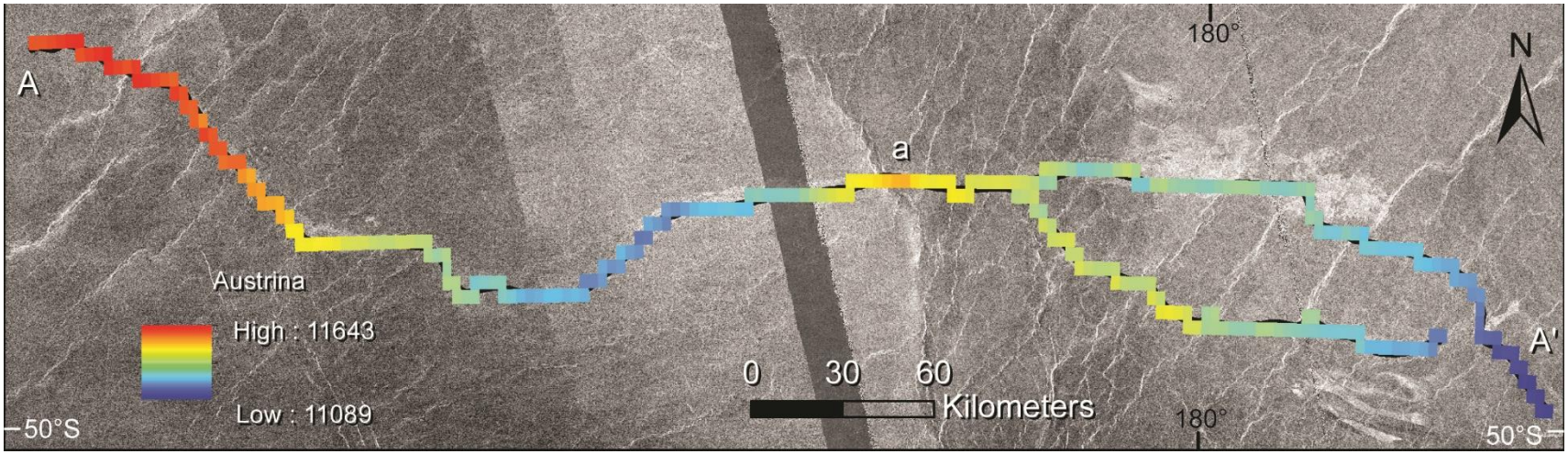

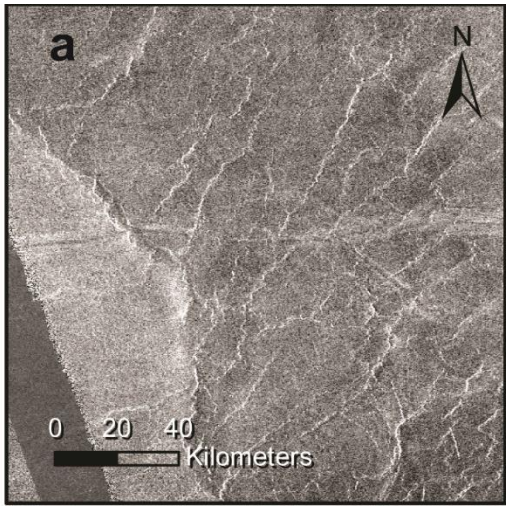

Figure 51: Magellan SAR left-look mosaic is projected to be centered on 178° E, 49° S in an orthographic projection showing Austrina Vallis. The length is illustrated by a color-coded line indicating elevation, with higher elevation shown in red and lower topography shown in dark blue. The dark polygon is a data gore in the left-look, and the other lines are artifacts from data collection. (a) AV crosses a topographically elevated ridge.

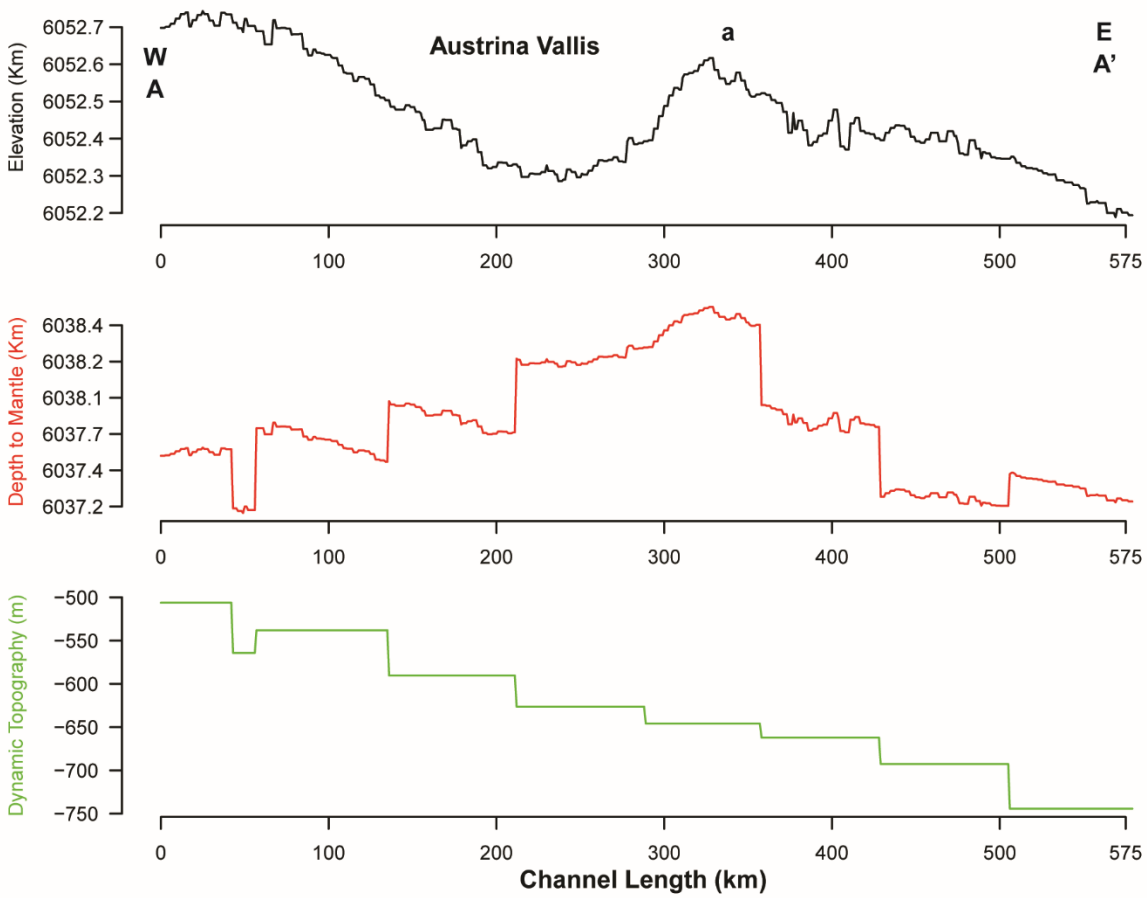

Figure 52: Profile view of topography (black line), depth to the mantle (red line), and dynamic topography (green line) along the flow path of Austrina Vallis.

3.2.22 Bayara Vallis

Bayara Vallis (BV) is visible in the left-look Magellan SAR mosaic in one bin from the 10x10 grid. After mapping, two points were removed, leaving a total of 573 vertices. The geodesic length of BV is 581 km. The channel has several offshoots that I have mapped; their additional length is 133 km. The straight-line distance between endpoints is 379 km, resulting in an overall channel sinuosity of 1.53.

BV lies between Parma Corona and Sulis Corona (Figure 53). Audhumla Corona (not on map) lies further west by ~200 km, and Sand Corona is (not on map) ~200 km to the south. Along the boundary of Ausra Dorsa is where the northeastern terminus of BV becomes visible, mapped in a regional plain (rp1) (Figure 53) (Ivanov & Head, 2011). Describing from B to B', the channel floor is radar dark like the surroundings, with radar bright walls. The deformation from the dorsa is present in the channel floor, crosscutting the channel, meaning the dorsa is relatively younger than the channel. BV likely continues farther north, but this information is not visible either because of the dataset or because the dorsa overprinted its path. The northeastern terminus continues south alongside the dorsa until it curves west to avoid a circular feature, likely an unnamed corona, that is topographically elevated. Despite its avoidance, BV still increases in elevation here, revealing that the surface was elevated to the south when BV formed, but the surface continued to deform. This relatively dates the corona as older than BV with continued activity. This elevation change has a wavelength of ~54 km and an amplitude of ~264 m, shown in Figure 54a. BV crosses into the other regional plain (rp2) at this topographic change. Continuing west, BV curves sinuously around Parma Corona, following the orientation of wrinkle ridges, meaning that Parma Corona is older than BV.

The relative age between the two coronae cannot be determined since they are both older than BV. The channel reenters the rp1 regional plain, which is radar darker than the previous, and the channel floor is radar bright briefly. BV then splits into two channels before rejoining, shown in Figure 54b. BV curves south and follows the boundary between the rp1 and rp2 regional plains, notably staying at a moderate elevation rather than following the topographic decrease to the west. This means that this elevation difference is younger than BV. BV crosses into the rp2 regional plain rather than entering the densely lineated plain to the east (pdl), meaning the densely lineated plain is older than BV. The channel floor becomes radar bright, making it impossible to tell the relative relationship between BV and the surrounding wrinkle ridges within this data set. BV continues south between the two coronae and passes through a small topographically elevated region that extends from the northern ridge of Parma corona, shown in Figure 54c. This topographic change has a wavelength of ~65 km and an amplitude of ~279 m. Since Parma Corona was present during the emplacement of BV, this points to continued deformation from the corona after formation. Further south, BV splits and becomes anastomosing and radar bright, with the southwestern terminus located before a radar dark depression that is mapped as an rp1 regional plain.

The two topographic undulations caused by the two coronae are clearly visible within the elevation profile (black line) at points "a" and "c," as seen in Figure 55. The depth to the mantle (red line) shows the crustal thickness as mostly constant, with slight crustal thinning to the southwest. The dynamic topography (green line) decreases steadily to the southwest, which mimics the elevation trend and reveals the dynamic topography to be preserved at the surface. This means that the dynamic topography and, by

extension, mantle convection are relatively young processes to deform the surface. The coronae were present during the channel formation, then the channel formed, followed by the mantle process of upwelling, which caused an uplift. After these events, the coronae continued to deform and created short-wavelength changes.

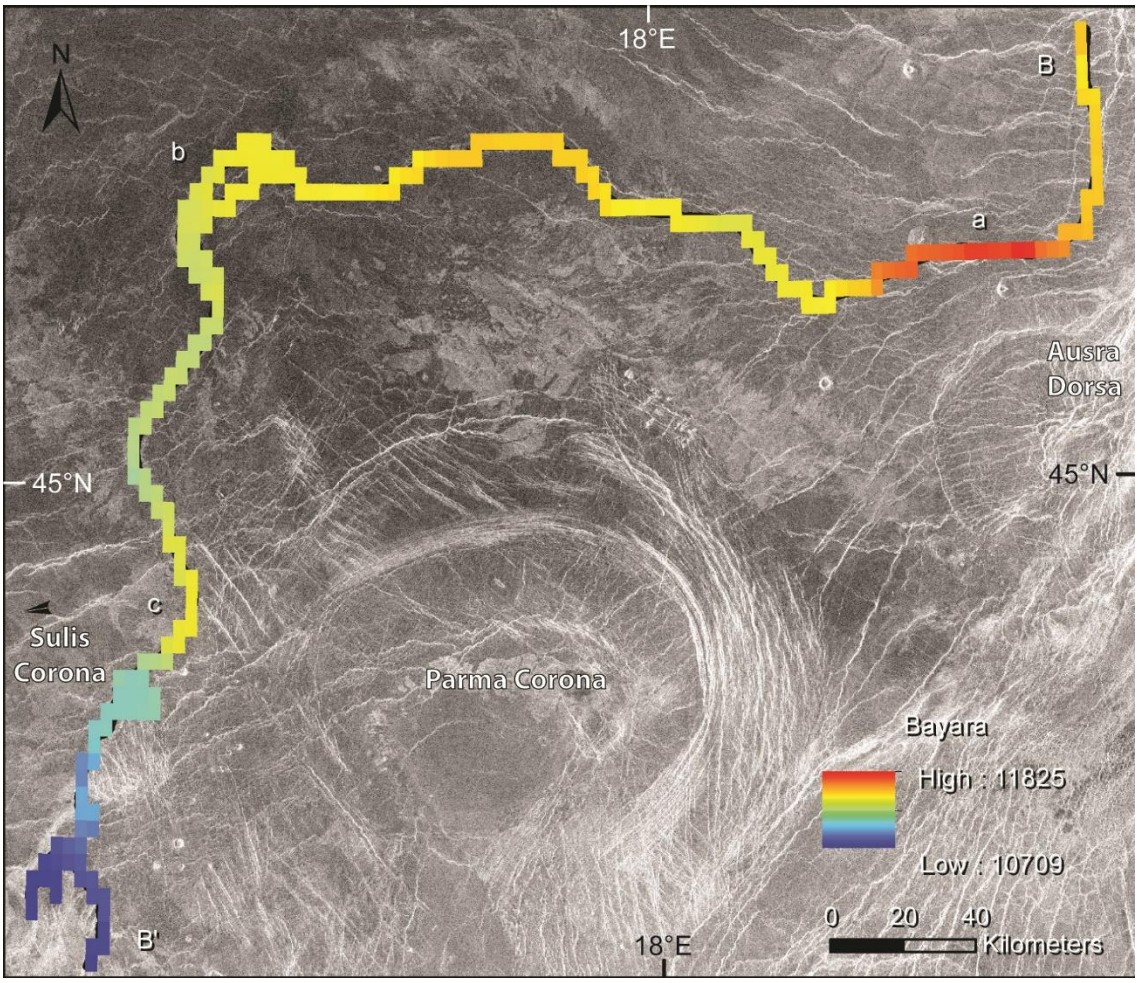

Figure 53: Magellan SAR left-look mosaic is projected to be centered on 17° E, 45° N in an orthographic projection showing Bayara Vallis. The length is illustrated by a color-coded line indicating elevation, with higher elevation shown in red and lower topography shown in dark blue.

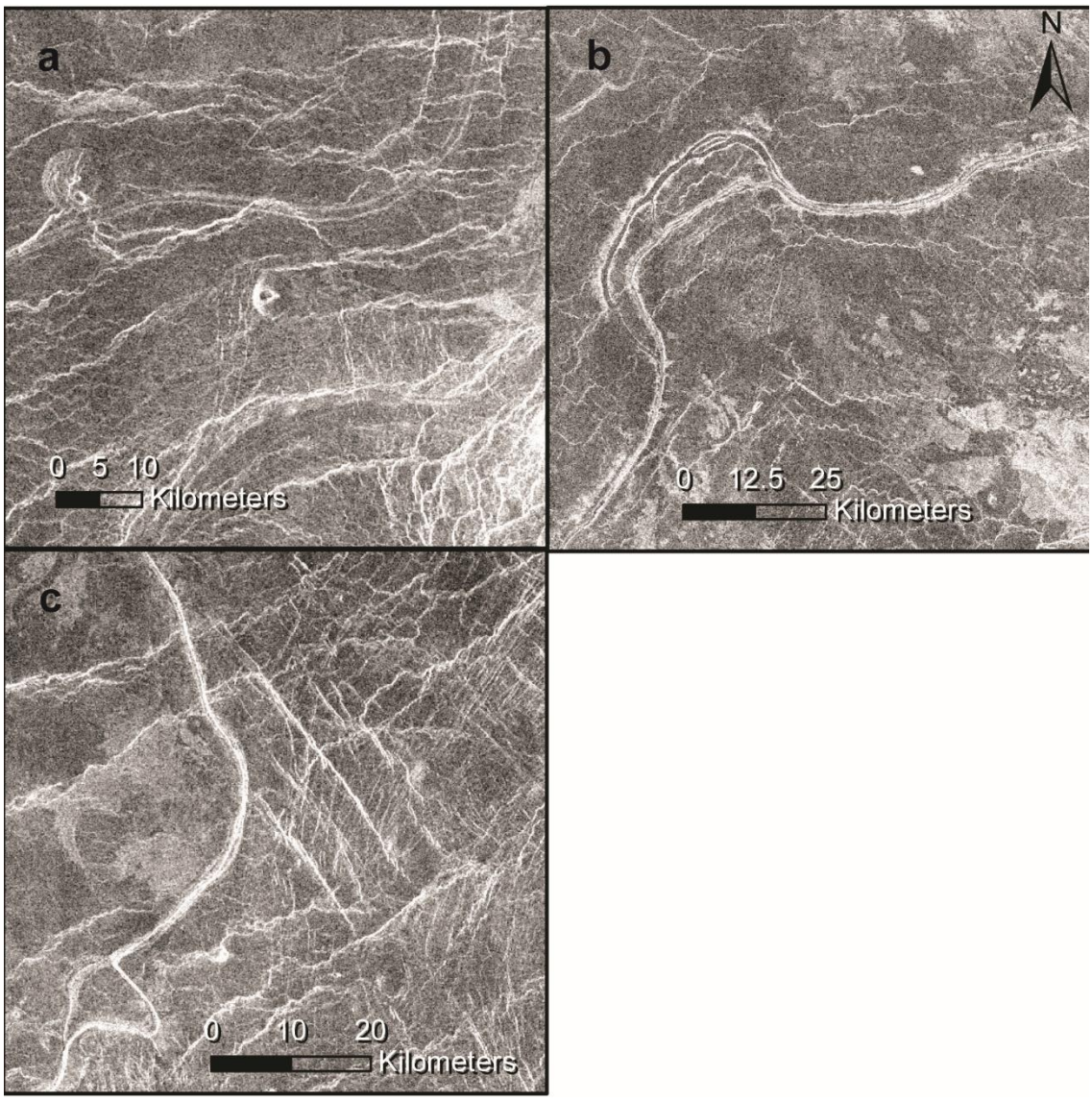

Figure 54: Magellan SAR left-look mosaics are projected to be centered on 17° E, 45° N in an orthographic projection showing close up sections of Bayara Vallis. (a) BV curves west to avoid Ausra Dorsa. (b) Small divergence in the channel. (c) BV passes over a topographically elevated region from Parma Corona.

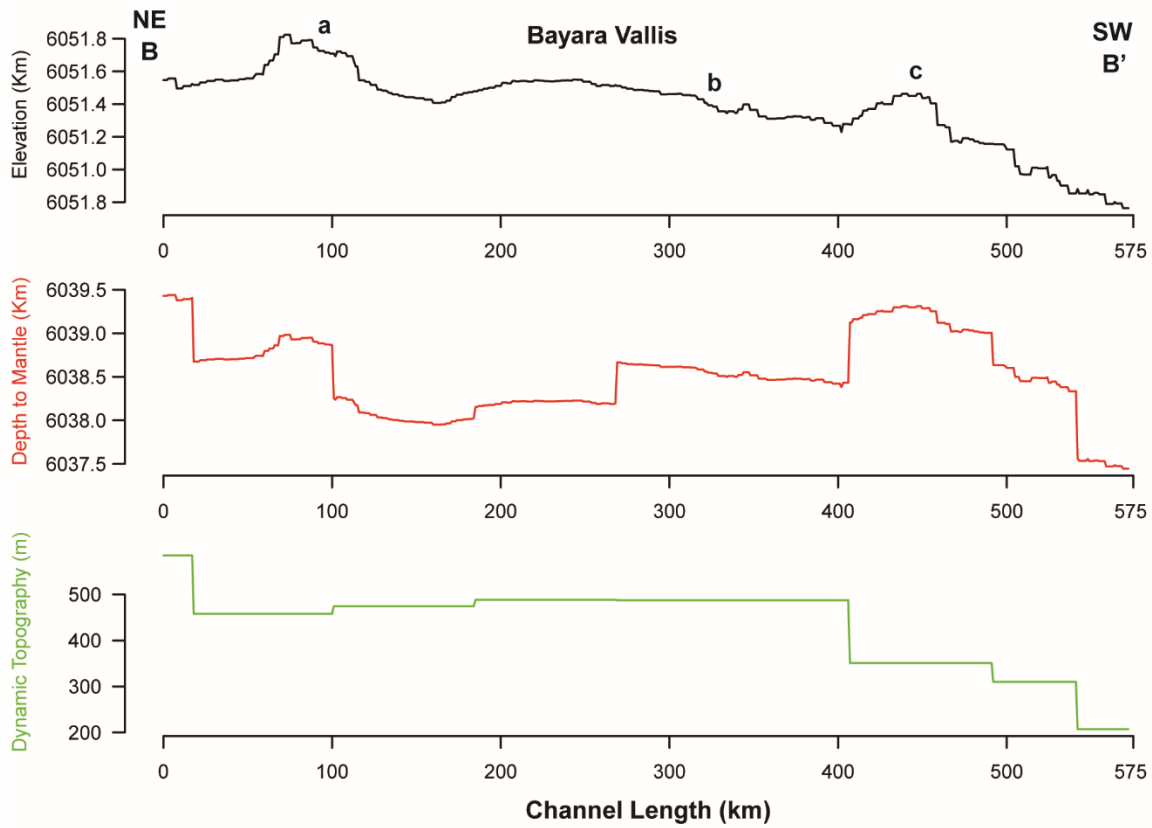

Figure 55: Profile view of topography (black line), depth to the mantle (red line), and dynamic topography (green line) along the flow path of Bayara Vallis.

3.2.23 Utrenitsa Vallis

I mapped Utrenitsa Vallis (UV) following the left-look Magellan SAR mosaic through two bins from our 10x10 DD grid (Figure 56). After mapping, three anomalous points were removed, leaving a total of 555 vertices. This channel is spread out with several branches, so I pull information from the longest segment; however, UV most likely did not flow how I describe it from U to U'. For channels that have gaps in their data, I have added a straight line for a minimum length measure. I do not feel comfortable adding that estimate for this channel because of the odd spread of the different channels. The source could be in the center of these channels, so my added straight line might overestimate the flow distance. I calculated the geodesic length is 566 km for the line I describe as connected. There are several offshoots with lengths less than 200 km. The straight-line distance of the longest one is 403 km, and the overall sinuosity for this segment is 1.40. These numbers obviously vary greatly with this channel.

Around UV are Charykh-Keyok Dorsa, Iyele Dorsa (300 km south, not on map), Atira Mons (650 km southwest, not on map), and three coronae: Demeter Corona ~1000 km east, Coaticue Corona ~500 km north, and Rananeida Corona ~800 km northwest (none on map) (Figure 56). Given the significant distance between UV and the features, a potential source cannot be identified. Describing from U to U', the southern terminus of UV is located in a radar-medium region with wrinkle ridges oriented NE/SW. This area is mapped as a regional plain (rp2) (Ivanov & Head, 2011). The channel continues northeast parallel with the wrinkle ridges, implying the ridges were present at channel formation, and steadily increases in elevation. UV curves north to follow the boundary of a shield plain (psh) and a different regional plain (rp1) before curving east to enter the rp1

regional plain. This relationship shows that these two lava flows were present at the time of channel emplacement. As shown in Figure 56a, the channel is obscured by faults for ~50 km, that likely are part of Charykh-Keyok Dorsa. Alternatively, this small section is mapped as a shield plain or a volcanic edifice. This location could be the origin of UV, with all the channels flowing radially. North of the shield plain, UV appears again within the rp1 regional plain and changes orientation to the northwest, perpendicular to the wrinkle ridges. The channel floor and walls are close in color to the surrounding area, and the wrinkle ridges crosscut them, meaning they are younger than UV. The channel continues between a topographically elevated region and a topographically depressed region, staying within a regional plain until it crosses into a smooth plain (ps). This topographic depression is younger than UV; otherwise, the channel would have continued downslope. Within the radar, the smooth plain is both radar dark and radar bright, with some faults that are E/W orientation in addition to the original NE/SW oriented ones. The channel continues through a topographically elevated region that is not associated with a landform or structure, shown in Figure 56b. The channel then is older than this topographic change and was deformed. This change has a wavelength of ~161 km and an amplitude of ~312 m. UV continues north, and the northern terminus lies within the radar dark rp1 regional plain. The overall path of UV curves around an unnamed groove belt to the west.

The depth to the mantle (red line) shows crustal thickness as mostly constant, although there is slight crustal thickening to the north (Figure 57). The dynamic topography (green line) increases steadily to the north. However, the length of the

channel is too short to infer the relationship between dynamic topography and topography due to the resolution.

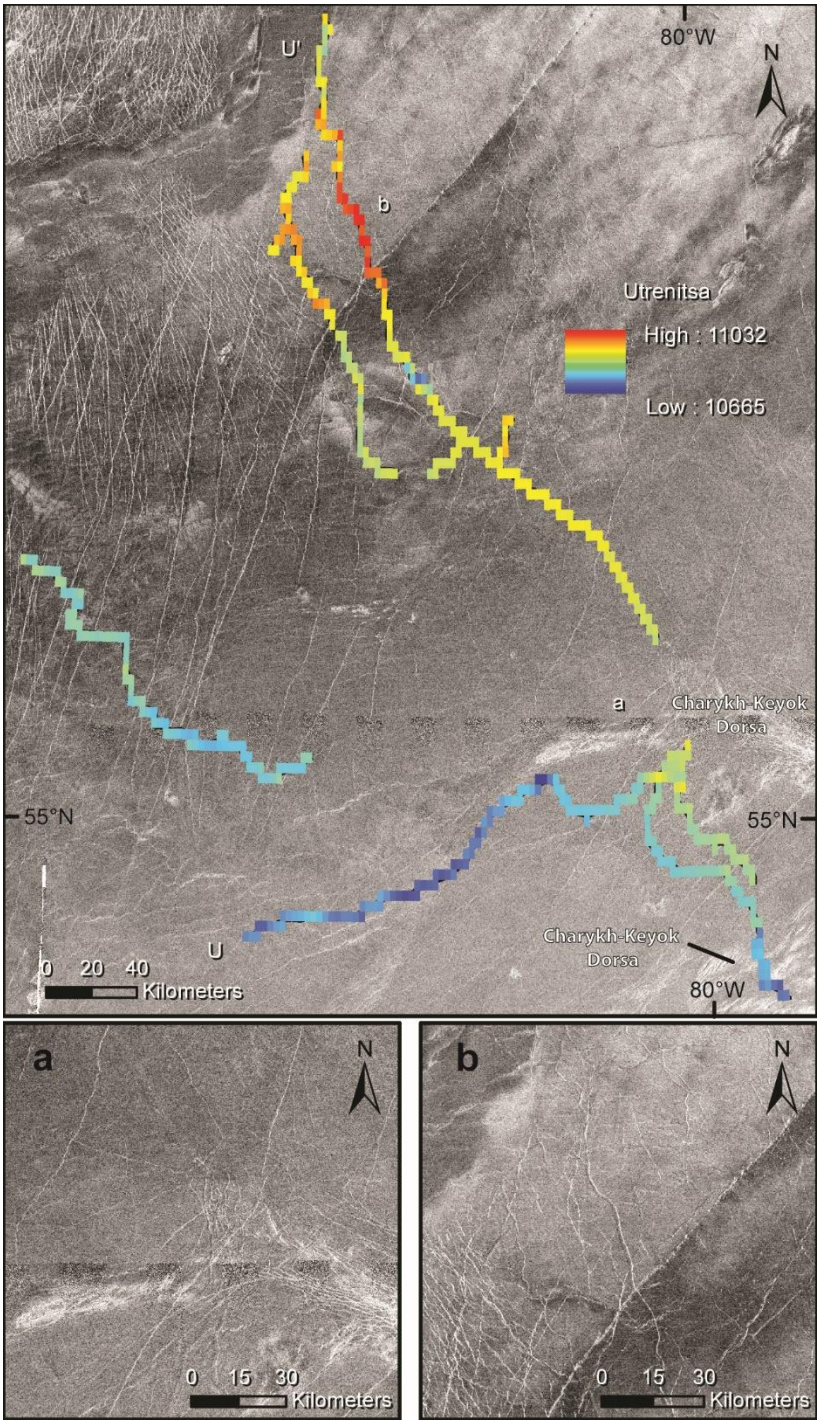

Figure 56: Magellan SAR left-look mosaics are projected to be centered on 82° W, 56° N in an orthographic projection showing Utrenitsa Vallis. The length is illustrated by a color-coded line indicating elevation, with higher elevation shown in red and lower topography shown in dark blue. (a) UV is obscured by Charykh-Keyok Dorsa. (b) UV passes over a topographically elevated region.

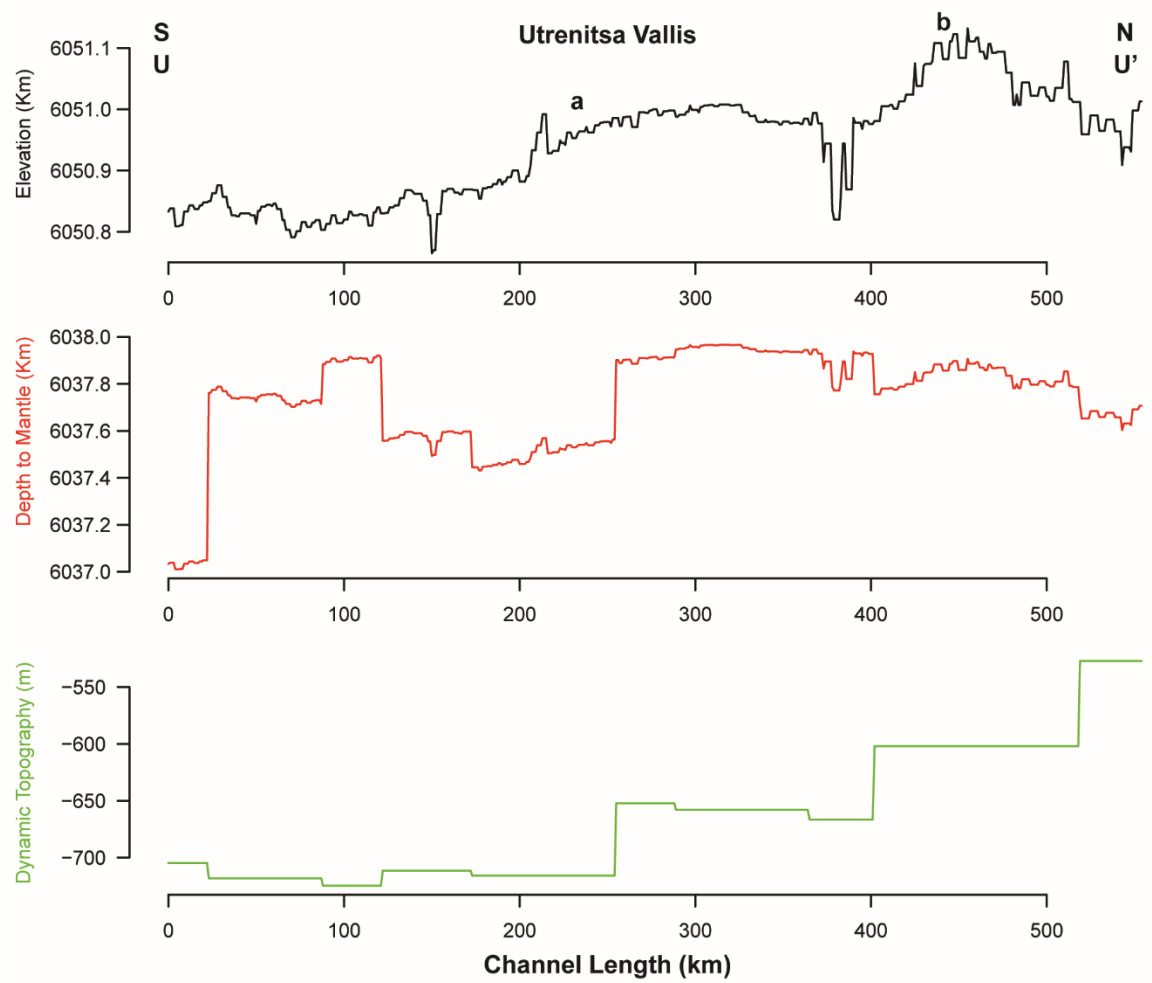

Figure 57: Profile view of topography (black line), depth to the mantle (red line), and dynamic topography (green line) along the flow path of Utrenitsa Vallis.

3.2.24 Kūmsong Vallis

Kūmsong Vallis (KV) lies within the left-look Magellan SAR mosaic in two of the 10x10 DD bins. Four anomalous points were removed, leaving a total of 486 vertices. The length is 494 km. There is a small offshoot with a length of 47 km. I measured the straight-line distance to be 391 km, making the overall sinuosity equal to 1.26.

The northwest terminus of KV is in a radar bright, heavily ridged area and continues southeast into a radar darker area with wrinkle ridges that have a NE/SW orientation (Figure 58). The radar bright area is mapped as a regional plain (rp1), and the radar dark region as a shield plain (psh) (Ivanov & Head, 2011). KV stays west of a topographic high but also does not choose the depression that is farther west of the channel. This behavior represents itself as the small topographic change at 50 km in Figure 59, which has a wavelength of ~66 km, an amplitude of ~100 m, and is relatively younger than KV. The wrinkle ridges are present in the channel floor, meaning they are also younger than KV. KV continues further east to curve around a densely lineated plain (pdl), as shown in Figure 58a and continues while gaining some elevation. The densely lineated plain must have been present during the formation of the channel and is thus older. This point is where the channel crosses into the shield plain, and the topographic change has a wavelength and amplitude of ~162 km and ~157 m, respectively. Then KV continues into a depression between the tesserae and a topographically elevated region, where the channel splits (Figure 58b). The offshoot continues southeast and gets lost in a heavily fractured region. The main channel turns northeast and continues through the center of a topographically elevated region in the direction of more tesserae (wavelength ~115 km, amplitude ~275 m). This topographic change is younger than KV and deformed

the flow path, and is not associated with a landform or structure. The southeastern terminus lies on the downslope of this topographic high, just before a radar bright lava flow, mapped as a regional plain (rp2). This lava flow potentially originates from Fotla Corona (not on map), 430 km to the east. If Fotla Corona is the source of KV, then the flow direction would be the opposite of how I have described it here.

The depth to the mantle (red line) shows a constant crustal thickness until 150 km (Figure 59). Then the crust thickens substantially until ~375 km, then remains constant towards the southeast. The dynamic topography (green line) increases steadily towards the southeast. The length of the channel is shorter than the spatial block size, making interpretation impossible.

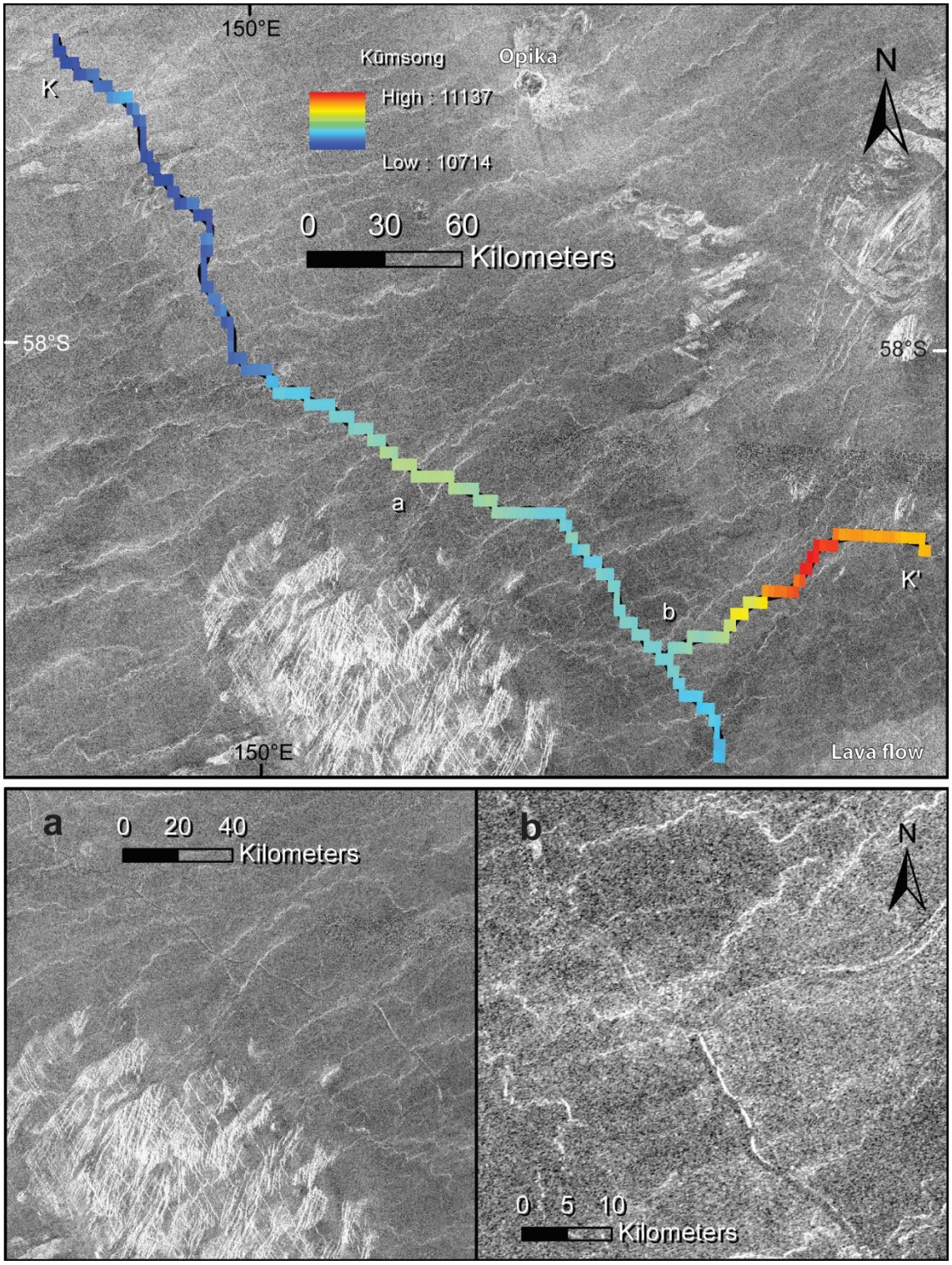

Figure 58: Magellan SAR left-look mosaics are projected to be centered on 151° E, 58° S in an orthographic projection showing Kūmsong Vallis. The length is illustrated by a color-coded line indicating elevation, with higher elevation shown in red and lower topography shown in dark blue. (a) KV curves around a densely lineated plain. (b) KV splits into two channels.

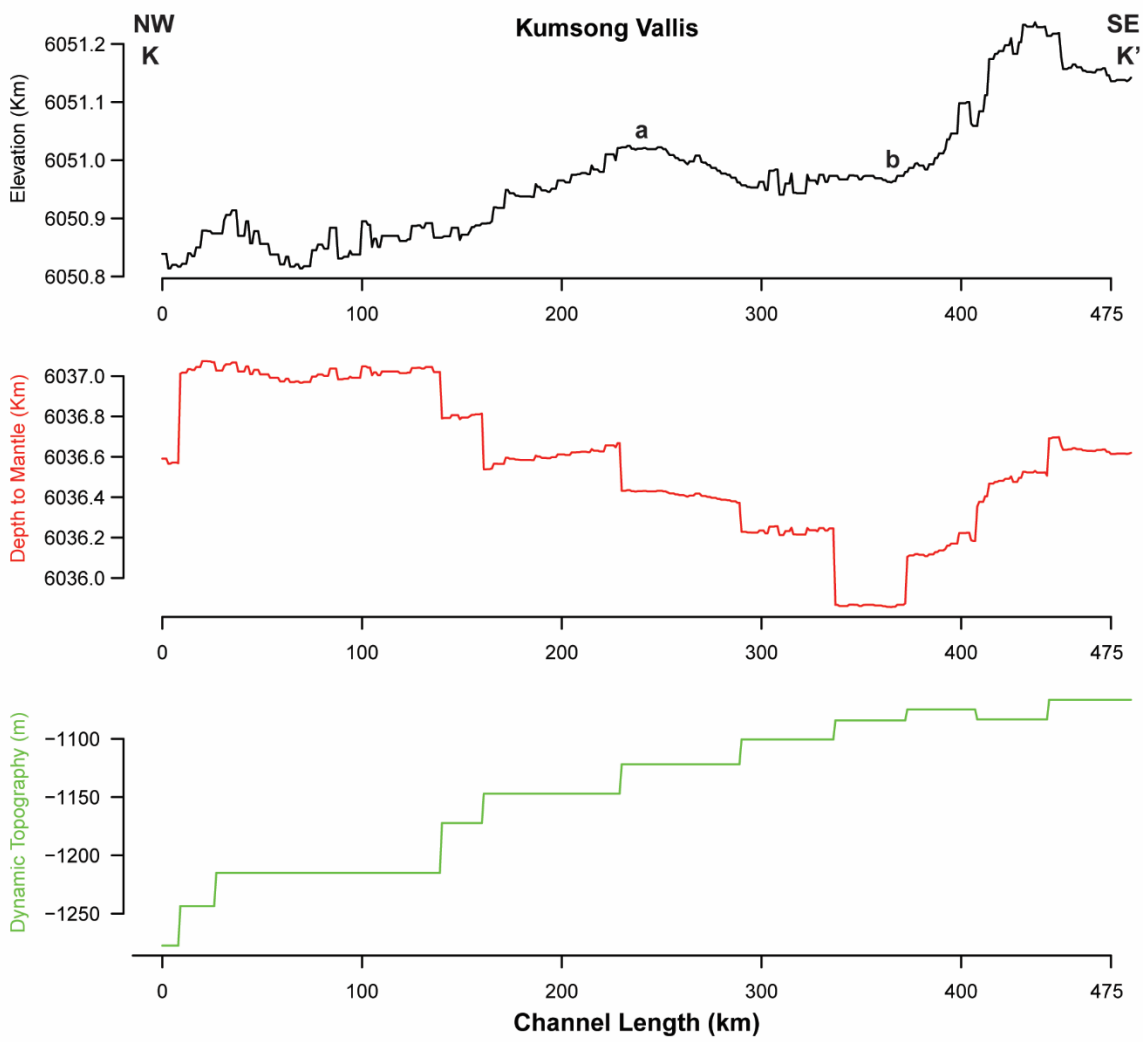

Figure 59: Profile view of topography (black line), depth to the mantle (red line), and dynamic topography (green line) along the flow path of Kūmsong Vallis.

3.2.25 Nepra Vallis

I mapped Nepra Vallis (NV) following the left-look Magellan SAR mosaic through one bin from the 10x10 DD grid. After mapping, I removed four anomalous points, leaving a total of 432 vertices. I calculated the geodesic length to be 443 km without the additional lengths across gaps in the data. The lines add another 47 km to equal a minimum length of 490 km. Using the total with the added length, I divide by 375 km, the straight-line distance, to calculate an overall channel sinuosity of 1.31.

The entirety of the channel is mapped in a regional plain (rp1) (Ivanov & Head, 2011). Two potential options for sources are Belet-Ili Corona (not on map) and Gaia Corona (not on map) to the northwest by ~400 km. To the east of NV, the terrain is radar brighter, and the channel follows that boundary. NV has a larger than average width of ~7-8 km wide, whereas the rest of the channels range from 2 – 5 km (Figure 60). The southeast terminus of the channel lies near E/W oriented wrinkle ridges, which are visible within the channel floor, relatively dating them as younger. Continuing northwest, NV has small sinuous movements to avoid a topographic high in the northeast, meaning this topographic elevation was present during channel emplacement. Then the channel increases in elevation as it continues through a topographically elevated region that is radar darker than the surroundings, shown in Figure 60a. This topographic change has a wavelength of ~114 km and an amplitude of ~470 m. The change is younger than the channel and deforms its elevation profile (Figure 61, point "a"). NV curves west, ignoring the topographic low to the east, and narrows. This topographic depression must be younger than the channel; otherwise, the lava would have continued downslope. The channel increases in elevation again and becomes more sinuous (wavelength ~188 km,

amplitude ~365 m). There is no landform or structure associated with this change, which is relatively younger than the channel. NV then turns north and is lost in a heavily fractured area with a NE/SW orientation, mapped as the edge to an unnamed corona (Figure 60b).

The depth to the mantle (red line) shows constant crustal thickness from 0 to 80 km, then substantial crustal thickening, which remains constant towards the northwest (Figure 61). The dynamic topography (green line) increases steadily to the northeast. The length of the channel is shorter than the spatial block size, rendering it impossible to discuss the relationship between topography and dynamic topography.

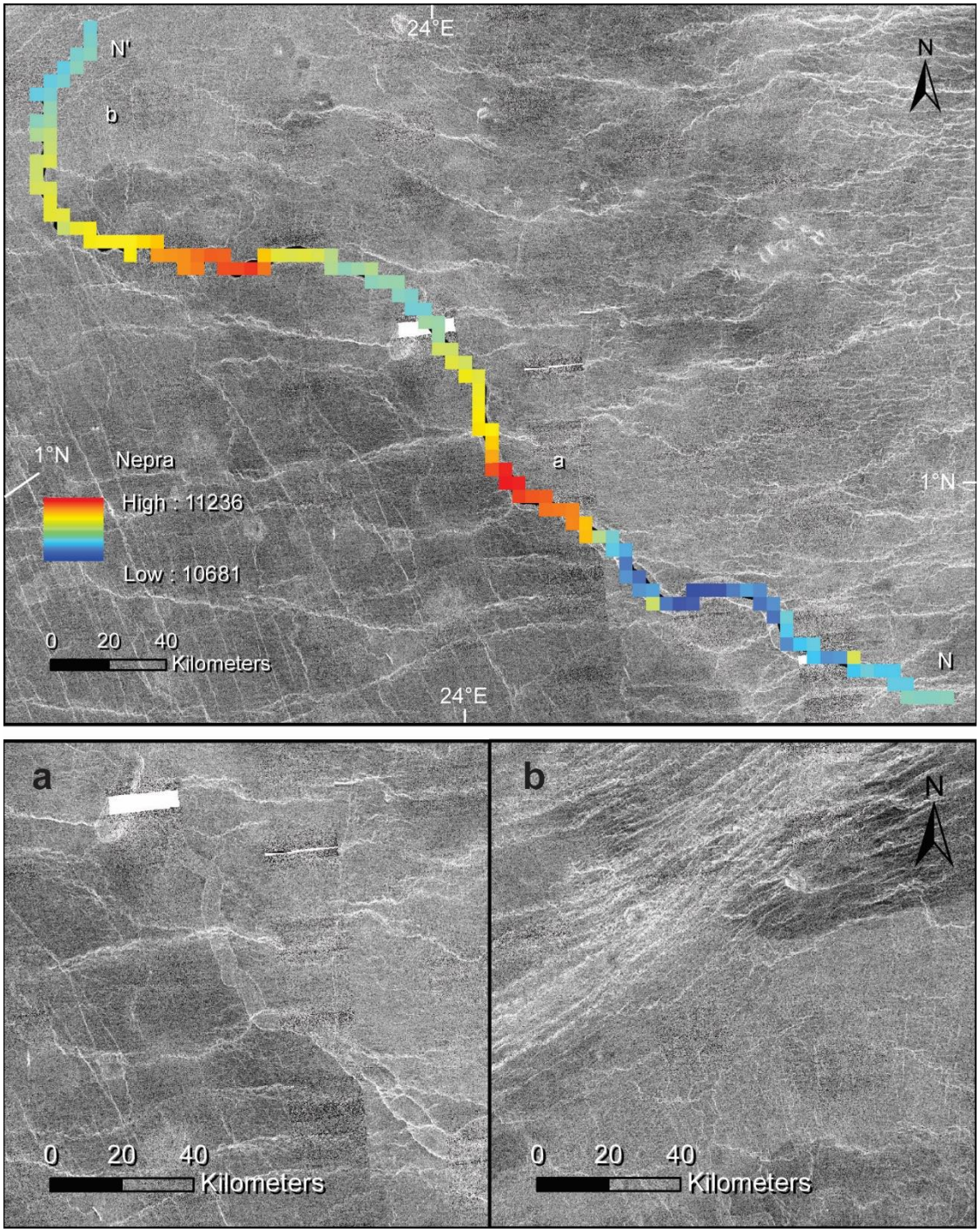

Figure 60: Magellan SAR left-look mosaic is projected to be centered on 24° E, 1° N in an orthographic projection showing Nepra Vallis. The length is illustrated by a color-coded line indicating elevation, with higher elevation shown in red and lower topography shown in dark blue. (a) NV passes over an elevated region that is radar dark. (b) The northern terminus of NV disappears within deformation.

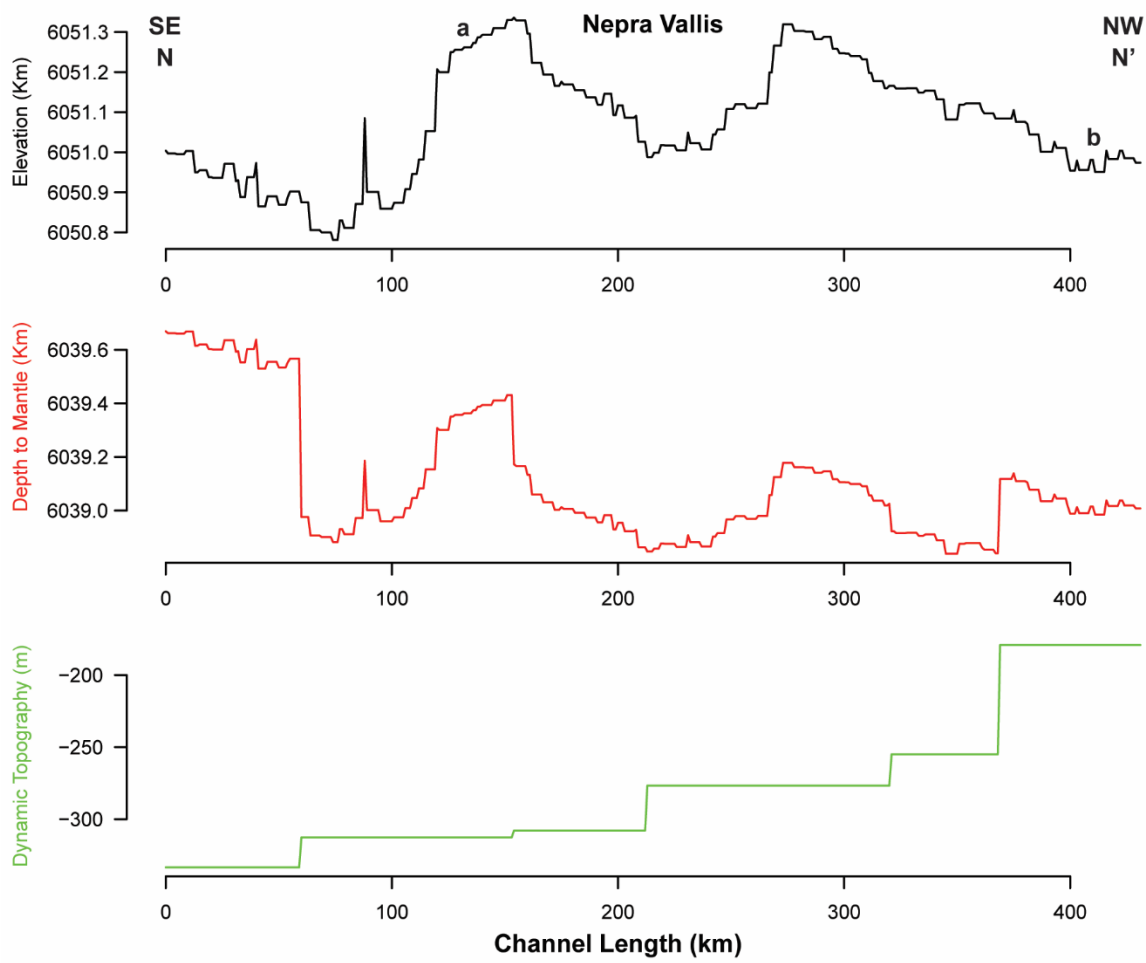

Figure 61: Profile view of topography (black line), depth to the mantle (red line), and dynamic topography (green line) along the flow path of Nepra Vallis.

3.2.26 Banumbirr Vallis

Banumbirr Vallis (BV) is visible within the left-look Magellan SAR mosaic in one 10x10 DD bin. One point was removed, leaving a total of 472 vertices. The measured geodesic length is 479 km, and the straight-length distance is 392 km, calculating the overall sinuosity to be 1.22.

Surrounding BV is Atargatis Corona (AC) ~350 km to the east (not on map), and Juan-Yin Corona, ~600 km away (not on map). A radar bright section separates BV and AC, meaning AC is likely the source for BV, and the radar bright section is a lava flow (Figure 62). Describing from B to B', the eastern terminus is visible out of the radar bright material mapped as crater material by Ivanov and Head (2011) but could also be a lava flow. The channel floor is initially radar bright and transitions to radar dark with -bright walls, shown in Figure 63a. The channel continues west with small eyelets into a shield plain (psh) (Ivanov & Head, 2011). The rest of BV stays within the shield plain, passing between tesserae to the northeast and a small groove belt to the southwest, meaning both of these structures were likely present during channel emplacement. The shield plain has faults oriented NW/SE and NE/SW that crosscut the channel, meaning they are younger than the channel. BV increases in elevation near a topographically elevated region that is not associated with a landform or structure, then decreases steadily. This topographic change has a wavelength of ~207 km, an amplitude of ~244 m, and is relatively younger than the channel. BV curves north briefly and stays within the radar dark area. The lighter radar to the west is a groove belt. Then the channel curves northwest to avoid the tesserae, meaning the tesserae are older than the channel, while the channel's width varies. BV splits and braids for 70 km, shown in Figure 63b, which also

shows the tesserae and groove belt. BV curves around small shield volcanoes, which were present during channel formation, and BV decreases in topography while splitting into two and recombining. The channel then continues through a topographically elevated region that has more wrinkle ridges present. This relationship reveals that the topographic change is younger and deformed the channel path. The northwestern terminus is no longer visible past this deformation. The decrease and increase in elevation form a bowl in the elevation profile (Figure 64, black line), has a wavelength of ~141 km and an amplitude of ~311 m, and is shown in Figure 63c near the shield volcanoes. The topographic depression and elevation are not associated with a landform or structure.

The depth to the mantle (red line) illustrates crustal thickening until ~260 km, then crustal thinning towards the northwest (Figure 64). The dynamic topography (green line) generally decreases to the northeast. The length of the channel is shorter than the spatial block size of the dynamic topography, making interpretation impossible.

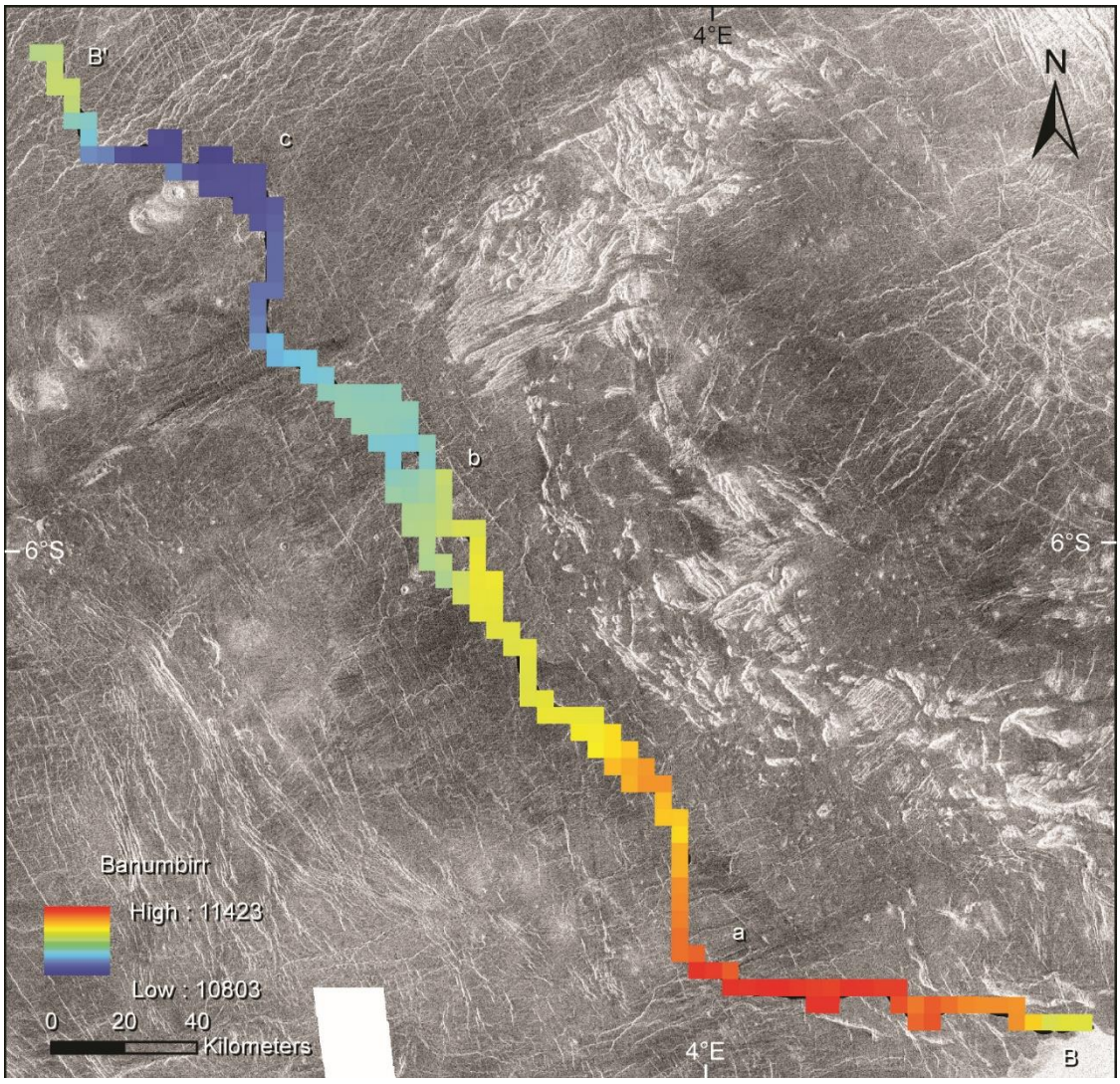

Figure 62: Magellan SAR left-look mosaic is projected to be centered on 3° E, 6° S in an orthographic projection showing Banumbirr Vallis. The length is illustrated by a color-coded line indicating elevation, with higher elevation shown in red and lower topography shown in dark blue.

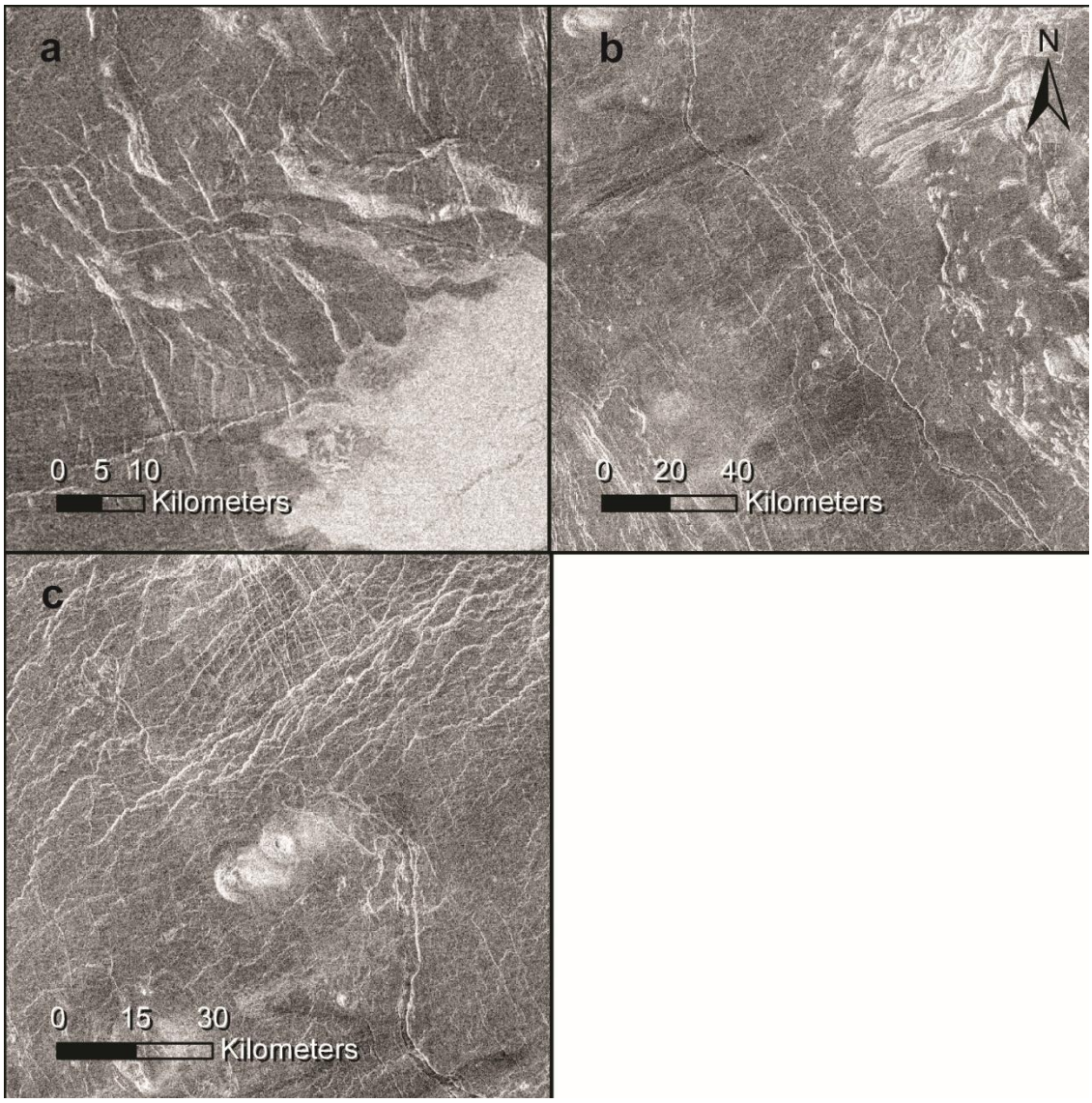

Figure 63: Magellan SAR left-look mosaics are projected to be centered on 3° E, 6° S in an orthographic projection showing close up sections of Banumbirr Vallis. (a) The southeastern terminus of BV is initially radar bright. (b) BV splits into a braided structure for 70 km. (c) BV curves northeast into a depression to avoid shield volcanoes.

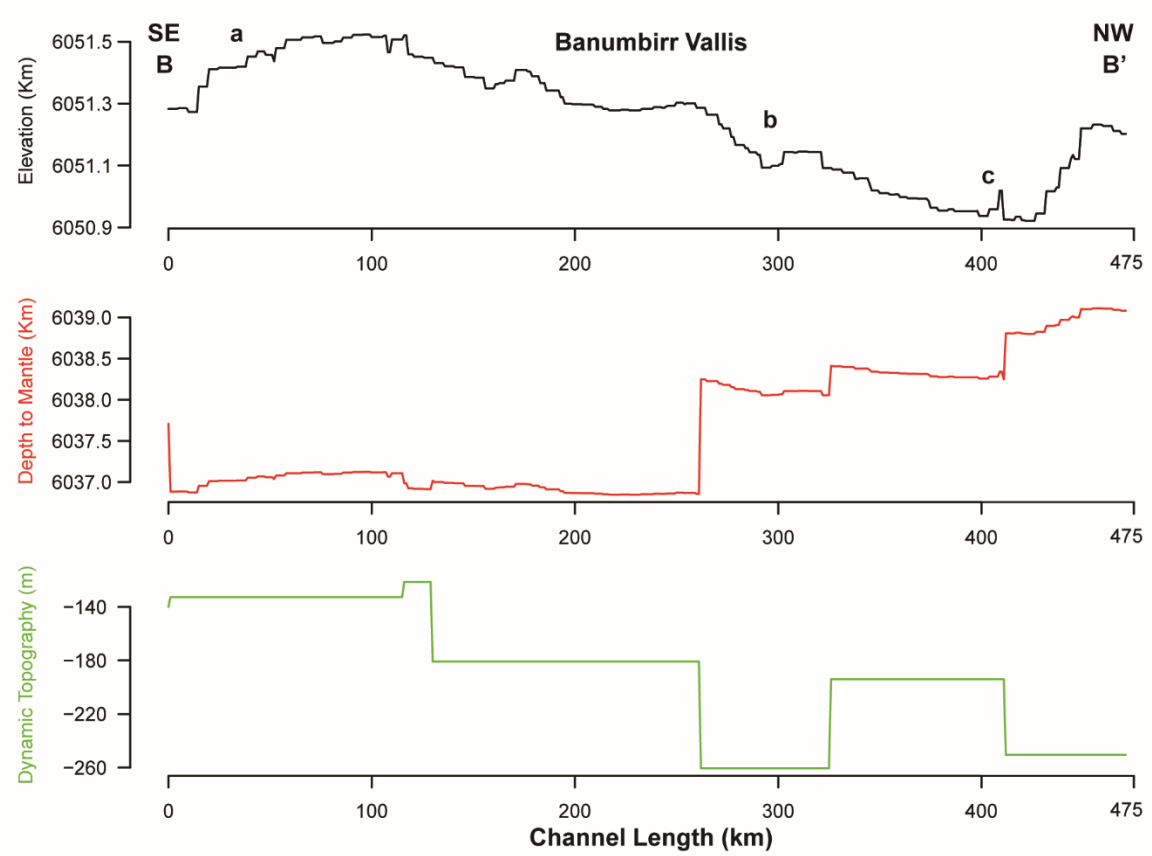

Figure 64: Profile view of topography (black line), depth to the mantle (red line), and dynamic topography (green line) along the flow path of Banumbirr Vallis.

3.2.27 Fetu-ao Vallis

I mapped Fetu-ao Vallis (FV) following the left-look Magellan SAR mosaic through two bins from the 10x10 DD grid. After mapping, I removed three anomalous points, leaving a total of 389 vertices. The calculated geodesic length is 393 km. The channel is not visible in the middle, so I include a straight line connecting the two sides to add the length of 70 km to equal a minimum total length of 463 km. The straight-line distance is 401.48 km, and the overall sinuosity with the added segment is 1.15.

Near FV is Gendenwitha Vallis, just ~120 km southeast (not on map). There is no discernable relationship between them with the SAR mosaics currently. To the northwest lies Naotsete Corona (~400 km distance) and Awenhai Mons (330 km distance), and to the southwest by ~600 km lies Seiusi Corona (none on map). Describing from F to F', the entire channel lies within a regional plain (rp1), as seen in Figure 65 (Ivanov & Head, 2011). Notably, there is a small channel that runs parallel to the main part of FV. I mapped it as part of FV but could not determine if and where they connect in the current radar mosaics. The southern terminus is in an area with NW/SE and N/S oriented wrinkle ridges. The radar coloring is inconsistent in this region, with artifact stripes. Continuing north parallel with the wrinkle ridges, FV continues through a topographically elevated region that is radar bright compared to the surroundings, shown in Figure 65a. This topographically elevated region is also experienced by Gendenwitha Vallis just south of Sui-ur Linea, which is 275 km east. This relatively dates the topographic change as younger than FV and Gendenwitha Vallis. Where FV crosses the region, it has a wavelength of ~178 km and an amplitude of ~387 m. North of the topographically elevated region, FV curves northeast into the radar darker area with wrinkle ridges. Some

of the wrinkle ridges crosscut the channel, and in other sections, the channel floor is untouched. Both of these relationships mean that fault-forming processes were present before and were ongoing after the channel emplacement. FV increases in elevation and disappears, obscured by increased deformation for 70 km, shown in Figure 65b. This deformation could possibly be part of Discordia Linea, but this label is ~700 km west. This relationship means that the deformation potentially caused by Discordia Linea is younger than FV. The channel reappears in the same orientation farther north. Because the disappearance happens right at a topographic increase, this topographically elevated region could be a fault that separates the channel. The wavelength and amplitude of this increase are ~204 km and ~614 m, respectively. FV avoids a small and topographically elevated densely lineated plain to the north, meaning the densely lineated plain is older than the channel. Then the channel begins anastomosing before reaching the northeastern terminus, which lies in the radar near shield volcanoes. Because of the location, these shield volcanoes are likely the source of FV, and the flow direction is the opposite of how I have described here.

The depth to the mantle (red line) reveals a constant crustal thickness underneath FV (Figure 66). The dynamic topography (green line) decreases until 200 km, then increases towards the northeast. The grey boxes represent where data was not taken because the channel was not visible. The length of the channel is shorter than the spatial block size, meaning the relationship between topography and dynamic topography cannot be determined.

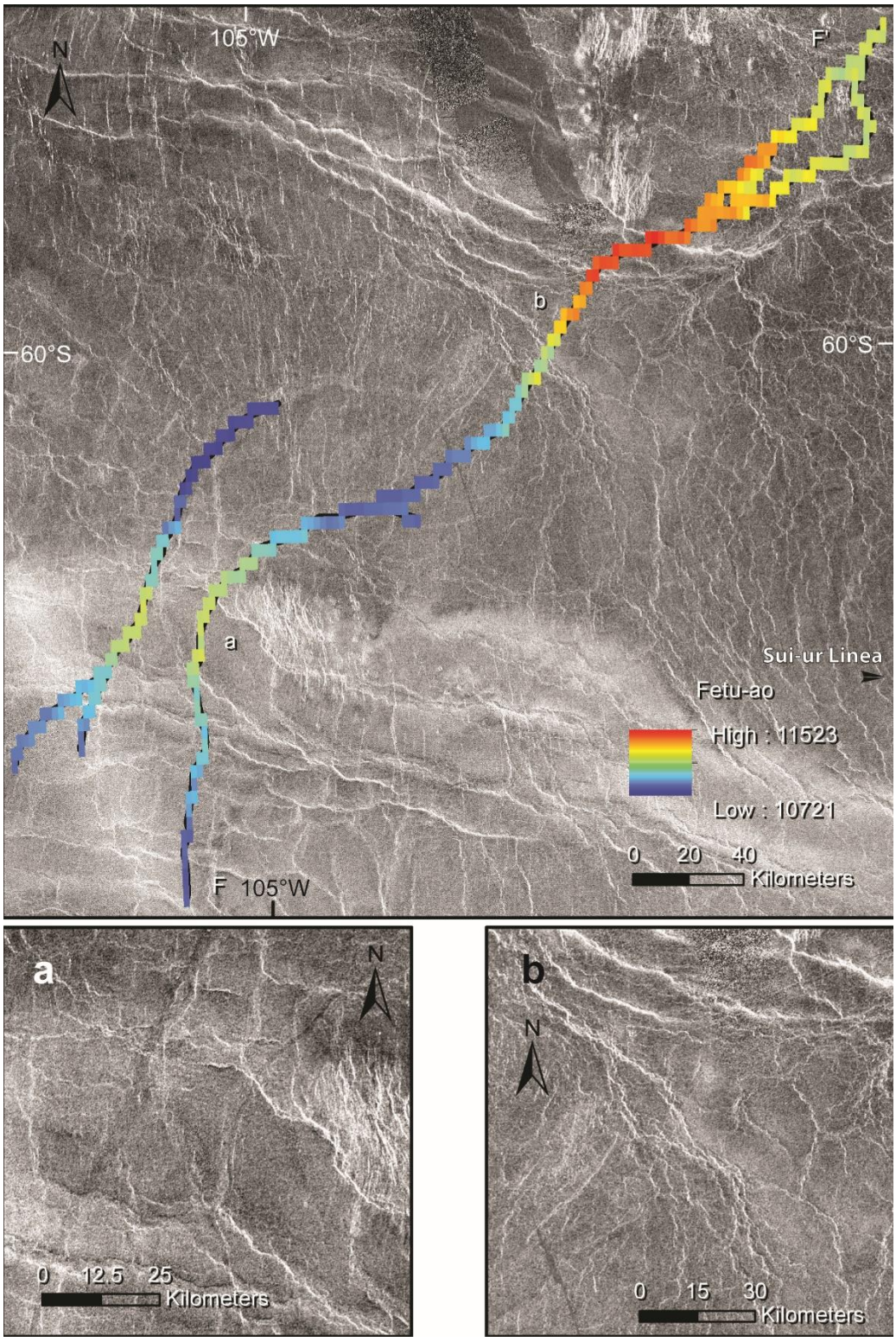

Figure 65: Magellan SAR left-look mosaic is projected to be centered on 103° W, 60° S in an orthographic projection showing Fetu-ao Vallis. The length is illustrated by a color-coded line indicating elevation, with higher elevation shown in red and lower topography shown in dark blue. (a) FV passes over an elevated region that is radar bright. (b) FV disappears within deformation after climbing in elevation.

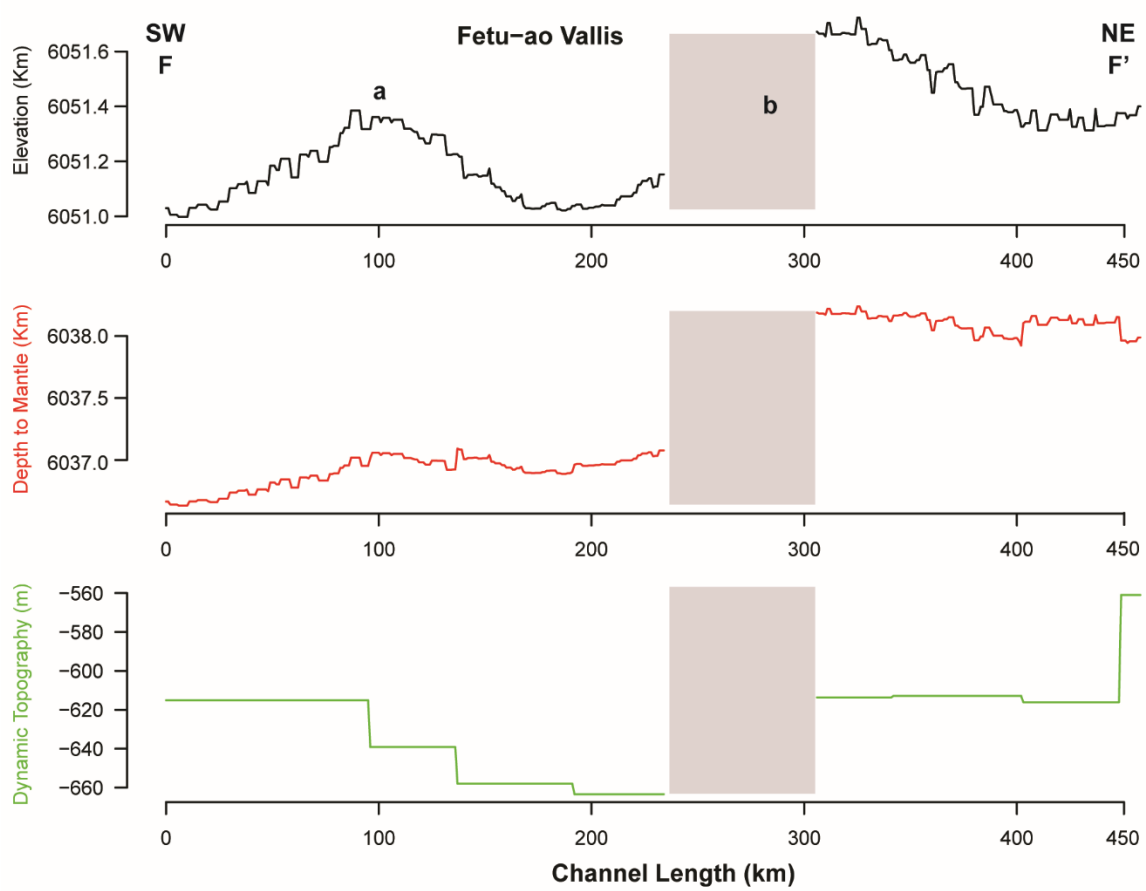

Figure 66: Profile view of topography (black line), depth to the mantle (red line), and dynamic topography (green line) along the flow path of Fetu-ao Vallis. The grey rectangles are where the channel is obscured, and no data was taken.

3.2.28 Lo Shen Vallis

Lo Shen Vallis (LSV) lies in the left-look Magellan SAR mosaic seen in two bins from our 10x10 DD grid. After mapping, I removed one anomalous point, leaving a total of 424 vertices. I calculated the geodesic length to be 428 km. The straight-line distance is 274 km, and the overall sinuosity is 1.56.

While no named features are near LSV, the northern part of the channel is surrounded by the tesserae of Ovda Regio (not on map), a highland called a crustal plateau. The channel walls are radar bright throughout, and the channel floor is initially radar bright but gradients to the same darkness as the surroundings. LSV is also tightly sinuous, with small oscillations within the overall curve. There is a secondary channel just to the west of the main part that has pooling at its northern terminus (Figure 67). At point L, the channel's southern terminus is located within a smooth plain (ps) and either originates from or ends in a radar bright lava flow (Ivanov & Head, 2011). LSV is oriented northeast and passes between small sections of tesserae, relatively dating the tesserae as older than the channel. Just northeast of the tesserae, the channel splits into two channels, with a levee break flowing to the east, shown in Figure 68a. The eastern channel is wider and more tightly sinuous than the western channel, which curves north and reaches its northern terminus in a lava pool that reconnects to the eastern branch. The eastern branch continues northeast, curving north to avoid the higher elevation of the tesserae to the east, meaning the topographic increase was present during the channel's formation. Right where LSV turns north, a crater called Teura obscures the channel, shown in Figure 68b. Continuing through the smooth plain, the eastern channel splits into two: the western side reconnecting with the northern terminus of the west side in a lava

flow, and the eastern side continuing north with small offshoots, shown in Figure 68c. The channel is thinner and straighter at this northern terminus. LSV curves west to avoid the tesserae with a higher elevation and fades into the radar dark smooth plain. This channel from the split overall curves around the east side of a small area mapped as tesserae.

From the topographic profile (black line), the elevation steadily increases from L to L', meaning that the channel has not undergone any apparent elevation deformation, and the flow path is likely opposite to what is described here (Figure 69). Since LSV curves around the tesserae, these tesserae also did not get tectonically altered since the formation of the channel. The depth to the mantle (red line) shows crustal thickening towards the northeast. The dynamic topography (green line) also increases steadily to the northeast. The length of the channel is shorter than the spatial block size, making interpretation impossible.

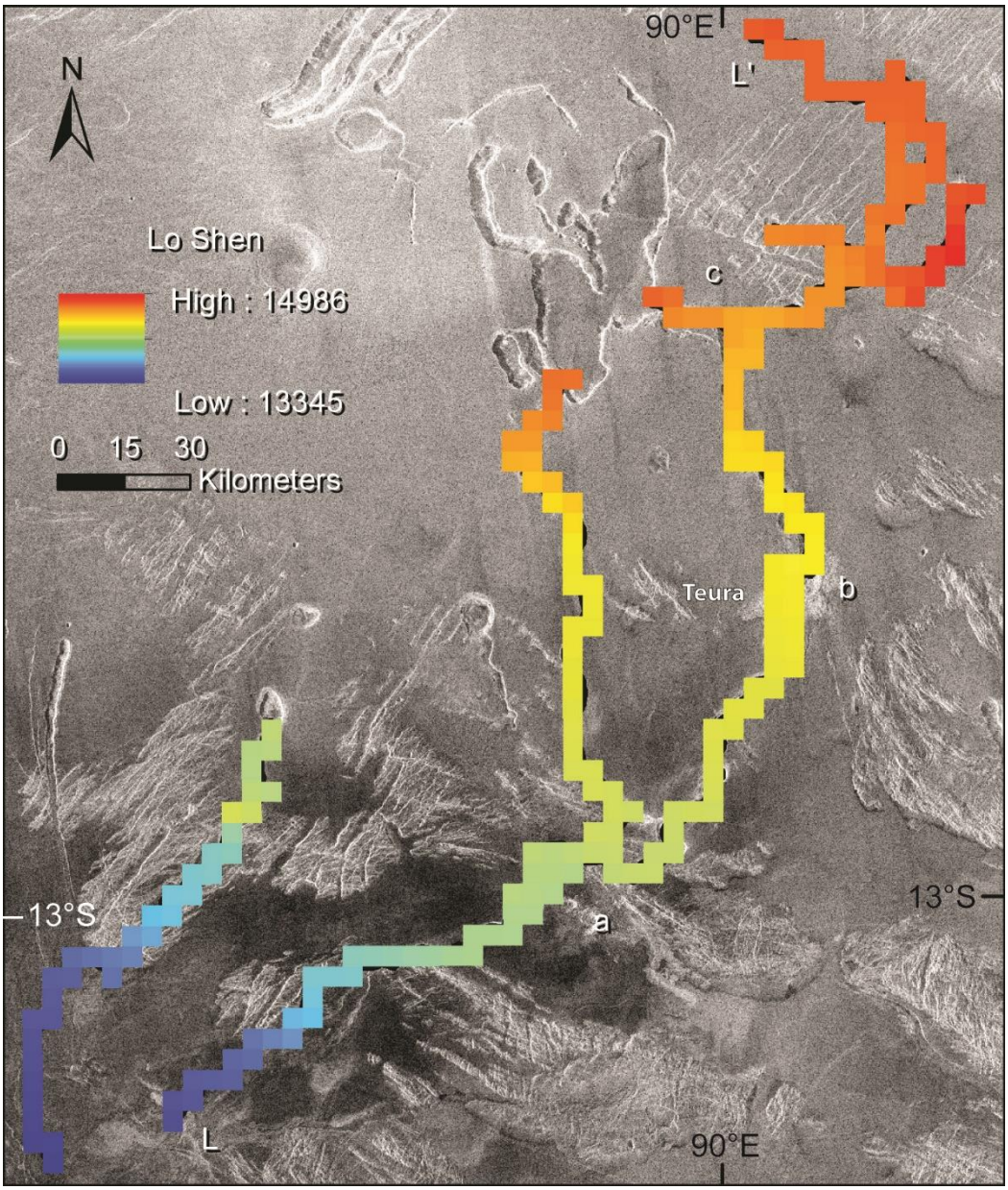

Figure 67: Magellan SAR left-look mosaic is projected to be centered on 90° E, 12° S in an orthographic projection showing Lo Shen Vallis. The length is illustrated by a color-coded line indicating elevation, with higher elevation shown in red and lower topography shown in dark blue.

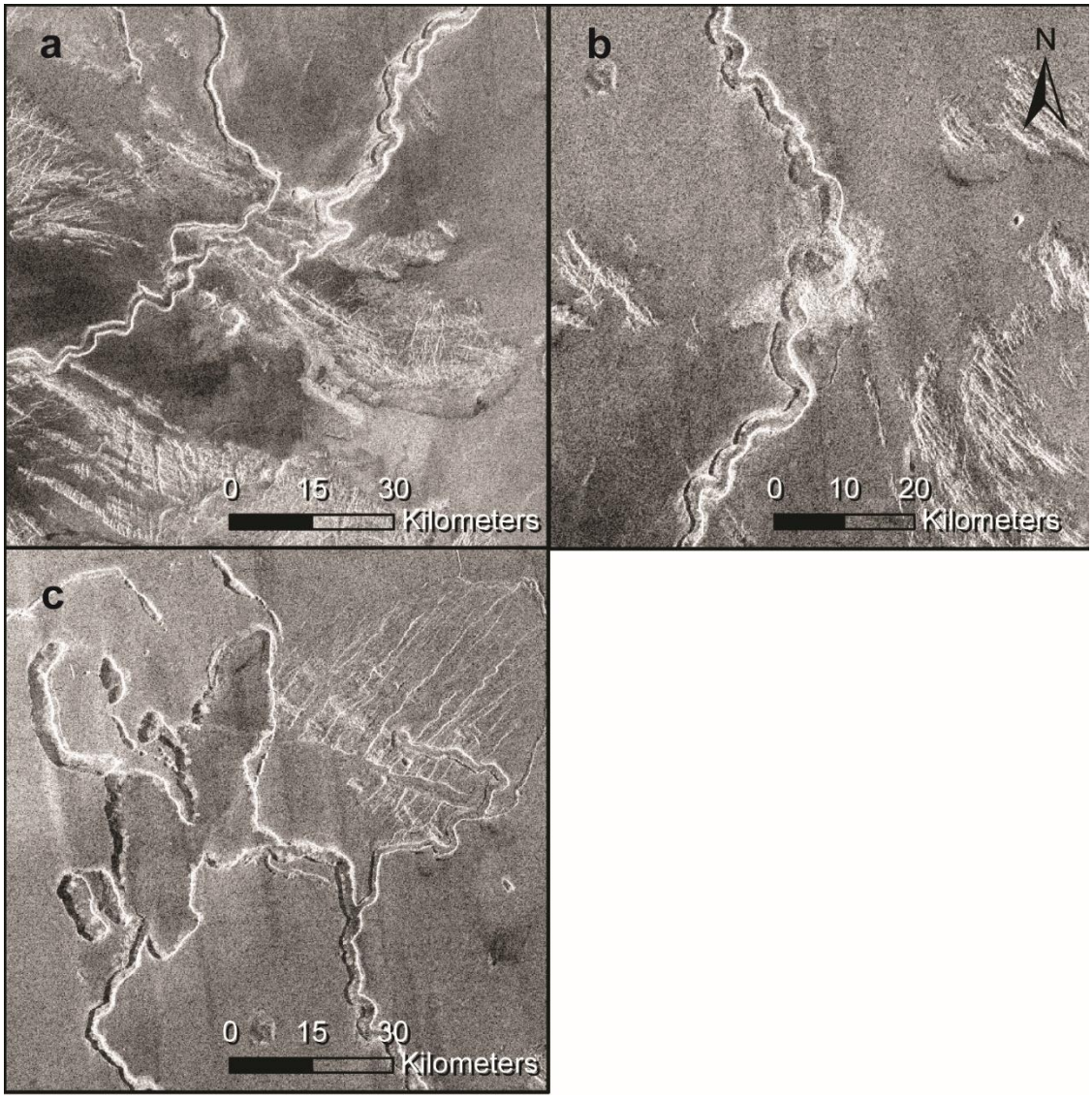

Figure 68: Magellan SAR left-look mosaics are projected to be centered on 90° E, 12° S in an orthographic projection showing close up sections of Lo Shen Vallis. (a) LSV splits into two channels. (b) Teura crater obscures the channel. (c) The pooling and continuation of the northern terminus.

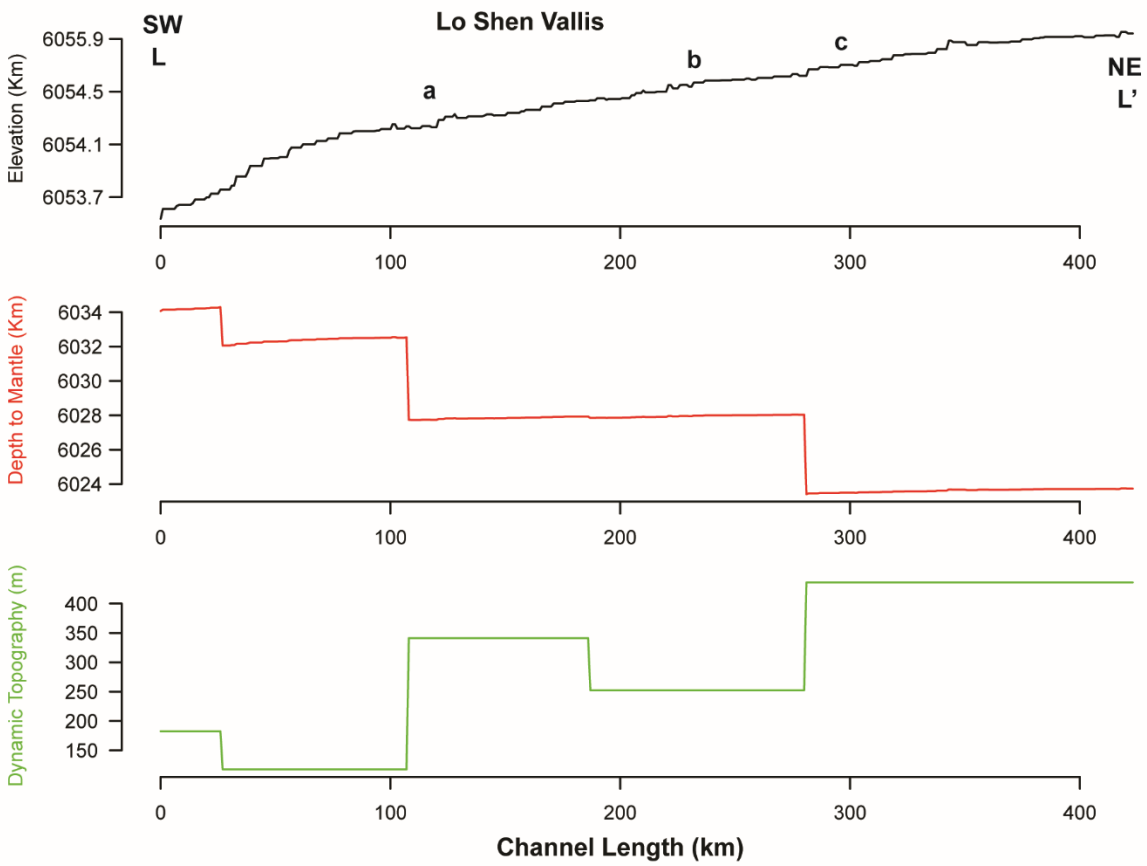

Figure 69: Profile view of topography (black line), depth to the mantle (red line), and dynamic topography (green line) along the flow path of Lo Shen Vallis.

3.2.29 Kinsei Vallis

I mapped Kinsei Vallis (KV) following the left-look Magellan SAR mosaic through two 10x10 DD bins. After mapping, I did not have to remove any points, leaving a total of 411 vertices. This channel is much wider than the others, with a width of around 10 –12 km. The geodesic length is 417 km, with a straight-line distance of 378 km. This results in an overall channel sinuosity of 1.10.

The surrounding region around KV is heavily fractured (Figure 70). To the west is a radar bright lava flow from Kubebe Corona, 600 km to the northwest (not on map). Kubebe Corona is the likely source of KV. The region that KV flows in is mapped as a regional plain (rp1) (Figure 70) (Ivanov & Head, 2011). The western terminus is surrounded by wrinkle ridges that have NE/SW and E/W orientations, and the channel continues northeast. KV continues downhill into a depression and turns to avoid a topographic high from a groove belt (gb); however, the channel still drastically increases in elevation as it flows past this topographically elevated region, as seen in Figure 70a. This topographic change has a wavelength of ~69 km and an amplitude of ~253 m. This relationship shows that the groove belt was present during the formation of KV, then the surface continued to deform after channel emplacement. The topographically elevated region is radar brighter and has more E/W-orientated fractures. Some of the deformation is present in the channel floor, but most of the floor is radar homogonous. KV turns east then northeast to avoid a more heavily fractured area, which clearly was present during the active flow phase, and in doing so, continues through another topographically elevated region, relatively dating the change as younger than the channel. This

topographic high is radar darker with thin E/W fractures. The eastern terminus of KV lies within Barbale Dorsa, also mapped as a groove belt.

The depth to the mantle (red line) shows crustal thinning towards the east (Figure 71). The dynamic topography (green line) decreases to the east; however, the channel length is too short to interpret the relationship between the dynamic topography and topography due to the resolution.

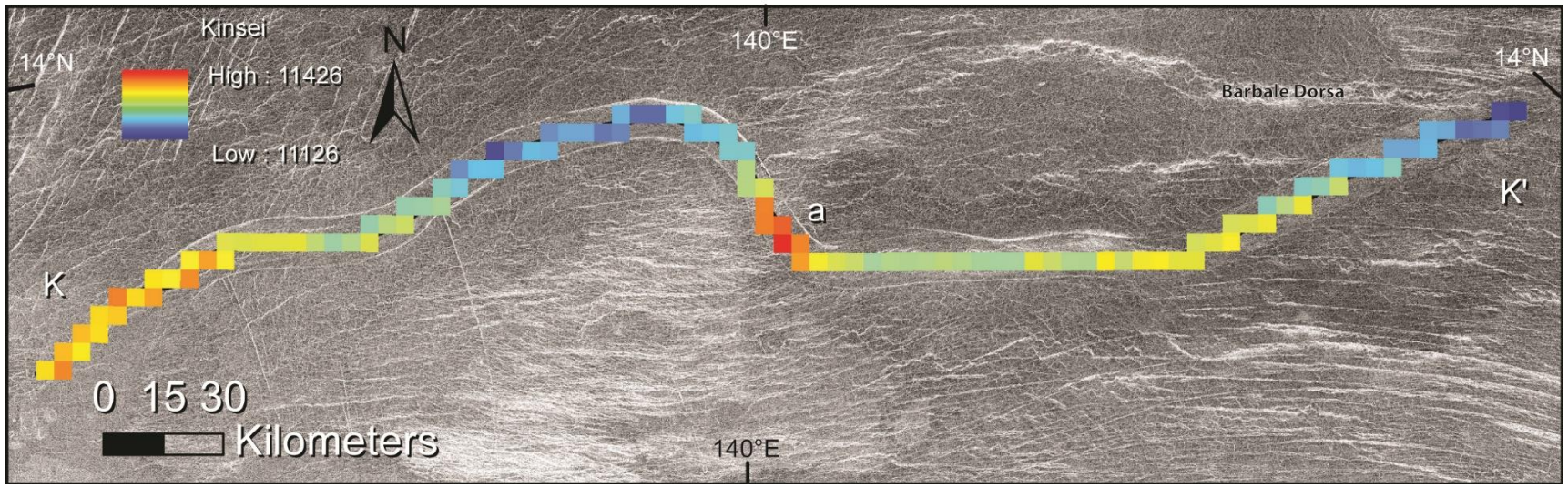

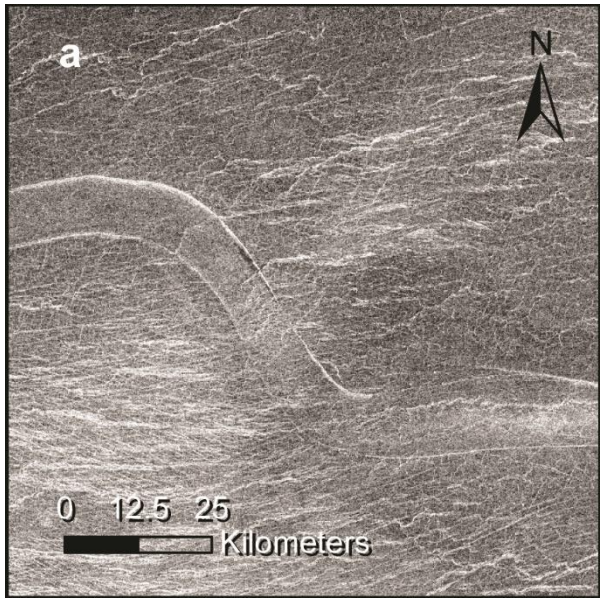

Figure 70: Magellan SAR left-look mosaic is projected to be centered on 140° E, 14° N in an orthographic projection showing Kinsei Vallis. The length is illustrated by a color-coded line indicating elevation, with higher elevation shown in red and lower topography shown in dark blue. (a) KV crosses a topographically elevated region.

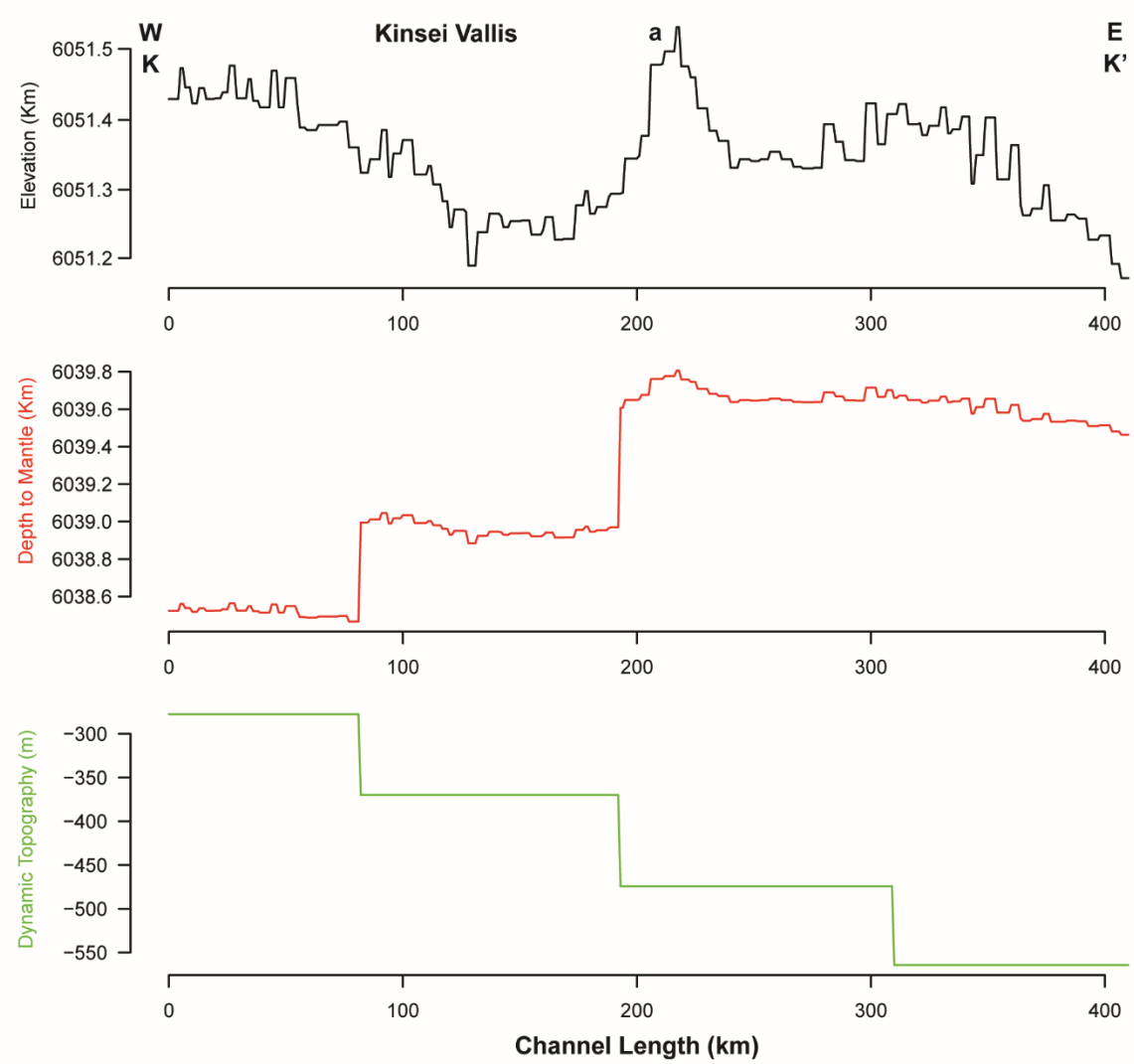

Figure 71: Profile view of topography (black line), depth to the mantle (red line), and dynamic topography (green line) along the flow path of Kinsei Vallis.

.

3.2.30 Tawera Vallis

Tawera Vallis (TV) is present in the left-look Magellan SAR mosaic in one bin from the 10x10 DD grid. After mapping, one anomalous point was removed, leaving a total of 400 vertices. The calculated geodesic length is 404 km, and the offshoots have another 629 km in length. The straight-line distance of the longest segment is 343 km, making the overall sinuosity 1.18.

The closest structures to the north of TV are Kvasha Patera, ~200 km northeast (not on map), and Verdandi Corona, ~590 km to the northwest (not on map). Despite the distance, one of these two could be the source TV rests in a valley about 100 km wide with tesserae on either side (Figure 72). Describing from T to T', the northern terminus of TV lies in a radar brighter, heavily deformed area mapped as a shield plain (psh) (Ivanov & Head, 2011). There is a significant dip in the topography, as seen in Figure 73, near 0 km, but there is no evidence that a topographic change is present, and considering its small nature, I do not consider it for this study. TV turns south and continues into a radar dark and homogonous area mapped as lobate plains (pl). The channel splits, and the small offshoots have a braiding behavior, as seen in Figure 72a. The radar is darker alongside the channel. Continuing south, TV splits again and anastomoses following the curve of the radar dark material and avoiding the shield plain (psh) to the east, meaning the shield plain was present during the channel formation and is relatively older. Two segments continue further than the rest. The west channel is the one used for the topographic profile, length, and other characteristics. The west channel continues into a shield plain, weaving between radar bright features (which must have been present during channel emplacement, Figure 72b) and reaches the southern terminus, which fades out in a radar

homogonous area at the southern terminus. The east side borders the shield plain to the east, dating the shield plain as older than TV, and disappears.

The topographic profile (black line) shows a direct and constant reduction in elevation, so TV could have flowed from north to south, as I describe here (Figure 73). The depth to the mantle (red line) shows crustal thickening to crustal thinning towards the south. The dynamic topography (green line) increases until 200 km, then decreases to the south. The length of the channel is shorter than the spatial block size of dynamic topography, making interpretation impossible.

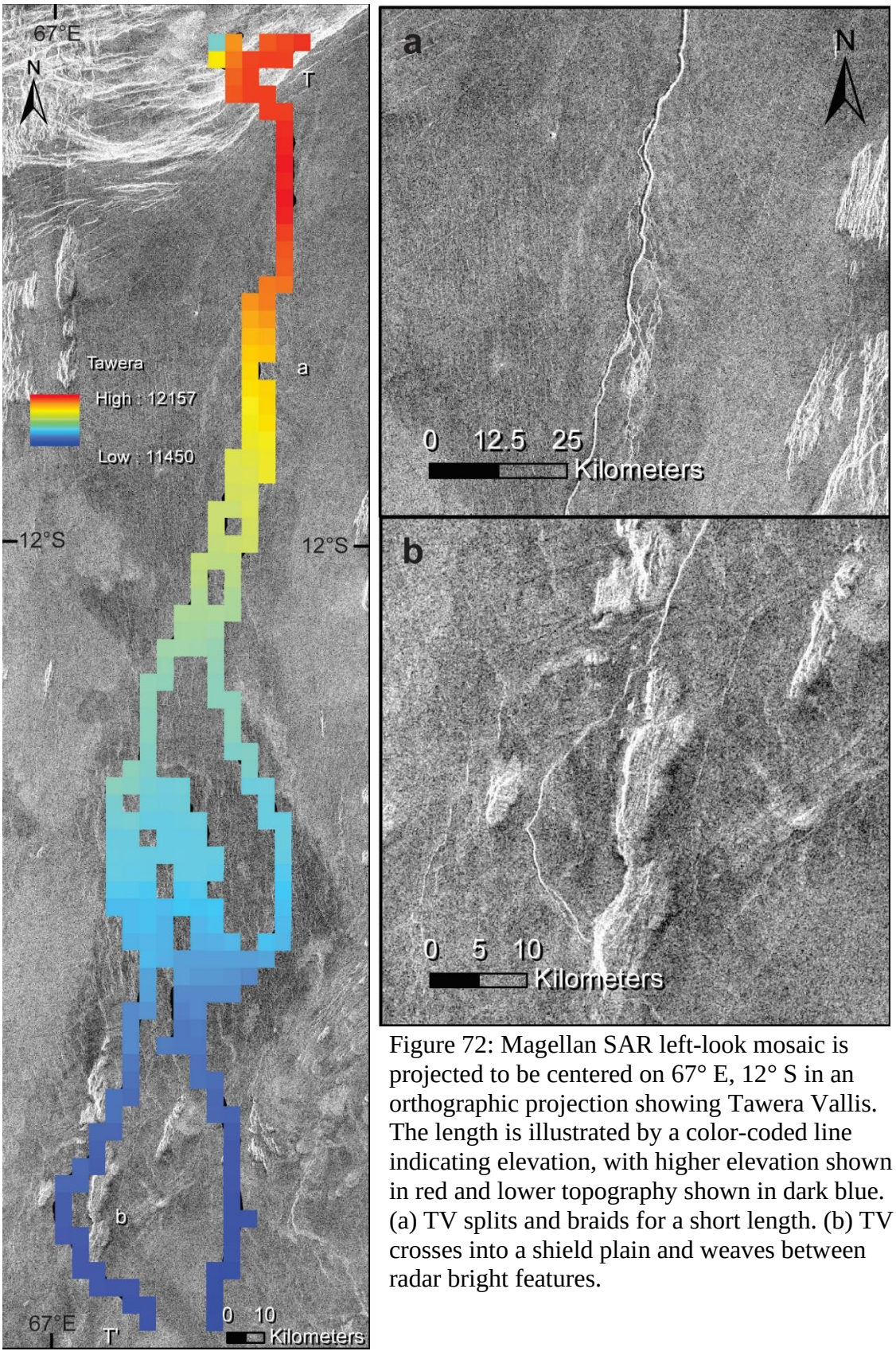

Figure 72: Magellan SAR left-look mosaic is projected to be centered on 67° E, 12° S in an orthographic projection showing Tawera Vallis. The length is illustrated by a color-coded line indicating elevation, with higher elevation shown in red and lower topography shown in dark blue. (a) TV splits and braids for a short length. (b) TV crosses into a shield plain and weaves between radar bright features.

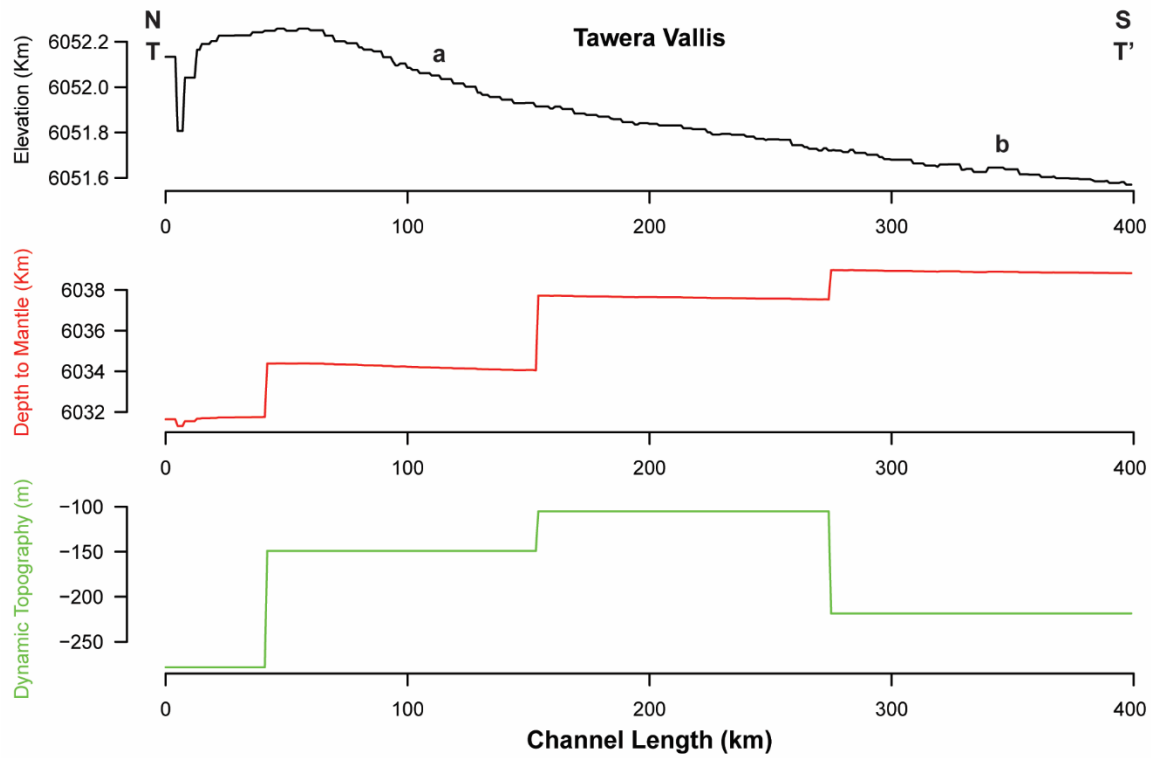

Figure 73: Profile view of topography (black line), depth to the mantle (red line), and dynamic topography (green line) along the flow path of Tawera Vallis.

3.2.31 Dzyzlan Vallis

I mapped Dzyzlan Vallis (DV) following the right-look Magellan SAR mosaic through one 10x10 DD bin. After mapping, I removed one anomalous point, leaving a total of 350 vertices. The geodesic length is 354 km, and the straight-line distance is 181 km, calculating the overall sinuosity to be 1.95.

DV lies within the tesserae between Atlas Regio (not on map) and Thetis Regio (not on map) (Figure 74). To the northeast, Zemina Corona lies ~350 km away with a ~400 km diameter (not on map). The entirety of DV lies within a rift zone (rz), with no interactions with surrounding units (Ivanov & Head, 2011). Describing from D to D', the eastern terminus interacts with the tesserae, temporarily increasing (Figure 74). Moving northwest, the channel curves sinuously with a small divergence into two channels; the west side of the channel is radar bright. DV diverges into two channels again, then curves sharply southwest around an area of tesserae that has NE/SW oriented lineations, shown in Figure 74a. This tessera is relatively older than DV in this relationship. The channel steadily decreases in elevation toward the turning point, then the channel continues southwest and gradually increases in elevation, creating a bowl as seen in the elevation profile in Figure 75. This topographic change has a wavelength of ~316 km and an amplitude of ~2780 m. Thus, the topographic increase is younger than the channel and has deformed the profile. In the profiles, there is a small topographic increase within the topographic low. This change is the difference of three pixels, but the wavelength and amplitude are ~26 km and ~798 m, respectively. There is no associated landform or structure with this topographic change, and it is relatively younger than DV. DV follows

the tesserae, oriented NE/SW briefly before anastomosing sinuously. The channels come back together and reach the western terminus, shown in Figure 74b.

The depth to the mantle (red line) shows constant crustal thickness until ~200 km, then the crust thickens to the west (Figure 75). The dynamic topography (green line) illustrates a general decrease towards the west. Since the length of the channel is shorter than the resolution for the dynamic topography dataset, the relationship with topography cannot be determined.

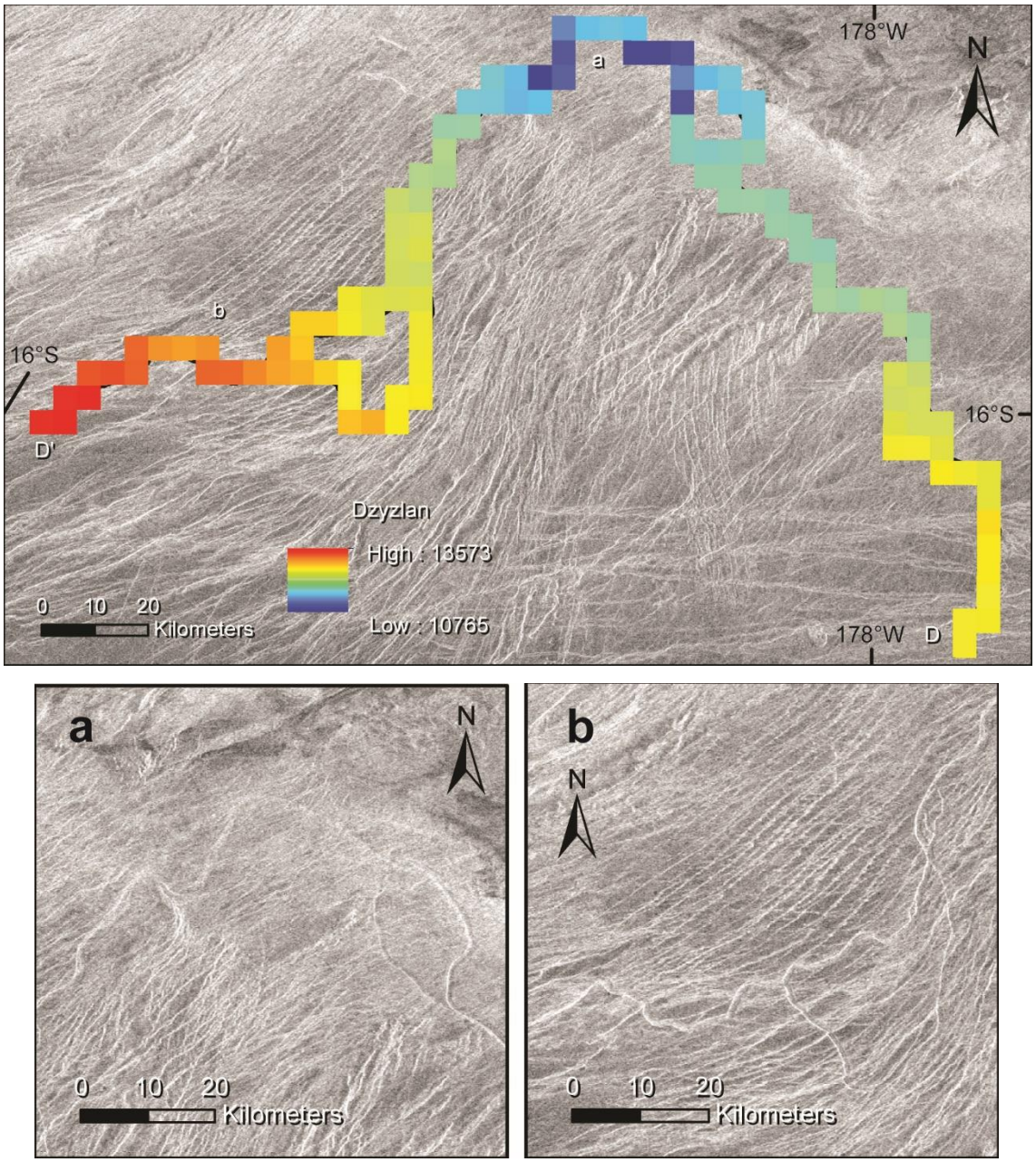

Figure 74: Magellan SAR right-look mosaic is projected to be centered on 179° W, 16° S in an orthographic projection showing Dzyzlan Vallis. The length is illustrated by a color-coded line indicating elevation, with higher elevation shown in red and lower topography shown in dark blue. (a) DV curves around the tesserae. (b) The channels converge end disappear at the western terminus.

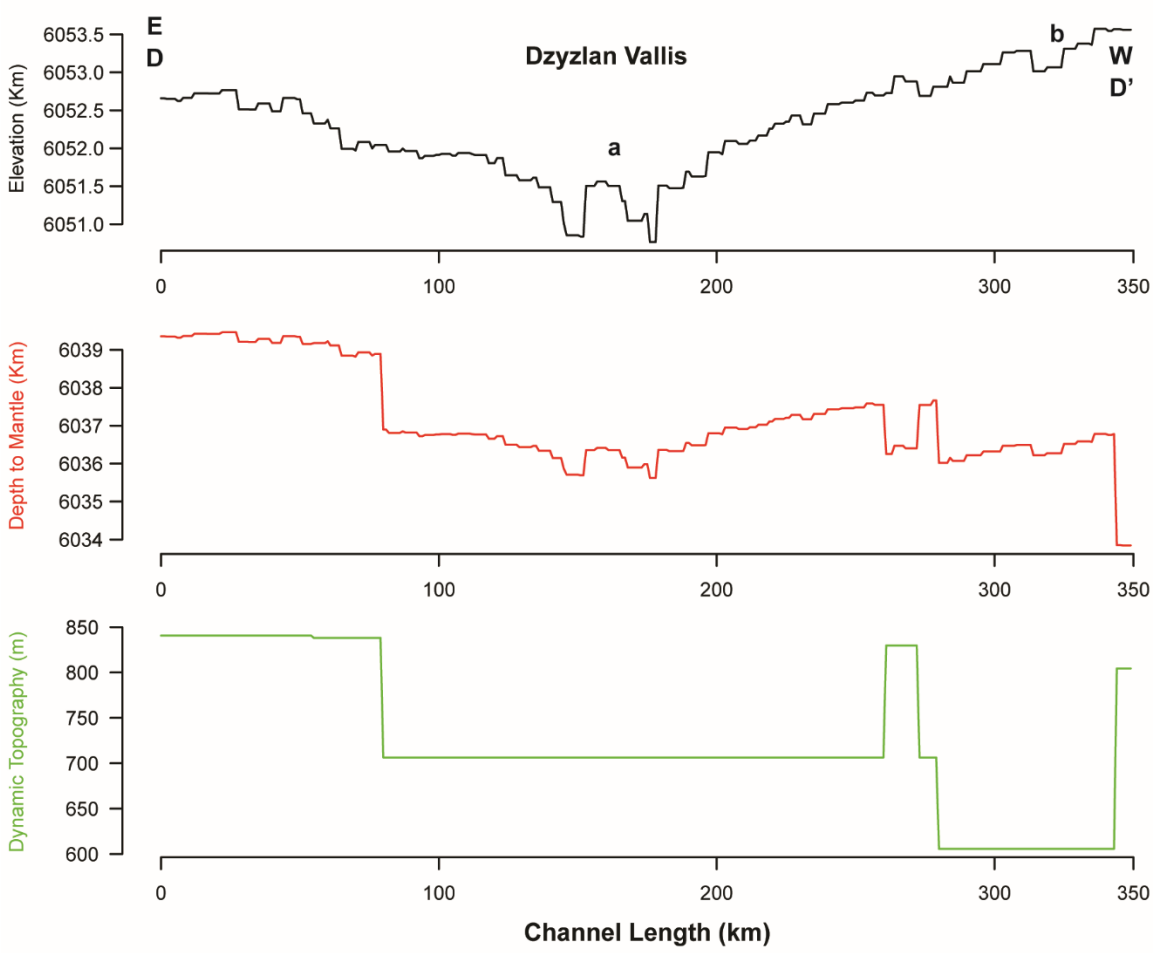

Figure 75: Profile view of topography (black line), depth to the mantle (red line), and dynamic topography (green line) along the flow path of Dzyzlan Vallis.

3.2.32 Apisuahts Vallis

Apisuahts Vallis (AV) is visible within the right-look Magellan SAR mosaic through one bin from our 10x10 DD bin. After mapping, one point was removed, leaving a total of 290 vertices. I calculated the geodesic length to be 293 km and the distance between the endpoints to be 251 km. This results in an overall channel sinuosity of 1.17.

AV is located within the Cocomama Tessera and near Erzulie Mons (not on map), which is ~300 km southwest. Other potential sources are Quetzalpetlatl Corona (not on map) and Boala Corona (not on map), which lie ~600 km from AV. Most of AV is mapped within the lobate plains (pl) that are radar-medium to -dark and featureless while the elevation increases steadily from A to A' with no variation (Ivanov & Head, 2011). Describing from A to A', the eastern terminus is in a radar darker area and gradually becomes visually distinct moving west (Figure 76). The channel is sinuous and briefly splits into two channels before rejoining. West of the rejoining, the channel floor is wider and more distinct. North and south of AV are tesserae, which AV curves around before continuing west. For 30 km, the channel is straight as it enters the area where the tesserae are much closer, then curves sharply for no apparent reason. The lobate plains thin as the tesserae encroach, and AV enters the tesserae unit at its western terminus. This behavior of flowing between the tesserae relatively dates the channel as younger than the tesserae.

The depth to the mantle (red line) shows crustal thickening to the west (Figure 77). The dynamic topography (green line) steadily increases to the west. The length of the channel is shorter than the spatial block size of the dynamic, meaning that the relationship with topography cannot be determined.

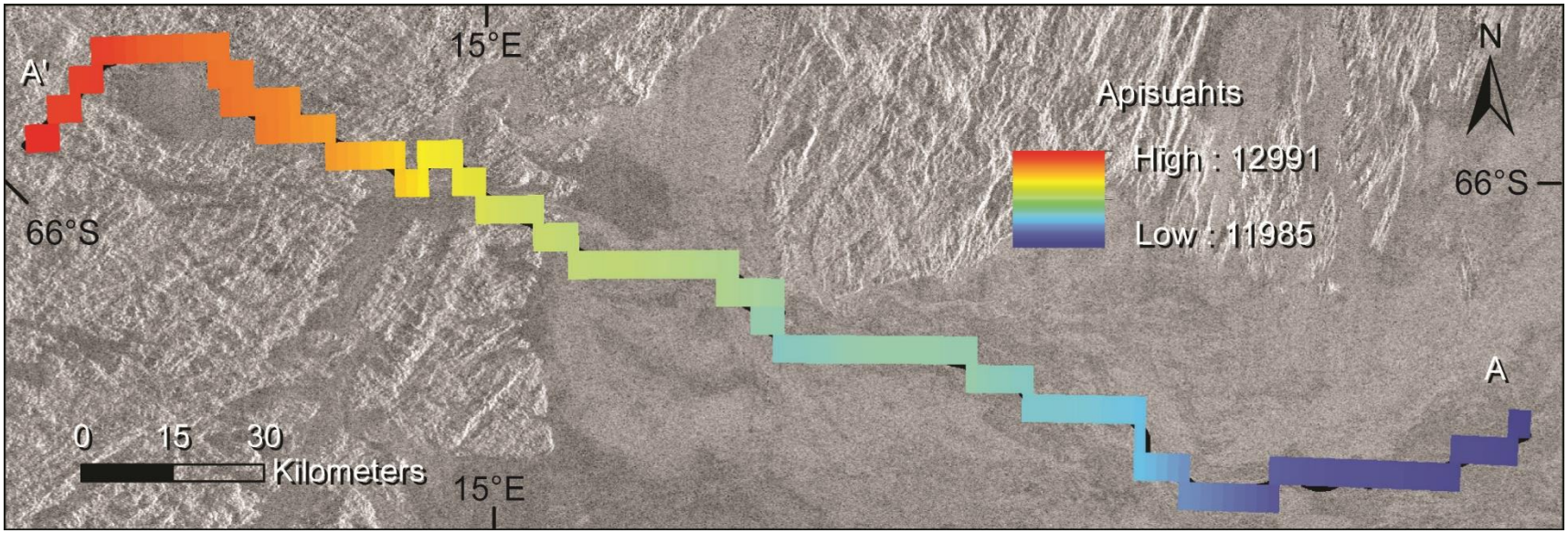

Figure 76: Magellan SAR right-look mosaic is projected to be centered on 16° E, 66° S in an orthographic projection showing Apisuahts Vallis. The length is illustrated by a color-coded line indicating elevation, with higher elevation shown in red and lower topography shown in dark blue.

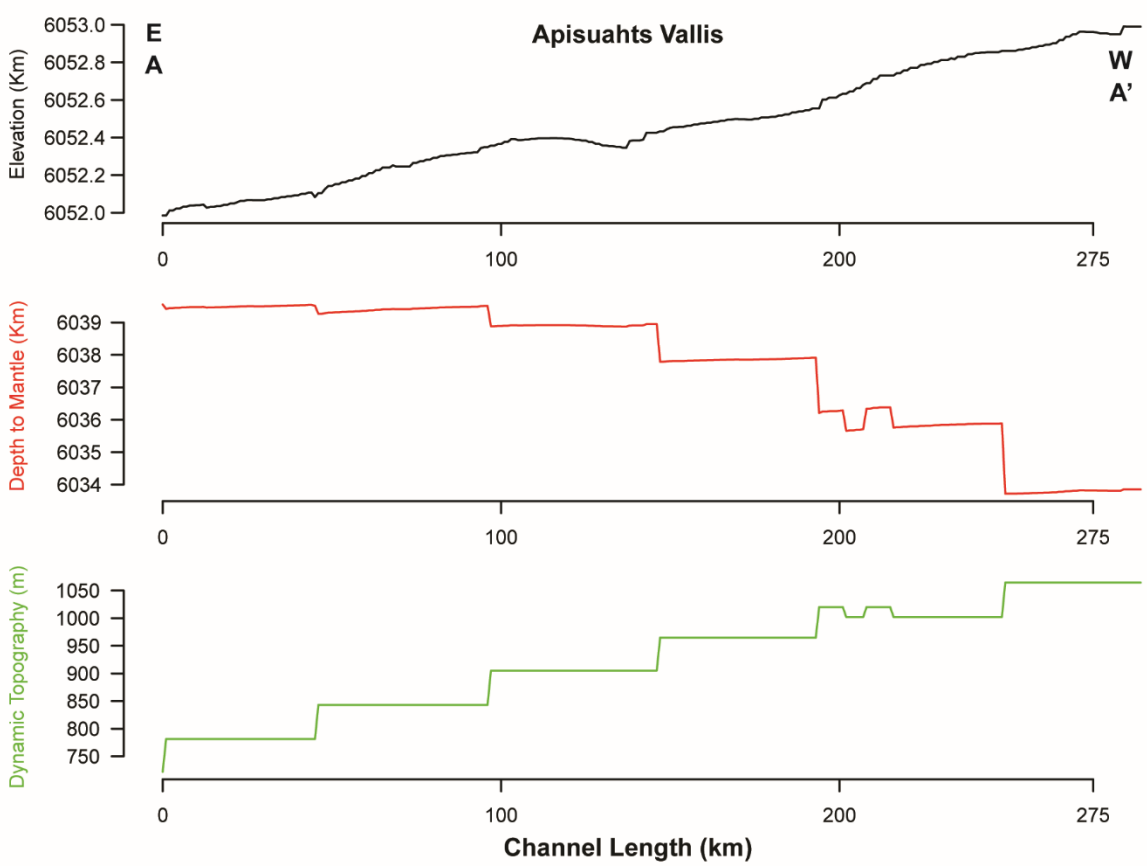

Figure 77: Profile view of topography (black line), depth to the mantle (red line), and dynamic topography (green line) along the flow path of Apisuahts Vallis.

3.2.33 Lunang Vallis

Lunang Vallis (LV) is visible in the left-look Magellan SAR mosaic through two 10x10 DD bins. After mapping, no vertices needed to be removed, resulting in a total of 232 points. From L to L', the geodesic length is 234 km, and the straight-line distance is 200 km, resulting in an overall channel sinuosity of 1.17.

Directly east of LV by ~150 km is Akna Montes (not on map) which extends to the north and south. Otau Corona (not on map) sits ~250 km west of the northwestern terminus of LV. The overall extent of LV lies within a radar dark, featureless regional plain (rp1) and avoids the densely lineated plains (pdl) to the north and south (Ivanov & Head, 2011). From L to L', the topography decreases steadily except for a small portion mentioned below. Unfortunately, the middle section, about ~40 km long, is not covered by the topography dataset. This channel is still included for its interaction with the surrounding terrain.

Describing from L to L', the eastern terminus of LV pools (Figure 78). Continuing west, the channel walls are radar bright, and it curves around the deformation of the lineated plains, shown in Figure 79a, which relatively dates the channel as younger. The densely lineated plains grow closer together to the west, and only one channel wall becomes visible, still curving in between the deformation. This location is where the topography dataset gap is located. The west side of the data set shows LV continuing through a topographically elevated region that is not associated with a landform or structure, shown in Figure 79b. This relationship reveals LV to be older than the topographic change. Curving northwest, LV continues out past the densely lineated plains into a radar dark homogenous plain with a radar bright lava flow that is mapped as

a lobate plain (pl). This plain appears to be an extension of the flow from Otau Corona, shown in Figure 79c. By these relationships, LV potentially originates from Otau Corona in the west and flows east, terminating in a small pool of lava. The flow direction would be the opposite of how the channel is described above. The elevation along the channel is potentially deformed and increases downflow caused by the mountain range to the east. This relatively dates Akna Montes as younger than Otau Corona and LV.

The depth to the mantle (red line) reveals crustal thinning to the northwest (Figure 80). The dynamic topography (green line) decreases toward the northwest. The length of the channel is shorter than the spatial block size of the dynamic topography, making interpretation impossible.

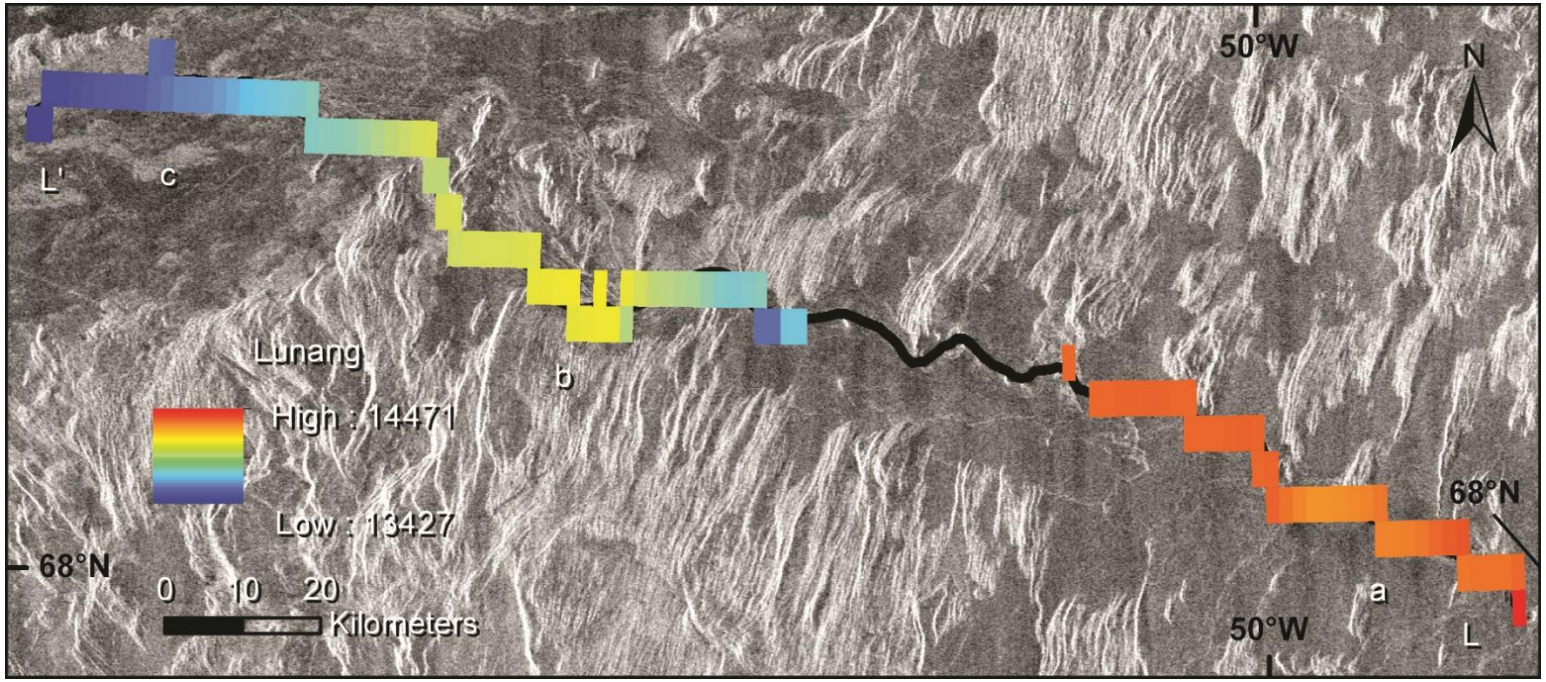

Figure 78: Magellan SAR left-look mosaic is projected to be centered at 51° W, 68° N in an orthographic projection showing Lunang Vallis. The length is illustrated by a color-coded line indicating elevation, with higher elevation shown in red and lower topography shown in dark blue.

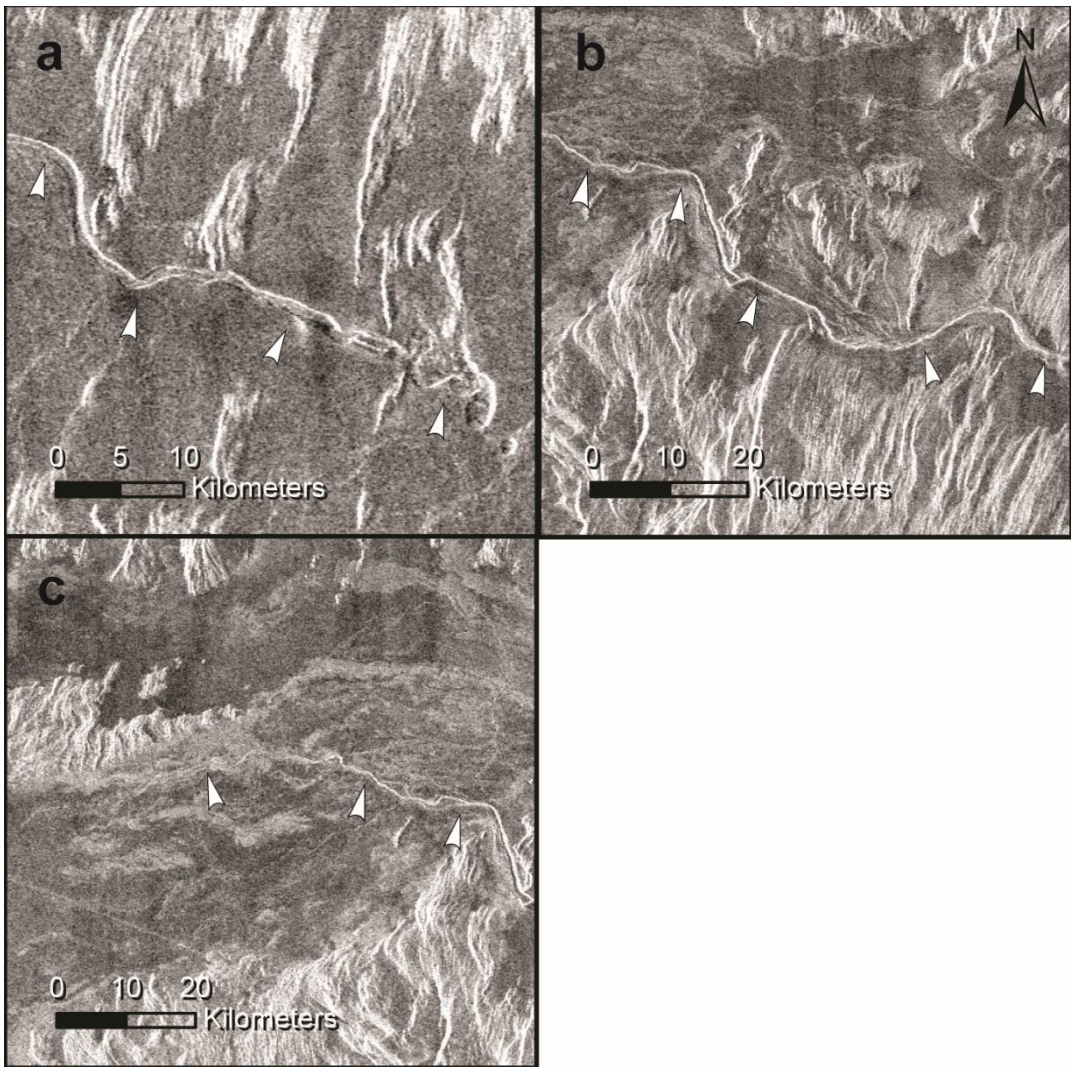

Figure 79: Magellan SAR left-look mosaics are projected to be centered at 51° W, 68° N in an orthographic projection showing close up sections of Lunang Vallis. White arrows point out the channel. (a) LV curves around the lineated plain. (b) LV passes over a topographically elevated region that is indistinguishable from the surrounding radar. (c).LV enters a radar bright lava flow.

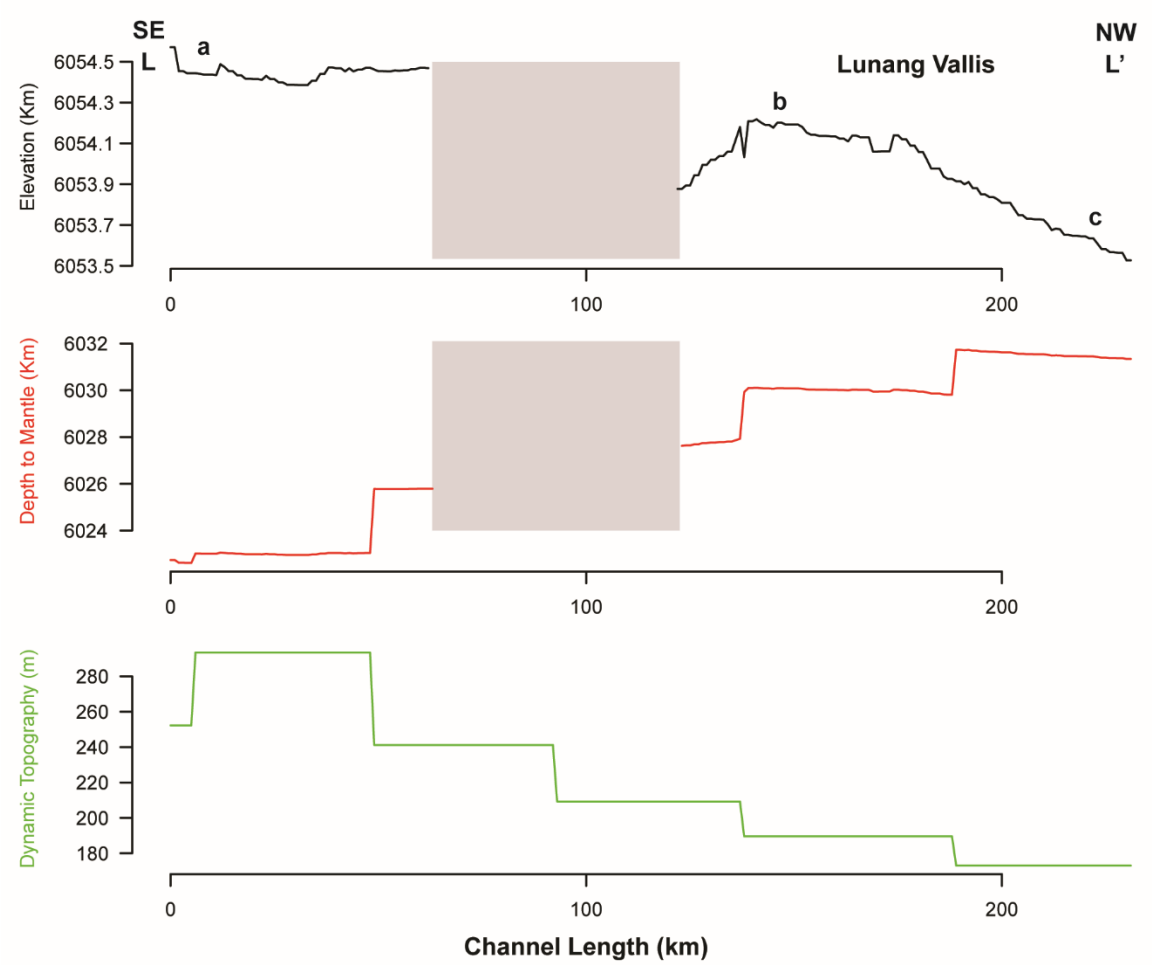

Figure 80: Profile view of topography (black line), depth to the mantle (red line), and dynamic topography (green line) along the flow path of Lunang Vallis. Grey boxes show where data gore in the topography and, by extension, the crustal thickness.

3.3 Future Work

Future missions are needed to improve the topography and gravity datasets in order to understand more fully the relationships I have described here. This work is limited by the resolution from the 30-year-old Magellan data, and our scientific capabilities have advanced significantly since the early 90s. Visiting Venus with the VERITAS orbiter and reimaging the surface with InSAR will answer whether volcanism is active and what geophysical processes evolve the planet while revealing so many features that are invisible to us now. This orbiter will result in new radar mosaics, DEMS, and gravity anomalies that will result in calculated crustal thickness and dynamic topography datasets that can be used to improve this study.

Future work to prepare for the possibility of new data involves mapping the rest of the channels with the same systematic method to complete the current global data set. With the improved data, the geologic relationships that could not be determined will be reevaluated for more accurate relative dating, and the shorter channels will be considered for the dynamic topography. Sources for each channel might become apparent, and entirely different canali-like lava channels might become visible and mappable.

CHAPTER 4

DISCUSSION

4.1 Topographic changes on Venus

I have collected geological and topographic/geophysical observations along 33 Venusian lava channels, which are synthesized between Tables 1 and 2. Of those, 28 channels have an elevation profile that shows that the topography was substantially modified after the lava channel was emplaced. The five that did not show topographic undulations are Uottakh-sulus, Lo Shen, Tawera, Apisuahts, and Lunang Valles. Of these, Lo Shen and Lunang Valles have unknown flow directions, so the topography may or may not represent the downhill flow paths. Figure 81 shows the channels with clear topographic undulations along their length, colored grey. The topographic changes are widespread and occur on a global scale. Even though the topographic changes are global, the channels are only located within the lowland lava plains. This means that topographic changes affected lava plains globally, but it is unknown to what extent other terrain types were affected by topographic changes. In the case of tessera terrain, Apisuahts, Lo Shen, and Tawera Valles show no topographic changes near the tesserae they interact with, while the tesserae around Dzyzlan Vallis are clearly deformed. The tesserae around Banumbirr, Kūmsong, L3usaber, and Jutrzenka Valles do not have clear relationships with the channels, and their state of topographic deformation is not determinable.

The relative timing of the topographic changes with surrounding geologic phenomena is different for each channel and also varies along the length. Several

channels, including Ikhwezi, Kūmsong, and Uottakh-sulus Valles, curve to avoid topographic highs, indicating that the topographic highs were established before channel emplacement (Table 1). For other areas, channels curve to avoid topographic highs but also show a marked undulation that indicates that a topographic high existed prior to channel emplacement but then continued to deform after channel emplacement. Examples of this type of relationship are found along Citlalpul, Gendenwitha, Morongo, and Bennu Valles. Yet other channels show topographic undulation with no change in the flow path, including those seen for Laidamlulum, Sinann, Bayara, and Merak Valles, indicating that topographic changes occurred after channel emplacement was complete.

The topography along the length of the channels can be affected by a multitude of processes. As mentioned previously, long-wavelength undulations are caused by regional uplift or subsidence from subsurface processes like volcanism and mantle convection. Our study agrees with the previous calculations along the length of Baltis Vallis, with a change of 1177 m over 2216 km (Table 2). However, several channels have elevation profiles that reveal interactions with dynamic topography at somewhat shorter wavelengths. For example, Laidamlulum, Ikhwezi, Kallistos, Lusaber, Morongo, and Ahsabkab Valles show topographic undulations varying from 620 to 1600 km wavelengths with amplitudes ranging from 240 to 1100 m. These long-wavelength changes correlate with dynamic topography. Short-wavelength topographic undulations are found to be caused by local structures such as individual faults or fault zones (groove belts, dorsa, tesserae, wrinkle ridges), shield volcanoes, and craters. These wavelengths and amplitudes vary greatly, as seen in Table 1, averaging to 171 km and 359 m. These

observations are only the minimum observed change; greater values undoubtedly exist but are not constrained by the lava channels.

The crustal thickness and its relationship to topographic changes also vary greatly between the different channels. Of the 19 channels that were long enough to allow meaningful comparisons of crustal thickness and topography, 12 showed a correlation between the crustal thickness and topography along parts or the entire length of the channels (Table 1). Crustal thickness was found to be anti-correlated with topographic resulting in crustal thinning (nine instances) or thickening (12 instances) along the channels. Crustal thickening was observed to predominantly occur at the channel termini, and crustal thinning occurred more frequently near the center of the flow path, e.g., Ikhwezi, Sholpan, Lusaber, and Austrina Valles.

Name	Length	Length w/ cvr (km)	Sinuosity	Prev. Rank	Harmonic	Cal. Wavelength (km)	Cal. Amplitude (m)	Primary Orientation	Topographic Changes	Number Changes	Elevation at A, A' (m)	Constant Crustal Thickness	Crustal Thickening	Crustal Thinning	Data Points
Baltis	6749.59	7431.44	1.83	1	y	~200-400	~200-400	N/S	Yes	Many	11547, 11947	x	x	x	6520
Citlalpul	3026.86	3177.39	1.36	2	y	333	376	NE/SW	Yes	At least 7	11205, 11207		x	x	2989
Laidamlulum	2249.79	2502.76	1.37	3	n	268	393	N/S	Yes	At least 2	11315, 10946	x	x		2211
Ikhwezi	1836.10	1919.25	1.91	4	n	-	-	N/S	Yes	At least 2	11799, 11263		x	x	1809
Gendenwitha	1286.05	1286.05	1.45	7	y	840, 274, 118	802, 242, 400	NE/SW	Yes	At least 3	10666, 10920	x			1262
Kallistos	1254.23	1254.23	1.92	8	y	-	-	E/W	Yes	At least 1	12149, 11954	x		x	1233
Sholpan	1080.11	1112.97	1.09	19	y	239, 241	189, 293	NW/SE	Yes	At least 1	11124, 10867		x	x	1049
Xulab	1079.08	1079.08	2.05	9	y, n	94, 375	202, 347	E/W	Yes	At least 5	10954, 10996	x	x		1067
Jutrzenka	864.21	1032.52	1.23	6	y	184, 222, 91	811, 566, 228	NW/SE	Yes	At least 5	11173, 10766	x			877
Lusaber	906.91	906.91	1.36	22	y	112	146	E/W	Yes	At least 1	11401, 11547		x	x	897
Sinann	856.05	856.05	1.28	24	y	262	230	E/W	Yes	At least 2	11287, 11567	x			846
Morongo (1)	811.38	826.25	1.27	16	y	-	-	NW/SE	Yes	At least 1	13071, 12939		x	x	797
Koidutäht	810.56	810.56	1.11	13	n	246	307	N/S	Yes	At least 2	11042, 11509		x		801
Uottakh-sulus	619.61	765.44	1.15	5	-	-	-	E/W	No	-	12195, 10985	x			611
Tan-yondozo	760.44	760.44	1.12	10	y	60, 151, 129	105, 91, 171	NE/SW	Yes	At least 3	10965, 10859	x	x		840
Bennu	752.70	752.70	1.23	11	n	212	283	NE/SW	Yes	At least 2	10655, 10969	x	x		741
Ahsabkab	670.48	670.48	1.46	12	n	-	-	N/S	Yes	At least 1	10939, 11009	x		x	663
Austrina	589.90	589.90	1.15	18	n	138	321	E/W	Yes	At least 1	11598, 11094		x	x	580
Bayara	580.99	580.99	1.53	21	n	65, 54	279, 264	NE/SW	Yes	At least 2	11547, 10763	x			573

Name	Length	Length w/ cvr (km)	Sinuosity	Prev. Rank	Harmonic	Cal. Wavelength (km)	Cal. Amplitude (m)	Primary Orientation	Topographic Changes	Number Changes	Elevation at A, A' (m)	Constant Crustal Thickness	Crustal Thickening	Crustal Thinning	Data Points
Utrenitsa	565.52	565.52	1.40	15	y	161	312	N/S	Yes	At least 1	10733, 10913	Too short	Too short	Too short	555
Dilbat	482.09	510.63	1.11	25	y	157, 142	365, 232	N/S	Yes	At least 2	10910, 10865	Too short	Too short	Too short	476
Kūmsong	493.73	493.73	1.26	14	y	66, 162, 115	100, 157, 275	N/S	Yes	At least 2	10739, 11042	Too short	Too short	Too short	486
Nepra	443.3	489.85	1.31	29	n	114, 188	470, 365	NW/SE	Yes	At least 2	10904, 10874	Too short	Too short	Too short	432
Banumbirr	478.72	478.72	1.22	26	n	207, 141	244, 311	NW/SE	Yes	At least 2	11183, 11102	Too short	Too short	Too short	472
Fetu-ao	392.99	462.65	1.15	27	y	178	387	NW/SE	Yes	At least 2	10830, 11200	Too short	Too short	Too short	389
Lo Shen	427.85	427.85	1.56	32	-	-	-	N/S	Unknown	-	13436, 14841	Too short	Too short	Too short	424
Kinsei	417.37	417.37	1.10	28	n	69	253	E/W	Yes	At least 1	11340, 11126	Too short	Too short	Too short	411
Tawera	403.62	403.62	1.18	23	-	-	-	N/S	No	-	12033, 11470	Too short	Too short	Too short	400
Vesper	376.92	376.92	1.21	17	y	252	184	E/W	Yes	At least 1	10931, 11009	Too short	Too short	Too short	374
Dzyzlan	353.48	353.48	1.95	30	y	316, 26	2780, 798	E/W	Yes	At least 1	12659, 13561	Too short	Too short	Too short	350
Morongo (2)	304.52	304.52	1.21	NA	y	80	87	NE/SW	Yes	2?	12960, 13255	Too short	Too short	Too short	300
Apisuahts	292.58	292.58	1.17	20	-	-	-	E/W	No	-	11985, 12990	Too short	Too short	Too short	290
Merak	269.15	269.15	1.06	33	y	149	144	NE/SW	Yes	At least 1	11391, 11309	Too short	Too short	Too short	266
Lunang	233.96	233.96	1.17	31	-	-	-	E/W	Unknown	-	14471, 13427	Too short	Too short	Too short	232

Table 1: Synthesis of the data collected from the 33 channels. "Length w/ cvr" means the geodesic length with the added straight-line distance. "Prev. Ranks" refers to the order in which each channel was ranked, with one being the longest. The calculated wavelengths and amplitudes are the short-wavelength structures.

Name	Cal. Wavelength (km)	Cal. Amplitude (m)	Uplift	Subsidence	Unidentified Change	Dyn. Topo. Young	Dyn. Topo. Only	Structure Youngest
Baltis	2216	1177	x	x	x	x	x	
Citlalpul	-	-		x	x	x		
Laidamlulum	622	577		x		x		Dorsa
Ikhwezi	1691	1127		x		x	x	
Gendenwitha	840?	802?		x	x			
Kallistos	666	439	x			x	x	Dorsa
Sholpan	-	-		x	x	x	x	
Xulab	341	347		x	x			
Jutrzenka	-	-		x				Dorsa, ridge plain
Lusaber	792	362		x	x	x	x	
Sinann	-	-		x		x		pdl, shield vol.
Morongo (1)	744	390	x			x	x	
Koidutäht	271	277		x	x			Shield plain
Uottakh-sulus	-	-	x	x		x	x	
Tan-yondozo	-	-		x		x	x	
Bennu	-	-		x	x			Shield vol?
Ahsabkab	650	242		x		x	x	
Austrina	-	-		x		x		Ridge
Bayara	-	-	x			x		Dorsa, Corona

Table 2: Observations from the dynamic topography dataset. "Dyn. Topo. Young" are the channels that have elevation profiles that mimic the trend of the dynamic topography in part or completely. The distinction between them is made in the "Dyn. Topo. Only", where only dynamic topography changes are visible, and "Structure Youngest", in which channels that show other topographic changes that seem younger than the dynamic topography are listed. The wavelength and amplitudes are those associated with changes that follow the dynamic topography.

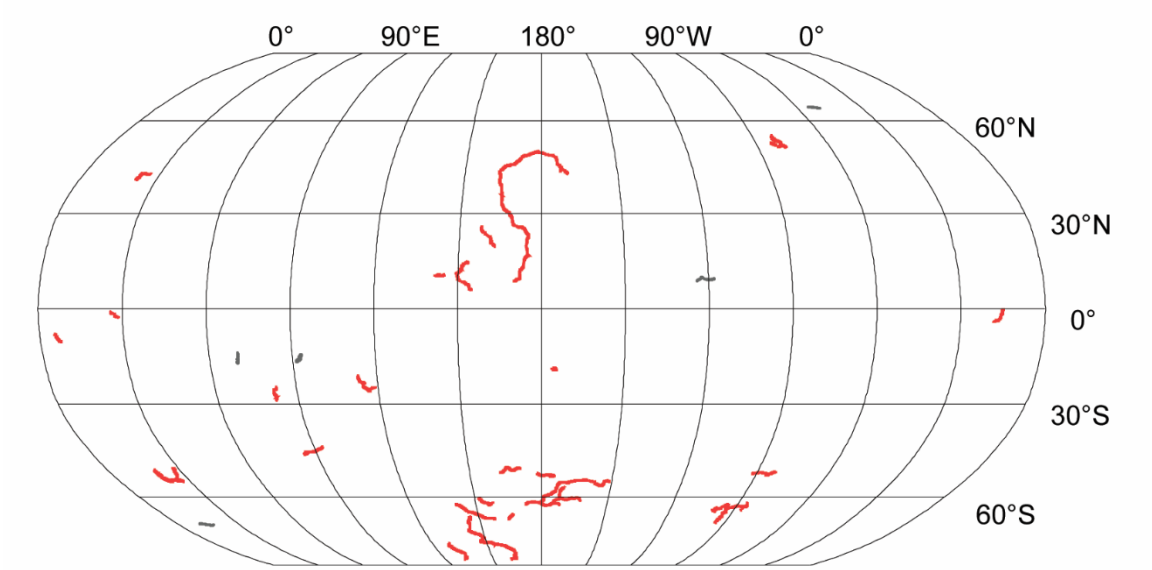

Figure 81: Global map of channels mapped and considered for this study. Channels colored in red have topographic undulations, while the five marked in grey do not or are undetermined. The map is projected to be centered at 180°, 0° in a Robinson projection.

4.2 Dynamic Topography

Out of the 19 lava channels that were long enough to allow meaningful comparisons of dynamic topography with observed topography, 14 of them have an elevation profile that correlates fully or in large parts with the dynamic topography (Table 2). Five channels that did not show a conclusive relationship between observed and dynamic topography are Gendenwitha, Xulab, Jutrzenka, Koidutäht, and Bennu Valles. When the topographic profile shows the same trend as the dynamic topography, this means that the dynamic topography is preserved at the surface and has not been overwritten by other deforming processes. Since dynamic topography is a direct measure of mantle convection, dynamic topography is confirmed by geologic observation to show that topographic undulations can be tied to mantle convection being responsible for the topography. Mantle convection is the method that heat transfers from the core to the surface and may still be active.

The geographic distributions of detected dynamic topography are shown in Figure 82. The map shows that the topographic undulations tied to dynamic topography are found globally. Nine of the channels that indicate the presence of dynamic topography show that topographic change along the channel is the youngest phenomenon (Figure 82, purple lines; Table 2). In the cases where dynamic topography is not detected to be the youngest phenomenon, short-wavelength topographic changes were caused by tectonic or volcanic landforms, such as dorsa, ridge plains, shield volcanoes or shield plains, and coronae. From the dataset, positive values indicate mantle upwelling, and negative values denote mantle downwelling, which is applied to the channels as uplift (five channels) and subsidence (16 channels), respectively.

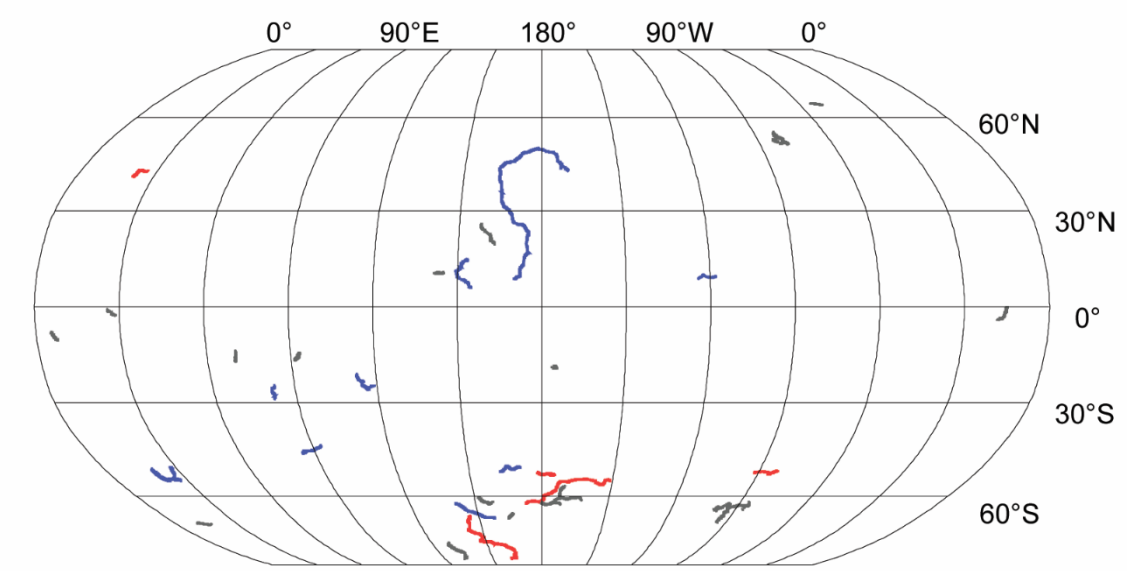

Figure 82: Global map of channels mapped and considered for this study. Channels colored in blue show dynamic topography as the youngest process; red channels have an elevation profile mostly or fully matching the dynamic topography but not as the youngest, while those marked in grey do not or are undetermined. The map is projected to be centered at 180°, 0° in a Robinson projection.

CHAPTER 5

CONCLUSIONS

Our understanding of the surface of Venus and its internal processes is still extremely limited because of the poor resolution and incompleteness of the datasets currently available. The tectonic history of Venus is heavily debated because of the apparent lack of plate tectonics and the surface geology comprised of 80% volcanic terrain. One of the volcanic features on Venus are long lava channels that allowed me to constrain the tectonic motions altering the topography on short and long wavelengths.

To do this, I used the data available to systematically map 33 lava channels using a grid with defined centers for reprojection that guaranteed that each channel is mapped no farther than $5\sqrt{2}$ decimal degrees from the center of projection. This method reduces the distortion of the length and angles, creating an accurate trace of each channel. From each line that maps the path of a channel, I extracted topography, crustal thickness, and dynamic topography values. I also cataloged the length, sinuosity, primary orientation, and geological phenomena to describe these channels.

From this research, I found that 28 of the 33 lava channels have an elevation profile that shows alteration to their respective flow paths in the form of topographic changes that caused the presumably original downhill flow path to show an undulatory topography. The temporal relationship between the channels and their topographic undulations was unique to each channel, with topographic changes detected to have taken place during and after the channel emplacement. Short-wavelength topographic changes

are found to be caused by faults and fault systems, coronae, volcanoes, and craters. For several channels, the long-wavelength topography correlated with dynamic topography, with wavelengths ranging from 620 km to 1600 km and amplitudes ranging from 242 m to 1177 m. Since dynamic topography was not overwritten by other deformation and the lava channels are one of the youngest structures through geologic descriptions, the dynamic topography is then one of the youngest deformed processes to affect the surface, as seen along the channels. Dynamic topography is the result of mantle convection, and thus mantle convection is geologically recent and very likely still active today.

REFERENCES

Airey, M. W., Mather, T. A., Pyle, D. M., & Ghail, R. C. (2017). The distribution of volcanism in the Beta-Atla-Themis region of Venus: Its relationship to rifting and implications for global tectonic regimes. *Journal of Geophysical Research: Planets*, *122*(8), 1626-1649. https://doi.org/https://doi.org/10.1002/2016JE005205

Baker, V. R., Komatsu, G., Gulick, V. C., & Parker, T. J. (1997). Channels and Valleys. In S. W. Bougher, D. M. Hunten, & R. J. Phillips (Eds.), *Venus II: Geology, Geophysics, Atmosphere, and Solar Wind Environment* (pp. 757-793). University of Arizona Press.

Baker, V. R., Komatsu, G., Parker, T. J., Gulick, V. C., Kargel, J. S., & Lewis, J. S. (1992). Channels and valleys on Venus: Preliminary analysis of Magellan data. *Journal of Geophysical Research*, *97*(E8), 13,421-413,444. https://doi.org/10.1029/92je00927

Baloga, S., Spudis, P. D., & Guest, J. E. (1995). The dynamics of rapidly emplaced terrestrial lava flows and implications for planetary volcanism. *Journal of Geophysical Research: Solid Earth*, *100*(B12), 24509-24519. https://doi.org/https://doi.org/10.1029/95JB02844

Banerdt, W. B., McGill, G. E., & Zuber, M. T. (1997). Plains tectonics on Venus. In S. W. Bougher, D. M. Hunten, & R. J. Phillips (Eds.), *Venus II: Geology, Geophysics, Atmostphere, and Solar Wind Environment* (pp. 901-930). University of Arizona Press.

Basilevsky, A. T., & Head, J. W. (1995). *Stratigraphic studies in the area of Baltis Vallis, Venus* Lunar and Planetary Science Conference XXVI, https://articles.adsabs.harvard.edu//full/1995LPI....26...81B/0000081.000.html

Basilevsky, A. T., & Head, J. W. (1996). Evidence for rapid and widespread emplacement of volcanic plains on Venus: Stratigraphic studies in the Baltis Vallis Region. *Geophysical Research Letters*, *23*(12), 1497-1500. https://doi.org/10.1029/96gl00975

Basilevsky, A. T., & Head, J. W. (2003). The surface of Venus. *Reports on Progress in Physics*(66), 1699-1734. https://doi.org/10.1088/0034-4885/66/10/R04

Bindschadler, D. L., Schubert, G., & Kaula, W. M. (1992). Coldspots and hotspots: Global tectonics and mantle dynamics of Venus. *Journal of Geophysical Research*, *97*(E8), 13495. https://doi.org/10.1029/92je01165

Borrelli, M. E., O'Rourke, J. G., Smrekar, S. E., & Ostberg, C. M. (2021). A Global Survey of Lithospheric Flexure at Steep-Sided Domical Volcanoes on Venus Reveals Intermediate Elastic Thicknesses. *Journal of Geophysical Research: Planets*, *126*(7), e2020JE006756. https://doi.org/https://doi.org/10.1029/2020JE006756

Bray, V. J., Bussey, D. B. J., Ghail, R. C., Jones, A. P., & Pickering, K. T. (2007). Meander geometry of Venusian canali: Constraints on flow regime and formation time. *Journal of Geophysical Research: Planets*, *112*(E4). https://doi.org/https://doi.org/10.1029/2006JE002785

Bromiley, G. D., & Law, S. (2020). Eruption of crystal mush and the formation of steep-sided volcanic domes on Venus: Insight from picritic bodies near Marki, Cyprus. *Icarus*, *337*, 113467. https://doi.org/10.1016/j.icarus.2019.113467

Brossier, J., Gilmore, M. S., & Toner, K. (2020). Low radar emissivity signatures on Venus volcanoes and coronae: New insights on relative composition and age. *Icarus*, *343*. https://doi.org/https://doi.org/10.1016/j.icarus.2020.113693

Brossier, J., Gilmore, M. S., Toner, K., & Stein, A. J. (2021). Distinct Mineralogy and Age of Individual Lava Flows in Atla Regio, Venus Derived From Magellan Radar Emissivity. *Journal of Geophysical Research: Planets*, *126*(3). https://doi.org/10.1029/2020je006722

Bussey, D. B. J., Sørensen, S.-A., & Guest, J. E. (1995). Factors influencing the capability of lava to erode its substrate: Application to Venus. *Journal of Geophysical Research: Planets*, *100*(E8), 16941-16948. https://doi.org/https://doi.org/10.1029/95JE00894

Byrne, P. K., Ghail, R. C., Şengör, A. M. C., James, P. B., Klimczak, C., & Solomon, S. C. (2021). A globally fragmented and mobile lithosphere on Venus. *Proceedings of the National Academy of Sciences*, *118*(26), e2025919118. https://doi.org/10.1073/pnas.2025919118

Byrne, P. K., Klimczak, C., Williams, D. A., Hurwitz, D. M., Solomon, S. C., Head, J. W., Preusker, F., & Oberst, J. (2013). An assemblage of lava flow features on Mercury. *Journal of Geophysical Research: Planets*, *118*(6), 1303-1322. https://doi.org/10.1002/jgre.20052

Conrad, J. W., & Nimmo, F. (2022). *Determining characteristic morphological wavelengths for Venus using Baltis Vallis*. WileyNOT PEER REVIEW. https://dx.doi.org/10.1002/essoar.10512401.1

Conrad, J. W., Nimmo, F., & Black, B. A. (2021). *Uplift record of Baltis Vallis, Venus* Lunar Planetary Science 52nd, https://www.hou.usra.edu/meetings/lpsc2021/pdf/1636.pdf

Crumpler, L. S., Aubele, J. C., Senske, D. A., Keddie, S. T., Magee, K. P., & Head, J. W. (1997). Volcanoes and centers of volcanism on Venus. In S. W. Bougher, D. M. Hunten, & R. J. Phillips (Eds.), *Venus II: Geology, Geophysics, Atmosphere, and Solar Wind Environment* (pp. 697-756). University of Arizona Press.

Esposito, L. W., Copley, M., Eckert, R., Gates, L., Stewart, A. I. F., & Worden, H. (1988). Sulfur dioxide at the Venus cloud tops, 1978–1986. *Journal of Geophysical Research*, *93*(D5), 5267. https://doi.org/10.1029/jd093id05p05267

Filiberto, J., Trang, D., Treiman, A., & Gilmore, M. S. (2020). Present-day volcanism on Venus as evidenced from weathering rates of olivine. *Science Advances*, *6*(1), eaax7445. https://doi.org/doi:10.1126/sciadv.aax7445

Ford, J. P., Plaut, J. J., Weitz, C. M., Farr, T. G., Senske, D. A., Stofan, E. R., Michaels, G., & Parker, T. J. (1993). *Guide to Magellan Image Interpretation* (Vol. 93-24). National Aeronautics and Space Administration, Jet Propulsion Laboratory. https://books.google.com/books?hl=en&lr=&id=cWbmaV2WZtoC&oi=fnd&pg=PA1&dq=guide+to+magellan+image+interpretation&ots=SxWmtDBX3W&sig=btRxQefNpN4KyaY2GVszBCGHISo#v=onepage&q&f=false

Gilmore, M., Treiman, A., Helbert, J., & Smrekar, S. (2017). Venus Surface Composition Constrained by Observation and Experiment. *Space Science Reviews, 212*(3-4), 1511-1540. https://doi.org/10.1007/s11214-017-0370-8

Gregg, T. K. P., & Greeley, R. (1993). Formation of Venusian canali: Considerations of lava types and their thermal behaviors. *Journal of Geophysical Research: Planets, 98*(E6), 10873-10882. https://doi.org/https://doi.org/10.1029/93JE00692

Hansen, V. L., Willis, J. J., & Banerdt, W. B. (1997). Tectonic overview and synthesis. In S. W. Bougher, D. M. Hunten, & R. J. Phillips (Eds.), *Venus II: Geology, Geophysics, Atmostphere, and Solar Wind Environment* (pp. 797-844). University of Arizona Press.

Head, J. W., Crumpler, L. S., Aubele, J. C., Guest, J. E., & Saunders, R. S. (1992). Venus volcanism: Classification of volcanic features and structures, associations, and global distribution from Magellan data. *Journal of Geophysical Research: Planets, 97*(E8), 13153-13197. https://doi.org/https://doi.org/10.1029/92JE01273

Hopper, J. P., & Leverington, D. W. (2014). Formation of Hrad Vallis (Mars) by low viscosity lava flows. *Icarus, 207*, 96-113. https://doi.org/https://doi.org/10.1016/j.geomorph.2013.10.029

Hurwitz, D. M., Head, J. W., & Hiesinger, H. (2013). Lunar sinuous rilles: Distribution, characteristics, and implications for their origin. *Planetary and Space Science, 79-80*, 1-38. https://doi.org/10.1016/j.pss.2012.10.019

Hurwitz, D. M., Head, J. W., Wilson, L., & Hiesinger, H. (2012). Origin of lunar sinuous rilles: Modeling effects of gravity, surface slope, and lava composition on erosion rates during the formation of Rima Prinz. *Journal of Geophysical Research: Planets, 117*(E12), n/a-n/a. https://doi.org/10.1029/2011je004000

Ivanov, M. A., & Head, J. W. (2011). Global geological map of Venus. *Planetary and Space Science, 59*(13), 1559-1600. https://doi.org/https://doi.org/10.1016/j.pss.2011.07.008.

Jaeger, W. L., Keszthelyi, L. P., McEwen, A. S., Dundas, C. M., & Russell, P. S. (2007). Athabasca Valles, Mars: A Lava-Draped Channel System. *Science, 317*(5845), 1709-1711. https://doi.org/doi:10.1126/science.1143315

James, P. B., Zuber, M. T., & Phillips, R. J. (2013). Crustal thickness and support of topography on Venus. *Journal of Geophysical Research: Planets, 118*(4), 859-875. https://doi.org/10.1029/2012je004237

Kane, S. R., Arney, G., Crisp, D., Domagal-Goldman, S., Glaze, L. S., Goldblatt, C., Grinspoon, D., Head, J. W., Lenardic, A., Unterborn, C., Way, M. J., & Zahnle, K. J. (2019). Venus as a Laboratory for Exoplanetary Science. *Journal of*

Geophysical Research: Planets, *124*(8), 2015-2028. https://doi.org/10.1029/2019je005939

Kargel, J. S., Kirk, R. L., Fegley, B., & Treiman, A. H. (1994). Carbonate-Sulfate Volcanism on Venus? *Icarus*, *112*(1), 219-252. https://doi.org/10.1006/icar.1994.1179

Kargel, J. S., Komatsu, G., Baker, V. R., & Strom, R. G. (1993). The Volcanology of Venera and VEGA Landing Sites and the Geochemistry of Venus. *Icarus*, *103*(2), 253-275. https://doi.org/https://doi.org/10.1006/icar.1993.1069

Keszthelyi, L., & Self, S. (1998). Some physical requirements for the emplacement of long basaltic lava flows. *Journal of Geophysical Research: Solid Earth*, *103*(B11), 27447-27464. https://doi.org/https://doi.org/10.1029/98JB00606

Klimczak, C., Byrne, P. K., Şengör, A. M. C., & Solomon, S. C. (2019). Principles of structural geology on rocky planets. *Canadian Journal of Earth Sciences*, *56*(12), 1437-1457. https://doi.org/10.1139/cjes-2019-0065

Knicely, J. J. C., & Herrick, R. R. (2021). Survey of mid-sized Venusian volcanoes using stereo-derived topography. *Icarus*, *368*, 114577. https://doi.org/10.1016/j.icarus.2021.114577

Komatsu, G., & Baker, V. R. (1994). Plains Tectonism on Venus: Inferences from Canali Longitudinal Profiles. *Icarus*, *110*(2), 275-286. https://doi.org/10.1006/icar.1994.1121

Komatsu, G., Baker, V. R., Gulick, V. C., & Parker, T. J. (1993). Venusian Channels and Valleys: Distribution and Volcanological Implications. *Icarus*, *102*(1), 1-25. https://doi.org/https://doi.org/10.1006/icar.1993.1029

Komatsu, G., Kargel, J. S., & Baker, V. R. (1992). Canali-type channels on Venus: Some genetic constraints. *Geophysical Research Letters*, *19*(13), 1415-1418. https://doi.org/10.1029/92gl01047

Lang, N. P., & Thomson, B. J. (2022). *Global distribution of "undeformed" channels on Venus: First look and thoughts* Lunar and Planetary Science Conference 53rd,

McGovern, P. J., Rumpf, M. E., & Zimbelman, J. R. (2013). The influence of lithospheric flexure on magma ascent at large volcanoes on Venus. *Journal of Geophysical Research: Planets*, *118*(11), 2423-2437. https://doi.org/https://doi.org/10.1002/2013JE004455

McKenzie, D. (1994). The Relationship between Topography and Gravity on Earth and Venus. *Icarus*, *112*(1), 55-88. https://doi.org/https://doi.org/10.1006/icar.1994.1170

Nimmo, F., & McKenzie, D. (1998). VOLCANISM AND TECTONICS ON VENUS. *Annual Review of Earth and Planetary Sciences*, *26*(1), 23-51. https://doi.org/10.1146/annurev.earth.26.1.23

Oshigami, S., & Namiki, N. (2007). Cross-sectional profiles of Baltis Vallis channel on Venus: Reconstructions from Magellan SAR brightness data. *Icarus*, *190*(1), 1-14. https://doi.org/10.1016/j.icarus.2007.03.011

Parker, T. J., Komatsu, G., & Baker, V. R. (1992, March 01, 1992). *Longitudinal Topographic Profiles of Very Long Channels in Venusian Plains Regions* Lunar and Planetary Science Conference XXIII, https://ui.adsabs.harvard.edu/abs/1992LPI....23.1035P

Phillips, R. J. (1990). Convection-driven tectonics on Venus. *Journal of Geophysical Research, 95*(B2), 1301. https://doi.org/10.1029/jb095ib02p01301

Phillips, R. J., & Hansen, V. L. (1994). TECTONIC AND MAGMATIC EVOLUTION OF VENUS. *Annual Review of Earth and Planetary Sciences, 22*(1), 597-656. https://doi.org/10.1146/annurev.ea.22.050194.003121

Roberts, C. E., & Gregg, T. K. P. (2019). Rima Marius, the Moon: Formation of lunar sinuous rilles by constructional and erosional processes. *Icarus, 317*, 682-688. https://doi.org/https://doi.org/10.1016/j.icarus.2018.02.033

Rolf, T., Weller, M., Gülcher, A., Byrne, P., O'Rourke, J. G., Herrick, R., Bjonnes, E., Davaille, A., Ghail, R., Gillmann, C., Plesa, A.-C., & Smrekar, S. (2022). Dynamics and Evolution of Venus' Mantle Through Time. *Space Science Reviews, 218*(8). https://doi.org/10.1007/s11214-022-00937-9

Russell, M. B., & Johnson, C. L. (2021). Evidence for a Locally Thinned Lithosphere Associated With Recent Volcanism at Aramaiti Corona, Venus. *Journal of Geophysical Research: Planets, 126*(8). https://doi.org/10.1029/2020je006783

Saunders, R. S., Spear, A. J., Allin, P. C., Austin, R. S., Berman, A. L., Chandlee, R. C., Clark, J., Decharon, A. V., De Jong, E. M., Griffith, D. G., Gunn, J. M., Hensley, S., Johnson, W. T. K., Kirby, C. E., Leung, K. S., Lyons, D. T., Michaels, G. A., Miller, J., Morris, R. B., . . . Wall, S. D. (1992). Magellan mission summary. *Journal of Geophysical Research: Planets, 97*(E8), 13067-13090. https://doi.org/https://doi.org/10.1029/92JE01397

Shalygin, E. V., Markiewicz, W. J., Basilevsky, A. T., Titov, D. V., Ignatiev, N. I., & Head, J. W. (2015). Active volcanism on Venus in the Ganiki Chasma rift zone. *Geophysical Research Letters, 42*(12), 4762-4769. https://doi.org/https://doi.org/10.1002/2015GL064088

Smrekar, S. E., Stofan, E. R., Mueller, N., Treiman, A., Elkins-Tanton, L., Helbert, J., Piccioni, G., & Drossart, P. (2010). Recent Hotspot Volcanism on Venus from VIRTIS Emissivity Data. *Science, 328*(5978), 605-608. https://doi.org/doi:10.1126/science.1186785

Solomon, S. C., Smrekar, S. E., Bindschadler, D. L., Grimm, R. E., Kaula, W. M., McGill, G. E., Phillips, R. J., Saunders, R. S., Schubert, G., Squyres, S. W., & Stofan, E. R. (1992). Venus tectonics: An overview of Magellan observations. *Journal of Geophysical Research, 97*(E8), 13199-13255. https://doi.org/10.1029/92je01418

Stewart, E. M., & Head III, J. W. (2000). *Evidence for temporal continuity of deformation in the Baltis Vallis region of Venus from observations of canali topography* Lunar Planetary Science XXXI, https://www.lpi.usra.edu/meetings/lpsc2000/pdf/1692.pdf

Stewart, E. M., & Head, J. W. (1999). *Stratigraphic relations and regional slopes in the Baltis Vallis region, Venus: implications for the evolution of topography* Lunar Planetary Science XXX, https://www.lpi.usra.edu/meetings/LPSC99/pdf/1173.pdf

Stofan, E. R., Hamilton, V. E., Janes, D. M., & Smrekar, S. E. (1997). Coronae on Venus: morphology and origin. In S. W. Bougher, D. M. Hunten, & R. J. Phillips (Eds.), *Venus II: Geology, Geophysics, Atmosphere, and Solar Wind Environment* (pp. 931-965). University of Arizona Press.

Stofan, E. R., Smrekar, S. E., Bindschadler, D. L., & Senske, D. A. (1995). Large topographic rises on Venus: Implications for mantle upwelling. *Journal of Geophysical Research*, *100*(E11), 23317. https://doi.org/10.1029/95je01834

Strom, R. G., Schaber, G. G., & Dawson, D. D. (1994). The global resurfacing of Venus. *Journal of Geophysical Research*, *99*(E5), 10899. https://doi.org/10.1029/94je00388

Tanaka, K. L., Senske, D. A., Price, M., & Kirk, R. L. (1997). Physiography, geomorphic/geologic mapping, and stratigraphy of Venus. In S. W. Bougher, D. M. Hunten, & R. J. Phillips (Eds.), *Venus II: Geology, Geophysics, Atmosphere, and Solar Wind Environment* (pp. 667-694). University of Arizona Press.

Turcotte, D. L. (1993). An episodic hypothesis for Venusian tectonics. *Journal of Geophysical Research*, *98*(E9), 17061. https://doi.org/10.1029/93je01775

Walker, J. C. G. (1975). Evolution of the Atmosphere of Venus. *Journal of Atmospheric Sciences*, *32*(6), 1248-1256. https://doi.org/10.1175/1520-0469(1975)032<1248:Eotaov>2.0.Co;2

Williams-Jones, G., Williams-Jones, A. E., & Stix, J. (1998). The nature and origin of Venusian canali. *Journal of Geophysical Research: Planets*, *103*(E4), 8545-8555. https://doi.org/https://doi.org/10.1029/98JE00243

Williams, D. A., Fagents, S. A., & Greeley, R. (2000). A reassessment of the emplacement and erosional potential of turbulent, low-viscosity lavas on the Moon. *Journal of Geophysical Research: Planets*, *105*(E8), 20189-20205. https://doi.org/https://doi.org/10.1029/1999JE001220

Williams, D. R. (2022). Chronology of Venus Exploration. Retrieved 1 January 2023, from https://nssdc.gsfc.nasa.gov/planetary/chronology_venus.html

Zampa, L. S., Tenzer, R., Eshagh, M., & Pitoňák, M. (2018). Evidence of mantle upwelling/downwelling and localized subduction on Venus from the body-force vector analysis. *Planetary and Space Science*, *157*, 48-62. https://doi.org/10.1016/j.pss.2018.03.013